Underlying dynamics of lithospheric plates and their controls on surface topography

A thesis submitted for the degree of
Doctor of Philosophy (Science) of
Jadavpur University

By

Joyjeet Sen

Department of Geological Sciences
Jadavpur University
Kolkata 700032, India

February
2025

যাদবপুর বিশ্ববিদ্যালয়
কলকাতা-৭০০০৩২, ভারত

JADAVPUR UNIVERSITY
KOLKATA-700032, INDIA

FACULTY OF SCIENCE : DEPARTMENT OF GEOLOGICAL SCIENCES

CERTIFICATE FROM THE SUPERVISOR

This is to certify that the thesis entitled **“Underlying dynamics of lithospheric plates and their controls on surface topography”** submitted by **Sri. Joyjeet Sen** who got his name registered on **26.02.2018** for the award of **Ph. D. (Science)** Degree of Jadavpur University, is absolutely based upon his own work under the supervision of **Professor Nibir Mandal** and that neither this thesis nor any part of it has been submitted for either any degree / diploma or any other academic award anywhere before.

Nibir Mandal
10.02.2025

(Signature of the Supervisor(s) date with official seal)

NIBIR MANDAL
Professor
Dept. of Geological Sciences
Jadavpur University
Kolkata - 700 032

দূরভাষ : ২৪১৪-৬৬৬৬/প্রসারণ : ২২৬৮
Website : www.jadavpur.edu
E-mail : hod_geological@jdvu.ac.in
Phone : 2414 6666/Extn. 2268

Acknowledgements

It is with immense gratitude that I begin by acknowledging my supervisor, Professor Nibir Mandal, whose unwavering support, guidance, and mentorship have been the linchpin of this doctoral journey. From the very beginning, Professor Mandal has been an enduring source of inspiration, not only through exceptional intellect but also with keen attention to detail and profound insight. Beyond academic mentorship, I am particularly grateful for his psychological support during the challenging moments. His encouragement and belief in my potential helped me face difficulties with resilience and his patient approach in addressing both my doubts and triumphs allowed me to grow as an independent thinker. Professor Mandal's pedagogical insights and teaching methods will continue to inspire and guide me, fostering a lifelong foundation for advancing my academic career.

I also extend a heartfelt thanks to my research advisory committee, Professor Sukhen Das, and HODs (Department of Geological Sciences), whose expertise and advice were essential to the development of this research. Their insightful suggestions, thoughtful critiques, and support helped shape the thesis. The committee's influence has undoubtedly enriched the research and significantly elevated its quality.

I am deeply grateful to the INSPIRE Programme, Department of Science and Technology (DST), India for their generous financial support through both the Junior and Senior Research Fellowships during my doctoral journey. Their invaluable assistance has significantly shaped my academic path and empowered me to explore new avenues of scientific inquiry.

A special thanks to Dr. Shamik Sarkar, whose expert assistance in Finite Element Modelling has played a pivotal role in the success of my work. His knowledge and generous willingness to guide me through complex aspects of this research have been indispensable. Additionally, I would like to acknowledge Dr. Dip Ghosh, who has been instrumental in helping me shape my theoretical and numerical knowledge. His dedication to discussing and solving tangled problems with me has greatly enriched my understanding and approach.

My lab colleagues have been an essential part of this journey. I am especially grateful to Dr. Giridas Maiti, Dr. Ritabrata Dasgupta, Dr. Manaska Mukhopadhyay, and Dr. Dip Ghosh, who worked alongside with me in the laboratory, assisting in numerous experiments and engaging in countless discussions that enhanced the depth of my knowledge. A special thanks to Dr. Sudip Kumar Mondal, Dr. Arnab Roy and Dr. Uddalak Biswas for bringing a sense of humour and lightness to daily life in the laboratory. I am also thankful to Nandan, Jyotipriyo, Pramit, Ayan, Gourishankar, Soham, and Soumyadip for their constant support and criticism throughout this journey. The teamwork, camaraderie, and mutual support in the lab created an environment that was both intellectually stimulating and personally fulfilling.

I am deeply grateful to Giri, Anupam, Ayan, Gourishankar, and Pramit, whose generous friendship and financial assistance during crucial times alleviated many of the pressures I faced throughout this journey.

I will cherish forever my Jadavpur days, as they have shaped both my academic and personal growth. The university, with its philosophy of subsidized education, inclusivity, and accessibility, provided an environment where students from all backgrounds could thrive. The Department of Geological Sciences, in particular, exemplifies this ethos through its commitment to equity, collaboration, and a culture that celebrates diversity. The resources and opportunities offered by the department have been pivotal in broadening my research perspectives and empowering me to grow within a supportive, intellectually stimulating space.

Finally, I would like to express my deepest gratitude to my parents and elder brother, whose unwavering love, support, and encouragement have been my foundation throughout this journey.

Joyjeet Sen

Table of Contents:

Chapter 6 | Plume-lithosphere interaction: Implications for Deccan volcanism 196-227

Chapter 7 | Discussions and Conclusions 228-269

Publications

Abstract

The lithosphere forms the mechanically strongest and outermost layer of the Earth, with its thickness varying from approximately 100 km in oceanic regions to about 150 km in continental regions. Lithospheric dynamics govern nearly all tectonically driven geological phenomena, including plate boundaries (sites of intense tectonic activity), mountain formation, and large-scale topographic developments in both continental and oceanic regions. Geophysical observations and geological evidence suggest that the mechanical and thermo-mechanical interactions between the lithosphere and the underlying mantle play a crucial role in shaping different dynamic regimes in the lithosphere, such as convergent and divergent plate boundaries, intra-cratonic rifting, and epeirogenic movements. Consequently, an important area of research focuses on conceptualizing large-scale mantle flow processes, e.g., thermal convection, slab movements, and plume ascent, to better understand lithospheric dynamics. Each of these processes creates a distinct dynamic environment in the lithosphere, characterized by specific geological and geophysical responses. Large-scale surface topography is a prominent manifestation of geodynamic processes in the mantle. However, establishing a quantitative relationship between mantle dynamics and surface topography poses complex challenges, and addressing such problems often requires an interdisciplinary approach. This thesis explores a set of outstanding topographic issues in critical tectonic regimes of Earth's lithosphere, as outlined below.

A part of this thesis deals with the origin of contrasting crustal topography in mid-ocean ridge (MOR) systems. Although there has been a significant research advancement on divergent plate boundaries and their associated phenomena, the problem of MOR axial topography is still inadequately explained. Consequence, this has remained a subject with many open-ended questions. A part of the thesis work utilizes an interaction dynamics of the elastic oceanic crust with the underlying mush complexes (MC) to constrain the axial topography of MORs. The effective bulk viscosity (μ_{eff}) of MC beneath MORs is projected as the crucial mechanical factor in modulating their axial high versus flat topography. Based on a two-stage viscosity calculation, utilizing the suspension and solid-melt mixture rheology, this work provides a theoretical estimate of μ_{eff} as a function of melt suspension characteristics (crystal content, polymodality and polydispersity, strain-rate), its volume fraction in the MC region. Subsequently, this study develops a solid (elastic lithosphere) – fluid (melt-rich mantle region) finite model to test the control of μ_{eff} on the axial topography. The model couples an enthalpy-porosity based fluid formulation to implement a one-way fluid-structure interaction (FSI) that transmits the dominating normal viscous force to the overlying lithosphere. The limiting non-rifted topographic elevations (-0.06 km to 1.27 km) of natural MORs are found to occur in the range $\mu_{eff} = 10^{12}$ to 10^{14} Pa s. The higher end (10^{13} to 10^{14} Pa s) of this spectrum produces axial highs, which are replaced by flat or axial valley topography as $\mu_{eff} \leq 5\text{x}10^{12}$ Pa s. The present thesis uses the FSI model to explain the following MOR phenomena: topographic stability, co-existence of melt-poor and -rich conditions in a ridge, and local variations of axial topography in fast-spreading ridges.

Geophysical evidence suggest that MOR systems evolve in strongly heterogeneous stress environments. However, the origin of such stress complexity still awaits a comprehensive explanation, which is the central theme of the present thesis. This study develops a thermo-mechanical model to demonstrate the multi-ordered 3D convective circulations, produced by decompression melting in the mushy region, as the key factor to modulate the MOR dynamics. The model mechanically couples the sub-ridge mushy regions with the elastic crustal layer within a mathematical framework of FSI mechanics. FSI model simulations show that the heterogeneous stress field of a MOR forms characteristic segmented patterns on a time scale of million years, resembling axial as well as off-axis topographic morphologies observed in MORs. This work provides a model calculated estimate of the total stress tensor, focusing on the following components: across- and along-axis horizontal tension / compression ($\sigma^{\perp}$ and $\sigma^{/\!/}$) and across-axis horizontal shear stress ($\sigma^{\#}$) that dominantly control the ridge-axis morphologies. The stress mapping reveals a distinct 30 km wide axial zone of tensile $\sigma^{\perp}$ localization (median < 250 MPa), whereas compressive $\sigma^{\perp}$ localization (median < 100 MPa) in off-axis ridge-parallel linear belts on either side of the MOR axis. This finding leads to an alternative explanation for the off-axis ridge-parallel second-order hill topography, located at a distance of 20 km to 50 km, as a consequence of compressional $\sigma^{\perp}$ localization. Along-axis compressional $\sigma^{/\!/}$ concentrates in a row of ridge-normal narrow, 10 to 30 km wide stripes, giving rise to segmentation of the stress field on a

wavelength of 40-150 km, which conforms to the second-order magmatic segmentation patterns of MORs. From $\sigma^{\#}$ mapping, it is also shown that ridge-transverse discontinuities, including transform offsets and transpression zones originate spontaneously from the FSI interactions during the MOR evolution.

The cause of eastward tilting of the Indian Peninsular (IP) plateau is a lively issue of ongoing debate in geoscience. This thesis invokes a fresh geodynamic perspective, employing extensive topographic analyses to recognize the mechanisms behind this tilting. By analyzing the eastward-flowing river systems in relation to the plateau's tilt, we constructed a series of east-west topographic profiles using digital elevation models (DEM). The DEM findings indicate a steady increase in eastward slopes (θ = 0.008° to 0.3°) from the northern boundary to the southern tip of the plateau. Large-scale thermo-mechanical simulations reveal that the configuration of the Indian plate plays a crucial role in driving this tilt. Specifically, this study finds that the older lithosphere beneath the Bay of Bengal (age ~ 140 Ma) has undergone subsidence at a significantly faster rate than the younger lithosphere beneath the Arabian Sea (age ~ 60 Ma). This differential subsidence has set in westward sub-lithospheric flows beneath the Indian Peninsula, interacting with east-directed mantle flows originating from regions below the Arabian lithosphere. This interaction has resulted in a localized mantle upwelling at the Western IP margin, contributing to the Western Ghats Escarpment (WGE) formation. Furthermore, we examine spatial variations in sub-lithospheric flow patterns to account for the increasing θ towards the south. The present findings suggest that the eastward topographic tilt of the IP originates from sub-lithospheric mantle dynamics, driven by lithospheric density contrasts between the Bay of Bengal and the Arabian Sea. The present thesis provides valuable insights into the drainage patterns in IP.

An important direction of the thesis focuses on the problem of plume-lithosphere interaction, which is thought to be a critical process involved in the development of many continental rift system. Using numerical models, a part of this study explores the structural evolution of a rift formed under the influence of a mantle. Additionally, the response of a pre-existing rift to a specific plume event is investigated to deal with the Indian rift systems. Indian craton comprises a number of old rifts, e.g., the Narmada and the Godavari rifts, which reactivated in multiple stages during the supercontinent breakup events. The latest reactivation of the Indian rift system occurred at the Cretaceous-Tertiary boundary when the Réunion plume interacted with the Indian plate, leading to the massive Deccan volcanism at 66 Ma. Although the plume-driven rift tectonics has been a subject of lively research over past decades, how a pre-existing rift system can modulate the plume dynamics, particularly in continental settings, remains inadequately explored. This study addresses this problem in the context of the Réunion plume encountering the Indian lithosphere. 2D thermomechanical models are developed to simulate plume-rift interactions, systematically investigating the modes of interactions as a function of plate velocity (V_p) and plume–rift (δ) distance. Numerical experiments reveal that small δ (< 250 km) or high V_p (> 1cm/year) conditions redirect a large portion of the plume material towards the pre-existing rift, resulting in significant underplating beneath the rift undergoing reactivation. Increasing δ or lowering of V_p weakens the plume-rift interaction, leaving the pre-existing rift zone almost passive, where the underplated plume materials stagnate beneath the rift with little melting. The model results suggest that the Narmada rift, which was closer to the Réunion plume, caused significant deflection of the plume and its melting with Moho upwrapping. In contrast, the Godavari rift, located at a larger distance from the plume, behaved passively, allowing underplating of the plume at the lithospheric base with no significant melting and Moho downwrapping, as supported by geophysical observations. Finally, this thesis provides a new insight into the differential responses of the Indian rift system during the Reunion plume event.

Chapter 1 | Introduction

1.1. Surface topography: Earth’s geodynamic manifestations

Topography is one of the most fundamental surface expressions of the Earth, providing reliable clues for exploring the interactions between deep-seated geodynamic processes and various exogenous phenomena, such as material loading, erosion, and denudation. The surface topography critically controls a range of Earth’s ecosystems, directs water and sediment transport patterns, influences climatic conditions and their spatio-temporal variations, and dictates human settlement behaviours. Beyond these practical and ecological bearings, Earth's topography also offers crucial insights into the internal dynamic processes and tectonic evolution on varied scales. From the high peaks of the Himalayas to the abyssal plains of the deep oceans, the Earth's surface reflects a complex interplay between endogenic and exogenous forces operating on a wide range of spatial and temporal scales. Understanding the mechanisms of topographic building vis-a-vis denudation has led to an important field of Earth science research, bridging the disciplines of geology, geophysics, geodynamics and tectonics.

Earth's large-scale topography in a terrain generally consists of two major components: tectonic topography and dynamic topography. Although both of them manifest forces generated in the lithosphere, they manifest specific processes. Tectonic topography primarily results from crustal and lithospheric density variations, isostatic dynamics, and crustal deformations, such as orogenesis, rifting, and faulting (Flament et al., 2013). For example, the Himalayan Mountain topography evolve through crustal shortening in the India-Asia collision zone, a tectonic process driven by the convergence of the continental lithospheric plates. Dynamic topography, on the other hand, originates from long-term upwelling or downwelling flows in Earth’s mantle (Flament et al., 2013; Forte and Rowley, 2022; Gurnis, 1993; Richards and Hager, 1989). Unlike tectonic topography, which is often localized and of relatively high-amplitude characteristics, dynamic topography typically occurs on long-wavelengths (>5000 km) and of much lower amplitudes (±2 km) and develops over geological timescales, exerting a profound influence on regional and global elevation patterns (Flament et al., 2013; Richards et al., 2020).

Plate tectonics serves as the primary mechanism in shaping Earth's lithosphere and its associated surface topography, including both dynamic and tectonic elements. Strong lithospheric plates, moving atop the mechanically weak asthenosphere, mutually interact with one another at divergent, convergent, and transform boundaries, leading to evolution of characteristic topographic features through localized tectonic deformations and mantle flows. At divergent boundaries, tectonic processes, such as seafloor spreading at mid-ocean ridges result from asthenospheric upwelling, which generates new oceanic lithosphere moving outward symmetrically (Dietz, 1961; Hamilton, 2019; Hess, 1962; Vine and Matthews, 1963). The tectonic topography of ridges and rift valleys is accompanied by dynamic topographic uplift due to the upwelling of buoyant mantle materials beneath these zones. Similarly, at convergent boundaries dense oceanic lithosphere subducts into the mantle, forming prominent tectonic features, such as deep-sea trenches, volcanic arcs, and orogenic belts (Isacks et al., 1968; Keith, 2001; Morgan, 1968). These regions also exhibit significant contributions of dynamic topography to the net topographic development due to slab-induced mantle flows, which gives rise to long-wavelength surface deformation modifying the overlying crustal architecture. Transform boundaries, characterized by lateral displacement along strike-slip faults, also contribute to tectonic topography through localized deformations, while influencing broader dynamic processes such as lithospheric shearing and mantle flow responses (McKenzie and Morgan, 1969; Wilson, 1965). These processes together underscore the interplay of tectonic mechanisms and mantle convection in shaping Earth’s surface topography.

The coupling of lithospheric plates at divergent and convergent boundaries ensures the conservation of mass and momentum on the spherical Earth, linking tectonic topography with the broader mantle dynamics that gives rise to dynamic topographic adjustments (McKenzie and Parker, 1967; Pichon, 1968). Subduction zones exemplify this interplay, where the gravitational pull of sinking slabs generates mantle flow, inducing dynamic topography that extends far beyond the immediate tectonic setting (Hess, 1962; McKenzie, 1969). Rollback of subducting slabs creates space for asthenospheric upwelling, driving active rifting and back-arc extension that shapes both tectonic and dynamic topography in subduction zones(Dewey, 1972; McKenzie and Morgan, 1969). In addition, passive rifting at some distant locations, triggered by slab pull and mantle flow, signifies how tectonic and dynamic forces operate on interconnected global scales. On geological timescales, intracontinental regions witness the reactivation of fossil suture zones, where asthenospheric upwelling causes lithospheric thinning, modifying both tectonic and dynamic topography (Hill, 1993; Paul and Ghosh, 2022; Sheth and Chandrasekharam, 1997). The transition from ancient tectonic systems during the Archean and Proterozoic eras to the modern plate tectonic regime in the Phanerozoic eon reflects changes in lithospheric rheology, mantle convection patterns, and surface expression.

During the Archean time, the warmer mantle and weaker lithosphere facilitated collisional thickening and warm subduction, producing broader, less pronounced tectonic topography (Hamilton, 1998). In contrast, modern plate tectonics, dominated by cold subduction and strong plate boundaries, generates sharper tectonic features, such as steep mountain ranges and deep oceanic trenches, while maintaining dynamic topography through mantle-driven processes (McKenzie, 1969).

1.2. Dynamic topography

Dynamic topography is a transient phenomenon driven by density anomalies within the Earth's interior, which result from variations in temperature, composition, and phase changes, and generate buoyancy forces that perturb the Earth's surface (Davies et al., 2019). The concept of dynamic topography has evolved significantly since it was first proposed by Pekeris (1935). Early models largely focused on steady-state mantle processes, but advances in computational facilities and seismic imaging techniques have refined our understanding of the mantle's structure and its dynamic evolution. Recent mantle convection models constrained by seismic tomography and plate reconstructions provide a detailed picture of how dynamic topography varies spatially and temporally (Flament et al., 2013; Liu, 2015). For example, the uplift of southern Africa during the Cenozoic, the tilting of the Australian continent since the Late Cretaceous, and the subsidence of North America during the Mesozoic have all been attributed to dynamic processes within the mantle (Gurnis et al., 2000; Shephard et al., 2010; Spasojevic et al., 2009).

Long-wavelength dynamic topography reflects mantle flows due to large-scale density anomalies distributed throughout the lithosphere and sub- lithospheric mantle. Observations of residual topography—calculated by removing the isostatic contributions of the lithosphere, crust, and sediments from observed topography—have provided critical constraints on the present-day expression of dynamic topography (Hoggard et al., 2017; Thomas Crough, 1983). Residual topography maps often reveal highs associated with mantle upwellings, such as the African Super- swell, and lows corresponding to subduction zones and slab stagnation, such as the Argentine Basin (Richards et al., 2020). These observations are further supported by global mantle convection models that predict the surface deflections induced by sub- lithospheric flow (Conrad and Husson, 2009; Steinberger, 2007). The temporal evolution of dynamic topography presents additional challenges and opportunities for understanding Earth's geodynamic processes. Because mantle flow evolves over tens of millions of years, dynamic topography is inherently transient and leaves a subtle yet detectable imprint on the geological record. For example, the episodic flooding and subsequent uplift of continental interiors, such as the Western Interior Seaway of North America during the Late Cretaceous, are attributed to dynamic topography associated with the subduction of the Farallon plate (Liu et al., 2008; Spasojevic et al., 2009). Similarly, in South America, the Andean orogeny provides a striking example of the interplay between tectonic and dynamic forces. While tectonic convergence has thickened the crust to form the Andes, dynamic topography driven by mantle upwelling beneath the South American plate adds to the region's anomalous elevation (Shephard et al., 2010). On the other hand, tectonic topography reflects the interaction of lithospheric plates and the forces driving their motion. The formation of mountain belts, rift valleys, and large-scale fault systems are classic examples of tectonic processes shaping the Earth's surface. This kind of topography is often associated with isostatic compensation, whereby variations in crustal thickness and density give rise to surface reliefs with characteristic elevation patterns. For instance, mountain ranges, such as the Andes are underpinned by thickened continental crust, while rift zones like the East African Rift are characterized by crustal thinning (Mooney et al., 1998). Unlike the gradual, long-wavelength adjustments of dynamic topography, tectonic processes can produce abrupt and localized changes (Zoback and Mooney, 2003).

Many continental regions exhibit a complex interplay of tectonic forces and mantle flows in producing their surface topography. For example, the Andes Mountains, primarily a product of tectonic convergence, are thought to be superimposed on a dynamic topographic high driven by mantle upwelling beneath the South American plate (Shephard et al., 2010). Similarly, the Colorado Plateau in the United States owes its anomalous elevation to a combination of lithospheric buoyancy and dynamic support from the underlying mantle (Moucha et al., 2009). A direction of studies integrates observational data and numerical models to decouple the contributions of dynamic and tectonic processes to Earth's topography (Bishop, 2007; Flament et al., 2013; Forte and Rowley, 2022). Seismic tomography provides three-dimensional images of the mantle's thermal and compositional structure, which can be used to infer mantle flow patterns and their surface expression (Grand, 2002; Romanowicz, 2008). Plate reconstructions are further used to constrain the temporal evolution of mantle flow, linking surface geology to subduction history and plate motions (Seton et al., 2012). These approaches have led to a growing consensus on the importance of dynamic topography in shaping large-scale Earth's surface features. However, significant uncertainties remain, particularly in quantifying the relative contributions of dynamic and tectonic processes at different spatial and temporal scales (Flament et al., 2013). This thesis addresses both dynamic and tectonic topography across different tectonic settings, ranging from divergent boundaries to stable cratons. By examining these distinct geological environments, the present study aims to provide a comprehensive understanding of the processes shaping the Earth's surface and their profound connectivity to the deep interior. Such an integrated approach highlights the intricate interactions between mantle convection and lithospheric deformation.

1.3. Mid-oceanic ridge processes

In the framework of plate tectonics, mid ocean ridges (MORs) constitute a complex plate boundary, involving broadly synchronous melting and solidification processes. MORs exhibit a remarkable diversity in their axial topographies, ranging from elevated axial highs to deep rift valleys, driven by a complex interplay of tectonic, magmatic, and mantle processes. The axial morphology has traditionally been attributed to spreading rates, with faster spreading ridges, like the East Pacific Rise producing smoother and elevated axial highs, while slower spreading ridges, like the Mid-Atlantic Ridge tend to form axial valleys (Sinton and Detrick, 1992; Small, 1998). However, the spatial variability of MOR topographies is hard to account for with this simplistic view. For instance, the South-East Indian Ridge (SEIR) shows uniform spreading rates, but of varying topographies, such as flat crests and axial highs (Carbotte et al., 2016). Conversely, the South-West Indian Ridge (SWIR), characterized by ultra-slow spreading, displays deep axial valleys despite abundant magma supply (Jian et al., 2017). These discrepancies suggest that there must be factors beyond spreading rates, such as magmatic supply, sub-crustal viscosity, and upper crustal faulting in controlling the MOR axial topography (Buck et al., 2005; Keller et al., 2017; Mandal et al., 2018). By combining magmatic and tectonic controls, this study aims to bridge the existing gaps in the light of a comprehensive thermo-mechanical model that accounts for sub-crustal ridge processes.

Recent MOR models have introduced a factor, called M factor, defined as the ratio of dike intrusion rates to plate-spreading rates, in explaining axial topography(Chadwick and Embley, 1998; Sen et al., 2023). A M value of 1, signifying a balance between dike intrusion and spreading, results in elevated axial highs, while $M < 1$ produces faulted axial valleys due to the dominance of tectonic extension over magmatic input (Buck et al., 2005; Ito et al., 2008). Although this framework integrates tectonic and magmatic contributions, it oversimplifies the complex dynamics of MORs by ignoring the role of sub-crustal melt processes, such as melt transport and crystallization (Carbotte et al., 2021; Martinez et al., 2020). Additionally, models relying solely on the M factor fail to account for the varying viscosity of mush-rich zones beneath ridges, which play a critical role in determining axial morphology (Choi and Buck, 2010). For example, low-viscosity regions beneath MOR axes have been associated with buoyancy-driven upwelling, resulting in axial highs (Buck, 2001; Eberle and Forsyth, 1998). Conversely, high-viscosity zones can hinder melt upwelling, promoting the formation of axial valleys. These shortcomings highlight the need for an alternative modelling approach, one that integrates sub-crustal dynamics with surface processes. This thesis addresses these issues by incorporating a three-dimensional fluid-structure interaction (FSI) model to evaluate the mechanical influence of mush complexes on axial morphology, and provide a more robust explanation for the observed variations in MOR topographies.

Sub-crustal processes, particularly melt transport, solidification, and crystallization, appear to be the key processes in controlling the formation of axial highs and valleys at MORs. Earlier studies have demonstrated that melt-rich zones beneath MORs often localize into discrete channels, mediating the magma supply to ridge axes (Sarkar et al., 2014; Sparks et al., 2019). These channels, characterized by high melt fractions, facilitate focused magma transport, which contrasts with the broader divergence-driven flow patterns observed in the mantle (Hewitt, 2010). Numerical models have shown that the crystallization of ascending melts forms mush complexes—regions of crystal-bearing melts—that significantly influence the viscosity structure beneath MORs (Braun et al., 2000; Sparks et al., 2019). Choi and Buck (2010) highlighted that shallow mantle viscosities as low as 10^{18} Pa s are required for axial highs, while viscosities exceeding 10^{21} Pa s can result in axial valleys due to the suppression of melt upwelling. Furthermore, dehydration during partial melting can increase viscosity, affecting the mechanical properties of the mush zones (Hirth and Kohlstedt, 2004). However, experimental data suggest that such effects may be limited to deeper mantle regions, as partial melting typically ceases at greater depths (Kelemen et al., 2000). This thesis aims to systematically quantify the effective viscosity of sub-crustal mush complexes in analysing the possible role of mush viscosity in determining MOR topography using coupled fluid-structure interaction modelling.

Despite significant advances in the studies of MOR dynamics, as discussed above, existing models are yet to offer a unified explanation for the topographic variations observed in MORSs. Recent studies emphasize that sub-crustal melt processes, such as the localization of melt-rich zones and their mechanical interactions with the overlying crust, are critical to

MOR evolution (Carbotte et al., 2016; Martinez et al., 2020; Sparks et al., 2019). However, most numerical models have focused on either tectonic or magmatic processes in isolation, without any attempt for their coupled effects. For example, while the M factor provides a simplified measure of the balance between magmatic and tectonic forces, it does not account for the spatial variability in sub-crustal viscosity or the influence of mush complexes on axial morphology (Buck et al., 2005; Liu and Buck, 2018). To address these gaps, a part of thesis integrates sub-crustal dynamics with tectonic processes in a three-dimensional thermo-mechanical framework. By modelling the mechanical connection between mush complexes and the overlying crust, this study offers a novel perspective on the factors governing axial highs, flat crests, and valleys. The results aim to establish a comprehensive understanding of MOR processes, contributing to broader geodynamic theories of crustal formation and mantle behaviour.

Stress estimation of MOR tectonic settings is crucially important to explore the origin of their characteristic topographic features, as it allows us to directly correlate the mechanical forces with the lithosphere and the underlying magmatic processes. It is now evident that the stress fields at MORs are far more complex than the simplistic ridge-axis normal tensional setting, as often speculated in the perspective of divergent tectonics. Bi-axial stress regimes, characterized by along-axis tension and across-axis compression, as well as localized shear stress zones, are now recognized as the integral components of MOR dynamics. Such stress complexities are reflected from various observed features, such as ridge segmentation, transform fault activities, and variations in axial topography. For instance, transverse segmentation and stress intensification at segment ends, as reported by Gràcia et al. (1999) and Behn and Ito (2008), highlight the interaction of magmatic and tectonic forces, which cannot be fully explained without a robust stress analysis. Additionally, borehole stress measurements and earthquake focal mechanisms demonstrate the critical role of off-axis and ridge-parallel stress fields in influencing the mechanical behaviour of oceanic lithosphere (Moos and Zoback, 1990; Parnell-Turner et al., 2017). This thesis delves into the significance of these stress regimes by developing a unified thermomechanical model, which incorporates magmatic, tectonic, and thermal interactions, with an objective to find a quantitative relation between stress distributions and MOR morphological patterns.

Accurate stress estimation is essential not only for characterizing the topographic features of MORs, but also for a dynamic analysis of the underlying mushy regions. It is important to note that sub-ridge mushy zones critically govern melt transport and lithospheric deformations at MOR settings. Current models, especially those based on lithospheric bending (Sohn and Sims, 2005) and topographic relief (Luttrell and Sandwell, 2012), are somewhat incomplete as they do not fully capture the interplay between axial tension, across-axis compression, and ridge-parallel shear stresses. These stress fields directly impact the development of faulting patterns, abyssal hill structures, and transform fault zones, and all of them significantly contribute to the observed variability in ridge topography. Moreover, the spatial heterogeneity in stress regimes—such as the co-occurrence of compressive and tensile stresses along ridge axes (Craddock et al., 2004; Maia et al., 2016)—indicates a more intricate stress-strain relationship that demands a unified modelling approach. By integrating the mechanical effects of partial melting, melt migration, and crustal deformation, this thesis bridges these gaps, providing a dynamic framework to analyze the role of stress in shaping the morphotectonic evolution of MOR systems.

1.4. Indian peninsular craton: geodynamic and geological issues

The eastward tilting of Peninsular India presents a long-standing geodynamic enigma, characterized by a distinct asymmetric topography that has shaped its drainage patterns and landscape evolution. This tilt originates from the elevated Western Ghats (WG) along the western margin, which stands at ~1,500 meters, and gently slopes towards the Bay of Bengal (BOB) in the east. Unlike the tectonically active Himalayan-Tibetan orogen to the north, Peninsular India lies in a tectonically stable setting with relatively infrequent seismic activity (M., 1999; Valdiya and Sanwal, 2017). Despite its stability, the region exhibits a persistent topographic gradient and a predominant eastward flow of rivers, such as the Godavari, Krishna, and Kaveri, traversing the entire plateau. The origin of this large-scale physiographic feature remains uncertain, with hypotheses ranging from ancient tectonic processes, such as rifting and magmatism during the breakup of Gondwana (~65 Ma) (Cox, 1989; White and McKenzie, 1989) to more recent neo-tectonic activities (Valdiya and Sanwal, 2017; Vita-Finzi, 2004).The present thesis aims to address this unresolved question through an integrated geodynamic approach, combining numerical modelling and topographic analysis to explore the underlying mechanisms responsible for the eastward tilting of the Indian peninsular plateau.

Existing hypotheses on the cause of continental scale tilting include lithospheric flexural responses to sediment loading along passive margins (Watts and Cox, 1989), mantle-driven regional uplift(Radhakrishna et al., 1991), and differential lithospheric subsidence beneath the Arabian Sea and BOB (Hoggard et al., 2016). Notably, residual depth anomaly measurements suggest that the tilt extends into the adjacent oceanic lithosphere, with higher subsidence rates in the denser, older lithosphere beneath the BOB compared to the Arabian Sea (Becker, 2017; Cox, 1989).This differential subsidence likely drives mantle flows directed westward beneath the Indian subcontinent, causing upwelling at the western boundary and subsequent uplift of the WG. Furthermore, paleoclimatic and geomorphological evidence, such as lateritic deposits along both continental margins (Bonnet et al., 2014; Raju, 2013), points to significant denudation events during the Paleogene and Neogene, which could have accentuated the tilt. However, competing models, including asthenospheric flow patterns (Becker et al., 2012; Russo and Silver, 1994) and Proterozoic tectonic imprints (Mishra and Ravi Kumar, 2014), highlight the complexity of the problem. The study presented in this thesis develops 3D numerical simulations to test the interplay of lithospheric properties, mantle flow, and isostatic adjustments in shaping the eastward-sloping topography. By integrating these findings, the simulations are performed to find a comprehensive explanation for the asymmetric physiography and its implications for the drainage pattern in Peninsular India.

The interaction between mantle plumes and continental rift systems is an important direction of geoscience research, especially to deal with the problems of large igneous provinces (LIPs), as seen in the Deccan Volcanic Province (DVP) in peninsular India. The DVP, which is associated with the Réunion hotspot, represents one of the most significant volcanic events in Earth's history, producing extensive flood basalts that cover over 500,000 km^2 and reach thicknesses exceeding 1.5 km. The geological and geophysical evidence indicates that the Réunion plume interacted significantly with pre-existing rift structures in the Indian craton, such as the Cambay Rift (CBR), the Godavari Graben (GG), and the Mahanadi Rift (MHR). These rift systems, which formed during previous tectonic events, created zones of weakness in the lithosphere, and it is believed that they played an important role in controlling the emplacement of plume-derived magmatism. The CBR, for example, divides the Deccan Traps into two distinct units, one to the northwest and the other to the southwest (Danda et al., 2020), with evidence suggesting that the rift’s extensional tectonics facilitated the migration and accumulation of plume material along these zones. Similar processes have been observed in the Godavari and Mahanadi rift systems, which, although considered passive features, influenced magma pathways and focused volcanic activity along the rift zones. This thesis work explores how these pre-existing rifts within the Indian craton modulated the plume–rift interactions during the Deccan volcanic event, investigating how the presence of these structural weaknesses affected plume dynamics and the spatial distribution of the resulting magmatic provinces.

Numerical simulations and laboratory experiments have revealed that pre-existing rift zones play a significant role in modifying plume dynamics during continental rifting and magmatism. The thermo-mechanical effects of mantle plumes, such as upwelling and associated magma emplacement, are known to weaken the overlying lithosphere, thereby facilitating the rifting process (Hill, 1993; Van Hinsbergen et al., 2011; Paul and Ghosh, 2022). In the case of the DVP, this weakening effect possibly contributed to the reactivation of rift zones, promoting localized magma extraction followed by decompression melting. The interaction of the Réunion plume with these pre-existing rifts is particularly crucial in understanding the spatial distribution of volcanic activity. For instance, the Godavari Graben has been shown to influence the migration of plume materials, redirecting them to accumulate beneath the rift axis, which contributed to the formation of a more concentrated volcanic province in the western part of peninsular India (Rao et al., 2022; Sheth and Chandrasekharam, 1997; Veeraswamy and Harinarayana, 2006). Furthermore, the Narmada-Son Lineament (NSL), an east-west tectonic feature, appears to have served as a major structural boundary that separated different tectonic zones in northern and southern India (Meert et al., 2010), playing a significant role in modulating the movement of plume material beneath the lithosphere. The interaction between the plume and the rift systems is governed by a combination of forces, including tectonic plate movements, gravitational forces, and the extensional stress generated by the rifting process (Ribe and Christensen, 1999, 1994). These forces can either draw plume material toward the rift or divert it away, depending on the relative positions of the rift and the plume source, as well as the geological properties of the rift zones themselves. A part of the present thesis explores the modes of such complex interactions in the context of the Deccan volcanic event, and provide new insights into how the pre-existing rift systems in the Indian continent influenced the plume ascent, the distribution of magmatism, and the overall volcanic architecture of the region.

1.5. The thesis structure

This thesis is organized into seven chapters, each addressing specific aspects of geodynamic modelling, with a focus on the interplay between mantle dynamics, tectonics, and volcanic phenomena in the process of topographic developments in various lithospheric settings. The next chapter, **Chapter 2** provides an introduction to the fundamental theory used in computational fluid dynamics (CFD) modelling. This chapter begins with an outline of the basic principles of fluid mechanics, followed by a detailed explanation of the computational fluid dynamic model. It also discusses the theory and applications of finite element modelling (FEM) and finite difference methods (FDM), providing a detailed description of the numerical techniques used to simulate fluid behaviour in the context of geodynamics. **Chapter 3** is dedicated to deal with the problems of mid-ocean ridges (MOR), specifically addressing the outstanding issues of axial highs and axial lows. The chapter investigates the topographic features of mid-ocean ridges, particularly focusing on the mechanisms of formation of axial highs and lows. This chapter centres on the question- how do dynamic processes beneath the ridge axis produce topographic features, such as the axial high and lows. A significant part of this chapter covers an original theoretical treatment on the bulk viscous rheology of mushy materials beneath MORs and its control on the development of ridge topography. **Chapter 4** explores the stress fields of mid-ocean ridges (MOR) in the light of sub-ridge mush dynamics. This chapter also elaborates how the mechanical properties of the mush layer can modulate the way stress is transmitted across the ridge system and the broader oceanic lithosphere. **Chapter 5** focuses on the lively issue on the cause of eastward tilting in stable cratons of Indian Peninsula. The chapter describes the topographic characteristics of the peninsular plateau, with a quantitative analysis of the eastward tilt of the peninsular landmass. A geodynamic model is presented to demonstrate the underlying causes of this eastward topographic gradient, especially in relation to sub-lithospheric mantle dynamics. **Chapter 6** delves into the plume-rift interaction within the context of Deccan volcanism, showing how mantle plumes, such as the Réunion plume, interact with pre-existing rift structures in the Indian craton and how such plume-rift interactions influence the magmatic events responsible for the formation of the Deccan Traps. This study accounts for the Cambay Rift and the Godavari Graben in showing their effects on the plume, especially in guiding the plume ascent behaviour and influencing the timing, location, and scale of volcanism during the Cretaceous period. **Chapter 7** presents the final discussion and synthesis of key findings from the studies covered in the previous chapters. This chapter highlights the significance of axial highs and lows in mid-ocean ridges and the role of mush dynamics in controlling ridge topography. It also provides a detailed analysis of the eastward tilting of the peninsular Indian topography, offering a geodynamic explanation for this phenomenon. Additionally, this chapter discusses the interaction between pre-existing rift structures and plume dynamics during the Deccan volcanic event, shedding light on how these rifts influenced the migration and emplacement of plume materials.

1.6. References

Becker TW. Superweak asthenosphere in light of upper mantle seismic anisotropy. Becker, T.W., 2017. Superweak asthenosphere in light of upper mantle seismic anisotropy. Geochemistry, Geophysics, Geosystems 18, 1986–2003. https://doi.org/10.1002/2017GC006886

Becker, T.W., Lebedev, S., Long, M.D., 2012. On the relationship between azimuthal anisotropy from shear wave splitting and surface wave tomography. J Geophys Res Solid Earth 117, 1306. https://doi.org/10.1029/2011JB008705

Bishop, P., 2007. Long-term landscape evolution: linking tectonics and surface processes. Earth Surf Process Landf 32, 329–365. https://doi.org/10.1002/ESP.1493

Bonnet, N.J., Beauvais, A., Arnaud, N., Chardon, D., Jayananda, M., 2014. First 40Ar/39Ar dating of intense Late Palaeogene lateritic weathering in Peninsular India. Earth Planet Sci Lett 386, 126–137. https://doi.org/10.1016/J.EPSL.2013.11.002

Braun, M.G., Hirth, G., Parmentier, E.M., 2000. The effects of deep damp melting on mantle flow and melt generation beneath mid-ocean ridges. Earth Planet Sci Lett 176, 339–356. https://doi.org/10.1016/S0012-821X(00)00015-7

Buck, W.R., 2001. Accretional curvature of lithosphere at magmatic spreading centers and the flexural support of axial highs. J Geophys Res Solid Earth 106, 3953–3960. https://doi.org/10.1029/2000JB900360

Buck, W.R., Lavier, L.L., Poliakov, A.N.B., 2005. Modes of faulting at mid-ocean ridges. Nature 2005 434:7034 434, 719–723. https://doi.org/10.1038/nature03358

Carbotte, S.M., Marjanović, M., Arnulf, A.F., Nedimović, M.R., Canales, J.P., Arnoux, G.M., 2021. Stacked Magma Lenses Beneath Mid-Ocean Ridges: Insights From New Seismic Observations and Synthesis With Prior Geophysical and Geologic Findings. J Geophys Res Solid Earth 126, e2020JB021434. https://doi.org/10.1029/2020JB021434

Carbotte, S.M., Smith, D.K., Cannat, M., Klein, E.M., 2016. Tectonic and magmatic segmentation of the Global Ocean Ridge System: A synthesis of observations. Geol Soc Spec Publ 420, 249–295. https://doi.org/10.1144/SP420.5/ASSET/24640339-477B-4C6A-9E6C-8E0522353236/ASSETS/GRAPHIC/SP420-995F14.JPEG

Chadwick, W.W., Embley, R.W., 1998. Graben formation associated with recent dike intrusions and volcanic eruptions on the mid-ocean ridge. J Geophys Res Solid Earth 103, 9807–9825. https://doi.org/10.1029/97JB02485

Choi, E., Buck, W.R., 2010. Constraints on shallow mantle viscosity from morphology and deformation of fast-spreading ridges. Geophys Res Lett 37. https://doi.org/10.1029/2010GL043681

Conrad, C.P., Husson, L., 2009. Influence of dynamic topography on sea level and its rate of change. Lithosphere 1, 110–120. https://doi.org/10.1130/L32.1

Cox, K.G., 1989. The role of mantle plumes in the development of continental drainage patterns. Nature 1989 342:6252 342, 873–877. https://doi.org/10.1038/342873a0

Craddock, J.P., Farris, D.W., Roberson, A., 2004. Calcite-twinning constraints on stress-strain fields along the Mid-Atlantic Ridge, Iceland. Geology 32, 49–52. https://doi.org/10.1130/G19905.1

Danda, N., Rao, C.K., Kumar, A., Rao, P.R., Rao, P.B.V.S., 2020. Implications for the lithospheric structure of Cambay rift zone, western India: Inferences from a magnetotelluric study. Geoscience Frontiers 11, 1743–1754. https://doi.org/10.1016/J.GSF.2020.01.014

Davies, D.R., Valentine, A.P., Kramer, S.C., Rawlinson, N., Hoggard, M.J., Eakin, C.M., Wilson, C.R., 2019. Earth's multi-scale topographic response to global mantle flow. Nature Geoscience 2019 12:10 12, 845–850. https://doi.org/10.1038/s41561-019-0441-4

Dewey, J.F., 1972. PLATE TECTONICS. Sci Am 226, 56–72.

Dietz, R.S., 1961. Continental and Oceanic Differentiation. Nature 1961 192:4798 192, 124–124. https://doi.org/10.1038/192124a0

Eberle, M.A., Forsyth, D.W., 1998. An alternative, dynamic model of the axial topographic high at fast spreading ridges. J Geophys Res Solid Earth 103, 12309–12320. https://doi.org/10.1029/98JB00437

Flament, N., Gurnis, M., Dietmar Müller, R., 2013. A review of observations and models of dynamic topography. Lithosphere 5, 189–210. https://doi.org/10.1130/L245.1

Forte, A.M., Rowley, D.B., 2022. Earth's Isostatic and Dynamic Topography—A Critical Perspective. Geochemistry, Geophysics, Geosystems 23, e2021GC009740. https://doi.org/10.1029/2021GC009740

Grand, S.P., 2002. Mantle shear–wave tomography and the fate of subducted slabs. Philosophical Transactions of the Royal Society of London. Series A: Mathematical, Physical and Engineering Sciences 360, 2475–2491. https://doi.org/10.1098/RSTA.2002.1077

Gurnis, M., 1993. Phanerozoic marine inundation of continents driven by dynamic topography above subducting slabs. Nature 1993 364:6438 364, 589–593. https://doi.org/10.1038/364589a0

Gurnis, Michael, Mitrovica, Jerry X, Ritsema, Jeroen, Van Heijst, Hendrik-Jan, Gurnis, M, Mitrovica, J X, Ritsema, J, Van Heijst, H.-J, 2000. Constraining mantle density structure using geological evidence of surface uplift rates: The case of the African Superplume. Geochemistry, Geophysics, Geosystems 1, 1020. https://doi.org/10.1029/1999GC000035

Hamilton, W.B., 2019. Toward a myth-free geodynamic history of Earth and its neighbors. Earth Sci Rev 198, 102905. https://doi.org/10.1016/J.EARSCIREV.2019.102905

Hamilton, W.B., 1998. Archean magmatism and deformation were not products of plate tectonics. Precambrian Res 91, 143–179. https://doi.org/10.1016/S0301-9268(98)00042-4

Hess, H.H., 1962. History of Ocean Basins. Petrologic Studies 599–620. https://doi.org/10.1130/PETROLOGIC.1962.599

Hewitt, I.J., 2010. Modelling melting rates in upwelling mantle. Earth Planet Sci Lett 300, 264–274. https://doi.org/10.1016/J.EPSL.2010.10.010

Hill, R.I., 1993. Mantle plumes and continental tectonics. Lithos 30, 193–206. https://doi.org/10.1016/0024-4937(93)90035-B

Hirth, G., Kohlstedt, D., 2004. Rheology of the Upper Mantle and the Mantle Wedge: A View from the Experimentalists. Geophysical Monograph Series 138, 83–105. https://doi.org/10.1029/138GM06

Hoggard, M.J., White, N., Al-Attar, D., 2016. Global dynamic topography observations reveal limited influence of large-scale mantle flow. Nature Geoscience 2016 9:6 9, 456–463. https://doi.org/10.1038/ngeo2709

Hoggard, M.J., Winterbourne, J., Czarnota, K., White, N., 2017. Oceanic residual depth measurements, the plate cooling model, and global dynamic topography. J Geophys Res Solid Earth 122, 2328–2372. https://doi.org/10.1002/2016JB013457

Isacks, B., Oliver, J., Sykes, L.R., 1968. Seismology and the new global tectonics. J Geophys Res 73, 5855–5899. https://doi.org/10.1029/JB073I018P05855

Ito, Garrett, Behn, Mark D, Ito, G, Behn, M D, Teagle, D.A.H., Wilson, D., 2008. Magmatic and tectonic extension at mid-ocean ridges: 2. Origin of axial morphology. Geochemistry, Geophysics, Geosystems 9, 9–12. https://doi.org/10.1029/2008GC001970

Jian, H., Singh, S.C., Chen, Y.J., Li, J., 2017. Evidence of an axial magma chamber beneath the ultraslow-spreading Southwest Indian Ridge. Geology 45, 143–146. https://doi.org/10.1130/G38356.1

Keith, M., 2001. Evidence for a plate tectonics debate. Earth Sci Rev 55, 235–336. https://doi.org/10.1016/S0012-8252(01)00060-5

Kelemen, Peter B, Braun, Michael, Hirth, Greg, Kelemen, P B, Braun, M, Hirth, G, 2000. Spatial distribution of melt conduits in the mantle beneath oceanic spreading ridges: Observations from the Ingalls and Oman ophiolites. Geochemistry, Geophysics, Geosystems 1, 1005. https://doi.org/10.1029/1999GC000012

Keller, T., Katz, R.F., Hirschmann, M.M., 2017. Volatiles beneath mid-ocean ridges: Deep melting, channelised transport, focusing, and metasomatism. Earth Planet Sci Lett 464, 55–68. https://doi.org/10.1016/J.EPSL.2017.02.006

Liu, L., 2015. The ups and downs of North America: Evaluating the role of mantle dynamic topography since the Mesozoic. Reviews of Geophysics 53, 1022–1049. https://doi.org/10.1002/2015RG000489

Liu, L., Spasojević, S., Gurnis, M., 2008. Reconstructing Farallon plate subduction beneath North America back to the Late Cretaceous. Science (1979) 322, 934–938. https://doi.org/10.1126/SCIENCE.1162921/SUPPL_FILE/LIU_SOM.PDF

Liu, Z., Buck, W.R., 2018. Magmatic controls on axial relief and faulting at mid-ocean ridges. Earth Planet Sci Lett 491, 226–237. https://doi.org/10.1016/J.EPSL.2018.03.045

Luttrell, K., Sandwell, D., 2012. Constraints on 3-D stress in the crust from support of mid-ocean ridge topography. J Geophys Res Solid Earth 117. https://doi.org/10.1029/2011JB008765

M., W., 1999. Large-scale stratigraphical, structural geomorphological constraints for earthquakes in the southern Deccan Traps, India : The case for denudationally-driven sesmicity. Deccan Volcanic Province.

Maia, M., Sichel, S., Briais, A., Brunelli, D., Ligi, M., Ferreira, N., Campos, T., Mougel, B., Brehme, I., Hémond, C., Motoki, A., Moura, D., Scalabrin, C., Pessanha, I., Alves, E., Ayres, A., Oliveira, P., 2016. Extreme mantle uplift and exhumation along a transpressive transform fault. Nature Geoscience 2016 9:8 9, 619–623. https://doi.org/10.1038/ngeo2759

Mandal, N., Sarkar, S., Baruah, A., Dutta, U., 2018. Production, pathways and budgets of melts in mid-ocean ridges: An enthalpy based thermo-mechanical model. Physics of the Earth and Planetary Interiors 277, 55–69. https://doi.org/10.1016/J.PEPI.2018.01.008

Martinez, F., Hey, R., Höskuldsson, Á., 2020. Reykjanes Ridge evolution: Effects of plate kinematics, small-scale upper mantle convection and a regional mantle gradient. Earth Sci Rev 206, 102956. https://doi.org/10.1016/J.EARSCIREV.2019.102956

McKenzie, D.P., 1969. Speculations on the Consequences and Causes of Plate Motions. Geophys J Int 18, 1–32. https://doi.org/10.1111/J.1365-246X.1969.TB00259.X

McKenzie, D.P., Morgan, W.J., 1969. Evolution of Triple Junctions. Nature 1969 224:5215 224, 125–133. https://doi.org/10.1038/224125a0

McKenzie, D.P., Parker, R.L., 1967. The North Pacific: an Example of Tectonics on a Sphere. Nature 1967 216:5122 216, 1276–1280. https://doi.org/10.1038/2161276a0

Mishra, D.C., Ravi Kumar, M., 2014. Proterozoic orogenic belts and rifting of Indian cratons: Geophysical constraints. Geoscience Frontiers 5, 25–41. https://doi.org/10.1016/J.GSF.2013.03.003

Mooney, W.D., Laske, G., Masters, T.G., 1998. CRUST 5.1: A global crustal model at 5° × 5°. J Geophys Res Solid Earth 103, 727–747. https://doi.org/10.1029/97JB02122

Moos, D., Zoback, M.D., 1990. Utilization of observations of well bore failure to constrain the orientation and magnitude of crustal stresses: Application to continental, Deep Sea Drilling Project, and Ocean Drilling Program boreholes. J Geophys Res Solid Earth 95, 9305–9325. https://doi.org/10.1029/JB095IB06P09305

Morgan, W.J., 1968. Rises, trenches, great faults, and crustal blocks. J Geophys Res 73, 1959–1982. https://doi.org/10.1029/JB073I006P01959

Moucha, R., Forte, A.M., Rowley, D.B., Mitrovica, J.X., Simmons, N.A., Grand, S.P., 2009. Deep mantle forces and the uplift of the Colorado Plateau. Geophys Res Lett 36. https://doi.org/10.1029/2009GL039778

Parnell-Turner, R., Sohn, R.A., Peirce, C., Reston, T.J., MacLeod, C.J., Searle, R.C., Simão, N.M., 2017. Oceanic detachment faults generate compression in extension. Geology 45, 923–926. https://doi.org/10.1130/G39232.1

Paul, J., Ghosh, A., 2022. Could the Réunion plume have thinned the Indian craton? Geology 50, 346–350. https://doi.org/10.1130/G49492.1

Pichon, X. Le, 1968. Sea-floor spreading and continental drift. J Geophys Res 73, 3661–3697. https://doi.org/10.1029/JB073I012P03661

Radhakrishna, T., Gopakumar, K., Murali, A. V., Mitchell, J.G., 1991. Geochemistry and petrogenesis of Proterozoic mafic dykes in north Kerala, southwestern Indian Shield — preliminary results. Precambrian Res 49, 235–244. https://doi.org/10.1016/0301-9268(91)90035-9

Raju, D.S.N., 2013. Regional and Standard Stratigraphic Classifications and Correlation in India. Proceedings of XXIII Indian Colloquium on Micropaleontology and Stratigraphy and International Symposium on Global Bioevents in Earth's History 98–124. https://doi.org/10.17491/CGSI/2013/63295

Rao, J.V.R., Ravikumar, B., Golani, P.R., 2022. What lies beneath the Deccan volcanic province? Perspective on tectonic elements and sub-trappean geology from gravity signatures. Journal of Earth System Science 131, 1–20. https://doi.org/10.1007/S12040-021-01787-9/FIGURES/8

Ribe, N.M., Christensen, U.R., 1999. The dynamical origin of Hawaiian volcanism. Earth Planet Sci Lett 171, 517–531. https://doi.org/10.1016/S0012-821X(99)00179-X

Ribe, N.M., Christensen, U.R., 1994. Three-dimensional modeling of plume-lithosphere interaction. J Geophys Res Solid Earth 99, 669–682. https://doi.org/10.1029/93JB02386

Richards, F.D., Hoggard, M.J., White, N., Ghelichkhan, S., 2020. Quantifying the Relationship Between Short-Wavelength Dynamic Topography and Thermomechanical Structure of the Upper Mantle Using Calibrated Parameterization of Anelasticity. J Geophys Res Solid Earth 125, e2019JB019062. https://doi.org/10.1029/2019JB019062

Richards, M.A., Hager, B.H., 1989. Effects of lateral viscosity variations on long-wavelength geoid anomalies and topography. J Geophys Res Solid Earth 94, 10299–10313. https://doi.org/10.1029/JB094IB08P10299

Romanowicz, B., 2008. Using seismic waves to image Earth's internal structure. Nature 2008 451:7176 451, 266–268. https://doi.org/10.1038/nature06583

Russo, R.M., Silver, P.G., 1994. Trench-Parallel Flow Beneath the Nazca Plate from Seismic Anisotropy. Science (1979) 263, 1105–1111. https://doi.org/10.1126/SCIENCE.263.5150.1105

Sarkar, S., Baruah, A., Dutta, U., Mandal, N., 2014. Role of random thermal perturbations in the magmatic segmentation of mid-oceanic ridges: Insights from numerical simulations. Tectonophysics 636, 83–99. https://doi.org/10.1016/J.TECTO.2014.08.008

Sen, J., Sarkar, S., Mandal, N., 2023. Control of mush complex viscosity on mid-ocean ridge topography: A fluid-structure model analysis. Physics of Fluids 35. https://doi.org/10.1063/5.0152667/2896764

Seton, M., Müller, R.D., Zahirovic, S., Gaina, C., Torsvik, T., Shephard, G., Talsma, A., Gurnis, M., Turner, M., Maus, S., Chandler, M., 2012. Global continental and ocean basin reconstructions since 200 Ma. Earth Sci Rev 113, 212–270. https://doi.org/10.1016/J.EARSCIREV.2012.03.002

Shephard, G.E., Müller, R.D., Liu, L., Gurnis, M., 2010. Miocene drainage reversal of the Amazon River driven by plate–mantle interaction. Nature Geoscience 2010 3:12 3, 870–875. https://doi.org/10.1038/ngeo1017

Sheth, H.C., Chandrasekharam, D., 1997. Plume-rift interaction in the Deccan volcanic province. Physics of the Earth and Planetary Interiors 99, 179–187. https://doi.org/10.1016/S0031-9201(96)03220-7

Sinton, J.M., Detrick, R.S., 1992. Mid-ocean ridge magma chambers. J Geophys Res Solid Earth 97, 197–216. https://doi.org/10.1029/91JB02508

Small, C., 1998. Global Systematics of Mid-Ocean Ridge Morphology. Geophysical Monograph Series 106, 1–25. https://doi.org/10.1029/GM106P0001

Sohn, R.A., Sims, K.W.W., 2005. Bending as a mechanism for triggering off-axis volcanism on the East Pacific Rise. Geology 33, 93–96. https://doi.org/10.1130/G21116.1

Sparks, R.S.J., Annen, C., Blundy, J.D., Cashman, K. V., Rust, A.C., Jackson, M.D., 2019. Formation and dynamics of magma reservoirs. Philosophical Transactions of the Royal Society A 377. https://doi.org/10.1098/RSTA.2018.0019

Spasojevic, S., Liu, L., Gurnis, M., 2009. Adjoint models of mantle convection with seismic, plate motion, and stratigraphic constraints: North America since the Late Cretaceous. Geochemistry, Geophysics, Geosystems 10. https://doi.org/10.1029/2008GC002345

Steinberger, B., 2007. Effects of latent heat release at phase boundaries on flow in the Earth's mantle, phase boundary topography and dynamic topography at the Earth's surface. Physics of the Earth and Planetary Interiors 164, 2–20. https://doi.org/10.1016/J.PEPI.2007.04.021

Thomas Crough, S., 1983. Rifts and swells: Geophysical constraints on causality. Tectonophysics 94, 23–37. https://doi.org/10.1016/0040-1951(83)90007-0

Valdiya, K.S., Sanwal, J., 2017. The Dynamic Indian Crust. Developments in Earth Surface Processes 22, 1–14. https://doi.org/10.1016/B978-0-444-63971-4.00001-3

Van Hinsbergen, D.J.J., Steinberger, B., Doubrovine, P. V., Gassmöller, R., 2011. Acceleration and deceleration of India-Asia convergence since the Cretaceous: Roles of mantle plumes and continental collision. J Geophys Res Solid Earth 116. https://doi.org/10.1029/2010JB008051

Veeraswamy, K., Harinarayana, T., 2006. Electrical signatures due to thermal anomalies along mobile belts reactivated by the trail and outburst of mantle plume: Evidences from the

Indian subcontinent. J Appl Geophy 58, 313–320. https://doi.org/10.1016/J.JAPPGEO.2005.05.007

Vine, F., Matthews, D., 1963. Magnetic anomalies over oceanic ridges.

Vita-Finzi, C., 2004. Buckle-controlled seismogenic faulting in peninsular India. Quat Sci Rev 23, 2405–2412. https://doi.org/10.1016/J.QUASCIREV.2004.01.008

Watts, A.B., Cox, K.G., 1989. The Deccan Traps: an interpretation in terms of progressive lithospheric flexure in response to a migrating load. Earth Planet Sci Lett 93, 85–97. https://doi.org/10.1016/0012-821X(89)90186-6

White, R., McKenzie, D., 1989. Magmatism at rift zones: The generation of volcanic continental margins and flood basalts. J Geophys Res Solid Earth 94, 7685–7729. https://doi.org/10.1029/JB094IB06P07685

Wilson, J.T., 1965. A New Class of Faults and their Bearing on Continental Drift. Nature 1965 207:4995 207, 343–347. https://doi.org/10.1038/207343a0

Zoback, M. Lou, Mooney, W.D., 2003. Lithospheric Buoyancy and Continental Intraplate Stresses. Int Geol Rev 45, 95–118. https://doi.org/10.2747/0020-6814.45.2.95

Chapter 2 | Computational Fluid Dynamic Modelling: Basic Theory, Approach and Application

2.1. Fluid mechanics: basic theory and approach

The present thesis addresses a set of important geodynamic problems, treating large-scale geological systems as fluid media within a rheological framework applicable for long-term (million years) mechanical/thermo-mechanical processes. This chapter provides a comprehensive theoretical outline of fluid mechanics, covering the geometry of motion (kinematics) and forces (dynamics) acting on fluids, grounded in the continuum mechanics approach. Fluid mechanics relies primarily on foundational physics laws, such as Newton's law of motion and thermodynamic laws, to describe how fluids behave under various physical conditions. In fluid mechanics, the theoretical development requires a set of governing equations, namely the continuity equation, conservation of momentum, and conservation of energy in accurately describing fluid motion and its changing physical states, represented by key parameters: velocity v_i, pressure p, and density ρ under a given set of boundary conditions. To deal with the problems of fluid motion, the choice of reference frames is crucial to describe the motion in a spatial $\vec{x}$ and a temporal frame t. These frames can be defined from either a *Lagrangian* perspective, where fluid elements (material particles) are tracked over time in a space, or a *Eulerian* perspective, which observes moving fluid particles at a given fixed spatial point in the frame. By choosing the appropriate frame, we can better describe and predict fluid motion within a geological system.

In the Eulerian framework, fluid motion is characterized by defining fluid properties—such as density, velocity, and pressure—as functions of spatial coordinates (x, y, z) and time (t). In this approach, flow characteristics are observed at fixed points in space, capturing how the fluid passes through these points at any given moment. For instance, the rate of change in density over time at a specific location within the flow can be represented as $\frac{\partial \rho}{\delta t}$, indicating the local or partial time derivative of density. This derivative is taken with respect to a fixed spatial frame (x, y, z). To obtain a more comprehensive expression for the rate of change, known as the total derivative, an additional convective term that accounts for the fluid's motion through space must be included. Conversely, the Lagrangian specification describes fluid motion by tracking individual fluid parcels as they move through space and time, offering a "particle-based" perspective. In this approach, the observer follows a single parcel or "material element" of the fluid, enabling the path line of that specific parcel to be recorded as it moves through the flow. The change in density of a fluid parcel under this approach is represented by the material derivative $\frac{D\rho}{Dt}$, which accounts for the parcel's dynamic motion as it evolves. The Eulerian approach is widely used in hydrodynamics for its convenience in examining properties at fixed locations in a flow field. However, it is limited in tracing the specific trajectories of individual particles, as particle paths are not explicitly defined within this framework. Recognizing these limitations, researchers like Person (1962) and Okubo (1967) have highlighted the advantages of the Lagrangian approach for particular applications. Additionally, Eckart (1960) derived Lagrangian equations of motion for both incompressible and compressible inviscid fluids by employing the principles of variational mechanics, demonstrating the method's utility in handling diverse fluid scenarios. The distinctions between the kinematic descriptions of the Eulerian and Lagrangian approaches are explored in greater detail in the following sections.

2.1.1. Material derivative and acceleration

The Lagrangian and Eulerian descriptions of motion are two complementary approaches for dealing with the kinematics and dynamics of fluid flow fields, where their relationship is governed by the substantial, or material, derivative. This derivative acts as a bridge between observing fluid behavior from two perspectives: tracking the motion of individual fluid particles over time (Lagrangian) and examining the behavior at fixed spatial points as the fluid flows past (Eulerian). To clarify this, consider an example of the expression of acceleration of a fluid element in space. The acceleration term can be decomposed into two distinct parts: local acceleration and convective acceleration. Local acceleration arises from changes in velocity at a specific point in space over time, reflecting the temporal evolution of the flow field at that location. Convective acceleration, on the other hand, results from the movement of the fluid element from one spatial location to another, thus capturing the change in velocity due to spatial movement. This second component of acceleration is particularly noteworthy as it remains present even in steady flows, where the fluid kinematics at any point remains constant in time, pointing to the essential difference between a spatial point-wise observation of different moving particles in space and that by tracking a fixed particle moving through different spatial points during the flow.

In the Eulerian framework, analyzing the rate of change of scalar quantities, such as density or temperature, in a moving fluid element requires a tailored approach. For instance, the density field in this context can be represented as $\rho(\vec{r}, t)$, where $\vec{r}$ denotes a fixed spatial position, and t represents time. Similarly, the velocity field can be described as $\vec{u}(\vec{r}, t)$, with $\vec{r}(x, y, z)$ corresponding to a fixed location within the observer's frame of reference. Here, $\vec{u}$ and ρ correspond to the instantaneous velocity and density of the fluid particles that are passing through the location $\vec{r}$ at time t. This instantaneous measurement approach highlights the Eulerian perspective's focus on observing how properties at a given point vary as different fluid particles pass by.

To elaborate further, consider a fluid particle located at $\vec{r}$ at time t that subsequently moves to a new position $\vec{r} + \partial\vec{r}$ after an interval δt. As the particle shifts position, the substantial derivative allows us to express its velocity at the new location and time. In the limit where δt approaches zero, the velocity $\vec{u}(\vec{r}, t)$ of the particle at $\vec{r}$ can be described mathematically, facilitating the calculation of acceleration by accounting for both the local and convective components. This framework is essential to accurately describe the complexity in flows, as it allows us to enumerate fluid properties that evolve both in space and time in the flow field. Setting δt as an infinitesimal quantity, the velocity $\vec{u}(\vec{r}, t)$ can be written as:

$$\partial\vec{r} = \vec{u}(\vec{r}, t)\, \delta t \tag{2.1}$$

Then the total rate of change of density (ρ) of the fluid or *material derivative*, is

$$\frac{D\rho}{Dt} = \lim_{\partial t \to 0} \frac{\rho\left(\vec{r} + \overrightarrow{\delta r}, t + \delta t\right) - \rho(\vec{r}, t)}{\partial t}$$

$$\frac{D\rho}{Dt} = \lim_{\partial t \to 0} \frac{\rho(x + \delta x,\ y + \delta y,\ z + \delta z,\ t + \delta t) - \rho(x, y, z, t)}{\partial t}$$

$$\frac{D\rho}{Dt} = \frac{\partial\rho}{\partial x}\frac{\partial x}{\partial t} + \frac{\partial\rho}{\partial y}\frac{\partial y}{\partial t} + \frac{\partial\rho}{\partial z}\frac{\partial z}{\partial t} + \frac{\partial\rho}{\partial t}$$

$$\frac{D\rho}{Dt} = \frac{\partial\rho}{\partial t} + u\frac{\partial\rho}{\partial x} + v\frac{\partial\rho}{\partial y} + w\frac{\partial\rho}{\partial z}$$

$$\frac{D\rho}{Dt} = \frac{\partial\rho}{\partial t} + \vec{u}\,.\nabla\rho \tag{2.2}$$

where, ∇ is the vector differential operator in cartesian coordinate system. Similarly, we can deduce *x*-component of acceleration, which is,

$$\frac{Du}{Dt} = \frac{\partial u}{\partial t} + u\frac{\partial u}{\partial x} + v\frac{\partial v}{\partial y} + w\frac{\partial w}{\partial z} = \frac{\partial u}{\partial t} + \vec{u}\,.\nabla u \tag{2.3}$$

Now, by combining all three components of acceleration, we get,

$$\frac{D\vec{u}}{Dt} = \frac{\partial\vec{u}}{\partial t} + (\vec{u}\,.\nabla)\vec{u} \tag{2.4}$$

2.1.2. Conservation of mass

The mass conversation formulation is extensively used in handling a wide range of fluid mechanical problems. This formulation ensures that for any closed volume fixed in space, the rate at which mass influx occurs in that volume must be equal to the rate of fluid outflux across the volume boundary. In other words, the change in mass inside a stationary control volume directly corresponds to the net influx of fluid mass across its surrounding surface. When applied to an arbitrarily small rectangular control volume (as shown in Figure 2.1), this principle yields the following result:

$$\Delta x\Delta y\Delta z\frac{\partial\rho}{\partial t} = \Delta y\Delta z([u]_x - [\rho u]_{x+\Delta x}) + \Delta z\Delta x\big([\rho v]_y - [\rho v]_{y+\Delta y}\big) + \Delta x\Delta y([\rho w]_z - [\rho w]_{z+\Delta z}) \tag{2.5}$$

Now, dividing the Eq. 2.5 by $\Delta x\Delta y\Delta z$ And considering the volume to be very small, we get,

$$\frac{\partial\rho}{\partial t} = -\frac{\delta}{\delta x}(\rho u) - \frac{\delta}{\delta y}(\rho v) - \frac{\delta}{\delta z}(\rho w)$$

$$= -\nabla.(\rho\vec{u})$$

$$= (\rho\nabla.\vec{u} + \vec{u}.\nabla\rho) \tag{2.6}$$

Now, further differentiating the products in Eq. 2.6 and using Eq. 2.2 we get,

$$\frac{D\rho}{Dt} = -\rho\nabla.\vec{u} \tag{2.7}$$

Eq. 2.7 indicates that the rate of change of density of a fluid element is positive if the divergence of the velocity field is negative, i.e., if the flow tends to converge in the element. In specific cases,

$$\frac{D\rho}{Dt} = 0 \tag{2.8}$$

This condition refers to incompressible systems where the density can be non-uniform (in Earth's mantle). Hence the velocity field satisfies,

$$\nabla.\vec{u} = \frac{\partial u}{\partial x} + \frac{\partial v}{\partial y} + \frac{\partial w}{\partial z} = 0 \tag{2.9}$$

Hence, Eq. 2.7, here, represents the conservation for any fluid.

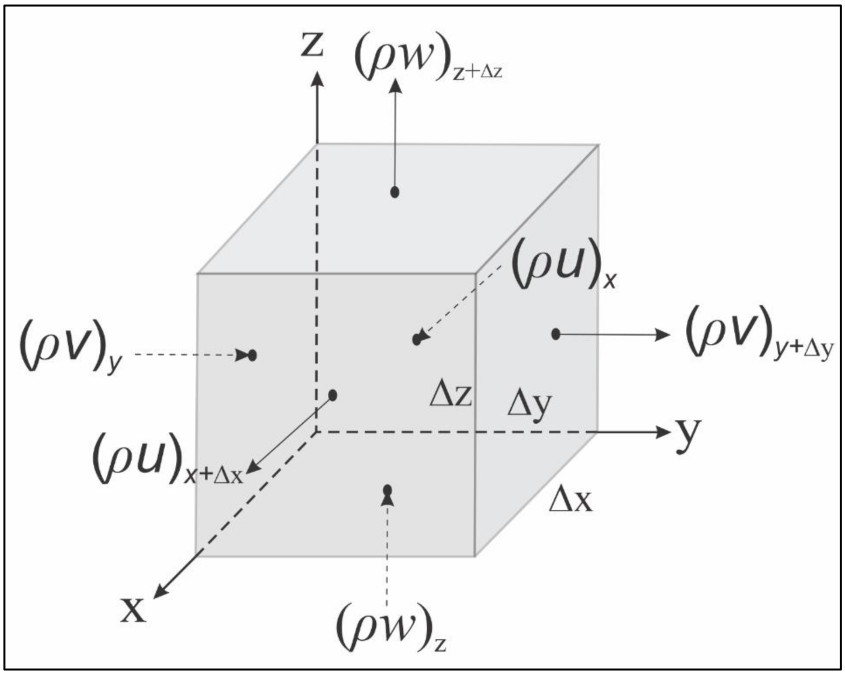

Figure 2.1 *Schematic presentation of inflow and outflow of mass for a small rectangular body*

2.1.3. Conservation of momentum

Consider a volume V enclosed by a moving material surface S that flows along with the medium, ensuring it always contains the same material elements. The momentum within this volume is expressed as $\int_v dv\, \rho\vec{v}$, and the rate of change in momentum is given by:

Rate of change of momentum $= \frac{d}{dt}\int_v dv\, \rho\vec{v} = \int_v dv\, \rho \frac{d\vec{v}}{dt}$ (2.10)

This rate of change must be equal to the net force acting on the volume. We can now distinguish between two types of forces that affect any fluid:

A. ***Body forces***: These are long-range external forces that penetrate the material and act uniformly on all mass elements within the volume dv. In geophysical systems, body forces are typically due to gravity, represented by $\rho g dv$.

B. ***Surface forces:*** These are short-range interactive forces between particles on both internal and external surfaces of the fluid. Surface forces do not cause any internal deformation of the fluid body being considered. The total surface force can be found by taking the surface integral $\int \vec{\tau}.\overrightarrow{ds}$, where$\vec{\tau}$ is the traction vector per unit area.

An element bounded by three sets of surface planes experiences a three-component force system, implying nine total force components throughout the domain. These components form the stress tensor, denoted $[\sigma]$, representing the force exerted per unit area. The force acting on a surface element $d\vec{S} \equiv \vec{n}.dS$ is given by $[\sigma].\vec{n}dS$.

Thus, the total force, combining body and surface forces, can be expressed as:

Total force (Surface + Body) = $\int_V dv\,\rho\vec{g} + \int_S dv\,\rho\vec{g} = \int_V dV(\rho\vec{g} + \nabla.[\sigma])$. (2.11)

According to Newton's second law, we have:

$$\rho\frac{D\vec{v}}{Dt} = \rho\vec{g} + \nabla.[\sigma]. \tag{2.12}$$

This eq. 2.12, commonly known as the equation of motion, represents a set of three component equations:

$$\rho\frac{Du}{Dt} = \rho g_x + \frac{\delta}{\delta x}(\sigma_{xx}) + \frac{\delta}{\delta y}(\sigma_{xy}) + \frac{\delta}{\delta z}(\sigma_{xz}) \tag{2.13}$$

$$\rho\frac{Dv}{Dt} = \rho g_y + \frac{\delta}{\delta x}(\sigma_{yx}) + \frac{\delta}{\delta y}(\sigma_{yy}) + \frac{\delta}{\delta z}(\sigma_{yz}) \tag{2.14}$$

$$\rho\frac{Dw}{Dt} = \rho g_y + \frac{\delta}{\delta x}(\sigma_{zx}) + \frac{\delta}{\delta y}(\sigma_{zy}) + \frac{\delta}{\delta z}(\sigma_{zz}) \tag{2.15}$$

The stress tensor σ_{ij} includes nine components (Figure 2.2), each defining the force per unit area in the direction of the i -axis on a plane normal to the j -axis. To ensure equilibrium, the stress tensor is symmetric, so that the off-diagonal components satisfy:

$$\sigma_{xy} = \sigma_{yx}, \sigma_{zx} = \sigma_{xz}, \sigma_{yz} = \sigma_{zy}. \tag{2.16}$$

If this symmetry condition were not met, the fluid would experience infinite angular acceleration, violating physical laws.

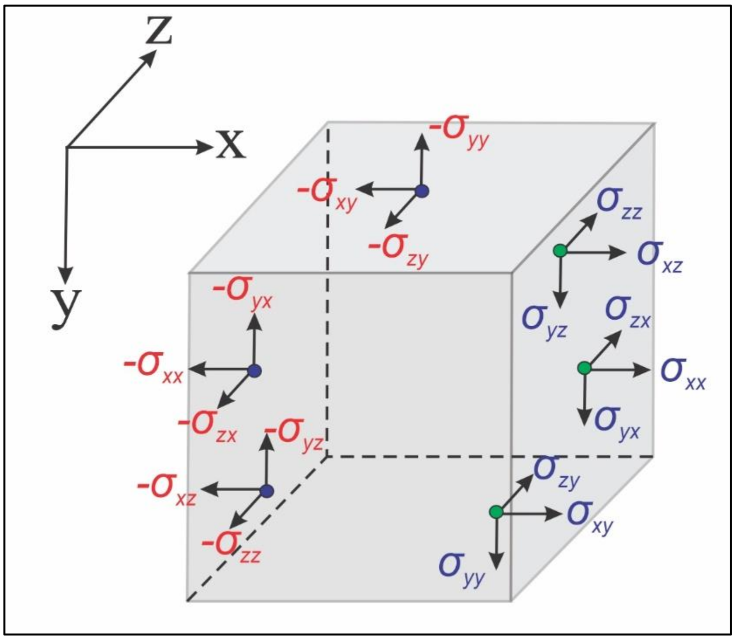

Figure 2.2 *Three-dimensional stresses (normal and tangential) on a small rectangular fluid element in a Cartesian frame.*

2.1.3.1 Constitutive relation

The surface stresses $[\sigma]$ on any element is a combination of pressure p and viscous friction. As described by the following relations,

$$\sigma_{xx} = -p + \lambda\nabla.\vec{v} + 2\mu\frac{\delta u}{\delta x}, \ \sigma_{xy} = \mu(\frac{\partial u}{\delta y} + \frac{\delta v}{\delta x}) \tag{2.17}$$

$$\sigma_{yy} = -p + \lambda\nabla.\vec{v} + 2\mu\frac{\delta v}{\delta y}, \ \sigma_{xy} = \mu(\frac{\partial v}{\delta z} + \frac{\delta w}{\delta y}) \tag{2.18}$$

$$\sigma_{zz} = -p + \lambda\nabla.\vec{v} + 2\mu\frac{\delta w}{\delta z}, \ \sigma_{xy} = \mu(\frac{\partial u}{\delta z} + \frac{\delta w}{\delta x}) \tag{2.19}$$

where, μ and λ are the coefficient of dynamic and bulk viscosity. These aforementioned expressions yield a relation between stress and strain rate tensors for: (a) linear (applicable to Newtonian fluids) and (b) isotropic (i.e., directional properties of fluid absent).

2.1.3.2 Incompressible Navier-Stokes equations

For incompressible fluid flow ($\nabla.\vec{v} = 0$), the constitutive relation (Eqs. 2.17 – 2.19) become,

$$\sigma_{ij} = -p\delta_{ij} + (\frac{\delta u_i}{\delta x_j} + \frac{\delta u_j}{\delta x_i}), \tag{2.20}$$

where the suffix notation represents $u_i = (u, v, w)$ and $x_i = (x, y, z)$. δ_{ij} is Kronecker delta whose value is 1, if *i=j* and 0 if $i \neq j$. The incompressible Navier-Stokes can be derived from Eq. 2.20 and Eq. 2.12, we have-

$$\text{Continuity: } 0 = \frac{\partial u}{\partial x} + \frac{\partial v}{\partial y} + \frac{\partial w}{\partial z} \tag{2.21}$$

$$\text{Momentum (x-component): } \rho\frac{du}{dt} = \rho g_x - \frac{\partial p}{\delta x} + \mu\left(\frac{d^2u}{\delta x^2} + \frac{d^2u}{\delta y^2} + \frac{d^2u}{\delta z^2}\right) \tag{2.22}$$

$$\text{Momentum (y-component): } \rho\frac{dv}{dt} = \rho g_y - \frac{\partial p}{\delta y} + \mu(\frac{d^2v}{\delta x^2} + \frac{d^2v}{\delta y^2} + \frac{d^2v}{\delta z^2}) \tag{2.23}$$

$$\text{Momentum (z-component): } \rho\frac{dw}{dt} = \rho g_z - \frac{\partial p}{\delta z} + \mu(\frac{d^2w}{\delta x^2} + \frac{d^2w}{\delta y^2} + \frac{d^2w}{\delta z^2}) \tag{2.24}$$

Now, the continuity equation can be written in as, $\nabla.\vec{v} = 0$ and momentum equation can be written as,

$$\rho\frac{\delta\vec{v}}{dt} = \rho\vec{g} - \nabla p + \mu\nabla^2 v \tag{2.25}$$

in which ∇^2 is the Laplacian operator. Eq. 2.25 can be further simplified to,

$$\rho \frac{\delta \vec{v}}{dt} = -\nabla P + \mu \nabla^2 v \tag{2.26}$$

Gravitational force here balanced by a pressure gradient, $\nabla p_0 = \vec{g}$ and $P = p - p_0$. The expression on the left side represents an inertial term, which is generally zero for most of the extremely slow (long time scale) geodynamic processes.

2.1.4. Conservation of Energy

2.1.4.1 Heat flow equation and conservation of energy

Conduction and convection are the primary mechanisms through which heat is transported inside the Earth. The geothermal structure within the continental crust and lithosphere is largely determined by the conductive heat flow mechanism, coupled with heat production from various geological processes such as radioactive decay, viscous dissipation, and exothermic chemical reactions. To theoretically predict the temperature distribution (geotherm) within the lithosphere, a plethora of heat flow models are employed in solid earth geophysics. The fundamental principle of heat conduction, known as Fourier's law, states that the heat flux through a given area is directly proportional to the temperature gradient in the direction of heat flow. Mathematically, Fourier's law for one-dimensional heat flows can be expressed as:

$$q = -k \frac{\partial T}{\partial x} \tag{2.27}$$

where q is the heat flux, k is the thermal conductivity (a material-specific constant), and $\frac{\partial T}{\partial x}$ represents the temperature gradient.

The conservation of energy can be expressed by the following energy equation:

$$\rho \left[\frac{\partial h}{\partial t} + \nabla.(h\vec{v}) \right] = \frac{D\rho}{Dt} + \nabla.(k\nabla T) + \varphi \tag{2.28}$$

Here, h, is the specific enthalpy, which is related to the specific internal energy e and pressure p by the relation $h = e + p/\rho$. T denotes the absolute temperature, and ρ is the density of the material. The term φ is the dissipation function, representing the work done against viscous forces, which is irreversibly converted into internal energy. It is defined as,

$$\varphi = (\tilde{\tau}.\nabla)v = \sigma_{ij} \frac{\delta v_i}{\delta x_j} \tag{2.29}$$

where $\tilde{\tau}$ is the viscous stress tensor. In deriving this particular form of the energy equation, conductive heat transfer is assumed to follow Fourier's law. Other forms of heat transfer, such as radiative heat transfer and internal heat generation, are typically neglected for simplicity in this model.

2.1.4.2 Equation of state

The equation of state is a fundamental relationship in thermodynamics that links density, pressure, and temperature, particularly for compressible flows. In compressible flow, these three properties are interdependent, meaning that changes in one variable affect the others. The ideal gas law is commonly used to express this relationship mathematically:

$$p = \rho R T \tag{2.30}$$

where p represents hydrostatic pressure, ρ is the fluid density, R is the specific gas constant (a unique constant for each real gas), and T is the absolute temperature. This relationship is especially useful in describing gases, where density varies with changes in temperature and pressure, an important factor in high-speed or high-temperature flow dynamics, such as those found in aerodynamics, gas turbines, and other compressible flow applications.

For an ideal gas, the thermodynamic properties of enthalpy and internal energy are also directly related to temperature. These relations are expressed as:

$$dh = c_p dt \text{ and } de = c_v dt \tag{2.31}$$

In these equations, c_p and c_v are the specific heats at constant pressure and constant volume, respectively. The term dh represents a small change in enthalpy, while de represents a small change in internal energy, both as a function of temperature. These relationships simplify the thermodynamic treatments of gases, allowing temperature to serve as a bridge to calculate other properties, such as enthalpy and energy under various physical conditions.

When analyzing a compressible flow, it is crucial to apply all three conservation laws—mass, momentum, and energy—which together form a comprehensive framework for solving fluid flow problems. These laws are often solved numerically due to the complexity of real-world scenarios, such as non-linearities and spatio-temporally varying fluid properties. The equations involve six unknowns: density, pressure, the three velocity components in the flow field, and temperature. Conservation of mass ensures that mass is neither created nor destroyed in the flow; conservation of momentum accounts for the net forces (body force and surface force) acting on fluid elements; and conservation of energy includes thermal and kinetic energy exchanges.

In the specific case of incompressible flow, where density is assumed constant, the equations simplify significantly. The conservation of energy equation, originally expressed in a more complex form (Eq. 2.28), can be reduced to a simpler version that depends on temperature and velocity without requiring variations in density. By incorporating the enthalpy relation, the energy equation can be rewritten as:

$$\rho c_p \left[\frac{\delta T}{\delta t} + (\vec{v}.\nabla)T\right] = K\nabla^2 T + \varphi \tag{2.32}$$

where c_p is the specific heat at constant pressure, K is the thermal conductivity of the fluid, and φ represents the viscous dissipation function, which accounts for internal energy generated due to viscous effects. This modified energy conservation equation, valid for incompressible flows, simplifies a theoretical treatment by focusing on heat conduction and convection while neglecting small density changes.

It's important to note that the ideal gas equation of state, as derived for compressible flows, does not apply to incompressible flows. In incompressible flow analysis, the continuity and Navier-Stokes equations suffice to obtain velocity and pressure distributions, provided that the fluid properties do not vary significantly with temperature. However, if temperature does affect fluid properties, such as viscosity or thermal conductivity, then temperature must be determined by solving the energy equation along with the continuity and Navier-Stokes equations.

In buoyancy-driven flows, e.g., natural convection, even small temperature-induced density variations can create significant body forces in setting flows in a fluid medium. This effect is incorporated through the Boussinesq approximation, where density changes due to temperature affect the body force term in the momentum equation, satisfying the condition of continuity equation (i.e., retaining the conditions for incompressible flow). Furthermore, if the flow is isothermal, meaning temperature remains constant throughout, the energy equation becomes largely irrelevant to the analysis, as temperature does not influence other flow variables under these conditions.

2.2. Computational fluid dynamic modelling (CFD)

Computational Fluid Dynamics (CFD) is a remarkable development in the field of fluid mechanics, extensively utilized to treat various numerical methods and algorithms in handling complex fluid mechanical problems. The CFD applications enable engineers and scientists to simulate fluid phenomena, such as turbulence, heat transfer, chemical reactions, and multiphase interactions without relying on expensive and time-consuming physical experiments. The versatility of CFD lies in its ability to handle complex geometries and intricate flow physics. Central to CFD modeling are the numerical techniques used to discretize and solve the governing equations of fluid dynamics, namely the Navier-Stokes equations, continuity equation, and energy equation. Among the most widely employed numerical methods are the finite difference approach, finite element approach, control volume method, and spectral method. Each of these techniques has unique features, advantages, and limitations, making them suitable for specific types of problems. Based on different numerical techniques, the present study uses common software packages ANSYS FLUENT, ABAQUS (Chapter 3 and Chapter 4) and open-source software packages ASPECT (Chapter 6) and UNDERWORLD2 (Chapter 5) for solving different problems.

Numerical methods are foundational tools for solving partial differential equations (PDEs), enabling the analysis of a wide range of scientific and engineering problems. These methods exhibit universality, as they are capable of addressing scenarios involving both continuous and discontinuous variable distributions, providing a versatile framework for various applications (Gustafsson, 2008). Among the numerical techniques applied in computational modeling, four primary approaches have gained prominence in geodynamic simulations. These are: (a) the finite difference method (FDM), which approximates derivatives using discrete grid points and is well-suited for structured domains; (b) the finite volume method (FVM), known for its strong conservation properties through the integration of governing equations over discrete control volumes; (c) the finite element method (FEM), which leverages flexible discretization with unstructured grids to handle complex geometries and boundary conditions efficiently; and (d) spectral methods, which utilize global basis functions for high-precision solutions, particularly in problems involving smooth or periodic systems (Lynch, 2005; Van Zelst et al., 2022; Zhong et al., 2007). These methodologies collectively form the backbone of numerical modeling in geodynamics, offering robust solutions to the complex physical processes governing Earth's interior dynamics. each method is elaborately described in the following sections.

2.2.1. Finite difference approach (FDA)

It is one of the earliest numerical methods applied in CFD modelling and remains a fundamental technique over the last several decades. FDA discretizes the computational domain into a grid and approximating the derivatives in the governing equations using difference equations. Numerical methods used in computational geodynamic modeling are fundamentally based on the local discretization of derivative operators, typically employing Taylor series expansions. This approach assigns a specified order of accuracy about a given grid point, ensuring a systematic approximation of governing equations (Zhong et al., 2007). In finite difference methods (FDM), the unknown quantities at each grid point are computed as a function of the neighboring points, determined by the local Taylor series expansion. This dependency reflects the local form of the numerical scheme, which is well-suited for structured grids. In the context of two-dimensional (2-D) isoviscous geodynamic fluid flows under the Boussinesq approximation, a commonly used FDM formulation invokes stream function (Ψ) and vorticity (ω) as variables. This approach effectively eliminates direct dependence on pressure and velocity by reformulating the governing equations in terms of Ψ and ω, and temperature (T) (McKenzie et al., 1974). The governing equations for such flows are:

$$\nabla^2 \Psi = -\omega \tag{2.33}$$

$$\nabla^2 \Psi = R_a \frac{\partial T}{\partial x} \tag{2.34}$$

$$\frac{\partial T}{\partial t} = \nabla^2 T - \left(\frac{\partial \Psi}{\partial x}\frac{\partial T}{\partial z} - \frac{\partial \Psi}{\partial z}\frac{\partial T}{\partial x}\right) + \gamma \tag{2.35}$$

Here, x and y are the horizontal and vertical coordinates, respectively, with the z-axis oriented upward, and t represents time. This formulation inherently satisfies the continuity equation, as the stream function ensures mass conservation. Notably, equations (2.33) and (2.34) are second-order partial differential equations, but they can be combined into a single fourth-order partial differential equation for Ψ, referred to as the biharmonic equation. Such a formulation was implemented by Christensen (1984) using bicubic splines and later adapted by Schott and Schmeling (1988) using finite difference techniques. Alternatively, in 2-D geodynamic flow problems, a primitive variable formulation can be employed. This approach retains velocity and dynamic pressure as primary variables and solves the coupled equations of mass and momentum conservation directly at each time step. While this method avoids the intermediate variables of stream function and vorticity, it introduces additional numerical complexity due to the increased number of unknowns, requiring greater computational efforts. Examples of this approach are found in the works of Auth and Harder (1999) and Gerya and Yuen (2003, 2007), where the primitive variable formulation is applied to study intricate geodynamic processes. These formulations exemplify the diversity and adaptability of numerical techniques in addressing the challenges of geodynamic modeling, enabling accurate simulations of Earth's interior dynamics. The key advantage of FDA is its simplicity and ease of implementation, particularly for problems involving structured grids and simple geometries. It is highly effective in handling problems with regular, uniform grids, such as those in rectilinear domains. However, FDA struggles with complex geometries and irregular boundaries, as the structured grid system often fails to conform accurately to such shapes. Despite this limitation, finite difference methods are widely used in academic research and handling relatively simple CFD problems due to their mathematical clarity and computational efficiency.

2.2.2. Finite volume method (FVM)

The finite volume method (FVM), often considered the cornerstone of CFD, is particularly used in engineering applications due to its physical intuition and conservation properties. In FVM, the domain is divided into discrete control volumes, and the governing equations are integrated over these volumes (Patankar, 2018). FVM can be implemented on both structured and unstructured grids, making it versatile for various types of problems. The partial differential equations (PDEs) are converted into a set of discrete algebraic equations by integrating them over each infinitesimal control volume. This approach ensures that conservation laws—mass, momentum, and energy—are inherently satisfied for each control volume, providing a strong physical foundation for the numerical solution. The FVM is founded on the principle that the net flux of a conserved quantity entering or leaving a control volume must equal the rate of change of that quantity within the volume itself. This principle ensures strict adherence to conservation laws, making the method highly reliable for physical simulations. While FVM shares similarities with finite difference (FD) and finite element (FE) methods, it is distinct in its approach to discretization. FVM discretizes partial differential equations (PDEs) by integrating them over a control volume or cell, followed by approximating the lower-order differential operators at the boundaries of these cells (Patankar, 1980). This integration-based approach ensures local conservation within each cell, which is particularly advantageous for physical problems involving fluxes. As Patankar (1980) observed, the FVM formulation can be interpreted as a specific case of the weighted residual method in finite element analysis, where the weighting function is set to one inside the control volume and zero elsewhere. Similar to FD methods, FVM approximates differential operators using the values at discrete grid points. To illustrate the fundamental concept of FVM, consider an one-dimensional heat conduction equation with a source term, ξ:

$$\frac{d}{dx}\left(k\frac{dT}{dx}\right) + \xi = 0 \tag{2.36}$$

where k represents thermal conductivity and T is the temperature. This equation is integrated over a control volume, leading to the following expression:

$$(k\frac{dT}{dx})_e + (k\frac{dT}{dx})_w + \int_e^w \xi dx = 0 \tag{2.37}$$

where *e* and *w* are the two ends of control cell. By approximating the fluxes at these boundaries and the source term within the control volume, Equation (2.37) is transformed into:

$$\frac{k_e(T_E - T_P)}{(\partial x)_e} + \frac{k_w(T_P - T_W)}{(\partial x)_w} + \bar{\xi}\Delta x = 0. \tag{2.38}$$

In this discretized form, k_e and k_w are heat conductivity at cell boundaries, T_E, T_P, T_W are the temperature at grid points, $\bar{\xi}$ signifies the average source in the control cell and Δx is the size of the control cell. This discrete equation represents the nodal temperatures, which serve as the primary unknowns associated with specific control volumes. By applying this discretization process to all control volumes, a system of linear equations is generated. The resulting system has a similar structure to that of the finite difference method, as the temperatures at all grid points become the unknowns to be solved. The finite volume method is particularly well-suited for solving problems that involve multiphase flows, turbulence, and compressible fluid dynamics, all of which are commonly encountered in industrial applications such as aerospace design, automotive engineering, and process optimization. Its inherent conservation properties and versatility make it a preferred choice in these fields. Many commercial computational fluid dynamics (CFD) tools, such as ANSYS Fluent and OpenFOAM, rely on the control volume method as their core numerical approach. Despite its several advantages, FVM has certain limitations, including increased complexity in implementation when dealing with unstructured grids or higher-order numerical schemes. Nonetheless, its ability to handle complex physical phenomena has established it as a cornerstone of the modern CFD applications.

2.2.3. Spectral method (SM)

The *spectral method* is used to tackle a different paradigm in CFD, focusing on global approximations, rather than any local discretization. This method allows the solution to expand in terms of global basis functions, such as Fourier series or orthogonal polynomials, over the entire computational domain. This method is particularly suited for handling problems with smooth solutions and periodic boundary conditions, as it achieves exponential convergence with increasing resolution—often referred to as "spectral accuracy." Spectral methods are widely used in turbulence research, weather modeling, and other problems requiring high precision. However, their reliance on global basis functions makes them less effective for problems involving sharp gradients, discontinuities, or complex geometries. Additionally, the spectral method demands a deeper understanding of mathematical concepts and is computationally intensive for large, irregular domains, limiting its use in general engineering practice. The spectral method is designed to operate within orthogonal curvilinear coordinate systems, making it particularly suitable for analyzing complex geometries and physical processes in mantle geodynamics. In such contexts, horizontal variability in the field can be represented using Fourier series for Cartesian geometries or spherical harmonics in the case of three-dimensional spherical shells. This approach provides a mathematically robust framework in dealing with the complexities of geodynamic problems. Mathematically, the spectral expansion of a field variable $F(x_1, x_2, x_3)$ can be expressed as:

$$F(x_1, x_2, x_3) = \sum_{ijk} a_{ijk} f(x_3) g(x_1) h(x_2) \tag{2.39}$$

In this representation, F denotes the field variable being expanded, while a_{ijk} represents the spectral coefficients that define the contribution of each term in the expansion. The variables x_1 and x_2 are the horizontal coordinates, and x_3 is the vertical or radial coordinate. The functions g and h are eigenfunctions corresponding to the horizontal coordinates, whereas f captures the vertical or radial dependence. The function f is typically determined through methods such as solving two-point boundary value problems, orthogonal function expansions, or employing the finite difference method (FDM), as demonstrated in prior studies (Csrepes et al., 1988; Cserpes and Rabinowicz, 1985; Gable et al., 1991; Glatzmaier, 2006; Machetel et al., 2006; Travis et al., 1990). Spectral methods (SM) have earned remarkable recognitions for their exceptional accuracy, often surpassing the finite difference method (FDM), when comparable computational resources are taken into account. The reason is, spectral methods achieve exponential convergence for sufficiently smooth problems, provided the underlying physics is well-represented by the eigenfunctions employed. The convergence of spectral methods can be quantitatively evaluated by examining the decay rate of energy in the spectrum as the number of terms in the spectral expansion (Equation 2.39) increases (Peyret and Taylor, 1983). Faster decay rates indicate better performance and higher accuracy for the method. In addition to their convergence properties, spectral methods offer several notable advantages. They are particularly well-suited for problems involving periodic or smooth boundary conditions, as the use of global basis functions allows for efficient and highly accurate representation of the solution. All these positive aspects make them ideal for addressing a wide range of geodynamic problems, such as mantle convection and large-scale flow patterns, where the physical phenomena often exhibit smooth variations. Spectral methods thus provide a powerful computational technique that balances mathematical rigor with practical efficiency, making them an indispensable tool in the study of geodynamic systems.

2.2.4. Finite element method (FEM)

The finite element approach (FEA*)* is probably the most widely used method in CFD, particularly for problems involving complex geometries and irregular domains. Unlike FDA, which uses a structured grid, FEA relies on discretizing the domain into smaller elements, often triangles in 2D or tetrahedra in 3D. Within each element, the solution is approximated using basis functions, typically polynomials. The finite element method is particularly powerful in handling intricate boundary conditions and geometric complexity, making it popular in engineering fields, such as structural analysis, heat transfer, and fluid-structure interactions. Furthermore, its versatility in employing unstructured grids allows it to model intricate domains with ease. However, FEA can be computationally intensive, particularly for large-scale problems, as assembling and solving the global system of equations requires substantial resources (May et al., 2013; Salomon, 2018; Thieulot and Bangreth, 2022). Its implementation also demands a higher level of mathematical sophistication compared to FDA.

Consider a function u, which represents a dependent variable in a partial differential equation (PDE), such as temperature, velocity, or pressure. The function u can be approximated by a related function, u_h, constructed as a weighted combination of basis functions. Mathematically, this approximation is expressed as:

$$u = u_h \text{ and } u_h = \sum_i u_i \Psi_i \tag{2.40}$$

Here, Ψ_i denotes the basis functions, and $u_i$are the coefficients corresponding to each basis function. These coefficients are determined such that the approximation $u_h$closely represents the actual function u. This formulation forms the foundation of many numerical methods, including finite element and spectral methods, which are widely used to solve PDEs. To illustrate this concept, consider a one-dimensional problem involving a rod subjected to non-uniform heating along its length, represented by a spatial variable x. In this case, u represents the temperature distribution along the rod length. The approximation u_h is constructed using linear basis functions, which have a value of 1 at their respective nodes (points of definition) and 0 at all other nodes. These basis functions facilitate the representation of the temperature distribution as a piecewise linear function, enabling a simplified yet accurate approximation of the physical behavior. For the given problem, the rod is divided into eight elements along its length. Within each element, the function u is defined to represent the temperature variation locally. The use of linear basis functions ensures that the temperature profile across the rod is approximated in a way that maintains continuity at the element boundaries. This approach provides a straightforward and computationally efficient means of approximating the temperature distribution, while preserving the essential characteristics of the original function u. By discretizing the domain into finite elements and employing basis functions, the problem is reduced to solving for the coefficients u_i, which are associated with each node. This process not only simplifies the complexity of the original PDE, but also enables numerical techniques to model real-world problems involving heat transfer, fluid dynamics, and other phenomena accurately.

2.2.4.1 FEM Weak Formulations: Test and Basis Function

The temperature distribution within a heat sink is governed by the following equation:

$$\rho C_P \frac{\delta T}{\delta t} + \nabla.(-\kappa \nabla T) = g(T, t, x_k) \tag{2.41}$$

where the parameters ρ, C_P, κ denote the density, specific heat capacity, and thermal conductivity of the medium, respectively. Temperature, T is a dependent variable that changes with time t. The function g describes the heat source, which is a function of T, t and spatial coordinates x_k $[(x_k = x, y, z)]$. Under steady-state conditions, where the temporal derivative of the temperature field becomes zero, equation (2.41) simplifies to the following form for the domain Ω:

$$\nabla.(-\kappa \nabla T) = g(T, t, x_k) \; in \; \Omega \tag{2.42}$$

For this system, it is assumed that the temperature along one boundary, denoted as $\delta\Omega_1$, is known and prescribed. On another set of boundaries, $\delta\Omega_2$, there exists a heat flux normal to the surface, while the remaining boundaries, $\delta\Omega_{3.}$, are thermally insulated, with no outward heat flux. Thus, the model boundary conditions are set as:

$$T = T_0 \; on \; \delta\Omega_1 \tag{2.43}$$

$$-\kappa \nabla T. n_k = h\,(T - T_a) \; on \; \delta\Omega_2 \tag{2.44}$$

$$-\kappa\nabla T.n_k = h\,(T - T_a)\ on\ \delta\Omega_3 \tag{2.45}$$

Here, h is the heat transfer coefficient, T_a represents the ambient temperature, and n_k is the outward unit normal vector to the boundary surface. To analyze this system further, equation (2.41) is multiplied by a test function φ, and the resulting expression is integrated over the domain Ω:

$$\int_\Omega \nabla.(-\kappa\Delta\mathrm{T})\,\varphi\delta\mathrm{v} = \int_A g\varphi\delta v, \tag{2.46}$$

The test function φ and the solution T are both members of a class of functions, called Hilbert spaces. A Hilbert space is an infinite-dimensional function space characterized by specific properties that make them analogous to an ordinary vector space. In such spaces, the functions can be combined linearly, with a well-defined length (referred to as the norm), and the angle between them can be measured, much like Euclidean vectors. The finite element method (FEM) provides an efficient way to transform functions in an infinite-dimensional Hilbert space into a finite-dimensional subspace, enabling one to obtain numerical solutions using computational techniques.

The weak formulation of the problem is derived by ensuring that equation (2.46) holds for all test functions ϕ\phi in their respective functional space. Unlike the original form of equation (2.41), which must be satisfied at every point in Ω, the weak formulation requires that the integral form (equation 2.46) is satisfied. The original equation (2.41) is therefore referred to as a "pointwise function." In the Galerkin method, it is assumed that the solution T and the test functions φ belong to the same Hilbert space H, such that $T \in H$ and $\varphi \in H$. Applying Green's theorem to equation (2.46) transforms it into the following form:

$$\int_\Omega \kappa\nabla T.\nabla\varphi\delta v + \int_\Omega -\kappa\nabla T.n_k\varphi\delta s = \int_\Omega g\varphi\delta v. \tag{2.47}$$

This reformulation, called the weak or variational formulation, relaxes the stringent requirements of equation (2.46). While equation (2.41) demands the solution to have well-defined derivatives at every point in Ω, the weak formulation only enforces equality in an integral sense. However, if the solution has sufficient smoothness (i.e., well-defined second derivatives), the weak and pointwise formulations yield equivalent results.

The weak formulation, combined with the boundary conditions in equations (2.43) through (2.45), forms the foundation for solving the problem using FEM. Since computers cannot directly solve equations within infinite-dimensional spaces, it is necessary to approximate the weak formulation by discretizing it within a finite-dimensional subspace. This process, called discretization, transforms the mathematical model into a numerical one. The Galerkin method is a commonly employed approach for discretization within the weak formulation framework. In the discretization process, the approximate solution $T_H x_k$ is expressed as a linear combination of a finite set of basis functions ψ_i, which belong to the finite-dimensional subspace. The approximate solution can be written as:

$$T_H x_k = \sum_i T_i \psi_i(x_k) \tag{2.48}$$

where $T_i$are the unknown coefficients to be determined. Substituting these basis functions into equation (2.47) yields the discretized form of the weak formulation. For every test function ψ_i, the equation becomes:

$$\sum_i T_i \int_\Omega k\Delta\psi_i \,.\, \Delta\, \psi_j dv + \sum_i T_i \int_{\delta\ \Omega} (-kT_i\Delta\psi_i)\,.\,n_k\, \Delta\, \psi_j ds = \int_g g(\textstyle\sum_i T_i\psi_i)\psi_j dv \tag{2.49}$$

This discretized equation represents a system of linear equations where the number of equations is equal to the number of basis functions. For example, if n test functions ψ_j ψ_j $where\ j\ ranges\ from\ 1\ to\ n)$ are chosen, the resulting system consists of n equations with n unknown coefficients T_i.

After incorporating the boundary conditions and discretizing the system, the set of equations can be represented in matrix form as:

$$AT_h = b \tag{2.50}$$

where $T_h\{= (T_{1,} \ldots . T_{i,} \ldots . T_{n,})\}$ is the vector of unknown coefficients, A is a $n \times n$ system matrix, and b is a vector of size n.

FEM typically uses finite-dimensional subspaces comprising local polynomial functions, such as piecewise bi-linear functions, to construct the basis functions or elements. This choice facilitates straightforward implementation. Alternatively, the Petrov-Galerkin method employs test functions that differ from the basis functions. This approach is particularly useful for convection-diffusion problems, where different variables may require different types of approximations. For example, in solving Navier-Stokes equations, the pressure is often approximated more smoothly than the velocity. Such methods, where the basis and test functions belong to different function spaces, are known as mixed finite element methods.

2.2.4.2 Mesh Elements in FEM

Mesh elements are the foundation of finite element modelling (FEM), enabling the division of a complex geometry into smaller, manageable components for numerical analysis. The mesh discretizes a physical domain into elements, allowing the governing equations of the problem to be solved locally and assembled to approximate the solution for the entire domain. Mesh elements come in various shapes, sizes, and dimensions, which are chosen based on the geometry of the model and the nature of the physical problem being analyzed. The primary aim of meshing is to achieve an accurate representation of the domain while maintaining computational efficiency.

In FEM, the dimensionality of the mesh depends on the problem being studied. For one-dimensional (1D) problems, the mesh consists of line elements defined by their endpoints, or nodes. These elements are commonly used for analyzing in different geodynamic setup the physical behaviour can be reduced to linear structures. For planar or axisymmetric problems, two-dimensional (2D) elements, such as triangular or quadrilateral shapes, are employed. Triangular elements are advantageous due to their ability to conform to irregular geometries, whereas quadrilaterals often provide higher accuracy with fewer elements, making them more computationally efficient. For three-dimensional (3D) problems, volumetric elements are necessary to represent the domain. Examples of 3D elements include tetrahedra, hexahedra, pyramids, and prisms. Each type has unique advantages: tetrahedral elements are versatile and easily adapt to complex geometries, while hexahedral elements are preferred for their superior accuracy and convergence properties. Pyramids and prisms, though less commonly used, serve as transitional elements in hybrid meshes (Figure 2.3a-b). The choice of element type is influenced by the geometry and complexity of the domain, as well as the desired accuracy of the solution. 2D

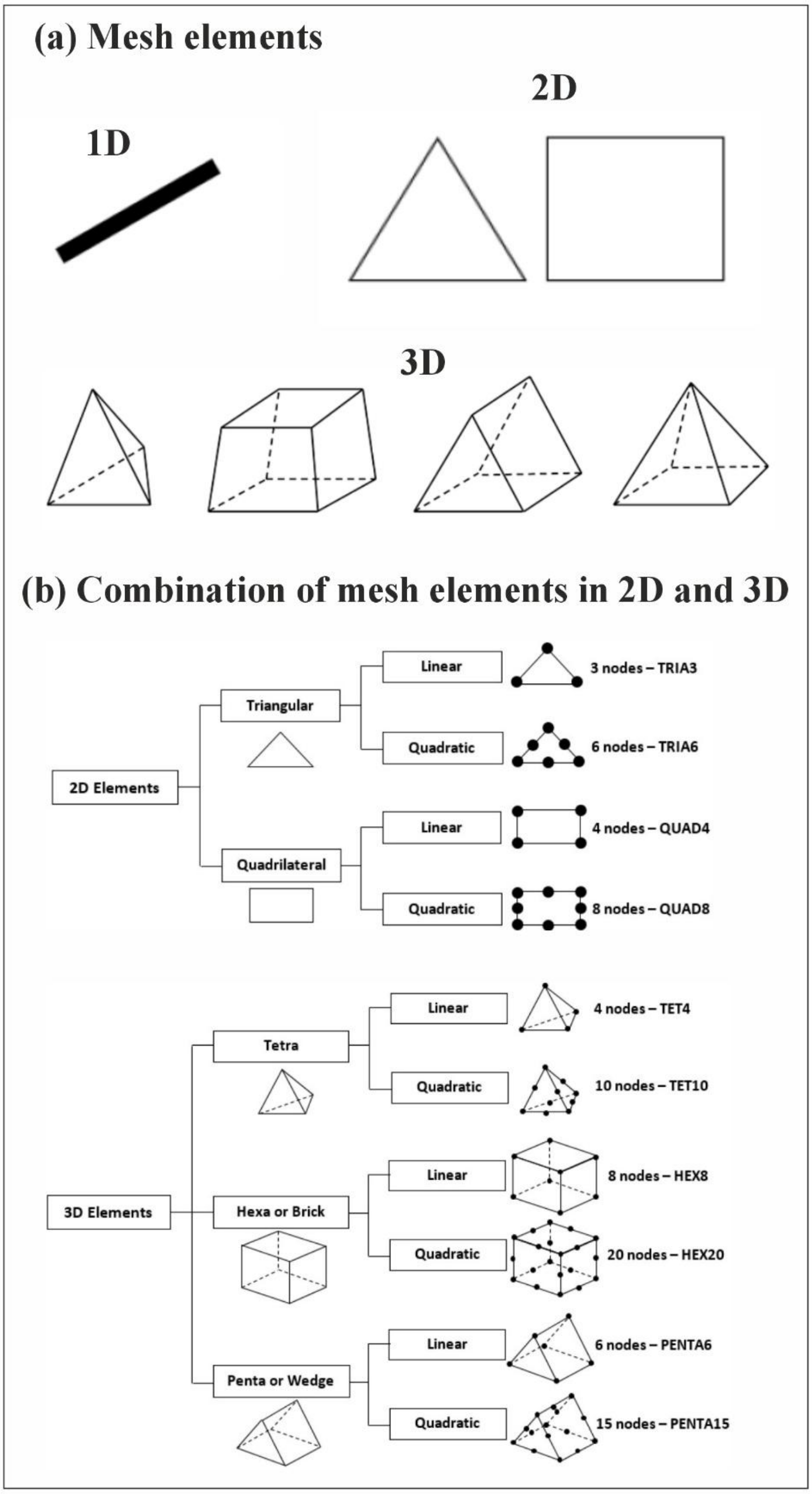

Figure 2.3 *(a) Different types of mesh elements in 1D, 2D and 3D. (b) Combination of different mesh elements in 2D and 3D used in FEM modelling.*

meshing involves discretizing surfaces into smaller planar elements. For instance, a flat rectangular plate can be meshed using quadrilateral elements arranged in a grid. Conversely, for a curved surface like an aircraft wing, triangular elements are often preferred due to their ability to conform to the curvature and capture geometric details effectively. In 3D meshing, volumetric elements are employed to model the domain. A classic example is the design of a car engine, where hexahedral elements are used for cylindrical components, and tetrahedral elements are applied to intricate features such as cooling channels and valve geometries.

Meshing techniques can be broadly classified into structured, unstructured, and hybrid approaches. Structured meshes consist of elements arranged in a regular, grid-like pattern. These meshes are straightforward to generate and are computationally efficient, making them ideal for simple geometries. However, they are less effective for irregular domains due to difficulties in conforming to complex shapes. In contrast, unstructured meshes consist of irregularly arranged elements, offering the flexibility needed for intricate geometries. While unstructured meshes provide better adaptability, they typically require more computational resources due to their complexity. Hybrid meshes combine structured and unstructured approaches, optimizing the balance between accuracy and efficiency. For example, a hybrid mesh may use structured elements in regions with uniform geometry and unstructured elements in areas of high curvature or complexity. The choice of meshing technique and element type plays a critical role in the accuracy and efficiency of FEM analysis. A finer mesh with smaller elements generally results in higher accuracy but requires greater computational effort. Adaptive meshing strategies are often used to optimize computational resources. These techniques refine the mesh in regions with high stress gradients, temperature changes, or fluid flow variations while maintaining a coarser mesh in areas of less importance. This approach ensures accurate results without excessive computational cost. Mesh quality is another crucial aspect of FEM modelling. Factors such as element shape, size, and aspect ratio influence the numerical accuracy and stability of the solution. Strongly non-ideal element shapes, such as highly skewed or distorted triangles and tetrahedra, can lead to numerical inaccuracies and convergence issues. To avoid these problems, mesh quality metrics are used to evaluate and improve the mesh. For example, ensuring a low aspect ratio and minimizing skewness are standard practices for generating high-quality meshes.

Modern FEM software offers robust tools for mesh generation and quality assessment. Programs like ANSYS, Abaqus, COMSOL Multiphysics, Underworld2, and ASPECT provide a range of automatic and manual meshing options. These tools allow engineers to create structured, unstructured, or hybrid meshes tailored to specific applications. Additionally, algorithms for mesh optimization and refinement ensure that the final mesh meets the quality criteria necessary for accurate simulations.

Different types of meshing are adopted for different applications. For instance, in computational fluid dynamics (CFD), 2D meshes with triangular or quadrilateral elements are commonly used to modelling geodynamics. In contrast, structural analyses of any solid material (i.e., different microstructure) often employ beam and truss elements in 1D or quadrilateral elements in 2D. For complex geometries, e.g., oblique subduction or in MOR settings, 3D meshing with tetrahedral or hexahedral elements is needed to capture the intricate stress and temperature distributions accurately. Hybrid meshing is particularly valuable in multiphysics problems, where regions with varying levels of geometric detail and physical behaviour coexist. The meshing process is inherently iterative, requiring adjustments based on preliminary results and simulation goals. For example, in case of multilayered convection, a thermal analysis of a heat sink, an initial coarse mesh might identify regions of high heat flux. These areas can be then refined with finer meshes to capture the thermal gradients more accurately. Similarly, in structural mechanics, areas near stress concentrations, such as sharp corners or notches, benefit from localized mesh refinement to ensure accurate stress predictions.

2.2.4.3 Solution Strategies in FEM

Solution strategies in finite element modeling (FEM) encompass various methods and techniques for solving the discretized governing equations of physical systems. These strategies are selected based on factors like the problem's size, complexity, nonlinearity, and whether it involves steady-state or transient behavior. **Direct solvers** are widely used for small to medium-sized systems due to their robustness and reliability. Methods such as Gaussian elimination, LU decomposition, and Cholesky decomposition fall into this category. These solvers guarantee exact solutions for linear systems but are computationally expensive for large-scale problems, as they require significant memory and computational resources. **Iterative solvers** are better suited for large-scale problems, especially when the system matrix is sparse, as is often the case in FEM. Techniques such as the conjugate gradient (CG) method, generalized minimal residual (GMRES), and biconjugate gradient stabilized (BiCGSTAB) methods approximate solutions iteratively. Preconditioning, which involves transforming the system matrix to improve numerical properties, is commonly used with iterative solvers to enhance convergence rates and efficiency.

For **nonlinear problems**, such as those involving material nonlinearities or large deformations, iterative methods like the Newton-Raphson method are employed. The Newton-Raphson method linearizes the nonlinear system around a current solution estimate and solves the resulting linear equations iteratively. Modified versions, like the quasi-Newton method or incremental-iterative schemes, are used to improve stability and convergence in highly nonlinear systems. When dealing with **transient problems**, where the solution evolves over time, time-step methods are utilized. Implicit methods, such as the backward Euler or Crank-Nicolson schemes, are stable for large time steps, but they require solving a system of equations at each step. Explicit methods, like the forward Euler method, are relatively simple and computationally efficient for small time steps, but the solutions may become unstable for stiff problems. The choice between implicit and explicit schemes depends on the balance between accuracy, stability, and computational cost.

Adaptive solution strategies play a significant role in FEM (as adapted in ASPECT code which is further discussed in Chapter 6), especially for problems with localized phenomena, such as stress concentrations and sharp temperature gradients. Adaptive meshing, for instance, refines the mesh dynamically in critical regions based on error estimates, improving accuracy without significantly increasing computational effort. Similarly, an adaptive time-step algorithm adjusts the time-step size based on the solution's temporal behavior, ensuring accuracy in rapidly changing regions and efficiency in slower phases. Coupled multiphysics problems, such as fluid-structure interaction or thermomechanical analysis, require advanced solution strategies that account for interactions between different physical domains. Partitioned approaches solve each domain separately with coupling conditions applied iteratively, while monolithic approaches solve the entire coupled system simultaneously. These strategies are chosen based on the problem's complexity and the need for computational efficiency. Parallel computing and high-performance computing (HPC) have further expanded the scope of FEM solution strategies. Domain decomposition methods, where the computational domain is divided into smaller subdomains solved independently, enable the efficient use of multi-core processors or distributed systems. This approach is particularly effective for large-scale 3D problems and multiphysics simulations.

2.2.4.4 Numerical convergence in FEM

Numerical convergence in Finite Element Modeling (FEM) is a critical concept that determines the accuracy and reliability of a computational solution to a physical problem. In FEM, the domain of the problem is discretized into smaller, simpler elements, and a system of equations is formed to approximate the behavior of the system. These approximations depend heavily on the mesh, the element type, and the method of solving the equations. Convergence refers to the idea that as the size of the mesh is reduced or the order of the elements is increased, the numerical solution should approach the true solution of the governing partial differential equations. The process of achieving convergence involves both the accuracy of the discretization and the stability of the numerical solution procedure. Numerical convergence can be studied through various techniques, but it is generally concerned with how the solution changes as the mesh is refined. In other words, it asks if the solution becomes closer to the exact solution as the computational grid becomes finer. A key requirement for ensuring convergence is that the governing equations are correctly approximated by the finite element discretization. In this context, the mesh plays an essential role because as the mesh becomes finer, the accuracy of the solution should increase. However, the convergence rate can vary depending on the problem type, the element order, and the solver used. The type of elements used for discretization also significantly influences convergence behavior. Higher-order elements, such as quadratic or cubic elements, typically exhibit faster convergence compared to linear elements, particularly for problems with higher-order gradients in the solution field. This is because higher-order elements can capture more detailed variations in the solution field, which can be crucial for achieving accurate results.

Convergence also depends on the type of boundary conditions and the nature of the physical problem being solved. For example, linear problems tend to converge faster and more reliably compared to nonlinear problems. Nonlinear problems, such as those involving material nonlinearity or large deformations, require special care in terms of both discretization and solution algorithms. Nonlinear FEM problems often require iterative solvers and can be susceptible to convergence difficulties, such as divergence or slow convergence, which is a particular concern in the context of highly nonlinear materials or large deformation analyses. One important aspect of numerical convergence is the distinction between convergence in the weak sense and convergence in the strong sense. In FEM, convergence in the weak sense refers to the solution of the discrete problem converging to a weak solution of the continuous problem, often in terms of some norm, such as the L2 norm or the energy norm. In contrast, convergence in the strong sense implies that the solution converges to the exact solution in every point of the domain, which is often harder to achieve and typically applies to very specific types of problems. For practical applications, convergence in the weak sense is often sufficient, as it accounts for the overall behavior of the system without needing to achieve exact pointwise accuracy. As the mesh is refined, the discretized solution typically converges in the weak sense, and the error between the numerical and exact solution decreases. However, the rate of convergence can depend on several factors, such as the element formulation, the smoothness of the solution, and the nature of the boundary conditions.

The concept of mesh refinement is central to ensuring convergence. A finer mesh, consisting of more elements, reduces the discretization error and allows for more accurate solutions. The error associated with the FEM solution is often quantified in terms of the "mesh convergence," which describes how the error changes as the mesh is refined. In general, as the mesh is refined, the error between the FEM solution and the true solution tends to decrease, provided that the problem is well-posed and the finite element method is appropriately implemented. Mesh refinement studies are crucial in practical FEM applications, as they help identify the optimal balance between computational cost and solution accuracy. In some cases, however, it may be impractical to use an extremely fine mesh due to the high computational cost. In such situations, techniques such as adaptive mesh refinement are employed, where the mesh is dynamically refined in areas with high gradients or where the solution exhibits significant variations, and coarser elements are used in regions with less variation. This approach helps to reduce computational cost while maintaining a high level of accuracy. Another key aspect of numerical convergence is the choice of numerical solver and the method used to solve the system of equations. The solution algorithm plays a significant role in ensuring that the numerical solution converges within a reasonable time frame. Direct solvers, which involve factorizing the system matrix, are typically used for small to medium-sized problems and offer fast convergence, but they become inefficient for very large systems due to their high computational cost and memory requirements. Iterative solvers, such as the conjugate gradient or GMRES (Generalized Minimum Residual) methods, are often used for large-scale problems because they are more memory-efficient and can be parallelized. However, iterative methods can sometimes exhibit slow convergence, particularly for ill-conditioned problems, and their performance heavily depends on the choice of preconditioner, which is designed to improve convergence by transforming the system into a form that is easier to solve. Preconditioning techniques are essential for ensuring faster convergence in iterative solvers. The well-known convergence criteria for FEM solutions typically focus on both the residual error and the rate of convergence. The residual error measures the difference between the left- and right-hand sides of the governing equations after applying the numerical scheme.

Convergence is often determined by setting a threshold for the residual error, and once the residual is sufficiently small, the solution is deemed converged. The rate of convergence is a measure of how fast the solution error decreases as the mesh is refined. Convergence analysis is performed to determine the order of convergence, which is typically characterized by the relation between the error and the mesh size. In linear problems with first-order elements, the error is typically expected to decrease linearly with respect to the mesh size. Higher-order elements lead to faster convergence, and in some cases, the error may decrease quadratically or even cubically with respect to the mesh size. It is important to note that numerical convergence does not ensure a physical accuracy. Despite a satisfactory numerical convergence in a mathematical perspective, the solution may not attest the real system if the governing equations or boundary conditions are not properly taken into account. A careful validation of the numerical model is thus essential, using either experimental data or well-established analytical solutions. Numerical convergence is an indispensable concept in the application of Finite Element Modeling, but achieving convergence requires a thoughtful attention to mesh design, element selection, boundary conditions, solver choice, and computational resources. Through a proper convergence analysis, the use of FEM can provide accurate and reliable solutions to complex engineering problems, although achieving true physical accuracy demands not only convergence, but also demands careful validation against real-world data.

2.3. Computational Fluid Dynamic Model: Application

2.3.1. Fluid-Structure interaction (FSI) in CFD-FEM modelling

Fluid-Structure Interaction (FSI) refers to the phenomenon where a fluid and a structure interact in such a way that both the fluid flow and the structural deformation affect each other. This interaction is crucial in numerous engineering applications, especially in natural phenomena such as the behaviour of tectonic plates at mid-oceanic ridges (detailed in chapter 2 and chapter 3). In such contexts, the interaction between the solid lithospheric plates and the underlying fluid-like mantle plays a fundamental role in the formation and dynamics of ocean basins. Numerical simulations involving FSI are essential to understand these complex interactions and to predict the behaviour of the system under various environmental conditions.

The primary objective of modelling FSI in computational tools like ANSYS and Abaqus is to predict the structural deformation and fluid dynamics in a coupled manner, which can provide insights into the interactions at geological scales. These tools, with their ability to perform both structural analysis and fluid dynamics simulations, are used to solve the complex systems governing fluid-structure interactions, especially in geological applications like those found at mid-ocean ridges.

In the context of FSI, the primary physical equations that govern the behaviour of fluids and structures need to be carefully coupled. For fluid flow, the Navier-Stokes equations provide a fundamental description of the motion of fluid substances. These equations are derived from the principles of conservation of mass, momentum, and energy. The incompressible form of the Navier-Stokes equations is often used for fluid-structure interaction problems involving oceans or the mantle beneath tectonic plates, where density variations are small, and the flow is generally incompressible. The general form of these equations is as follows:

$$\frac{\partial u}{\partial t} + (u.\nabla)u = -\frac{1}{\rho}\nabla p + \upsilon\nabla^2 u + f \qquad (2.51)$$

Here, u is the velocity field of the fluid medium, t is time, ρ is the density of the fluid, p is the pressure field, υ is the kinematic viscosity, and f represents external forces acting on the fluid, such as gravity. These equations describe the behaviour of the fluid in response to external forces and internal dynamics.

In FSI simulations, the fluid domain interacts with the solid domain, and both influence each other. The solid domain is typically modelled using structural mechanics equations that describe the deformation of materials under various loading conditions. The general equation for the motion of a solid body is given by:

$$\rho_s \frac{\delta^2 u_s}{\delta t^2} = \nabla.\sigma + f_s \qquad (2.52)$$

Here, $u_s$is the displacement field of the solid, ρ_s is the density of the solid, σ is the stress tensor, and f_s represents external forces acting on the solid, such as pressure from the fluid or gravity. The stress tensor σ\sigma is related to the strain in the solid through a material-specific constitutive relation, such as Hooke’s Law for elastic materials.

In the case of FSI at a mid-oceanic ridge, the solid deformation of the lithospheric plates due to mantle convection and tectonic forces is coupled with the mantle flow, which is itself a fluid system. This creates a complex interaction where the fluid flow beneath the plates can alter their motion and deformation, and the plates' motion can, in turn, affect the flow patterns of the mantle. The coupling between the fluid and solid domains requires the resolution of boundary conditions at the interface between the two, where the velocity of the fluid must match the displacement of the solid, and the pressure in the fluid must be balanced by the stress in the solid.

In the mechanical setting of a typical mid-oceanic ridge , the boundary conditions at the interface between the fluid and solid domains are as follows. The velocity of the fluid at the boundary must match the velocity of the structure, which is defined by the displacement of the tectonic plate. This is known as the no-slip condition in fluid mechanics, where the relative velocity between the fluid and the solid at the interface is zero. Mathematically, this is expressed as:

$$u_f = u_s \; at \; the \; fluid \; structure \; interface \; , \tag{2.53}$$

where u_f and u_s are the fluid and solid velocity fields, respectively. Additionally, the pressure in the fluid at the interface must balance the stress in the solid. This is a direct consequence of the mechanical equilibrium at the fluid-structure boundary:

$$p_f = \sigma_s . n \tag{2.54}$$

Where p_f is the fluid pressure, σ_s is the stress tensor in the solid, and n is the unit normal vector at the interface. This equation ensures that the forces exerted by the fluid on the solid are balanced by the forces in the solid.

The solution to the fluid-structure interaction problem involves solving these coupled equations simultaneously, or iteratively, depending on the method chosen for the FSI simulation. Two primary approaches are used to deal with FSI problems: the partitioned approach and the monolithic approach. In the partitioned approach, the fluid and solid equations are solved separately, with information exchanged between the solvers at each time step. This approach is often used in situations where the coupling between the fluid and structure is weak, and the two domains can be solved independently. In contrast, the monolithic approach involves solving the coupled fluid-structure system in a single system of equations, which is more computationally expensive but necessary for strongly coupled FSI problems, such as those involving high fluid velocities or large structural deformations.

In the context of a mid-oceanic ridge, the interaction between the mantle (modelled as a fluid) and the tectonic plates (modelled as solids) is weakly coupled, and one can employ the partitioned approach in handling the mechanical problem. However, as the plates move and undergo deformation due to convection in the mantle, the mantle flow can be influenced by the plate movement. This interaction is particularly important in the study of mid-ocean ridges, where the mantle is convecting upward, forcing the lithosphere laterally apart and creating new oceanic crust. The FSI simulations in such contexts need to account for the dynamic nature of both the fluid flow and the solid deformation.

For a simplified approach to this interaction, a system of equations can be derived that represents the coupling between the fluid and solid domains. In a typical FSI problem, the relationship between the fluid and solid motions is governed by the condition that the velocity of the fluid at the interface matches the velocity of the solid:

$$u_f = u_s \; at \; the \; interface \tag{2.55}$$

And the pressure balance at the interface is given by:

$$p_f = \sigma_s . n \tag{2.56}$$

Where these equations enforce the physical constraints at the fluid-structure interface. However, the system is more complicated in a real-world scenario, as it requires the solution of both the fluid equations (for the mantle flow) and the solid equations (for the tectonic plate movements) simultaneously or iteratively. For the mantle convection at a mid-oceanic ridge, the equations governing the fluid flow must include the effects of heat transfer and the temperature dependence of viscosity. The energy equation, which governs the temperature distribution within the mantle, is:

$$\frac{\partial T}{\partial t} + u_f . \nabla T = \kappa \Delta^2 T + Q \tag{2.57}$$

Here, T is the temperature, κ is the thermal diffusivity, and Q represents the internal heat sources, such as radioactive decay within the mantle. This equation must be solved alongside the momentum equations for the fluid, taking into account the effects of temperature on viscosity, which in turn affects the flow behaviour.

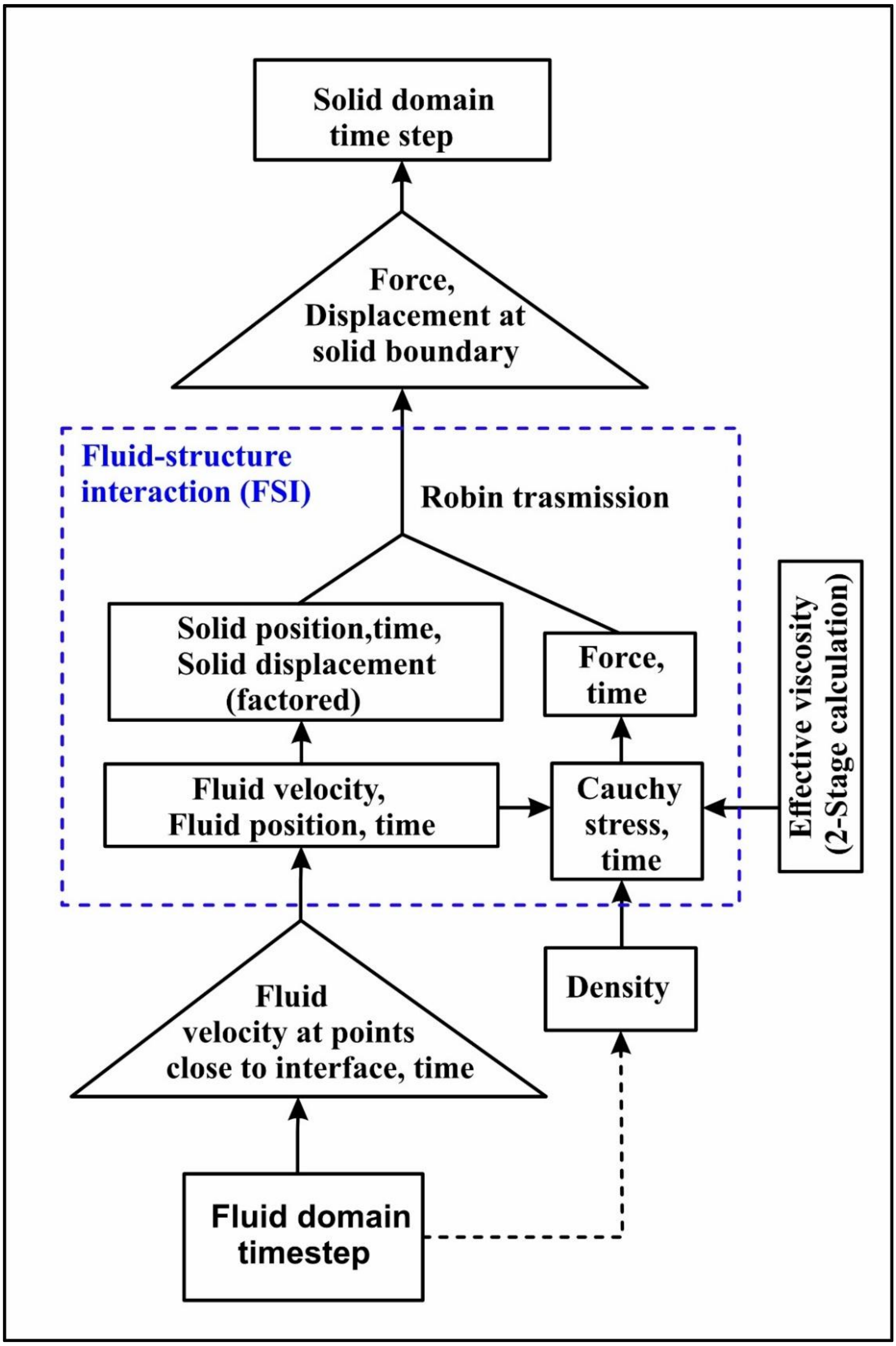

Figure 2.3 *Flow chart of single iteration of one-way CFD-FSI-FEM coupling*

The deformation of the solid lithospheric plates is governed by the equation for solid mechanics, which can be written as:

$$\rho_s \frac{\delta^2 u_s}{\delta t^2} = \nabla . \sigma_s + f_s, \tag{2.58}$$

where $\sigma_s$is the stress tensor, and f_s represents the external forces, such as the pressure exerted by the fluid. This equation describes the response of the solid to the forces acting on it, including the dynamic pressure from the convecting mantle beneath the plates. A detailed flow chart of single iteration has been described in Figure 2.3.

2.4. References

Auth, C., Harder, H., 1999. Multigrid solution of convection problems with strongly variable viscosity. Geophys J Int 137, 793–804. https://doi.org/10.1046/J.1365-246X.1999.00833.X/2/137-3-793-FIG011.JPEG

Christensen, U., 1984. Convection with pressure- and temperature-dependent non-Newtonian rheology. Geophys J Int 77, 343–384. https://doi.org/10.1111/J.1365-246X.1984.TB01939.X

Cserepes, L., Rabinowicz, M., 1985. Gravity and convection in a two-layer mantle. Earth Planet Sci Lett 76, 193–207. https://doi.org/10.1016/0012-821X(85)90159-1

Cserepes, L., Rabinowicz, M., Rosemberg-Borot, C., 1988. Three-dimensional infinite Prandtl number convection in one and two layers with implications for the Earth's gravity field. J Geophys Res Solid Earth 93, 12009–12025. https://doi.org/10.1029/JB093IB10P12009

Eckart, C., 1960. Variation Principles of Hydrodynamics. Phys Fluids 3, 421–427. https://doi.org/10.1063/1.1706053

Gable, C.W., O'Connell, R.J., Travis, B.J., 1991. Convection in three dimensions with surface plates: Generation of toroidal flow. J Geophys Res Solid Earth 96, 8391–8405. https://doi.org/10.1029/90JB02743

Gerya, T. V., Yuen, D.A., 2007. Robust characteristics method for modelling multiphase visco-elasto-plastic thermo-mechanical problems. Physics of the Earth and Planetary Interiors 163, 83–105. https://doi.org/10.1016/J.PEPI.2007.04.015

Gerya, T. V., Yuen, D.A., 2003. Characteristics-based marker-in-cell method with conservative finite-differences schemes for modeling geological flows with strongly variable transport properties. Physics of the Earth and Planetary Interiors 140, 293–318. https://doi.org/10.1016/J.PEPI.2003.09.006

Gustafsson, B., 2008. A Problem in Fluid Dynamics. High Order Difference Methods for Time Dependent PDE 219–243.

Lynch, D.R., 2005. Numerical partial differential equations for environmental scientists and engineers: A first practical course. Numerical Partial Differential Equations for Environmental Scientists and Engineers: A First Practical Course 1–388. https://doi.org/10.1007/B102052/COVER

Machetel, P., Yuen, D.A., 1988. Infinite Prandtl number spherical-shell convection. Mathematical geophysics 265–290. https://doi.org/10.1007/978-94-009-2857-2_12

May, D.A., Schellart, W.P., Moresi, L., 2013. Overview of adaptive finite element analysis in computational geodynamics. J Geodyn 70, 1–20. https://doi.org/10.1016/J.JOG.2013.04.002

Mckenzie, D.P., Roberts, J.M., Weiss, N.O., 1974. Convection in the earth's mantle: towards a numerical simulation. J Fluid Mech 62, 465–538. https://doi.org/10.1017/S0022112074000784

Ogden, D.E., Glatzmaier, G.A., Coe, R.S., 2006. The effects of different parameter regimes in geodynamo simulations. Geophysical and Astrophysical Fluid Dynamics 100, 107–120. https://doi.org/10.1080/03091920600723343

Okubo, S., Whittier, J.S., 1967. A Note on Buckling and Vibrations of an Externally Pressurized Shallow Spherical Shell. J Appl Mech 34, 1032–1034. https://doi.org/10.1115/1.3607814

Patankar, S., 1980. Source-Term Linearization. Numerical Heat Transfer and Fluid Flow 143–145.

Patankar, S. V., 2018. Numerical Heat Transfer and Fluid Flow. https://doi.org/10.1201/9781482234213

Pearson, J.R.A., 1962. Handbook of Fluid Dynamics. Edited by V. L. STREETER. McGraw-Hill, 1961. 1215pp. £9. 6s. J Fluid Mech 14, 630–631. https://doi.org/10.1017/S0022112062211494

Peyret, R., Taylor, T.D., 1983. Spectral-Method Solutions for Incompressible Flows. Computational Methods for Fluid Flow 228–247. https://doi.org/10.1007/978-3-642-85952-6_8

Salomon, C., 2018. Finite element modelling of the geodynamic processes of the Central Andes subduction zone: A Reference Model. Geod Geodyn 9, 246–251. https://doi.org/10.1016/J.GEOG.2017.11.007

Schott, B., Yuen, D.A., Schmeling, H., 2000. The diversity of tectonics from fluid-dynamical modeling of the lithosphere–mantle system. Tectonophysics 322, 35–51. https://doi.org/10.1016/S0040-1951(00)00056-1

Thieulot, C., Bangerth, W., 2022. On the choice of finite element for applications in geodynamics. Solid Earth 13, 229–249. https://doi.org/10.5194/SE-13-229-2022

Travis, B., Weinstein, S., Olson, P., 1990. Three-Dimensional Convection Planforms With Internal Heat Generation. Geophys Res Lett 17, 243–246. https://doi.org/10.1029/GL017I003P00243

Van Zelst, I., Crameri, F., Pusok, A.E., Glerum, A., Dannberg, J., Thieulot, C., 2022. 101 geodynamic modelling: How to design, interpret, and communicate numerical studies of the solid Earth. Solid Earth 13, 583–637. https://doi.org/10.5194/SE-13-583-2022

Zhong, S., Zhang, N., Li, Z.X., Roberts, J.H., 2007. Supercontinent cycles, true polar wander, and very long-wavelength mantle convection. Earth Planet Sci Lett 261, 551–564. https://doi.org/10.1016/J.EPSL.2007.07.049

Chapter 3 | Axial Mid-Oceanic Ridge Topography

3.1. Introductory notes

3.1.1. Global distribution of mid-ocean ridges

The global distribution of mid-ocean ridges (MORs) witnesses one of the most remarkable planetary scale manifestations, encompassing thousands of kilometres long linear topographic belts beneath the oceans, of Earth's internal dynamic states. Plate kinematics suggest that MORs track divergent plate boundaries, playing a crucial role in continuously creating new oceanic lithosphere. This introductory section describes basic elements of mid-ocean ridge systems in the perspectives of geodynamics, tectonics, and geochemistry, providing an outline of their processes and significance with examples of some notable ridges. At the divergent plate boundaries MORs act as upwelling sites of deep mantle materials, accompanying generation of partial melts produced by decompression melting at threshold depths. Melts then flow upward by buoyancy forces and eventually focuses into the ridge axis (Figure 3.1). Their progressive cooling and solidification give rise to new oceanic lithosphere, a process central to the theory of plate tectonics. The MOR global system covers approximately 65,000 kilometres ridges, and connect major tectonic plates, driving them laterally by the seafloor spreading mechanism. The ridges undergo lateral spreading at varying rates, which influence their morphology, structural segmentation, and magmatic processes.

The Mid-Atlantic Ridge (MAR) is a typical example of slow-spreading ridge, with a spreading rate of approximately 1.8-3.0 cm/year (Smith & Cann, 1993) (Figure 3.1). The MAR is characterized by a prominent rift valley, steep flanks, and significant tectonic segmentation. Prevailing tectonic models suggest that the slow spreading allows for extensive cooling and thickening of the lithosphere, resulting in rugged topography and deep rift valleys. Geochemically, basalts erupted from the MAR often exhibit heterogeneity in trace elements and isotopic compositions, reflecting a heterogeneous characteristic of the mantle sources and melt-rock interactions during ascent (White and Schilling, 1978; Gale et al., 2013). In contrast, the East Pacific Rise (EPR) represents the dynamics of a fast-spreading ridge, with rates up to 7.5 cm/year (Figure 3.2). The higher spreading rates at the EPR lead to smoother topography and narrower axial valleys. The magma supply is more continuous, creating a thinner lithosphere and more uniform crustal structure. Geochemically, the basalts in the EPR are less heterogeneous compared to those from slow-spreading ridges, often displaying higher degrees of partial melting and less contamination by mantle heterogeneities (Rubin & Sinton, 2007; Smith & Cann, 1993).

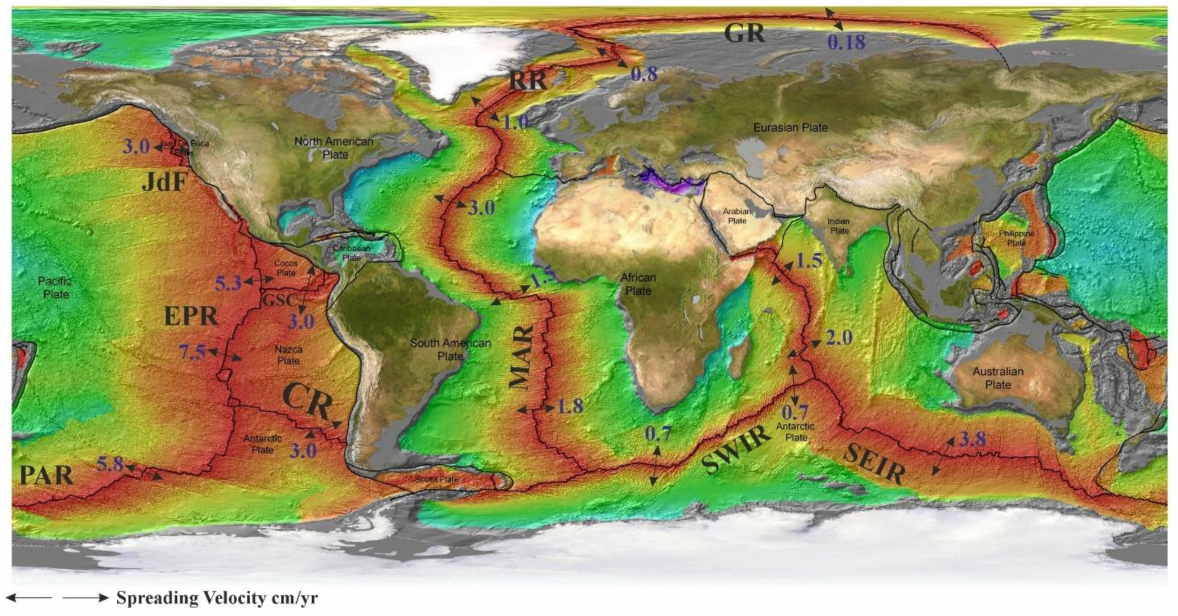

Figure 3.1 *Global distribution of Mid-oceanic ridges with sea-floor spreading rates. The mid ocean ridges and transform faults are shown in thick black-coloured lines. The notable ridges are: MAR: Mid-Atlantic Ridge. RR: Reykjanes Ridge. GR: Gakkel Ridge. JdF: Juan de Fuca Ridge. GSC: Galapagos Spreading Center. EPR: East Pacific Rise. CR: Chile Ridge. PAR: Pacific-Antarctic Ridge. SWIR: Southwest Indian Ridge. SEIR: Southeast Indian Ridge. CIR: Central Indian Ridge.*

The Indian Ocean hosts ridges with intermediate to ultra-slow spreading rates, and this system includes the Central Indian Ridge (CIR), the Southeast Indian Ridge (SEIR), and the Southwest Indian Ridge (SWIR) (Figure 3.1). The CIR (spreading rates of 1.5-2 cm/year) exhibits characteristic features, such as transform faults and fracture zones that offset ridge segments (Cannat et al., 2010). Geochemically, the basalts in the CIR are intermediate in composition, reflecting both depleted mantle sources and localized enrichment due to mantle plume interactions. The SEIR, relatively of higher spreading rates (3-3.8 cm/year) is an example of intermediate-spreading ridge (Figure 3.1). The SEIR morphology shows characteristics of both fast and slow-spreading ridges, with moderate axial valleys and faulting. Geochemical studies have identified the role of mantle flow and upwelling along this ridge, particularly in regions influenced by hotspots such as Amsterdam-St. Paul (Hanan et al., 2013). The basalts along the SEIR often reflect geochemical diversity, suggesting complex interactions between depleted mantle and enriched plume materials. The SWIR, by contrast, spreads at less than 1 cm/year, signifying it one of the slowest-spreading ridges across the globe (Figure 3.2). This ultra-slow spreading condition results in a wide, deep rift valley, extensive faulting, and limited magmatic activity. Geophysically, the SWIR displays strong along-axis pertrological variations, with regions dominated by tectonic extension and sparse volcanic activity interspersed with magmatically robust segments (Dick et al., 2003). Geochemically, the basalts from the SWIR show evidence of a highly depleted mantle source, with local enrichments implying recycled materials or small-scale mantle heterogeneities (Meyzen et al., 2005). The Gakkel Ridge in the Arctic Ocean is another slowest-spreading mid-ocean ridge, with rates below 0.5 cm/year (Tolstoy et al., 2008) (Figure 3.1). Despite its ultra-slow spreading, the ridge exhibits active volcanic and hydrothermal processes, as evidenced by localized magmatic centers and geophysical anomalies. Geochemical analyses of basalts from the Gakkel Ridge reveal extremely depleted compositions, consistent with low degrees of partial melting and significant lithospheric control on melt generation (Michael et al., 2003).

From a geodynamic perspective, the morphology and structure of mid-ocean ridges are directly linked to their spreading rates and mantle dynamics. Slow-spreading ridges, such as the MAR, SWIR, and Gakkel Ridge, generally have thick lithosphere, deep rift valleys, and extensive faulting due to the slow upwelling of magmas. Fast-spreading ridges, e.g., the EPR, in contrast, show markedly weak tectonic segmentation, and they are dominated by magmatic processes, reflecting a higher mantle melting rate and robust magma supply (Carbotte et al., 2016; Smith & Cann, 1993). Tectonic segmentation along mid-ocean ridges is another critical feature controlled by spreading rate and mantle heterogeneity. Segments are typically bounded by transform faults and non-transform discontinuities, which accommodate variations in spreading direction and magmatic supply. These features contribute to the complex interplay of tectonics and magmatism that characterizes ridge systems (Cannat et al., 2010; Macdonald et al., 1988).

Geochemically, mid-ocean ridge basalts (MORBs) provide insights into mantle processes and composition (detailed discussion in section 3.3). MORBs are generally classified as depleted due to the extraction of incompatible elements during partial melting. However, variations in trace element and isotopic compositions reflect mantle heterogeneities, melting dynamics, and interactions with lithospheric materials. For instance, enriched MORBs (E-MORBs) found at some ridge segments suggest localized input from enriched mantle domains or plume-ridge interactions, such as those observed near the Iceland hotspot along the MAR

(White et al., 1995; Gale et al., 2013). SEIR and CIR basalts, similarly, indicate plume-ridge interactions, reflected in the geochemical complexity of these systems (Hanan et al., 2013; Sauter et al., 2009). Hydrothermal processes at mid-ocean ridges also play a role in geochemical cycling and crustal evolution. Circulating seawater interacts with hot, newly formed crust, leading to the leaching and deposition of elements such as iron, manganese, and sulphur. This hydrothermal activity is closely linked to magmatic processes and tectonic setting, with fast-spreading ridges, such as the EPR exhibiting more continuous venting compared to episodic activity at slow-spreading ridges (Alt, 1995; Smith & Cann, 1993). Hydrothermal systems also influence the composition of seawater and contribute to the global carbon cycle through the precipitation of carbonate and sulphide minerals.

Advances in geophysical and geochemical techniques have provided new insights into the dynamics of mid-ocean ridges. For example, seismic studies reveal variations in crustal thickness and magma chamber structure, reflecting the interplay between mantle melting and tectonic processes (Carbotte et al., 2016). High-resolution geochemical analyses of MORBs have elucidated the role of mantle source variations and melting conditions in shaping the chemical diversity of ridge basalts (Gale et al., 2013). Additionally, isotopic studies of elements such as helium and strontium provide constraints on mantle dynamics and plume-ridge interactions (Hanan et al., 2013; Dick et al., 2003).

3.1.2. Classification of MORs and ridge morphology

Mid-ocean ridges (MORs) are the largest continuous volcanic and tectonic domains of the Earth, formed as a consequence of plate divergence at oceanic spreading centers. These ridges are not uniform; instead, their morphology and structural characteristics vary significantly depending on their spreading velocity. MORs are classified broadly into the following categories: *ultra-slow, slow, intermediate, fast,* and *ultra-fast spreading ridges,* each of which displays distinct topographic, tectonic, and structural features. The axial topography, in particular, reflects the balance of forces, such as magmatic supply, mantle upwelling, and tectonic extension, all of which are modulated by the rate of spreading (Carbotte et al., 2016; Macdonald et al., 1988; Semperé et al., 1990).

Ultra-slow spreading ridges, such as the Southwest Indian Ridge (SWIR) and the Gakkel Ridge, are characterized by spreading rates below 0.7 cm/year (Figure 3.2). These ridges exhibit some of the most extreme axial topographies, with wide and deep rift valleys that can reach depths of up to 5 km and widths exceeding 20 km (Carbotte et al., 2016). The morphology is primarily shaped by a severely limited magmatic supply, resulting in tectonic extension dominating over magmatic accretion. Amagmatic segments are a characteristic feature, where mantle peridotites and ultramafic rocks are exposed at the seafloor, indicative of limited melt production (Michael et al., 2003; Cannat et al., 2006). Segmentation is governed by long transform offsets and oblique spreading basins, where volcanic centers are sparse and alternate with fault-dominated terrains. At the Gakkel Ridge, volcanic activity is sporadic, and geophysical studies reveal highly variable crustal thicknesses, with localized magma chambers only beneath certain segments (Carbotte et al., 2016).

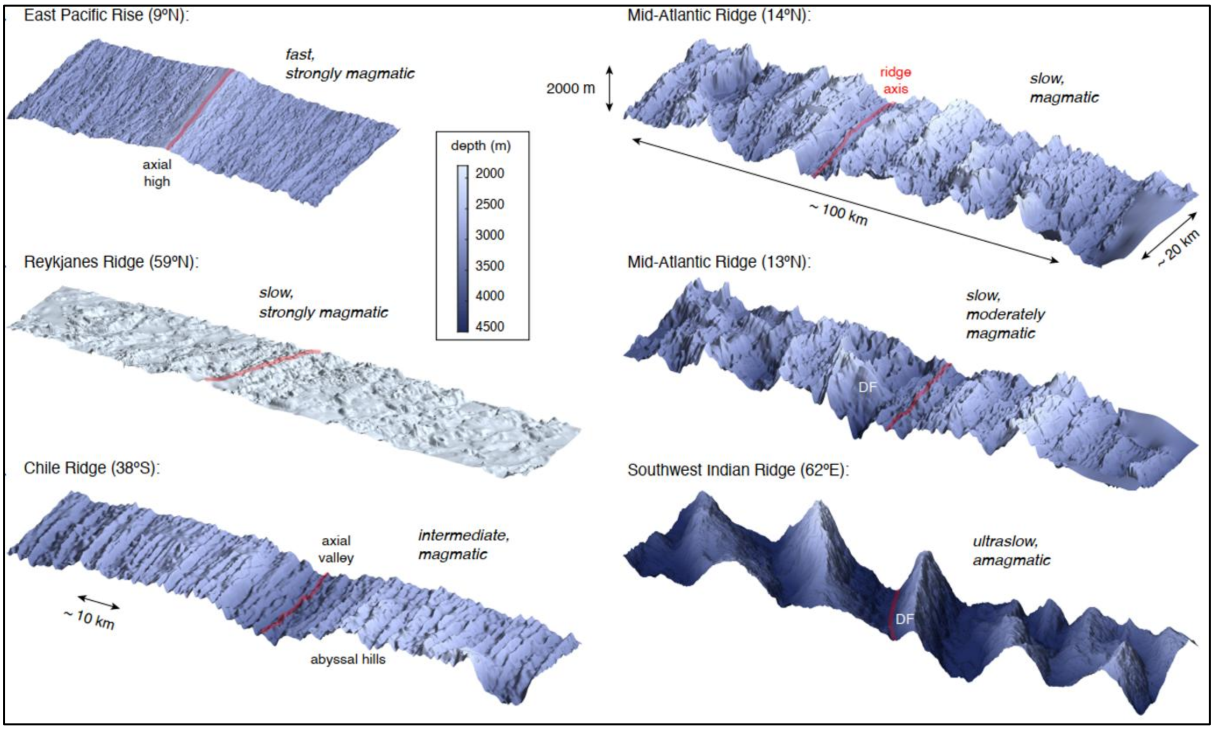

Figure 3.2 *Axial morphology variance of different mid-oceanic ridges system depending on spreading rate and magma supply (modified after, Olive, J.A., 2023).*

Slow-spreading ridges, such as the Mid-Atlantic Ridge (MAR), exhibit spreading rates of 1.8-3 cm/year and are dominated by tectonic processes that create rugged topography (Figure 3.2). The axial morphology includes a continuous, prominent rift valley flanked by steep abyssal hills formed by faulting and tectonic stretching. The MAR's segmentation is defined by a hierarchy of first-order transform faults, second-order non-transform offsets (NTOs), and third-order discontinuities, each contributing to variability in axial depth and fault structure (Semperé et al., 1990; Carbotte et al., 2016). Transform faults, such as the Romanche and Kane Fracture Zones, are associated with significant increases in axial depth due to reduced magma supply and cooler mantle temperatures (Macdonald et al., 1988). Rift valleys are generally narrower than those at ultra-slow ridges, suggesting a moderate but episodic magmatic supply that focuses melt at segment centers and diminishes toward segment ends. Carbotte et al. (2016) emphasize that these segments are shaped by a complex magmatic plumbing system, with localized melt delivery complemented by along-axis redistribution.

Intermediate-spreading ridges, such as the Southeast Indian Ridge (SEIR) and the Central Indian Ridge (CIR), spread at rates of 3-4 cm/year and exhibit a balance between magmatic and tectonic influences on axial topography (Figure 3.2). These ridges display moderate axial valleys with less pronounced faulting compared to slower spreading ridges but retain significant tectonic features. The transition from shallow axial highs to deeper axial valleys in the SEIR indicates along-axis variations in magma supply and lithospheric strength (Carbotte et al., 2016). For example, segments influenced by the Amsterdam-St. Paul hotspot exhibit elevated axial topography and thicker crust due to enhanced magmatic flux from mantle plumes (Hanan et al., 2013). The segmentation of intermediate ridges includes well-defined tectonic corridors where systematic variations in ridge morphology occur over hundreds of kilometers, driven by gradients in mantle upwelling and magmatic activity.

Fast-spreading ridges, such as the East Pacific Rise (EPR), spread at rates exceeding 5 cm/year and are characterized by smoother axial topography dominated by magmatic accretion. The axial high, typically 8-10 km wide, rises 200-400 meters above the surrounding seafloor and reflects robust magma supply that minimizes tectonic deformation (Macdonald et al., 1984; Carbotte et al., 2016) (Figure 3.2). Segmentation at fast-spreading ridges is dominated by second-order discontinuities, such as overlapping spreading centers (OSCs), and smaller third-order discontinuities, which manifest as subtle offsets or kinks in the axial summit trough (Macdonald et al., 1992). The axial high is underlain by well-developed magma chambers that sustain continuous crustal formation, with volcanic activity concentrated at segment centers. Transform offsets are less frequent and spaced farther apart compared to slower spreading ridges, further emphasizing the dominance of magmatic processes in shaping the axial morphology (Carbotte et al., 2016).

Ultra-fast spreading ridges, such as the Pacific-Antarctic Ridge, show their spreading rates > 10 cm/year, and they display the most subdued axial topographies among MORs (Figure 3.2). These ridges lack significant rift valleys or faulting, with the axial high forming a flat, continuous feature indicative of exceptionally high magma supply (Carbotte et al., 2016). Crustal accretion occurs at rates that outpace lithospheric cooling, resulting in uniform and

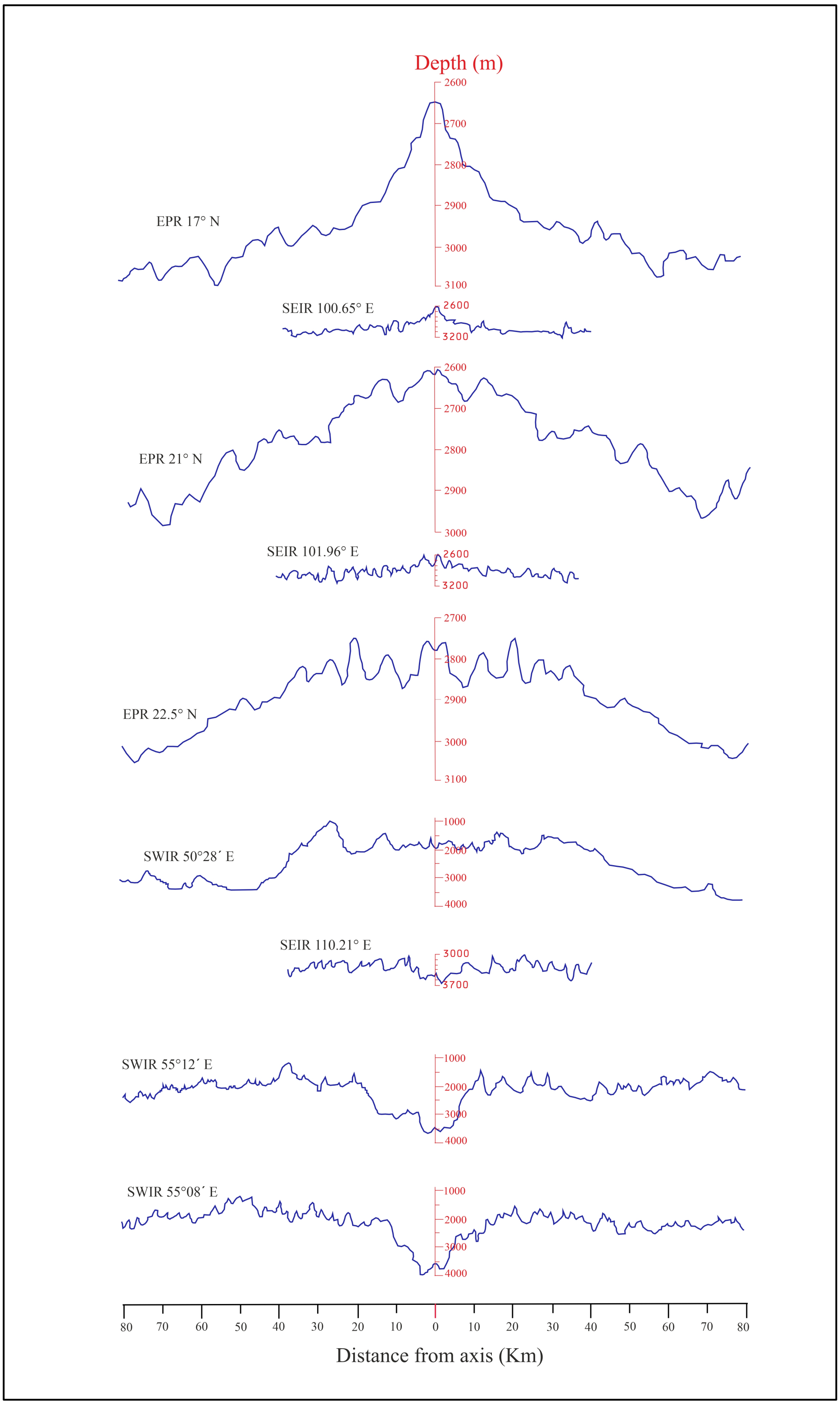

Figure 3.3 *Variation of mid axial topography (from axial-high to axial-valley) in different mid ocean ridge system. It is to be noted that the position of the bathymetric profiles is given in the left side of each profile*

continuous axial features. Segmentation is controlled by fine-scale discontinuities, with minimal along-axis variability in topography or volcanic activity. The efficient mantle melting at these ridges produces thick and homogeneous crust, with lithospheric thermal gradients contributing to the expansive axial highs (Macdonald et al., 1992).

The axial highs and valleys observed at mid-ocean ridges reflect the interplay of mantle melting, magma transport, and tectonic extension. At slow and ultra-slow ridges, axial valleys are deep and wide, indicative of limited magmatic support and dominant tectonic forces. These features are often interrupted by transform offsets and oblique fault systems, which define the large-scale segmentation of these ridges (Semperé et al., 1990; Carbotte et al., 2015). In contrast, fast and ultra-fast ridges exhibit axial highs that are shaped by continuous magma supply and minimal faulting, with finer-scale segmentation arising from overlapping spreading centers and subtle discontinuities. The hierarchy of segmentation—from first-order transform faults to third- and fourth-order offsets—is a defining characteristic of ridge morphology and reflects variations in mantle dynamics and lithospheric strength (Carbotte et al., 2016; Cannat et al., 2006).

The presence of axial highs and valleys, transform faults, and non-transform offsets highlights the dynamic nature of mid-ocean ridge systems (Figure 3.3), irrespective of their spreading rates. The feedback mechanisms between mantle processes, magmatic supply, and lithospheric cooling govern the morphological diversity of these ridges, from the rugged terrains of ultra-slow ridges to the smooth, elevated features of ultra-fast ridges. Carbotte et al. (2016) provide a comprehensive framework for understanding how these processes interact to shape the axial topography and segmentation of mid-ocean ridges at different spreading velocities.

Mid-ocean ridges (MORs) are tectonic and magmatic features that play a central role in the generation of new oceanic crust. The petrological characteristics of MORs vary widely across different ridges and are influenced by spreading rates, mantle source composition, and magmatic processes. This section delves into the detailed petrological features of MORs, with an emphasis on their diverse geochemistry and mineralogical characteristics across ultra-slow, slow, intermediate, fast, and ultra-fast spreading ridges, incorporating evidence from various studies, including Carbotte et al. (2016) and related works.

3.1.3. Petrological characteristics of MORs

At ultra-slow spreading ridges, such as the Southwest Indian Ridge (SWIR) and Gakkel Ridge, the petrology reflects the highly heterogeneous nature of mantle melting and limited magma supply. These ridges often expose peridotites and ultramafic rocks at the seafloor due to incomplete melt extraction and thin crustal formation (Cannat et al., 2006; Sauter & Cannat, 2010). The basalts from these ridges exhibit extreme geochemical variability, often being highly depleted in incompatible elements such as K, Ti, and P. These depleted mid-ocean ridge basalts (D-MORBs) are characterized by elevated Mg# values (Mg/(Mg+Fe)), indicating low degrees of mantle partial melting (Michael et al., 2003). Trace element patterns often show pronounced depletion in light rare earth elements (LREEs) relative to heavy rare earth elements (HREEs), consistent with melting of a depleted mantle source (Jokat et al., 2003). Isotopic compositions of Sr, Nd, and Pb at ultra-slow spreading ridges reveal significant mantle heterogeneity, with Gakkel Ridge basalts showing high 87Sr/86Sr and low 143Nd/144Nd ratios, indicative of interaction with enriched mantle domains or recycled lithospheric components (Carbotte et al., 2016). Additional petrological evidence comes from gabbros and peridotites recovered from SWIR and Gakkel Ridge, which provide insights into the magmatic and tectonic processes at these ridges. Peridotites often exhibit high degrees of serpentinization due to hydrothermal alteration, and their geochemical signatures reveal residual mantle that has undergone extensive melt extraction. Clinopyroxene and spinel within these peridotites show compositional variations that record partial melting processes and melt-rock interactions during ascent (Dick et al., 2003; Cannat et al., 2006).

At slow-spreading ridges, such as the Mid-Atlantic Ridge (MAR), the petrological features are more diverse due to the interplay of magmatic and tectonic processes. Basalts from the MAR include both depleted MORBs (D-MORBs) and enriched MORBs (E-MORBs). E-MORBs are enriched in incompatible elements such as Ba, Th, and U, and their isotopic compositions (e.g., higher 206Pb/204Pb ratios) suggest contributions from enriched mantle sources or plume-ridge interactions, such as those near the Iceland hotspot (Gale et al., 2011; Hanan et al., 2013). The geochemistry of MAR basalts exhibits systematic variations along the ridge axis, with segment centers typically showing more enriched signatures due to focused melt delivery and higher degrees of partial melting compared to segment ends (Reynolds & Langmuir, 1997). Tectonically exposed gabbros and peridotites from the MAR provide additional evidence of mantle melting and crustal accretion processes. Gabbros, often recovered from detachment fault zones, show compositional layering that indicates fractional crystallization and melt migration within crustal magma chambers. Peridotites, on the other hand, exhibit melt depletion signatures with spinel Cr# values (Cr/(Cr+Al)) that imply varying degrees of partial melting. Hydrothermal alteration of these rocks results in the formation of serpentine and talc, modifying their primary mineralogical and geochemical characteristics (Cannat et al., 2006).

Intermediate-spreading ridges, such as the Southeast Indian Ridge (SEIR) and Central Indian Ridge (CIR), exhibit petrological characteristics that balance magmatic and tectonic influences. MORBs from these ridges generally show higher TiO_2 and Na_2O concentrations compared to slow-spreading ridges, reflecting greater extents of partial melting (Klein & Langmuir, 1987). The SEIR, in particular, demonstrates a unique geochemical signature due to interactions with mantle plumes such as the Amsterdam-St. Paul hotspot. Basalts from this region display elevated concentrations of incompatible elements such as Nb and La, along with isotopic signatures that point to mixing between depleted MORB mantle (DMM) and enriched plume components (Hanan et al., 2013). Trace element ratios, such as Nb/Zr and La/Yb, highlight the variable mantle source contributions along intermediate-spreading ridges (Russo et al., 2009). The petrology of gabbros and ultramafic rocks at intermediate ridges also reflects their transitional nature. Gabbros from the CIR often display complex zoning in plagioclase and clinopyroxene, indicative of dynamic crystallization processes within evolving magma chambers. Peridotites from these ridges are characterized by melt depletion trends, similar to those at slow-spreading ridges, but they often include secondary enrichment signatures due to melt percolation and refertilization processes (Seyler et al., 2003).

Fast-spreading ridges, such as the East Pacific Rise (EPR), are dominated by magmatic accretion, and their petrology reflects extensive mantle melting and uniform crustal formation. MORBs from the EPR are typically less heterogeneous, as compared to those in slower spreading ridges. These basalts yield lower Na8 (Na_2O content at 8% MgO) values and higher Fe8, reflecting higher degrees of partial melting at elevated mantle temperatures (Rubin & Sinton, 2007). Trace element patterns of EPR basalts show relatively flat rare earth element (REE) profiles, consistent with a homogeneous mantle source. Isotopic compositions, including Sr, Nd, and Pb isotopes, display limited variability, further indicating a relatively uniform mantle source beneath fast-spreading ridges (Carbotte et al., 2016). Mineralogically, EPR basalts often contain phenocrysts of olivine, plagioclase, and clinopyroxene, which crystallize rapidly due to high magma ascent rates. The textures and compositions of these phenocrysts provide evidence of rapid cooling and limited magma storage within crustal reservoirs. Gabbros recovered from fast-spreading ridges show a narrow range of compositions, reflecting the efficient extraction and differentiation of melts within axial magma chambers (Kent et al., 1993; Sinton & Detrick, 1992).

Ultra-fast spreading ridges, such as segments of the Pacific-Antarctic Ridge, show petrological features suggesting extreme conditions of rapid crustal formation. MORBs from these ridges display highly uniform geochemical compositions, with high degrees of partial melting leading to low incompatible element concentrations. These basalts are characterized by elevated Mg# and FeO contents, indicative of efficient melt extraction and rapid cooling (Macdonald et al., 1984). Rare earth element (REE) patterns often show subtle depletion in light REEs, consistent with high extents of melting and minimal mantle heterogeneity (Carbotte et al., 2016). Phenocrysts in ultra-fast ridge basalts, including pyroxene and olivine, display minimal compositional zoning, suggesting limited magma differentiation during ascent. The rapid crustal accretion at these ridges also results in thinner lithospheric thermal gradients, influencing the depth and extent of mantle melting. Studies of isotopic compositions further highlight the homogeneity of mantle sources at ultra-fast spreading ridges, with limited evidence of enriched components or plume interactions (Carbotte et al., 2016).

The process of hydrothermal alteration at all MORs significantly influences the petrological characteristics of their oceanic crust. Basalts and gabbros are commonly altered to form secondary mineral assemblages, including chlorite, epidote, and actinolite, which record interactions with circulating seawater. Ultramafic rocks, particularly peridotites, undergo serpentinization, resulting in significant geochemical changes, such as the addition of water and loss of silica. These processes play a crucial role in modifying the primary mineralogy and geochemistry of MOR rocks, as well as contributing to the geochemical cycling of elements such as sulphur, iron, and magnesium (Alt, 2004).

3.2. Axial high versus axial valley topography of MORs

Many mid-ocean ridges (MORs) evolve with complex 3D axial topography, which is hard to explain with standard tectonic models. Their spatially varying axial topography, such as high, flat or valley, is generally attributed to the spreading rate (Small, 1998, Sim et al., 2020), the magma availability (Sinton and Detrick, 1992; Keller et al., 2017; Mandal et al., 2018) in a particular ridge-segment, and upper crustal faulting (Buck et al., 2005). Howver, these contrasting axial morphologies are often found in MORs, e.g., South-East Indian Ridge

(SEIR), where the spreading rate shows practically no variations (Carbotte et al., 2016), and ultra-slow South-west Indian Ridges (SWIR) displaying typical axial valley topography, where they have large magma availability (Jian et al., 2017). A direction of MOR studies explains the rift morphology as a product of the two competing processes- tectonic and magmatic, conceived as horizontal spreading and dike opening, respectively (Buck et al., 2005; Liu and Buck, 2018). A non-dimensional parameter, called the M factor (a ratio of the dike intrusion to plate-spreading driven widening rates), has been used to reproduce the axial structures in numerical models. $M = 1$, i.e., a condition of dike intrusion rate to completely balance with the plate spreading rate, gives rise to an axial high, whose height depends on the magma density. In contrast, $M < 1$, i.e., a condition of less effective diking than the spreading rate, yields faulted axial valley (Buck et al., 2005; Ito and Behn, 2008). Some studies have shown the axial morphology as a function of the extension rate and inherent short-wavelength seafloor heterogeneities (e.g., Small 1998). However, their interpretation faces disagreement with the Mid-Atlantic ridge model, which proposes the magma supply as a critical factor in determining the axial morphology (Liu and Buck, 2018). Although these models Ill integrate the axial morphological spectrum by a single factor- M, the modelling approach does not account for sub-crustal melt processes. It is noteworthy that many recent MOR studies demonstrated how the latter could significantly control the MOR evolution (Carbotte et al., 2016; Martinez et al., 2020), albeit a comprehensive model is still unavailable. This work aims to bridge this gap, treating the axial morphology in the thermo-mechanical framework of an ideal three-dimensional melt upwelling system, where divergence force components act along and across

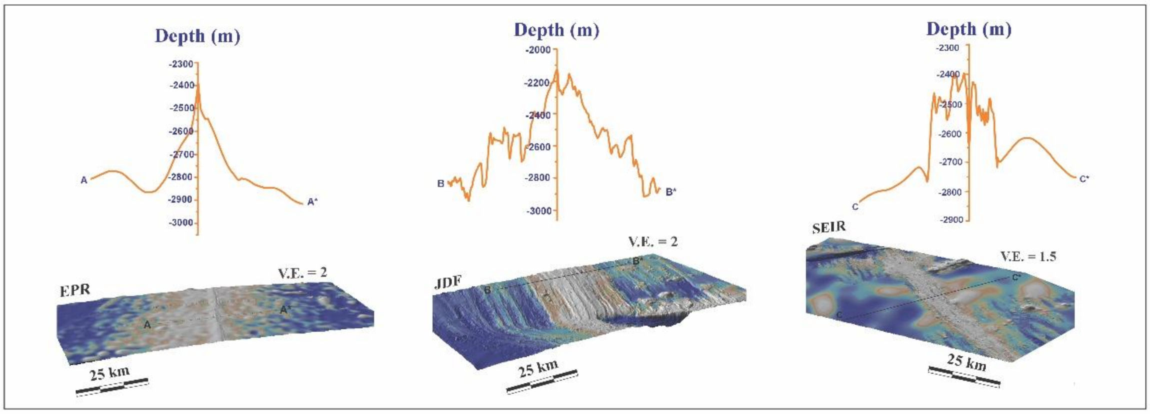

Figure 3.4 *Bathymetric profiles across the East Pacific Rise (EPR), Juan De Fuca (JDF) and South-Eastern Indian Ridge (SEIR). They show high (EPR-AA*), moderately high (JDF-BB*) and plateau dominated (SEIR-CC*) ridge-axis topography, respectively. Data source: GeoMapApp (**http://www.geomapapp.org/**)/CC BY.*

the ridge axis. This modelling approach allows us to investigate the extent of magmatic control on 3D axial morphology.

While emphasizing magmatic roots, several workers considered magma buoyancy as the principal factor to elucidate the origin of axial-high topography (Buck, 2001; Wilson, 1992). Eberle et al., (1998) provided a condition of the sub-ridge viscosity distribution required for buoyancy-driven axial high topography. On the other hand, Morgan et al., (1987) predicted that mantle viscosities beneath the ridge must be at least two orders higher than the generally accepted values to form an axial valley. Sleep and Rosendahl (1979) also indicated viscosity as the key factor, but it is ultimately the plate velocity to regulate the sub-crustal density or viscosity that determine the axial morphology. Here, the most critical question is – how the plate velocity regulates the sub-crustal viscosity? Choi and Buck (2010) show from a 2D numerical model that the mantle viscosity at shallow depths (< 20 km) beneath the ridge should be low (~ 10^{18} Pa s) to form axial high topography, but it should be high enough (~ 10^{21} Pa s) to form a low axial relief. According to their model, high-viscosity melt flows lower the hydrostatic pressure beneath the ridge, reducing the melt-upwelling height. However, none of these studies explicitly accounts for the viscosity effect of sub-crustal melt-rich zones on the axial morphology.

The problem of sub-crustal melt transport mechanisms has recently rejuvenated the MOR research in new directions (Sparks et al., 2019; Edmonds et al., 2019; Carbotte et al., 2020, 2021). It is now evident that melts start to localize in discrete zones during their ascent that eventually mediates for a heterogeneous magma supply to the ridge axes. Earlier numerical models (Sarkar et al. 2014, Mandal et al., 2018) should melt fraction as a function of spreading rates, suggesting that the melt fraction is substantially reduced from fast- to slow-spreading ridges. Secondly, the melt upwelling processes participate in solidification at the shallow level to form isolated mushy bodies, as reported by many earlier workers (Sinton and Dentrick, 1992; Smith and Cann, 1993; Singh et al., 2006). The crystal content in the mushy melts can largely vary depending on the degree of crystallization, and their varying relative volume ratios would determine the viscosity of the melt-bearing sub-ridge regions. Braun et al., (2000) provided a depth-wise viscosity profile based on melt content (~3%), dehydration, and grain boundary sliding. This model predicts an increase in overall viscosity with height, mainly due to water extraction during partial melting. However, later experimental studies suggested that such dehydration can hardly affect viscosity at shallower depths as partial melting generally ceases to occur at a deeper level (Hirth and Kohlstedt, 2003). The olivine rich high-fluid channels in subcrustal magma mush at a shallow depth (Kelemen et al., 2000) indicates crystal transport as suspension. A detailed viscosity analysis of the sub-crustal regions containing crystal-bearing melts beneath MORs, especially in view of the axial morphology, is yet to be fully explored.

This chapter introduces a novel approach to model sub-crustal/lower-crustal (hereafter sub-crustal) viscosity and offers a viscosity-based explanation for the axial morphologies: highs and flat topography of MORs, e.g., East Pacific Rise, Juan du Fuca, and South East Indian Ridge (Figure 3.4). In the first step, a series of systematic calculations is given to enumerate the effective viscosity of the *mush complex* (MC) beneath the ridge axes. The mush complex (MC) as a constitution of crystal-bearing-melts with large variation in crystal contents and host rocks (Sparks et al., 2019). The calculations considers the following parameters: the process-times, spatial magnitudes, and the constitution of sub-crustal materials (Figure 3.5). Finally, a three-dimensional fluid-structure interaction (FSI) approach is conceived to model the mechanical connection between the MC and the overlying crust at a mid-oceanic ridge. The FSI model allows me to investigate how the viscosity of the sub-crustal mushy region can modulate the flat versus high MOR axial topography.

3.3. Sub-crustal mush complex: viscosity modelling

3.3.1. Mush complex in MOR settings

Geophysical signatures, such as lower seismic velocities and high attenuation suggest the occurrence of mushy zones beneath mid-ocean ridges (Arnoux et al., 2019; Wilson 1992), containing suspension-rich melt bodies (super solidus) as the subsolidus host rocks (Sparks et al., 2019). Based on such sub-ridge mush-melt patterns reported in the literature (Mckenzie ,1984, Mckenzie and Bickle, 1988, Lin and Permentier, 1989; Hebert and Montesi, 2010; Keller et al., 2017; Sim et al., 2020), a mechanically distinct zone, is identified as mush complex (MC), treated as a continuum to implement the dynamic and kinematic coupling between the underlying mantle and the overlying elastic crust (Carbotte et al., 2021; Zhang et al., 2014). It is now a well-established fact that ascending mushy melts encounter the lithospheric base that acts as a melt barrier and forces the melts to focus into the ridge axis, forming a distinct melt-rich regime within the host rocks. (Lin and Permentier, 1989; Hebert and Montesi, 2010; Keller et al., 2017; Sim et al., 2020). From gravity anomaly data, Lin and Permentiere (1989) detected a low-density zone at the base of the lithosphere at EPR. Mckenzie and Bickle (1988) discussed the occurrence of underlying hot sheets at the decoupling zone betIen the circulating mantle and the spreading plates. On the other hand, many geophysical studies found sub-crustal melt lenses, 1-2 km wide and 100 m thick, containing 30-40% crystals as suspension, in several ridges (Figure 3.5). The lenses are extended horizontally up to 15-20 km with their melt content decreasing to 30%, forming spatially extensive mushy regions (Singh et al., 2006; Canales et al., 2005; Toomey et al., 2007). Singh et al. (2006) recognized 3-4 km thick axial magma chambers at a depth of 3 km in slow-spreading, magma-rich Lucky strike. Fast and intermediate spreading ridges are reported to have magma bodies at shallower depths, ~ 2.4 km in JdF (Canales et al., 2005) and ~ 1.8 km in EPR (Detrick et al., 1987), where their maximum thickness is ~ 4 to 6 km (Detrick et al. 1987; Kent et al., 1993). In contrast, slow ridges generally lack such distinct magma bodies, but have mushy regions (low-velocity zones) at the crustal base. Dunn et el., (2005) reported a 6 km thick mushy zone of sparse melt channels at a depth of 4 km at MAR (35°N). Besides melt pockets, which are prevalent in fast-spreading ridges, discrete melt channels in the lower crust and sub-crustal axial zones (Dunn et al., 2005; Canales et al., 2005) also constitute a typical feature (low-velocity mushy regions) at the crustal base, which is also considered as a part of the MC (Sinton and Detrick 1992). Geophysical studies have shown that ascending melts, produced by decompression melting at a depth of around 40 km, focus to the ridge axis, forming large, nearly 30 km wide melt-rich regions beneath mid-ocean ridges (McKenzie and Bickle, 1988). Seismic imaging and theoretical estimates indicate a wide variation in their partial melt content

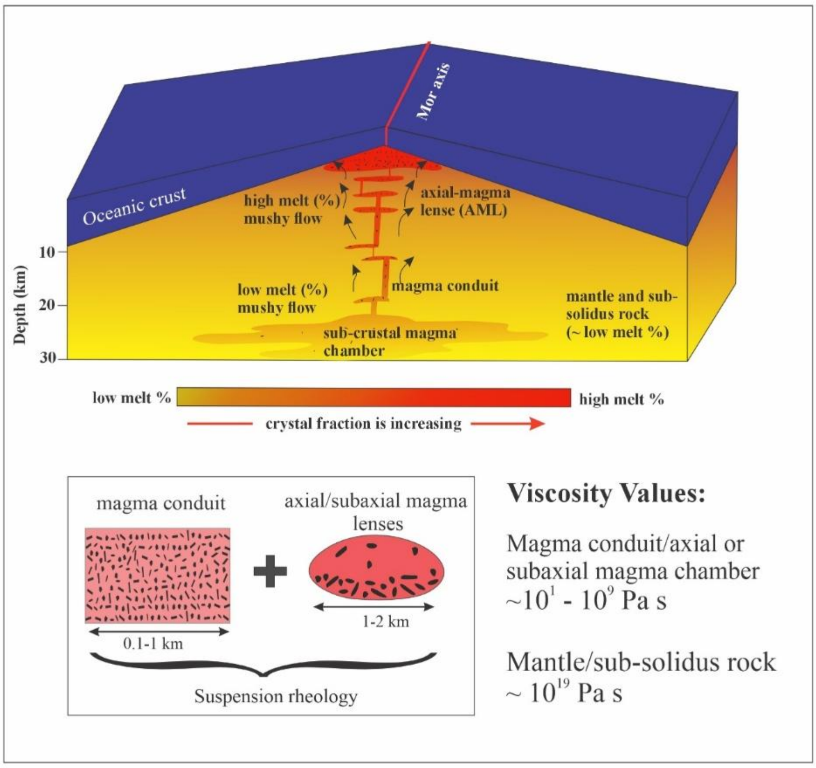

Figure 3.5 *A schematic cross-section beneath a mid-ocean ridge (MOR) illustrating the major components of the sub-crustal magmatic system. Melts are generated within the sub-crustal magma chamber and ascend to the axial magma lens through magma conduits. Notably, both the melt percentage and crystal fraction increase as the material approaches the axial magma chambers. In this study, the viscosity of magma conduits is considered to range from* 10^1-10^9 *Pa·s, whereas the viscosity of the mantle and other sub-solidus rocks is on the order of* 10^{19}*Pa·s.*

(~ 10 – 70 % at shallower levels, < 10 km and 5 – 25 % at deeper levels, ~ 30 km) from one ridge to the other or different segments within the same ridge (McKenzie and Bickle, 1988; Hewitt, 2010; Bergantz et al., 2015; Sauter et al. 2016). It is vital to assess how such variations in melt content can influence the mechanical strength of sub-crustal melt-rich regions (MC) at shallow depths and modulate the first-order ridge-axis topography. In submarine systems, the temperature calculated for the critical depth of partial melting cessation constrains the amount of available melt in the subcrustal MC system (McKenzie and Bickle, 1988). However, the melts ascend upward with a complex 3D pattern of their paths, determined by coupled convection-solidification processes (Sarkar et al., 2014; Mandal et al., 2018; Zhang et al., 2014). The volume fraction of melt-crystal aggregates goes up (Gonnerman and Manga, 2007; Hewitt, 2010) as subcrustal magma bodies form at mid-oceanic ridges. The plot shows a linear regression of the average melt fractions with depth (Figure. 3.7a). There can be large variations from the linear average at subcrustal regions due to significant spatial variations in the magma pool populations and their fractional crystallization beneath MORs (Figure. 3.7b).

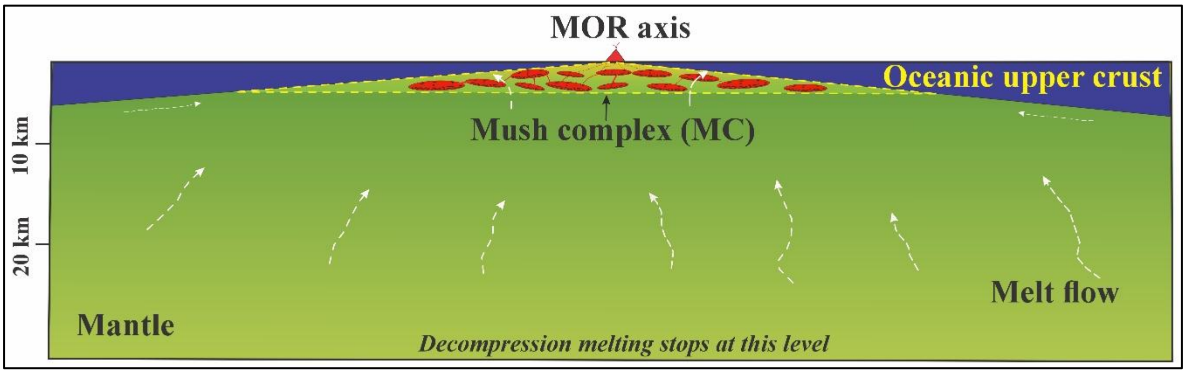

Figure 3.6 *A conceptual cartoon diagram of the sub-ridge melt/magma settings considered for the topographic modelling in this study. The mush complex (MC) represents a distinct zone consisting of melt bodies and conduits within a high-viscosity host rock matrix.*

Based on the available reports on substantial melt occurrences beneath MORs in the form of axial melt lenses and melt-rich bodies, the vertical extent of the mush complex (MC) was chosen in the present model in sub-crustal regions and in the uppermost mantle. The MC was allowed to evolve with progressively deforming overlying elastic crust under basal stresses that eventually decreased the axial depth and increased the MC thickness. The MC is modelled with a triangular cross-section, describing an along-axis prismatic area in the lower crust, with a maximum thickness of 4 km beneath the ridge axis (see, Figure 3.6). The upper crust (i.e., solid elastic crust) at the axis is chosen 4 km thick in the initial model setting, where the MC vertically covers the lower crust and a part of the topmost mantle region (see, Figure 3.6). The reason for choosing a larger MC depth, as compared to the available data (see preceding paragraph) in our initial model is that the solid crust progressively thins by elastic strains during the simulation. For example, the initial crustal thickness at the axis is reduced by 2 km to finally set the MC depth and thickness at 2 km and 6 km, respectively (Sinton and Detrick, 1992).

3.3.2. Melt-viscosity modelling: parametric considerations

The viscosity of melts and magmas at shallow depths is historically modelled within a framework of *suspension rheology*, following the landmark work of Einstein (1906). However, natural suspensions show viscous behaviour more complex than that predicted from Einstein's theory. The complexity originates primarily from the effects of additional factors, such as packing and shapes of solid particles in suspensions. The packing of solid components in the liquid phase is an influential factor to modify the effective viscosity of a mixture under the same solid volume fraction (Krieger and Dougherty, 1959). The packing vis-a-vis viscosity, depends significantly also on the solid particle size distribution in the liquid. For example, a bimodal size distribution with increasing size ratios up to a threshold point lowers the effective viscosity (Chong et al., 1971). Chang and Poll (1994) showed that the viscosity of a suspension decreases initially with increasing smaller particle volume fraction and then increases monotonously after reaching a critical volume fraction. Liquid suspensions attain their maximum packing fraction in the case of multimodal size distributions. Such multimodal (trimodal and tetramodal) particle packing increases viscosity higher than those for bimodal and unimodal distributions (Klein et al., 2017). This study also suggests that packing with different particle sizes yields a polydispersion effect on the bulk viscosity of suspensions for the same particle volume fraction. Polydispersity allows smaller particles to pack more closely by forming layers between larger particles or by occupying the void spaces between larger particles (Desmond and weeks, 2014). Such polymodal and polydisperse particle (heterogeneous packing) distributions can thus significantly enhance the bulk viscosity of melt suspensions in a mushy region.

Petrological and compositional data indicate mineral phases, e.g., olivine, plagioclase and clinopyroxene can crystallize in partially molten zones at successive stages during the melt ascent. However, their depth correlation becomes weak with decreasing spreading rate (Klein and Langmuir, 1987; Langmuir et al., 1992). Volcanic studies suggest that the polydispersity characteristics of mushy melts and their variations hold a connection with the spreading rates at MORs. Mushy melts can strongly differ in their crystal and bubble contents depending upon the spreading rates (Edmonds et al., 2019; Kavanagh et al., 2018). Slow-spreading ridges generally show larger compositional variations in erupting lavas than the fast-spreading ridges.

Higher degrees of compositional homogenization in the fast-spreading ridges are commonly attributed to the magma chamber processes (Ohara and Mathews, 1981), in contrast to slow-spreading ridges, e.g., the Mid Atlantic Ridge (MAR), which are devoid of large, stable magma chambers and involves fractional melting throughout the whole melting regime to produce melts with a strong compositional variability (Shizimu and Grove, 1998). It is noteworthy that magma chamber processes act as potential sites for hot mafic magma replenishment into the cold silicic resident magmas (Figures. 3.8). Several workers have reported mafic enclaves from volcanic rocks as evidence of the magma replenishing process (Figure. 3.8a-3.8b) (Murphy et al., 2000; Coombs et al., 2004; Martin et al., 2006).

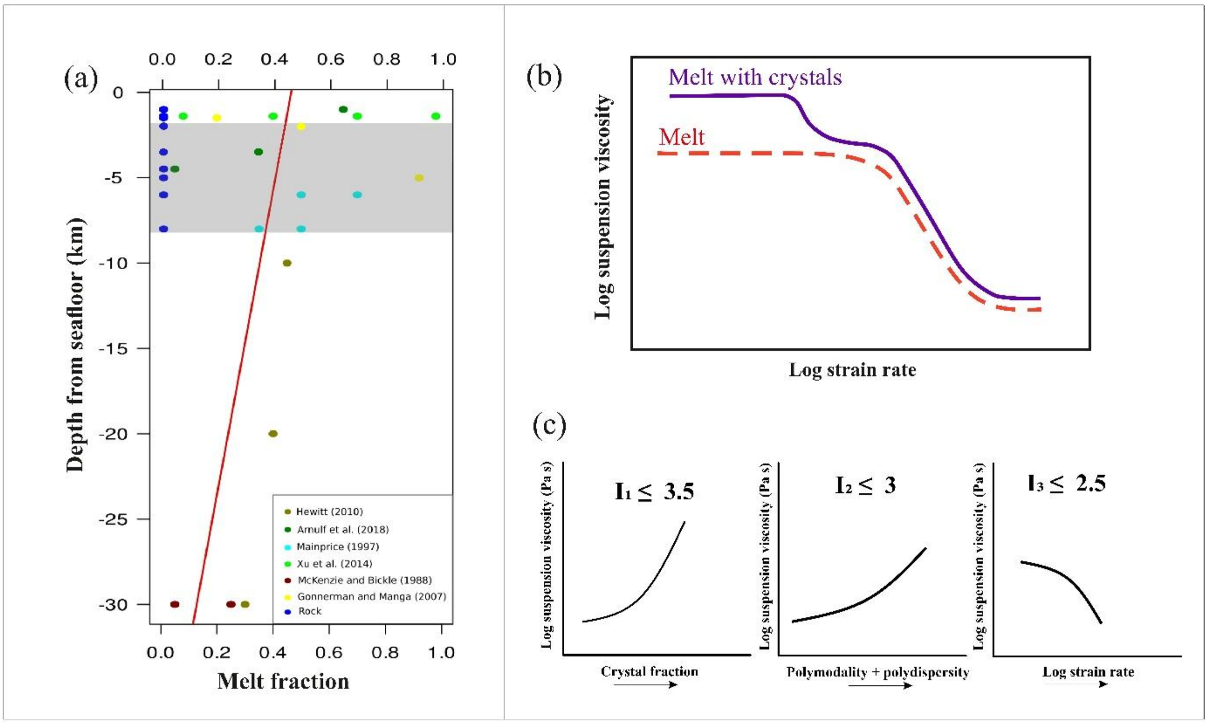

Figure 3.7 *(a) Variation of melt fractions with depth (plots based on available data in literature). All the data are taken from axial melt lenses, magma chambers and melt conduits. In the plot, these data points are complemented with rocks (1% melt), marked in deep blue. Red straight line shows the overall regression trend. Shaded area delineates the depth range (2-8 km) of evolved MC, where the average melt suspension fraction in MC is 0.3 - 0.4. (b) The plot shows the variation of suspension viscosity as a function of strain rate and characteristics of the melt suspension. (c) The graphical representation of variation of suspension viscosity with different suspension characteristics and their respective contributions.*

The effects of replenishment dynamics on magma chamber processes depend mainly on the magma flow conditions. Turbulent fountain-type injections produce dispersed spherical enclaves of crystals, whereas a non-turbulent slow influx of hot magma (*Re* <400) (Figure 3.8) results in ponding of groundmass crystals at the magma-chamber base (Coombs et al., 2004; Martin et al., 2006). Martin et al., (2006) also suggested that the more replenishing magma volume flux, the larger olivine phenocrysts would form, resulting in convection-driven churning within the magma chamber due to a longstanding steeper temperature gradient (Figure 3.8b). However, recent geochemical studies focus on the general mushy environment as a host of crystallization and magma mixing (Bachmann and Huber, 2016). Geochemical investigations of crystal-bearing enclaves within erupted lavas in volcanic settings allow us to recognize several factors controlling shallow magmatic environments beneath mid-oceanic ridges: a) occurrence of magma chamber, b) melt-upwelling velocity, and c) volume in the mushy regions. These factors determine whether magma-dominated, volatile environments can significantly influence the dispersion and multimodality characteristics of solid suspensions in hot magmas. In contrast, magma-poor mushy regions, consisting of small and unstable non-convecting magma chambers, can form dominantly monodispersed microlith ponds.

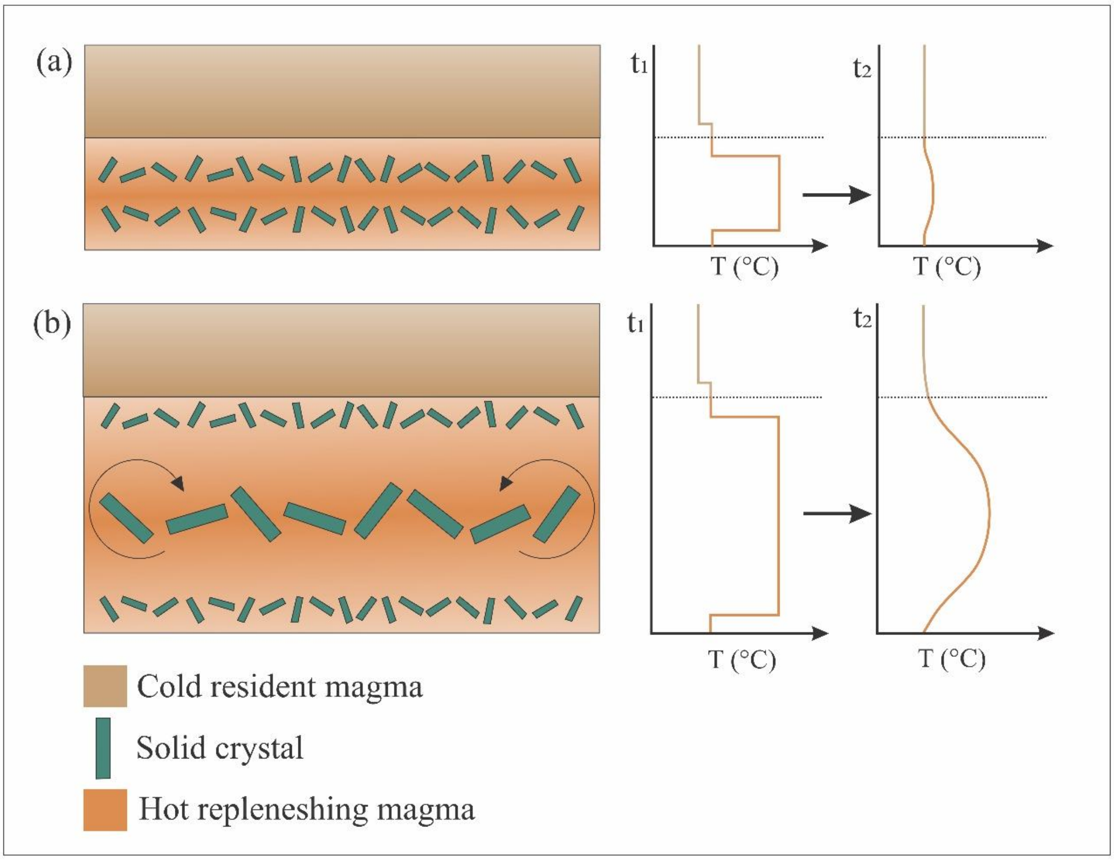

Figure 3.8 *A cartoon presentation of two different replenishment dynamics in the subcrustal magma-chambers. (a) Volumetrically small and slow magma replenishment. In this case a thin layer of groundmass crystallization forms, and the thermal gradient between the hot emplaced magma and the host mafic magma is dissipated and reduced. (b) Fast and large magma replenishment. In this case, the hot magma disperses into a magma chamber like fountains before crystallizing to form enclaves. Moreover, a large volume of replenishing magma causes a thicker hot layer, which sustains the thermal gradient for a longer period with convective churning and multimodal crystal enclaves.*

Petrogenetic analysis of a recent East Pacific Rise (EPR) eruption suggests the presence of sub-ridge crystal-bearing mushy regions, which are thought to be a product of consistent replenishment (Figures 3.8a and 3.8b) by evolved magmas from a deeper level source (Goss et al., 2010). Rubin et al., (2001) reported homogeneity in lava basalts from fast ridges [Heterogeneity Index (HI) ~ 1.6 for spreading rate > 10 cm/yr], but strong heterogeneity from slower ones [HI ~ 3 for spreading rate < 4 cm/yr]. They accounted for the relative thermal stability to explain the higher degree of homogeneity in the fast ridges. Phyric basalts containing mushy zone crystals suggest the injection of primitive magmas. However, the petrological estimates of mid-ocean ridge basalt (MORB) at MAR point to larger volumes of aphyric basalt, representing a collection of aphyric magmas within a mushy zone at shallow depths. The magmas originated from convection-assisted melt segregation. Lange et al., (2013) calculated mush viscosity (*cf.* Giordano et al., 2008) as a function of plagioclase phenocryst content. According to their estimate, the viscosity of melt suspensions can increase by eight times with an increase in small-size (~ max. 10 mm) plagioclase phenocryst fraction, where the crystallinity is 20%. Their analysis predicts the maximum size of olivine phenocrysts in erupting plagioclase-ultraphyric-basalts (PUB) in the range of 1 to 3 mm. They also explain the presence of PUB selectively in slow and intermediate ridges as a consequence of olivine phenocryst segregation in conduits during the magma ascent rather than in the magma chambers. Lange et al., (2013) hypothesized that during the ascent of melt-crystal aggregates through conduits, the melt to crystal ratio is high, and their bulk viscosity is thereby low. However, it is hard for low-viscosity magmas to transport crystals without segregation in the conduit. Going by these arguments for the petrogenesis of plagioclase-phyric basalts, this work infers that the bulk viscosity of magmas at the time of their ascent through conduits must be low in cases of slow and moderately spreading ridges, allowing extensive crystal segregation to produce monomodal crystal packing with little or no polydispersity. In contrast, the melt suspension viscosity in fast-spreading ridges, or ridges with prominent magma chambers, should be high due to greater polydispersity and polymodality even the melt volume fraction is relatively large. The polydispersity variation in sub-ridge magmatic processes is thus an influential factor to modulate the melt suspension viscosity (Figiure 3.7c). Based on the preceding discussions of melt characteristics, the packing factors is thus considered to be a factor in the viscosity analysis of crystal-bearing melts in mushy regions.

3.3.3. Mush complex viscosity: a two-step calculation

We can now calculate the viscosity of mush complex (MC) in two steps: 1) viscosity calculation of crystal-bearing melts, based on the theory of suspension rheology, and 2) viscosity of MC (host rock + melt suspensions), based on the theory of two-phase fluid mixtures. To calculate the viscosity of a crystal-melt aggregate, let assume the solid (crystals) component as a suspension in the liquid matrix, as described in the preceding section. Again, the solid part in suspension is treated as rigid particles and the liquid part as a continuous, viscous medium. The calculation is carried out using the equations and calculations found in the literature for erupted lavas. Figures 3.5 and 3.6 provides a cartoon diagram to show its conceptual framework.

3.3.3.1 Melt Suspension viscosity

Consider a scale of the magmatic process with characteristic lengths, 0.01 to 1 km, as applicable to shallow level magma conduit dimensions (diameter and length) in the sub-ridge region (Head et al., 1996). Lava eruption episodes determine the characteristic time through the conduits. According to the Volcanic Explosivity Index (VEI) (Newhall and Self, 1982) study, covering more than 75% of the documented Holocene eruptions, almost 50% of them record continuous blast duration of less than 6 hrs. Furthermore, 63% of the eruptions yield eruptive volumes ranging from 0.001 to 0.1 km^3. Considering the median of time intervals, successive eruptions of a volcano is found to occur in a time-frequency of 13 years (Siebert et al., 2015). These data are used to calculate the strain rates associated with magma flows in shallow conduits. To simplify the calculation, consider 0.001- 0.1 km^3 magma undergoing eruption through a cylindrical conduit of 0.01-1 km diameter and on a time duration of 13 years. This wider range of diameters and conduit lengths is chosen because eruptions generally occur through multiple magma conduits of varying lengths, and a cumulative effect of the aforesaid parameters is required in our present analysis. For further simplification, we can deal with a representative set of their values, where the magma conduit length (l_c) and diameter (d_c) are 1 km and 0.1 km, respectively, and the erupted magma volume (v_c) is 0.01 km^3, which passes through the conduit on a time scale (t_c) of 13 years. This set of values yields an average characteristic strain rate ($\acute{\varepsilon}$) of shallow-conduit upwelling of magma, $\acute{\varepsilon} = (v_c/(0.25\pi d_c^2 l_c t_c) = 10^{-9}$ s^{-1}. The characteristic strain rate $\acute{\varepsilon}$ can range from 10^{-6} to 10^{-12} s^{-1} if the parametric values Ire varied to cover the entire range discussed above. It is noteworthy that this strain rate scale supports suspended crystals to move passively within the melt phase (Caricchi et al., 2007).

It is necessary to treat lava eruption on a different time scale (designated as *lava scale*), which represents the duration of a continuous flow event. These events usually take place in a duration of 1 to 12 hours (Siebert et al., 2015). We can thus choose an average value of 5 hours to represent the lava scale. Considering the lava conduit length and cumulative diameter as 0.1 km and the erupted magma volume as 0.01 km^3, the analysis yields the characteristic strain rate 10^{-3} s^{-1} (Table 3.1).

Table 3.1 *Model parameters used in determining the viscosity scale*

Domains	Properties
Lava scale	Conduit length (l_c) = 0.1 km; Conduit diameter (d_c) = 0.1 km; Transmitted volume (v_c) = 0.01 km^3; Strain rate ($\dot{\varepsilon}$) = 10^{-3} s^{-1}; Transmitting time (t_c) = 5 hrs.
Magma scale	Conduit length (l_c) = 1 km; Conduit diameter (d_c) = 0.1 km; Transmitted volume (v_c) = 0.01 km^3; Strain rate ($\dot{\varepsilon}$) = 10^{-9} s^{-1}; Transmitting time (t_c) = 13 yrs.
Mantle scale	Conduit length (l_c) = 10 km; Conduit diameter (d_c) = 1 km; Transmitted volume (v_c) = 0.01 km^3; Strain rate ($\dot{\varepsilon}$) = 10^{-14} s^{-1}; Transmitting time (t_c) = 100 yrs.

The suspension parameters, polymodality, and polydispersity can increase the viscosity of melt suspensions (Figure 3.7c), as discussed in the preceding section. Let us now calculate the degree of viscosity increase possible in melt suspensions under a sub-crustal environment at MORs. Several studies have provided empirical relations to express the melt viscosity as a function of suspension properties (Einstein, 1906; Maron and Pierce, 1956; Kreiger & Dougherty, 1959; Chong et al., 1971; Shapiro and Probstein, 1992; Costa et al., 2010; Moitra and Gonnermann, 2015, Gonnerman and Manga, 2016). Consider first the effect of crystal content in melts. Costa (2005) enumerated crystal-free melt viscosity, μ_l= 10^5 Pa s at a temperature of 800°C and a pressure of 300 MPa. The effective viscosity of melts increases with increasing solid volume fraction (φ_s) in the suspension. Marsh (1981) suggested that melts erupt as lava with a maximum viscosity, μ_M= 10^7 Pa s corresponding to $\varphi_{s,c}$ = 0.55, called a *critical solid fraction*. However, vander Molen and Paterson (1979) suggested that the critical solid fraction can be further large, $\varphi_{s,c}$ = 0.6 ~ 0.7 at the time of lava eruption, implying crystal-bearing melt viscosity, μ_M= $10^{8.5}$ Pa s, which means the enhancement of suspension melt viscosity by an order: I_l = 3.5 (Costa and Dungan, 2005; Gonnerman and Manga, 2007).

Polydispersity (δ) is a measure of the size variation of suspended solid particles in magma. For packing with particle distribution on radii, *P(R)*, the parameter can be expressed as, $\delta = \sqrt{\langle \mathit{\Delta} R^2 \rangle}/\langle R \rangle$, where $\mathit{\Delta} R = R - \langle R \rangle$, and the moments of R is defined by $R^n > \int R^n\, P(R) dR$ (Desmond & weeks, 2014). It is noteworthy that an increase in δ allows the suspension to increase the maximum limit of critical solid fraction $\left(\varphi_{s,c}\right)$. The polydispersity, in turn, multiplies the suspension viscosity. The maximum packing ratio of mono-dispersed spheres accommodates a maximum solid fraction of 0.64, which can increase to 0.75 for suspensions with a polydispersity of 0.65 (Bernal and Mason, 1960). Roscoe (1952) derived a couple of equations using experimental results (Eilers, 1941; Ward and Whitmore, 1950), showing that various size distribution of rigid spheres influences the viscosity of suspensions less than a uniform size distribution. However, the present theoretical treatment considers the theoretical work of Klein et al., (2018), who showed that polydispersity would steeply increase the maximum packing fraction after a threshold limit for monomodal size distributions. This packing effect results in an exponential increase of the suspension viscosity and multiplies its magnitude 40 times. Moreover, the experimental study suggested that an increase in crystal polydispersity might augment volcanic lava viscosity up to 3 orders of magnitude at a higher deformation rate (Moitra and Gonnermann 2015; Roche and Carazzo, 2019). This theoretical model thus considers the maximum viscosity enhancement in the order, $I_2 = 3$, corresponding to the polydispersity of crystal-bearing melts.

Strain rate is another factor in the present viscosity calculation. Experimental studies suggest Newtonian melt rheology prevails at strain rates lower than 10^{-5} s^{-1} (Caricchi et al., 2011). But, at higher strain rates, the melts develop shear thinning behaviour (Ibb and DingIll, 1990), which reduces the viscosity by more than 2.5 orders in case of larger solid fraction ($\varphi_{s,c} \sim 0.8$) (Caricchi et al., 2017). Considering the strain rates in the order of 10^{-6} to 10^{-12} s^{-1} on the magma scale and 10^{-3} s^{-1} on the lava scale, we can choose a maximum viscosity enhancement in the order, $I_3 = 2.5$, solely due to the decreasing strain rate, leaving out other variables (Caricchi et al., 2017).

To summarize, the present theoretical treatment uses a suspension factor (I), taking into account the cumulative effects of solid crystal fraction (I_1), size distribution (polydispersity) (I_2), and strain rate (I_3), respectively. Considering pure melt viscosity in the order of 10^5 Pa s, as an example, the suspension viscosity (μ_M) can be enhanced to a maximum extent of $10^{8.5}$ Pa s for a limiting solid fraction (0.6 to 0.7), implying that $I_1 = 3.5$ (Costa and Dungan, 2005; Gonnerman and Manga, 2007). On the other hand, an increase in crystal polydispersity can multiply μ_M by an order of 10^3 at a higher deformation rate (Moitra and Gonnermann 2015;

Roche and Carazzo, 2019). I thus consider $I_2 = 3$. Finally, for the strain rate effects, μ_M can multiply by a factor of $10^{2.5}$ depending on the variation of strain rates in the range 10^{-3} to 10^{-12} s^{-1}, as applicable to the MC in our model. That means, $I_3 = 2.5$. Taking their net effects (i.e., $I_1 + I_2 + I_3$), we have: $I = 9$ (Figure 3.7c).

3.3.3.2 Viscosity of mush complex (MC)

In contrast to the conduit lava or conduit magma processes, sub-ridge mantle processes operate on longer time scales, with strain rates in the order of 10^{-11} – 10^{-14} s^{-1} (Rosenberg and Handy, 2005). This viscosity analysis, thus, adopts a different theoretical approach to calculate the MC viscosity. The theoretical model treats slow mushy flows in the mushy uppermost mantle as a two-phase fluid continuum and employ Arrhenius equations to calculate the viscosity of the complex, adopting the theory of mixture rheology within a framework of continuum mechanics (Zhmud, 2014). Consider a mixture of host rock ($\mu_R = 1 \times 10^{19} Pas$) and melt suspensions ($\mu_M = 1 \times 10^{0.5} - 1 \times 10^{11.5} Pas$). Its bulk viscosity, termed as *effective viscosity* (μ_{eff}) can be expressed by the Lederer-Roegiers equation for a two-phase liquid system as,

$$ln\mu_{12} = \frac{x_1}{x_1 + ax_2} ln(\mu_1) + \frac{(ax_2)}{x_1 + ax_2} ln(\mu_2), \tag{3.1}$$

where α is a constant used to represent the difference in intermolecular cohesive energy between the participating two components, 1 and 2. x_i and μ_i (i = 1, 2) are the mole fraction and the viscosity of i^{th} component in the mixture, respectively. The Lederer-Regiers equation provides an accurate viscosity calculation of multi-phase fluids with contrasting component viscosities (Zhmud, 2014). Equation (3.1) is close to the Arhenius equation, which can be demonstrated from Roegiers and Zhmud's (2011) approach. Fluidity (inverse of viscosity) of a fluid phase depends on the molar flow activation energy, ΔE (a measure of intermolecular cohesion). The Arrhenius relation describes the fluidity in the framework of Eyring's rate process theory (Glasstone et al., 1941) as,

$$\frac{1}{\mu} = \frac{K}{\hbar} exp\left(\frac{\Delta E}{RT}\right), \tag{3.2}$$

which leads to,

$$ln\mu_i = C_1 + \frac{\Delta E_i}{RT}, \tag{3.3}$$

where C_1 is a constant, $\hat{h}$ is Planck's Constant, T is absolute temperature, R is the universal gas constant, and K is the ratio of molar volume and Avogadro number. Subscript i refers to the fluid component.

For a two-phase liquid system, consider an additive principle to find the net activation energy of the mixture. According to Eyering's Rate Process theory of viscosity (Glasstone et al., 1941), the relative motion of one fluid layer over the other demands a molecule to overcome a potential-energy barrier, called flow activation energy per molecule. The total flow activation energy is obtained by taking a product of this quantity with the number of molecules in the system, neglecting any energy dissipation during the molecular transport. Based on this assumption, the total flow activation energy follows,

$$\Delta E_{12} = x_1 \Delta E_1 + x_2 \Delta E_2. \tag{3.4}$$

Using equations (3.3) and (3.4), we arrive at the Arrhenius equation for the binary mixture viscosity,

$$ln\mu_{12} = x_1 ln\mu_1 + x_2 ln\mu_2. \tag{3.5}$$

Equation (3.4) can be generalized with an asymmetric mixing rule (Roegiers and Zhumd 2011) for the flow activation energy:

$$\Delta E_{12} = \frac{(1-\gamma)x_1}{(1-\gamma)x_1+\gamma x_2}\Delta E_1 + \frac{\gamma x_2}{(1-\gamma)x_1+\gamma x_2}\Delta E_2, \tag{3.6}$$

where $0 < \gamma < 1$. For $\gamma < 0.5$, the contribution of component 1 to the flow activation energy is greater than that of component 2, and vice-versa for $\gamma > 0.5$. Using equations (3.3) and (3.6), we obtain the Roegiers equation (Equation 3.1) by replacing $\alpha = \frac{\gamma}{1-\gamma}$ in equation 1. $\alpha = 1$ implies an equal contribution of flow activation energy by the components, whereas $\alpha \neq 1$ indicates their unequal contributions. For asymmetric two-liquid mixtures, Roegiers and Roegiers (1946), and Roegiers (1951) considered α as the ratio of the specific intermolecular attraction energies of the components to derive Equation (3.1), where α was held constant for an ideal binary system at a particular temperature. The equation, validated experimentally by Roegiers (1951), and later tackled analytically by Zhmud (2014) yields α as the ratio $\ln(\mu_{12}/\mu_1) / \ln(\mu_2/\mu_{12})$ for a two-phase system with equal mole fraction of the participating components.

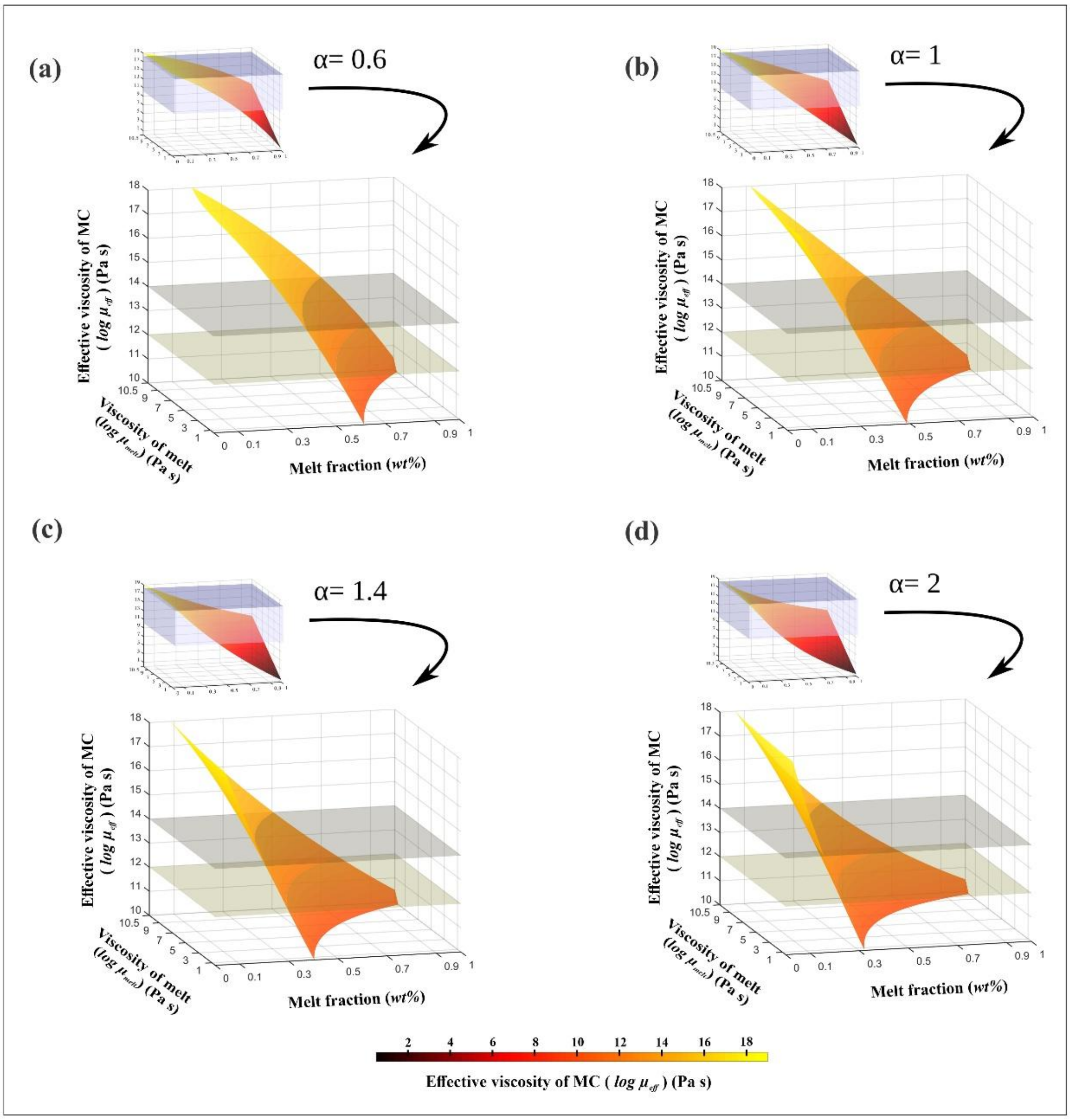

Figure 3.9 *Three-dimensional plots of the effective viscosity of MC (μ_{eff}) as a function of melt suspension viscosity (μ_M) and molar volume fraction (φ), obtained from the two-stage viscosity calculations for increasing values of the cohesion parameter, α.* ***(a)*** *α = 0.6, characterized by convex surface plot.* ***(b)*** *α = 1 (an ideal situation).* ***(c)*** *and* ***(d)*** *α = 1.4 and 2, respectively. Note the transformation of convex to concave curvature of the surface plot with increasing α. Insets show the full-length plots, highlighting the effective viscosity range of 10^{10} to 10^{18} Pa s. Two limiting effective viscosity (μ_{eff}) values, 10^{12} Pa s and 10^{14} Pa s are shown to constrain the viscosity range in our FSI model to reproduce the spectrum of axial high to flat topography. Host rock viscosity is chosen 10^{19} Pa s in these calculations, emulating mantle.*

In the foregoing analysis I use Equation (3.1) with $\mu_1 = \mu_R$ and $\mu_2 = \mu_M$, $x_2 = \varphi$ (molar volume fraction of melt suspension, and $\mu_{12} = \mu_{eff}$ (MC viscosity).

A set of 3D graphical plots presents the calculated μ_{eff} as a function of φ and μ_M for α = 0.6, 1.0, 1.4 and 2 (Figures 3.9 a-d). All of them show an inverse relation of the MC viscosity (μ_{eff}) with melt volume fraction (φ) and suspension viscosity (μ_M), as widely reported in the literature (Costa and Dungan, 2005; Gonnerman and Manga, 2007, Moitra and Gonnermann 2015), for the entire range of α values considered in the present calculations. μ_{eff} is reduced by two orders (10^{14} to 10^{12} Pa s) depending on the φ and μ_M variations. The model calculations suggest that μ_{eff} can increase with suspension melt fraction in specific conditions, e.g., suspensions with large volume fractions of crystals, as observed in magmatically robust ridge settings at fast-spreading ridges where magmas are extremely enriched with crystals. This model provides the MC viscosity estimates also in opposite environments in slow spreading ridges, characterized by magma poor and low in crystal content, where crystals readily settle down in the course of magma ascent (Lange et al., 2013).

3.4. Axial topography: fluid-structure interaction modelling

3.4.1. Sub-ridge fluid model

3.4.1.1 Decompression melting beneath MOR

The phenomenon of decompression melting beneath a MOR system generally occurs in a depth range 60 to 30 km, provided a set of conditions is satisfied. The primary condition, as defined by (Mckenzie and Bickle, 1988) is that an isotherm below the mid-oceanic ridge must be deflected upward from its horizontal position. In addition, the mantle adiabats would ideally follow potential temperature lines up to the surface, maintaining an isentropic state, and would change their courses as soon as they meet the solidus when there is a departure from the isentropic state with the onset of melting (Figure 3.10). Mckenzie and Bickle, (1988) used a value of 250 J/kg/^{0}C and obtained a thermal change of 80 ^{0}C to160 ^{0}C in the isentropic based potential temperature and the actual temperature at the moment of decompression melting, depending on the variation of potential temperature in the mantle region (Mckenzie & Bickle, 1988). Considering the MORB petrogenesis, the modelling of decompression melting demands a criticality analysis to constrain the melt fraction. Petrological calculations suggest a maximum of 24% melt for the polybaric fractional melting of lherzolite at the plagioclase-spinel lherzolite transition (Presnall et al., 2002). Langmuir et al., (1992), however, predicted a maximum of 20% melting possible beneath mid oceanic ridge, constrained by the disappearance of clinopyroxene. Mckenzie, (1984), on the other hand, provided an estimate of 24.5%. It has been shown that the melt fraction increases with decreasing pressure, by 1-2%/Kbar (Langmuir et al., 1992). Based on this dynamic constraint of decompression melting, the melt fraction goes up to 20%. The RTP is computationally manipulated to maintain the maximum melt fraction in the basal part of the mushy zone within this limit. In recent years, decompression melting processes at MOR are simulated considering a range of parameters, such as presence of volatile, spreading rate (Keller and Katz, 2016; Sim et al., 2020). We can, however, implement indirectly the effects of decompression melting, irrespective of its controlling factors, in our modelling by introducing random thermal perturbations (RTP) and influx velocity at the model base.

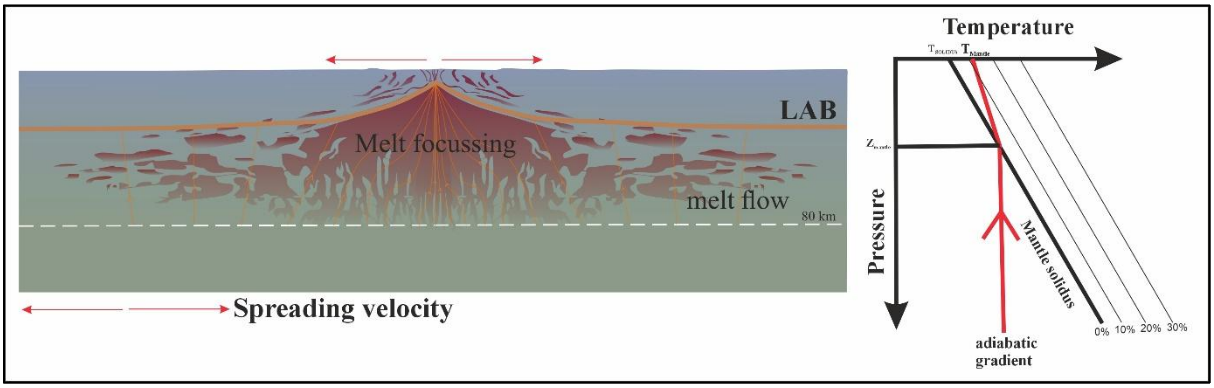

Figure 3.10 *The right panel presents a schematic perspective view of a mid-ocean ridge (MOR) system. At the top, the divergence of two tectonic plates (indicated by red arrows) leads to the generation of new oceanic crust. Plate separation drives the upwelling of the underlying mantle (shown in deep red), causing it to decompress and partially melt. The buoyant melt ascends through the partially molten region, accumulating along a low-permeability layer (lithosphere-asthenosphere boundary, or LAB) before migrating toward the ridge axis. At the axis, the melt is extracted and forms new oceanic crust. The left panel depicts a cartoon diagram of decompression melting beneath an MOR. Decompression melting initiates (along the red line) when the adiabatic gradient intersects the mantle adiabat. The process continues until it reaches the final depth of melting or the depth of melt-solid equilibrium.*

Seismological studies have been extensively used to estimate the amount of melting as well as to delineate melt-rich mushy zones beneath MORs. MELTS (Forsyth et al., 1998) observations in EPR suggest that although the total region of melt availability, as indicated by low seismic velocities, may cover a depth up to 180 km, extractable melts beneath the ridge occur up to a depth of 60 to 70 km. It is also observed that the low velocity zone can occur at a shallow depth (~15 km). The amount of melt here may not be well constrained, but the shapes of melt zones are well constrained. They occur as thin films or melt tubes/pockets (Eberle & Forsyth, 1998). The model is designed to account for such melt-rich zones by introducing the RTP at the model base.

3.4.1.2 Considerations for the model design

Mid-ocean ridges typically evolve through three major processes at different depths. The deepest process (30-60 km) causes decompression melting, covering a horizontal distance of ~50 - 150 km on either side of the ridge axis. The decompression melting process then follows another process, melt focusing into a narrow area around the ridge (Sim et al., 2020) during melt upwelling, which is coupled to a shallow convective process occurring in a shallow horizon. It is noteworthy that several studies have shown that decompression melting completely ceases to occur as the upwelling materials reach a threshold depth, ~ 30 km (Niu, 1997). The present modelling simulates the thermo-mechanical processes in the zone above this threshold depth. Based on the available data on sub-ridge mushy zones (Edmonds et al., 2019; Lissenberg et al., 2019; Singh et al., 1998, 2006; Sinton & Detrick, 1992; Sparks et al., 2019), this convective layer is chosen with its basal depth at ~28 km in our numerical model.

This theoretical study considers that the fluid convection layer at upper mantle and lower crust, and the solid upper crustal deformation layer should be coupled with a contingent one-way fluid structure interaction (FSI) process. The base of the convection layer in our model is subjected to melt flux from the decompression melting zone, which is implemented indirectly by introducing a narrow, along-the-axis, horizontal strip of random thermal perturbations (RTP) (see, Figure 3.11a), where the temperature fluctuates randomly between an upper (1800ºC) and a lower (500ºC) bound to initiate convection. Melt-driven small-scale convection processes in mushes are modelled by combining Navier-Stokes and Darcy (porous) flow dynamics (Figure 3.13a). The convecting flows develop 3D structures, with a strong spatial heterogeneity along the ridge axis (Figure 3.13b and Figure 3.13c). The top layer is represented as the solid oceanic crust with a minimum thickness of 4 km at the MOR centre, increasing to a thickness of 8 km at the model edge (75 km at each side of the ridge axis). This layer is modelled as an isotropic elastic layer with its elastic properties approximated to an average oceanic crust (Table 3.2). The key step in modelling the MOR mechanism includes the contingent process of FSI needed to mechanically bridge the convective mushy zone with the top solid layers (Figure 3.11b). To find exclusively the contributions of sub-ridge mush dynamics to the MOR stress fields, the present modelling excludes slab-pull and its effect on crustal base, as well as any thermal weakening of solid crust at the MOR.

The choice of a narrow RTP width (15 km from ridge axis) relies upon various studies available in the literature. Considering a cut off distance of 25 km from the ridge, Behn & Grove, (2015) estimated the crustal thickness, decreasing by 30% to 40% to attain a thickness of 4 km for a half-spreading rate of 2-6 cm/yr and a mantle potential temperature of 1300°C. However, had the mantle potential temperature been set at 1350°C or more (e.g., 1400°C and 1450°C), the crustal thickness reduction would be double or triple, albeit the final thickness

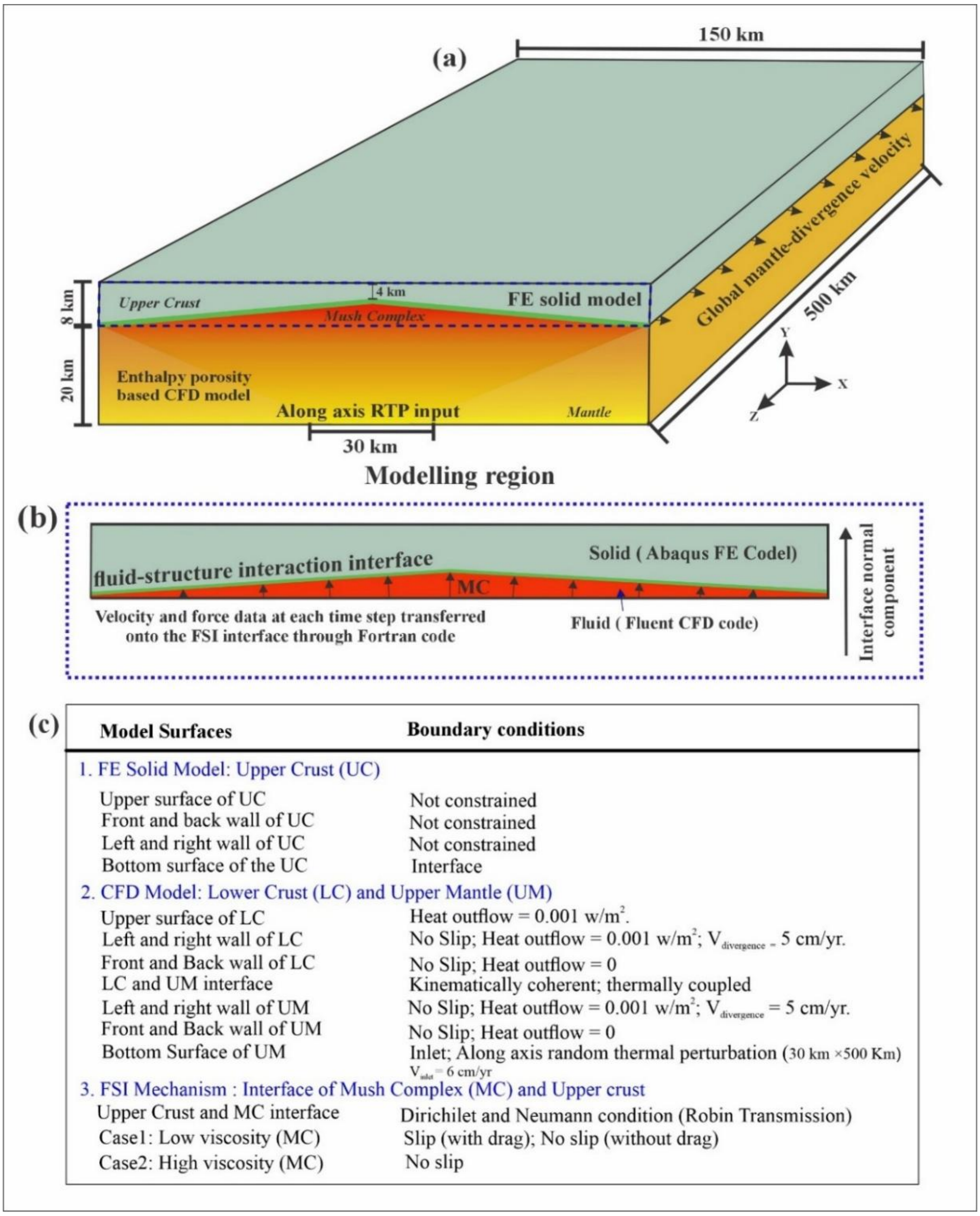

Model Surfaces	Boundary conditions
1. FE Solid Model: Upper Crust (UC)	
Upper surface of UC	Not constrained
Front and back wall of UC	Not constrained
Left and right wall of UC	Not constrained
Bottom surface of the UC	Interface
2. CFD Model: Lower Crust (LC) and Upper Mantle (UM)	
Upper surface of LC	Heat outflow = 0.001 w/m^2.
Left and right wall of LC	No Slip; Heat outflow = 0.001 w/m^2; $V_{divergence}$ = 5 cm/yr.
Front and Back wall of LC	No Slip; Heat outflow = 0
LC and UM interface	Kinematically coherent; thermally coupled
Left and right wall of UM	No Slip; Heat outflow = 0.001 w/m^2; $V_{divergence}$ = 5 cm/yr.
Front and Back wall of UM	No Slip; Heat outflow = 0
Bottom Surface of UM	Inlet; Along axis random thermal perturbation (30 km ×500 Km) V_{inlet} = 6 cm/yr
3. FSI Mechanism : Interface of Mush Complex (MC) and Upper crust	
Upper Crust and MC interface	Dirichilet and Neumann condition (Robin Transmission)
Case1: Low viscosity (MC)	Slip (with drag); No slip (without drag)
Case2: High viscosity (MC)	No slip

Figure 3.11 *a) Consideration of a three-dimensional fluid-structure interaction (FSI) model for numerical simulations of ridge-axis topography consisting of fluid subdomain and solid upper crust. (b) A schematic illustration of Robin-Neumann transmission is used to implement oneway fluid-structure interaction between mush complex (MC) and the overlying elastic crust. The CFD model for the fluid regime consists of 2,62,500 nodes, whereas the FE model for the solid structure consists of 96,635 nodes. The whole numerical calculations were implemented in a multinode and multiprocessing computer. Each of the FSI coupled FE simulations took a clock time of 504 hours, preceded by a common CFD simulation, which took a clock time of 192 hours. (c) All the model boundary conditions (mechanical and thermal) are summarized in the inset*

would remain above 5 km, sometimes close to 10 km. Given such a large crustal thickness for the cut-off distance of 25 km, the pooling area beneath first spreading ridges should be quite narrow. In cases of slow spreading ridges too, the crustal thickness is expected to be less than 5 km and the pooling area accordingly would become narrow. Thus, in any of the spreading scenarios, the melt focusing at the depth at which decompression melting stops should be much narrower. To verify further, we simulated two cases: one with RTP width of 15 km, and another with RTP width of 25 km on either side of the ridges. The comparison of temperature contours in the convecting fluid zone (Figure 3.13b) reveals that the wide RTP model does not produce sub-ridge small scale convection and thereby fails to produce any characteristic MOR topographic features.

3.4.1.3 CFD fluid modelling

The present model is designed to represent a thermo-mechanical setting above the decompression melting zone, as described in Table 1. This approach does not explicitly model the decompression melting process, but introduces random thermal perturbations (RTP) at the horizontal bottom model-boundary to capture the underlying decompression melting effects. The bottom boundary is placed at the base of the prismatic control volume (numerical domain for convection). The RTP regions cover a horizontal distance of 15 km on either side of the MOR axis (Figure 3.13a), considering that the melt accumulation zones narrow down upward due to the buoyant melt availability and porosity constraints (Cordery and Morgan, 1993; Faul, 2001). The chosen RTP width (i.e., melt pulling zone) in our MOR model agrees broadly with the available estimates of crustal thickness at MORs (Behn and Grove, 2015). We fix the model depth at 28 km (from the seafloor), which corresponds to the threshold depth at which decompression melting ceases (Shen and Forsyth, 1995). The thermal perturbations mentioned above are randomized within a temperature range: 500 °C – 1800 °C (Figure 3.13a) (Keller and Katz, 2016) to represent the whole solidus –liquidus spectrum in the decompression melting zone beneath the present model base. During a simulation run the temperature fluctuations after a few iterations, however, narrow down to a range close to 1000 °C (solidus) - 1250 °C (liquidus) in the upwelling zone (Figure 3.13), which is consistent with those reported in the existing MOR literature (Cherkaoui et al., 2003; Katz et al., 2003; Sarkar et al., 2014; Mandal et al., 2018, Lissenberg et al., 2019). To implement the randomization operation, a condition is imposed to keep the number of thermal points with temperatures above the liquidus not to exceed a threshold limit (20% of the total thermal points). This specific boundary condition allows us to constrain the basic melt production in the model (Figure 3.11c), as encountered in natural cases.

Random thermal points or melt points at the numerical domain's base are set in a porous convective circulation beneath the MOR. An elaborate description of the theoretical treatment of porous convective flows is available in Sarkar et al., (2014) and Mandal et al., (2018). This study provides a brief outline of the theoretical principle. The convection model considered here accounts for three material states: solid, liquid and mixed states, which are theoretically defined by the liquid fraction (LF), expressed as a linear function of the temperature that fluctuates between the liquidus and the solidus to modulate purely liquid versus solid states of a mushy continuum (Ricard et al., 2009; Mandal et al., 2018). The enthalpy via latent heat content controls the solid versus liquid phase proportions in mushy materials, which in turn determine the LF in the idealized single-phase (solid-liquid mixture) continuum. We can combine Navier-Stokes (NS) viscous and Darcy's porous flows to model the convective flows in mushes, where an increase in LF switches Darcy to NS flows (Ricard et al., 2009; Turner et al., 2015) (Figure 3.12).

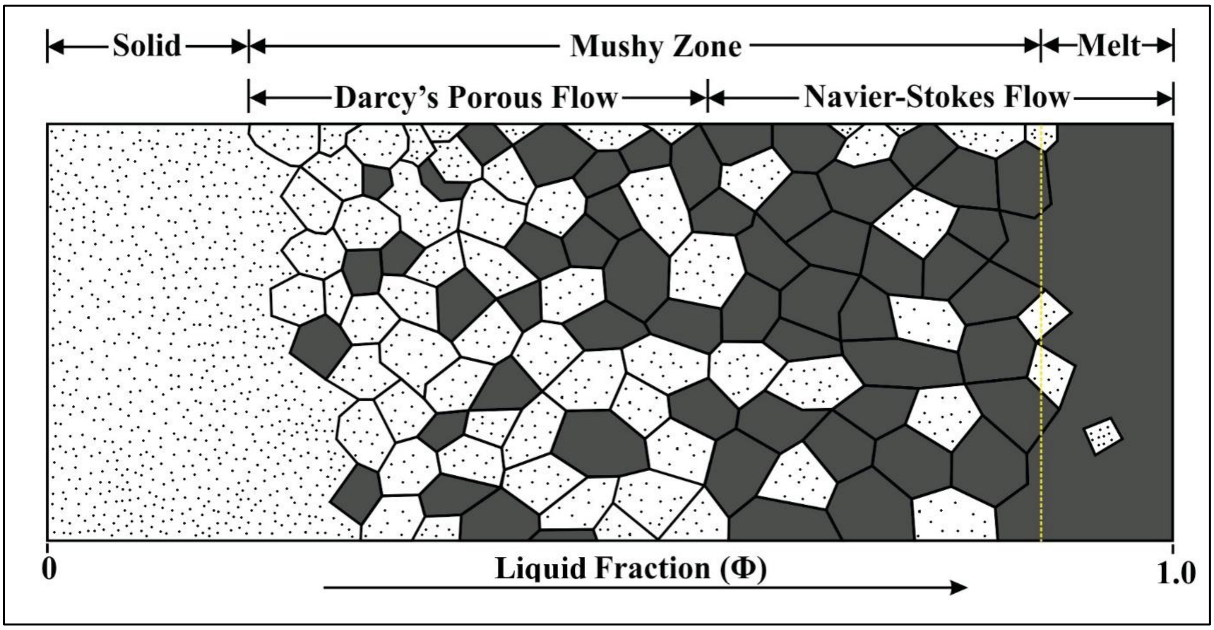

Figure 3.12 *A schematic illustration comparing Darcy (porous) flow and Navier-Stokes (viscous) flow as a function of increasing melt volume fraction. The interplay between these two flow regimes governs the melt dynamics within the mushy zone (Modified after Mandal et al., 2018).*

The enthalpy formulation uses a computational cell method (Voller and Prakash, 1987; Gartling, 1978), where the phase change is implemented through an average latent heat content, ΔH, which ranges from L (phase-transition latent heat) to 0. The system is treated as a pseudo-porous medium, with its porosity decreasing from 1 to 0 as ΔH decreases from L to 0. This enthalpy/porosity approach accounts for the zero solid-phase velocity (or reduced velocity in the case of mixed phases) by incorporating a parameter in the momentum equations as a source term. Consequently, velocities in the momentum equations for viscous liquid phases are inhibited through this 'Darcy' source term. As the system undergoes complete solidification, the Darcy term becomes dominant to yield a zero-velocity condition. It is noteworthy that this theoretical manipulation simplifies a two-phase problem into a single-phase idealization (Voller and Prakash 1987). The kinematics of this idealized continuum can be expressed with a predicted mixed-state velocity term as,

$$\begin{aligned} v &= \varphi v_l && \text{(mixed-state zone)} \\ v &= 0 && \text{(solid phase) and} \\ v &= v_l && \text{(liquid phase)} \end{aligned} \tag{3.7}$$

where, v_l is the velocity in the liquid phase.

φ is the liquid fraction, which varies between 0 and 1 for solid and liquid phases, respectively.

The present theoretical treatment follows Patankar's, (1980) numerical method of heat and fluid flow simulation in utilizing domain velocity (Equation 3.7) and the continuity (Equation 3.8), momentum (Equation 3.9), and the energy (Equation 3.10) equations in an enthalpy form as the governing equations. Three source terms: a *Darcy term* and a *buoyancy term* in the momentum equation, and an *enthalpy term* in the energy equation (Brent et al., 1988; Voller and Prakash, 1987) are (Brent et al., 1988; Voller and Prakash, 1987) incorporated to express them for the idealized single-phase flows as,(Voller and Prakash, 1987; Brent et al., 1988):

$$\nabla . v = 0 \tag{3.8}$$

$$\rho \frac{\partial}{\partial t} v + \rho v . \nabla v = -\nabla p + \mu_{fd} \nabla^2 v + S_g + S_D \tag{3.9}$$

$$\frac{\partial}{\partial t}(\rho h) + \nabla . (\rho v h) = \nabla . (a \nabla h) - S_h, \tag{3.10}$$

where p, ρ and μ_{fd} denote pressure, density, and viscosity of the fluid domain, respectively. *T*, *h* and *a* represent temperature, enthalpy, and thermal diffusivity ($a = k/\rho c$, k and c are the thermal conductivity and specific heat, respectively). The fluid-domain velocity, v is chosen to vary linearly with the melt fraction ϕ (Equation 3.7), and the material domain thus attains almost the liquid velocity where LF is extremely high. In contrast, the opposite LF trends causes the system to become rigid. In this single-phase idealization, the domain viscosity μ_{fd} is chosen to vary with temperature in a power-law function (Sarkar et al., 2014; Chen and

Morgan, 1990). In the momentum equation (Equation 3.9) the source term S_D regulates the dominance of Darcy (i.e. porous) flows, whereas S_g implements the buoyancy factor through Boussinesque approximation required for a convective flow. In the energy equation (Equation 3.10) the source term S_h acts as the latent heat factor, which is used to incorporate the energy involved in the solid-liquid phase transformation. The mathematical expressions of these source terms are:

$$S_D = -C\frac{(1-\phi)^2}{(\phi^3+\varepsilon)}v \tag{3.11}$$

$$S_g = \rho g\theta\Delta T \tag{3.12}$$

$$S_h = \frac{\partial\rho\Delta H}{\partial t} + \nabla.(\rho v\Delta H). \tag{3.13}$$

C and ε in Equation 3.11 are constants, whose values are taken as 10^5 and 0.001 (Sarkar et al., 2014). At high LF, S_D contributes little to the momentum equation (Equation 3.9), but its contribution becomes significant to overshadow the other terms in Equation 3.9 at low LF. In Equation 3.12, ΔT represents temperature fluctuations with respect to the reference temperature, and θ is the co-efficient of thermal expansion. The enthalpy source term (Equation 3.13) is derived from the enthalpy formulation of the convection-diffusion phase change (Voller et al., 1987a),

$$\frac{\partial\rho H}{\partial t} + \nabla(H\rho u) - \nabla(k\nabla T) = 0, \tag{3.14}$$

where $H = cT + \Delta H$, where ΔH denotes the mean latent heat content, expressed as a linear function of temperature and LF in a mixed-state zone.

The numerical mixed-state is materially conceived to represent mushes beneath the solid crust, envisaged as a mixture of mantle rock (μ_{mantle} ~ 10^{19} Pa s) and melt (μ_{melt} ~10^3 Pa s). Using the binary mixture method, their overall viscosity is calculated from basic Arrhenius equations. According to the various estimates in the MOR literature, the melt percentage in a mushy region in the upper mantle can go up to a maximum of about 25% (McKenzie and Bickle, 1988), which is considered as an upper limit for our viscosity calculations. Form the binary mixture theory (Roegiers and Roegiers, 1936; Roegiers 1951) we have,

$$log\mu_{fd} = \frac{x_{mantle}log\mu_{mantle}+x_{melt}log\mu_{melt}}{x_{mantle}+x_{melt}}, \tag{3.15}$$

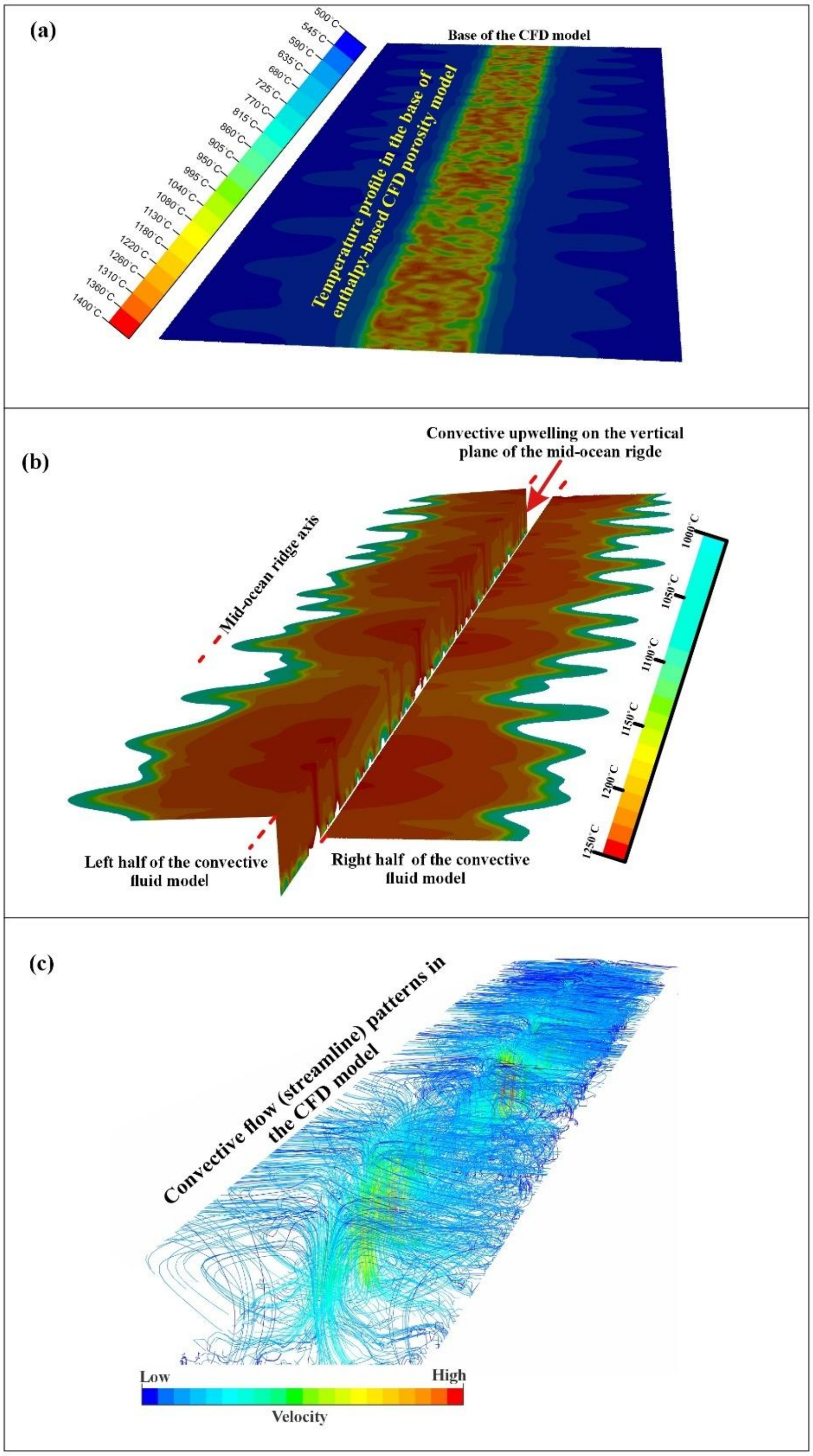

Figure 3.13 *(a) Thermal boundary condition imposed at the CFD model base (inlet). Random thermal perturbations (RTPs) are imposed on a 30 Km wide stretch of the model base. (b) Thermal maps of the MC, showing temperature contours on a sub-horizontal plane close to the interface and an along-axis vertical plane, obtained from a CFD model run at 3 Myr. Notice that, 3D convective upwelling is evident from this thermal structure. (c) Streamlines of the 3D convection structures in MC. Both the velocity and the thermal structures show asymmetric 3D convective flows in the model.*

where *x* indicates the molar percentage of participating materials (melt/mantle). Keeping μ_{mantle} as 10^{19} Pa s (Karato and Wu, 1993; Hirth and Kohlstedt, 1996) and μ_{melt} as 10^3 Pa s (Giordano et al., 2008), and the molar percentage of mantle rock at 75% as a limiting case at liquidus temperature, the upper mantle domain viscosity is found to be in the order of $\sim 5\times10^{15}$ Pa s (*cf.* McKenzie, 1984), which is designated for the fluid domain viscosity μ_{fd} in the momentum equation (Equation 3.9), as derived from equation 3.15. This rheological treatment of the single-phase model of sub-ridge upper mantle allows us to effectively model the mushy flows, considering the full range of liquid fraction ($1\geq\phi\geq0$) oscillates between the range of mantle presence (75% to 100%) in a computational cell. It is noteworthy, the input flux at inlet of the model depends on constant input velocity (6 cm/yr), as well as on liquid fraction at inlet. Therefore, any inlet temperature under solidus (1000 ^{0}C) effectively blocks input flux into the domain. However, this article excludes a thorough theoretical analysis of the mush rheology for the single-phase system, as it lies outside the main objective of this study.

3.4.2. Fluid - Structure Interaction: theoretical formulations

Considering a dynamic interaction of the elastic upper crust with the underlying mush complex (MC), comprising mantle rock, mush and crystal-carrying melts accumulated in lower crust and the topmost part of the upper mantle as the key factors to determine the upper crustal stress field in a MOR setting, we can conceptualize the present problem in the theoretical framework of fluid-structure interaction (FSI) mechanics. The FSI mechanics treats a problem allowing the solid structures to interact with the fluid domain, typically both solid and fluid layers mechanically influencing each other. The modelling idealizes the system with one-way interaction, assuming the influence of thin upper crust to the underlying mushy region is trivial . To model a solid-fluid interaction, the classical mechanics approach uses the equations of motion for the fluid domain and the solid structure in the same tensor notation, which on applying D'Alembert's principle (Belytschko, 1980) follow:

$$\rho\dot{v}_i - \sigma_{ij,j} + b_i = 0, \tag{3.16}$$

where the superscript dot indicates total time derivative, a comma a partial derivative with respect to the space variable; b_i is the body force term, ρ is the density, v_i is the velocity, and σ_{ij} is the stress tensor. Ideally, the fluid part induces forces onto the solid part, which is called the Neumann transmission condition, whereas the solid sub-problem transfers displacement onto the fluid part at the interface, which is described as the Dirichlet condition. In a fully coupled

FSI, the transmissions are calculated at each iteration. The present one-way model considers only the Neumann transmission condition, and the interface condition is updated after each time substep. The Neumann condition is, however, modified further with the Robin transmission conditions as a fractioned Dirichlet part is added therein (Badia et al. 2008), as elaborated below.

Table 3.2 *Model Parameters used in thermomechanical model*

Model materials	Properties
FE Model of Upper Crust	Model dimensions = $(4{\sim}8)$ km × 150 Km × 500 km; Density (ρ_s) = 2400 kg / m^3; Elastic modulus (E) = 10 GPa; Poisson's ratio (ν) = 0.26.
FSI Robin-Neumann transmission	Viscosity (μ_{eff}) = 1 × 10^{12} Pa s -1× 10^{14} Pa s Density (ρ_{eff}) = 2500 kg / m^3
CFD model of Upper Mantle and Viscous crust	Model dimensions = $(20{\sim}24)$ km × 150 Km × 500 km Viscosity of the upper-mantle (Single Phase Idealization; Temperature dependent) = 10^{15} Pa s {Viscosity of mantle rock = 10^{19} Pa s; Viscosity of melt = 10^3 Pa s} Density of the upper mantle = 2500 kg / m^3 (Boussinesq); Thermal Expansion Co-efficient = 5 × 10^5 / °C; Thermal diffusivity = 10^{-6} m^2/ s; Permeability = 10^{-5} m^2; Specific Heat = 1600 J / kg°C; Solidus Temperature = 1000 °C Liquidus Temperature = 1250 °C Viscosity of lower crust = 10^{21} Pa s; Density of Lower Crus = 2400 kg / m^3 ; Rayleigh number ~ 10^7

In the FSI approach, the partition procedure is used to separately model the fluid and the solid sub-problems. The velocity for each of the nearest cells of the crustal interfaces is calculated at an interval of ~ 60 Kyr from the convective fluid model described above. The calculated velocities are then imposed at the base of a separate solid model (that replicates the prismatic upper crust) following the FSI formulation. The Neumann boundary condition for the solid can be expressed as:

$$\tau_s{}^{k+1}.n_s = -\tau_f{}^{k+1}.n_f \quad \text{on the interface} \tag{3.17}$$

$$\rho_s \delta_{tt} \hat{w}^{k+1} - \nabla \hat{\tau}_s^{k+1} = \hat{b}_s \text{ in the solid domain,} \tag{3.18}$$

where, the subscripts *s* and *f* denote the solid domain and fluid domain respectively, b_s denotes the body force term. Superimposed hat (^) indicates that the variable is set at the reference configuration of the solid structure in Lagrangian kinematics. w denotes displacement in the solid medium with respect to the reference configuration. The time discretization is represented by the operator δ_{tt}, and an implicit first order backward difference scheme is invoked to enumerate it as $\delta_{tt}(.) = \delta_t(\delta_t(.))$ in which the backward difference operator δ_t is defined as $\delta_t f^{(n+1)} = (f^{(n+1)} - f^{(n)})/\Delta\, t$, where $f^{(n)}$ is an approximation for a time-dependent function f at time level $t^{(n)}$. Superscript k stands for the current iteration; hence $k+1$ represents the next iteration. n_f is the outward normal to solid domain on fluid-structure interface and $n_s = -n_f$. The solid medium is assumed to be elastic and characterized by a constitutive relation between Cauchy stress tensor τ_s and deformation gradient $F(\hat{w}) = I + \nabla\hat{w}$.

Use of the Robin transmission (a linear combination of Dirichlet and Neumann components) gives rise to a modified set of equations for the interface of the solid structure,

$$\frac{\beta_s}{\Delta t}\hat{w}^{(k+1)} + {\tau_s}^{(k+1)}.n_s = \frac{\beta_s}{\Delta t}\hat{w}^{(n)} + \beta_s {v_{int}}^{(k+1)} - {\tau_f}^{(k+1)}.n_f \tag{3.19}$$

where, v_{int} is the fluid velocity at the interface, and the constant β_s has a suitable positive and bounded value that determines the contribution of the Dirichlet component in the Robin transmission (Badia et al., 2008). β_s is set at 0.025 in the simulation runs. β_s has a suitable positive and bounded value that determines the contribution of the Dirichlet component in the Robin transmission (Badia et al., 2008). The present analysis assessed impact of this constant on the model calculations, and found little variations on its increasing or decreasing values. The nominal Dirichlet term acts as a perturbation to the crustal base to localize short-wavelength undulations, whereas the Neumann boundary condition gives rise to first-order, long-wave vertical undulations, and localizes 3D deformations in the elastic crust. In order to obtain both long- and short-wavelength axial topography, we impose a linear combination of the two types of interactions at the interface (Figueroa et al., 2006, Badia et al., 2008). The Dirichlet terms utilize the velocity of fluid domain at interface, described by a 3D array with three velocity components on one dimension, 18750 spatial points on the second dimension and 111 temporal points (covering 7 Myr) on the third dimension. For the Neumann term, the normal component of a strain-rate tensor at the fluid-solid interface in Equations (3.17) and (3.18) is obtained from the vertical component of the fluid velocity vector, corresponding to a two-dimensional array of spatiotemporal points, considering a very small slope (3°) of the interface. The estimate yields a strain-rate median of 10^{-5} s^{-1} at the axis, with upper and lower limits, 10^{-3} s^{-1} and 10^{-11} s^{-1} on the interface, depending on the vertical component of the velocity. The calculated strain rates cover values for the entire lava/magma movement range, which is discussed in section 3.3.3.1.

Assuming the fluid at the interface as a Newtonian, incompressible isotropic material (Badia et al., 2008), the Cauchy stress tensor in Equation 3.17 is given by the following equation:

$$\tau_f(v_{int}, p) = -pI + 2\mu G(v_{int}), \tag{3.20}$$

where p is the pressure, and μ is the dynamic viscosity of the fluid at the interface, and

$$G(v_{int}) = \frac{1}{2}(\nabla v_{int} + (\nabla v_{int})^T) \tag{3.21}$$

is the strain rate tensor, where v_{int} represents the fluid velocity at the interface, which we can find from the transient fluid sub-problem, as discussed above.

The pressure term in the Cauchy stress tensor (Equation 3.20) is written as

$$p = -\left(\rho g h + \frac{1}{2}\rho u^2\right), \tag{3.22}$$

where g stands for gravity, h is the depth of spatial points at the interface. The fluid domain density (Equation 3.22) is used in the pressure term of the Cauchy stress tensor (Equation 3.17), which is kept constant in the fluid simulation as the thermal expansion is used only in the source term (Equations 3.12 and 3.13). The present approach thus takes the kinematic output from the CFD calculations and couple with the solid crust for the FSI, excluding any material attributes. The fluid-solid interaction is then defined fully by the mechanical term- effective viscosity (μ_{eff}), calculated independently as presented in the preceding section.

Equation 3.19, signifies the introduction of the Dirichlet terms in the Neumann boundary condition (Equation 3.17) at fluid-structure interface. The Dirichlet term indicates the fractional transfer of fluid kinematics at the interface to the adjoining structure, while the Neumann term indicates the force transfer at normal direction (Equation 3.17). Thus, the viscous thrust term (Neumann term) almost solely controls the first-order axial topography, whereas the localized short-wavelength variation of reliefs is primarily triggered at crustal base by the nominal contribution of the Dirichlet term (factored by β_s= 0.025) of the Robin transmission of FSI. The rest is done through the material behaviour of the overlying crust.

This FSI analysis explains the physical mechanism why a particular effective viscosity at MC would generate a specific topography at MORs. Although the mantle and the overlying crust are primarily considered kinematically coherent, a relative motion between them can develop if the viscosity of the sub-crustal / lower crustal MC is comparatively low. Such kinematic state in turn produces shear stresses at the interface. This viscous drag is treated as an independent variable because it originates from the velocity difference (slip condition) between the moving plate and the underlying horizontal flow in the MC. The present treatment includes the drag factor selectively in low-viscosity models ($\mu_{eff} < 7.5\text{x}10^{12}$ Pa s), where the shear drag is given by,

$$\tau_x = 2\mu_{eff}\dot{e_x}, \tag{3.23}$$

where $\dot{e_x}$ is the horizontal shear rate away from the ridge axis. Equation (3.23) comes directly from Newtonian fluid's interaction with the wall as a shear stress term (Kundu and Cohen, 2002), applied in an area bounded by adjacent nodes. The horizontal shear rate is calculated considering an average value of the velocities measured at a point on the interface. As the Robin equation does not contain the horizontal viscous drag term (Badia et al., 2008), we introduce this term and update the equation to investigate the additional effects of this stress factor on the axial topography.

3.5. Model Topography

This study investigated the mode of axial topographic development in a series of FSI model simulations run with varying μ_{eff} (mush complex viscosity) in the Cauchy stress term of the Robin equation (Equation 3.19). μ_{eff} was chosen to vary in the range 10^{12} to 10^{14} Pa s, as discussed in the preceding section, and this viscosity range gives rise to a broad spectrum of axial reliefs (-0.06 km to 1.27 km at 7 Myr, see box-plot for minima and maxima in Figures 3.14a and 3.14b, as reported from non-rifted natural ridges. The post-processing of the model results shows that the linear relation between μ_{eff} and the median relief breaks as μ_{eff} is reduced to a threshold value of $7.5\text{x}10^{12}$ Pa s (Figure 3.14b).

Two 3D numerical simulations are first presented to show the vertical axial displacement as a function of μ_{eff} (Figures 3.15 and 3.16). The simulation run with μ_{eff} = 10^{13} Pa s produces a prominent linear zone of upward vertical displacement (axial high) with a

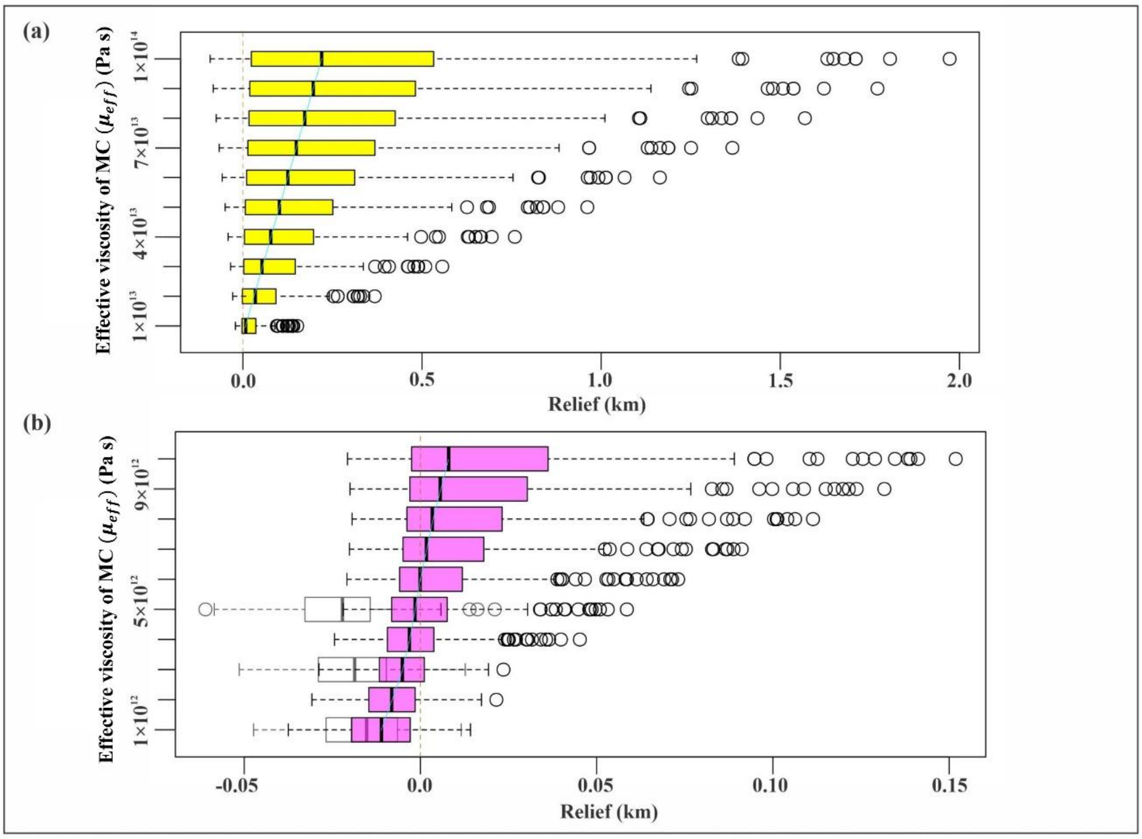

Figure 3.14 *Box plots of the vertical displacement at the top layer nodes in the evolution of ridge axis in FE models. The box plots show the median of axial reliefs at nodes on the axis as a thick black line. The coloured box is bounded by 25th and 75th percentile reliefs, named first quartile* (Q_1) *and third quartile* (Q_3)*. The box length defines the interquartile range (IQR) of data. The dotted line or the whisker delineates the "maximum" and "minimum" reliefs, represented by* ($Q_3 + 1.5\times IQR$) *and* ($Q_1 - 1.5\times IQR$)*, respectively. Empty circles mark some data points, called outliers, beyond the limiting range.* ***(a)*** *Calculated plots of axial relief data obtained from FSI models run with* $\mu_{eff} = 10^{13}$ *Pa s to* 10^{14} *Pa s.* ***(b)*** *A similar plot of the axial relief, but for a lower viscosity range:* 10^{12} *Pa s to* 10^{13} *Pa s. It is noteworthy that the viscosity versus axial relief relation becomes non-linear at* $\mu_{eff} = 7.5x10^{12}$ *Pa s. This nonlinearity indicates the weakening of normal viscous force component in the Robin transmission condition. We introduced an across-axis drag force component in the transmission condition for low-viscosity simulations (indicated by white box plots). The box plots in (3.14b) show a maximum relief of 1.27 km* ($\mu_{eff} = 10^{14}$ *Pa s) and a minimum relief of -0.06 km* ($\mu_{eff} = 5x10^{12}$ *Pa s + drag).*

maximum elevation of nearly 0.1 km on a time scale of 6 Myr (model run time) (Figure 3.16a). The topographic elevation becomes more than 1 km in the model with $\mu_{eff} = 10^{14}$ Pa s (Figure 3.15a). The model results clearly suggest a positive relation of the axial height with μ_{eff}. A time-series analysis (1.5 Myr to 6 Myr) reveals a characteristic temporal variation of the vertical displacement at the ridge axes, especially in their central regions (15 km on either side) (Figures 3.15 and Figure 3.16). The vertical uplift progressively weakens but remains active in the entire model run-time of 7 Myr (Figure 3.15). Both the models produce persistent along-axis linear zones of vertical uplift (axial high) in the initial stages (t = 1.5 Myr). However, the uplift pattern is strongly heterogeneous in the axial direction (Figure 3.17a), resulting in topographic segmentation of the axial highs, as widely reported from bathymetric studies (Carbotte et al., 2016 and references therein).

The median value of axial elevations (W_{AR}) at a given model run time (e.g., t = 1.5 Myr) increases consistently with μ_{eff}, resulting in a transition from flat to axial high topography. For example, W_{AR} = -1 m (i.e. almost flat) for μ_{eff}= 10^{12} Pa s (Figure 3.15d), which increases to 40 m at μ_{eff}= 10^{13} Pa s (Figure 3.16d), and to 467 m (i.e., axial high) when μ_{eff}= 10^{14} Pa s (Figure 3.15d). The axial highs are flanked by a pair of ridge parallel belts of downward vertical movement, forming narrow troughs at a distance of 40 to 60 km from the ridge axis (Figure 3.17a and 3.17b). The magnitude of average negative relief at the off-axis troughs (W_{OR}, median of reliefs at the nodes along axis-parallel troughs) also increases with increasing μ_{eff}; for example, at 6 Myr, W_{OR} = - 30 m for μ_{eff} = 10^{13} Pa s, (Figures 3.16a and 3.16d) whereas W_{OR} = - 350 m when μ_{eff} = 10^{14} Pa s (Figures 3.15a and 3.16d). A positive relation of W_{OR} with the axial elevation (W_{AR}, median of reliefs at axis nodes) suggests a correspondence between the axial-high loading and downward flexural deformation of the elastic crust to produce ridge-parallel depression zones. Model simulations with lower μ_{eff} (1 - 2.5 x10^{12} Pa s) show a dramatic change in the evolution of ridge-axis topography. The ridge axis develops a series of 60 to 80 km long discrete depressions (W_{AR} = - 11 m to -6 m at 6 Myr, Figures 3.15d and 3.16d) on a wavelength of 110 to 130 km along the axis, but without any axial highs (Figures 3.15b and 3.16b). The simulations with μ_{eff} varying in the range 10^{12} to 10^{14} Pa s, thus indicate that the viscosity of sub-crustal mush complex zones critically determines the evolution of flat versus axial high topography (W_{AR} > 0) in MORs. The axial high topography is possible to develop only when the viscosity of sub-crustal mush complexes exceeds a threshold value (~ 6 x10^{12} Pa s), as demonstrated in Figure 3.14b, showing crossovers from slightly negative or flat to positive relief at most of the points on the surface.

The additional effects of magmatic drag forces on the growth of axial highs were also assessed using the same model. As this factor becomes more effective in the case of a low-viscosity MC condition, two simulations run are presented with low μ_{eff} (= 5x10^{12} Pa s), one with and the other without basal drag factor. The drag-free model (Figures 3.15a-b and 3.16a-b) produces length-wise persistent axial highs of moderate elevations (W_{AR} = 13 m at 2 Myr), flanked by low-amplitude (W_{OR} = -50 m) ridge-parallel depressions (Figures 3.15d and 3.16d). However, the axial high progressively reduces its average elevation, forming an almost flat

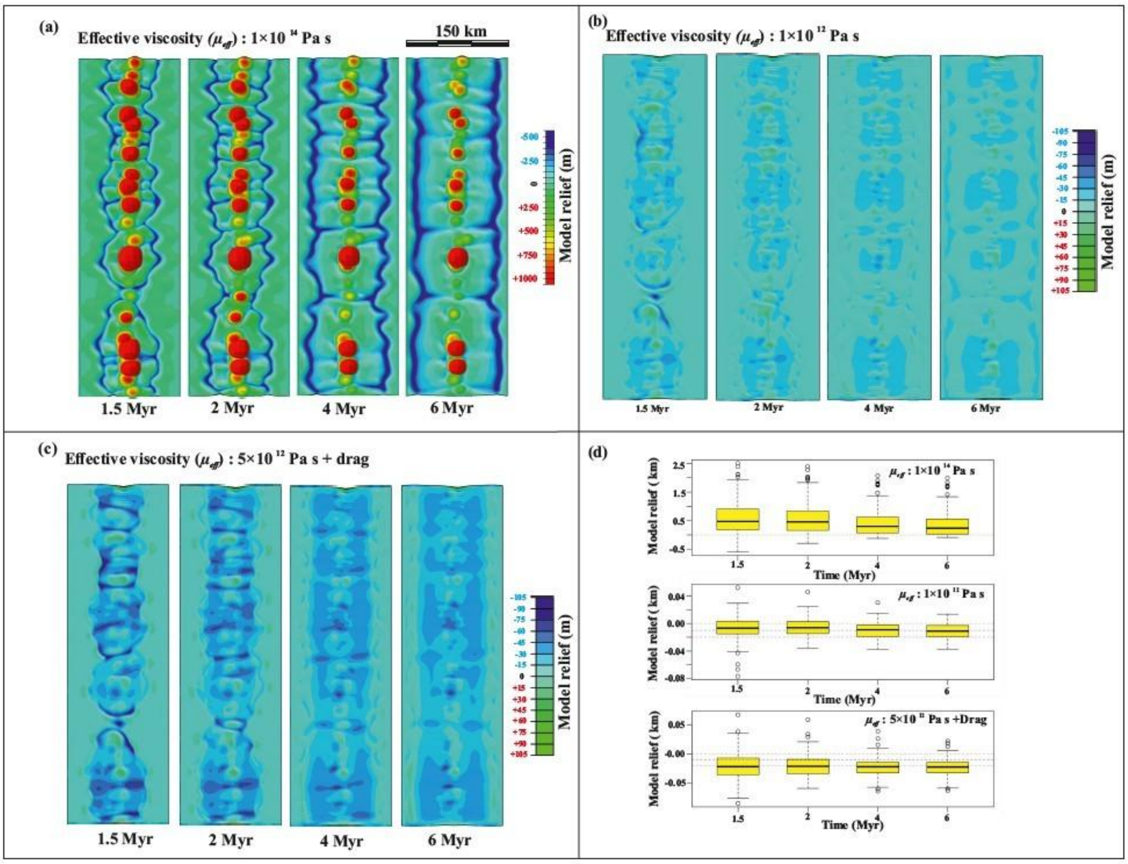

Figure 3.15 *Vertical elevation maps showing contrasting MOR topographic patterns in FE models for varying MC viscosities:* ***(a)*** *high ($\mu_{eff} = 10^{14}$ Pa s)* ***(b)*** *low ($\mu_{eff} = 10^{12}$ Pa s) and* ***(c)*** *low ($\mu_{eff} = 5x10^{12}$ Pa s), coupled with across-axis drag at the lithospheric base. Model run time: 1.5 Myr, 2 Myr, 4 Myr, and 6 Myr.* ***(d)*** *Box plots of the topographic reliefs calculated at the nodes of the evolved axes are shown in the three panels: (a) to (c). It is noteworthy that the median values change with time.*

topography (W_{AR} ~ 0 m, Figures 3.15d and 3.16d) at 6 Myr. The off-axis depressions reduce their negative relative relief to flat (W_{OR} = -25 m) (Figure 3.17a). The simulation with basal drag produces axial topography, dominated by a series of depressions, leaving sporadic small highs but not forming any persistent linear topographic high (Figures 3.15c and 3.16c). The axial depressions (W_{AR} = -22 m at 1.5 Myr, minima = - 75 m) hardly change their negative relief on a run time of 6 Myr (W_{AR} = - 22 m, minima = - 58 m, Figures 3.15d and 3.16d) and form a weak depression, flanked by a flat topographic belt (W_{OR} ~ 0) at a distance of 60 km from the ridge axis (Figure 3.15c-d; Figure 3.16c-d).

To summarize, the 3D views of a high- ($\mu_{eff} = 1x10^{14}$ Pa s) and a low-viscosity ($\mu_{eff} = 5x10^{12}$ Pa s) model reveal a spectacular difference in their stable ridge topography produced on a run time of 7 Myr (Figures 3.17a-b), which broadly agree with those observed in nature.

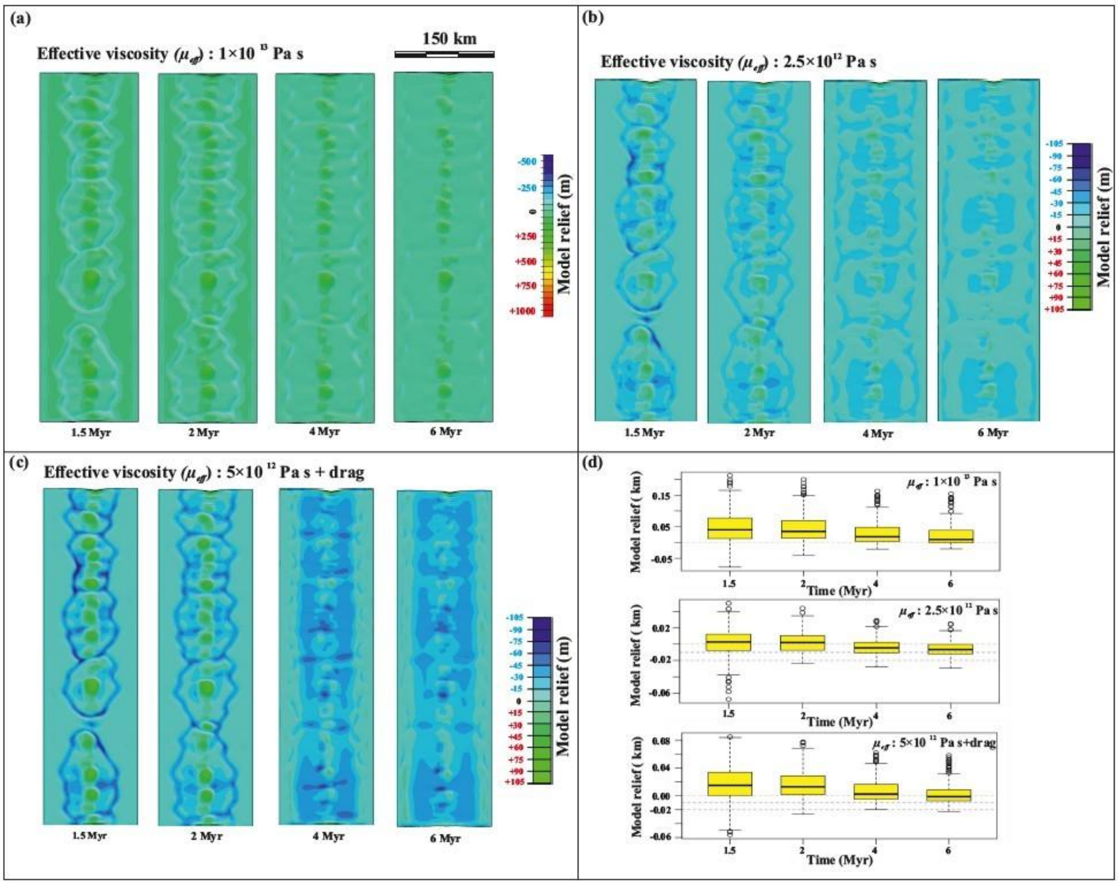

Figure 3.16 *Topographic elevation maps of FE model of MOR run with varying MC viscosity (μ_{eff}): **(a)** moderate ($\mu_{eff} = 10^{13}$ Pa s), **(b)** low ($\mu_{eff} = 2.5x10^{12}$ Pa s) and **(c)** low ($\mu_{eff} = 5x10^{12}$ Pa s + drag). Model run time steps: 1.5 Myr, 2 Myr, 4 Myr, and 6 Myr. (d) Box-plots of the reliefs at the nodes of the evolved axes in the three FE models: (a) – (c).*

A time-series analysis of the across-axis profiles of model topography shows that the off-axis troughs continuously migrate away from the ridge axis, leaving a flat region between the axial high and them (Figures 3.17a-3.17b). The FSI model explains the mechanics of MOR topographic modulation by μ_{eff}. The Cauchy stress term in the Neumann condition for the FSI consists of two terms – a) hydrostatic pressure b) viscous stress (Equation 3.20). The latter is significantly higher than that the density-controlled buoyancy pressure (i.e., the first term) (see for further discussion). However, the two dynamic terms turn to be in similar orders when the MC viscosity becomes low. For μ_{eff} <10^{12} Pa s, the axial topography no longer varies with viscosity; it is the static pressure term (Equation 3.22) that takes the control in producing a flat topography (Figure 3.18). We also varied the density contrast (100 to 200 kg/m^3) to evaluate its independent effect on the axial topography. The simulations hardly produce any relative relief due to differential topographic uplift in the horizontal direction (Figure 3.19). Thus, the axial highs in our models are not a manifestation of the density structure in the MOR system. This factor only influences the magnitude of flat axial topography under low-viscosity conditions in the MC.

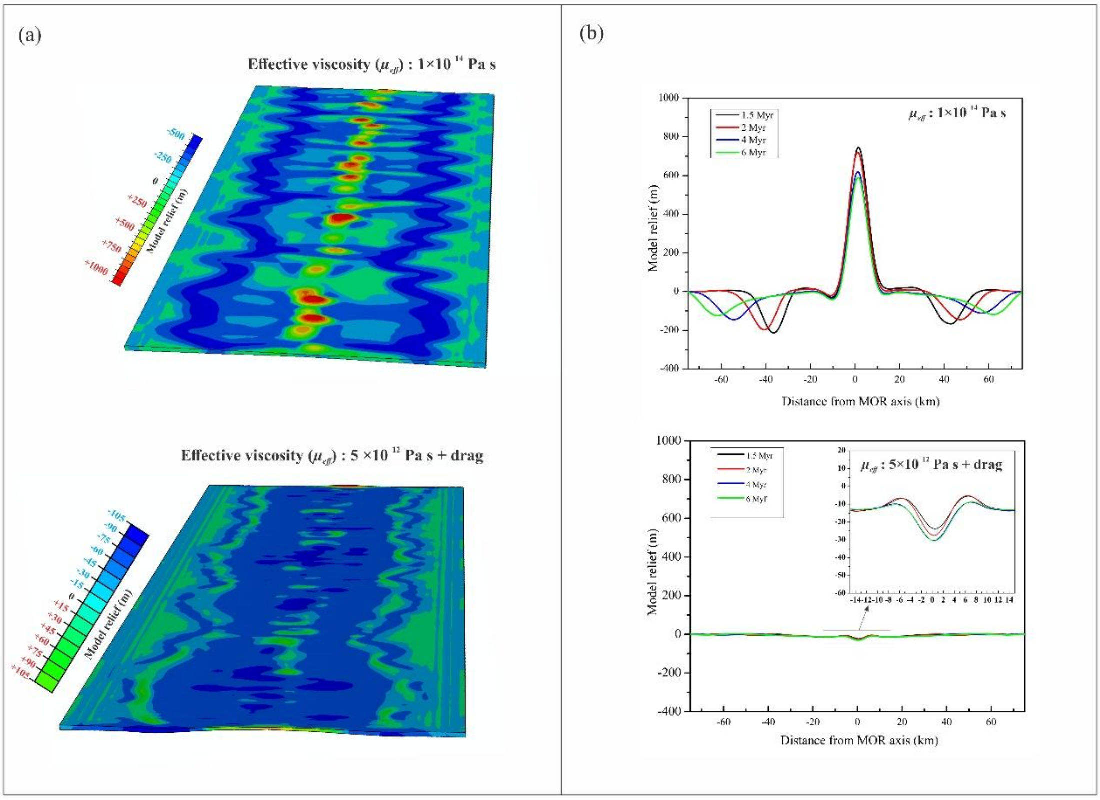

Figure 3.17 ***(a)*** *3D views of the axis topography in models with* $\mu_{eff} = 10^{14}$ *Pa s (upper panel) and* 10^{12} *Pa s (lower panel). Model run time: 7 Myr. The low-viscosity model was run with basal drag force.* ***(b)*** *A time-series analysis of the first-order across-axis topographic profiles from the high- and low-viscosity simulation runs. Inset shows a magnified view of the axial negative relief in the lower panel.*

This study examined the effect of densities of fluid subdomain and MC on the MOR topography. The density of the MC region is varied as a function of the temperature distribution using the thermal expansion coefficient. The extent of density variation (~ 100 kg/m^3) is used in the fluid-structure interaction process. Numerical simulations for this variation show little or no effect on ridge topography at low effective viscosities (for example at 3x10^{12} Pa, see Figure 3.19). Also, we ran simulations with a sufficiently high density (upto 2700 kg/m^3) and found very little difference in topography in case of lower effective viscosities (for example at 2x10^{12} Pa and at 3x10^{12} Pa) (Figure 3.19). The observed results can be explained by considering the relative magnitude between the pressure term (Equation 3.22) and the viscous stress term in Equation 3.20. The viscous stress term that varies with the strain rate largely controls the morphological undulations, when the pressure terms in Cauchy stress tensor (Equation 3.22) remain almost unaffected. The pressure created by flow velocities at the base is 0.5 x density x velocity^2, where the magnitude of velocity is extremely low, as calculated from the strain-rate range. The dynamic pressure part, involving square of the velocity term, is thus negligible small, as compared to the static pressure (density x gravity x depth). Again, the effect of static pressure becomes relatively weak in case of high viscosity conditions. For example, for a MC viscosity of 10^{13} Pa s the calculated viscous stress (Equation 3.22, in main text)) is in the order of hundreds of MPa at the interface for an average strain rate of 10^{-5} s^{-1}, whereas the static pressure is in the order of tens of MPa at the interface, implying that the viscosity will

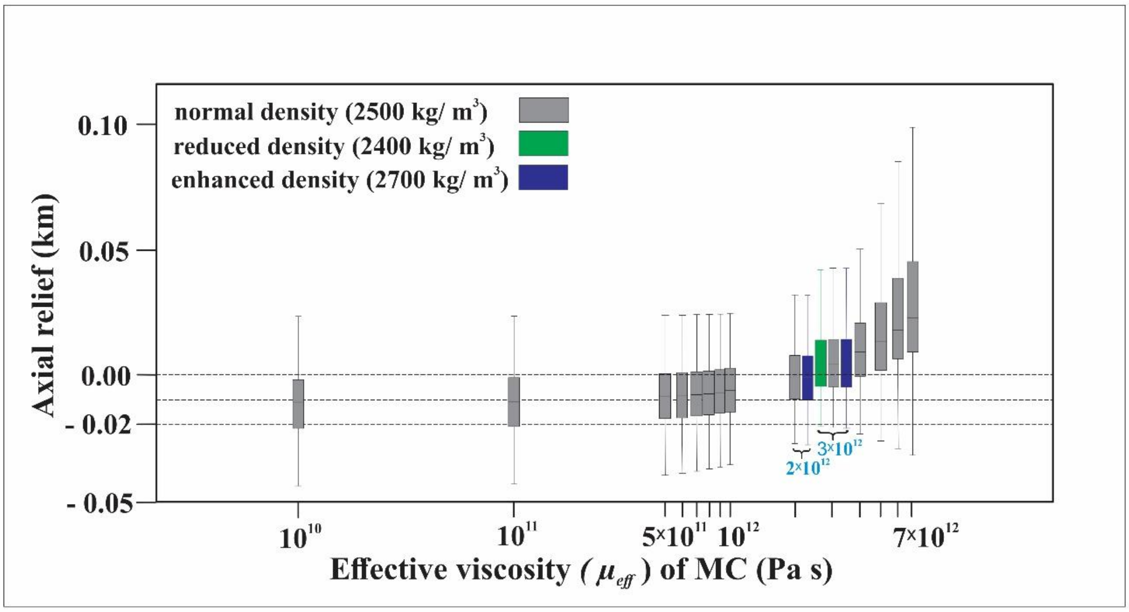

Figure 3.18 *Semi-log graphical plots (model run time 3 Myr) of the axial relief as a function of the effective viscosity (μ_{eff}) of MC. Note that, little or no fluctuations occur as the MC viscosity decrease down to a value $\leq 1x10^{12}$ Pa s. Also, the differential topographic variations are not sensitive to the MC density at low (μ_{eff}).*

dominantly control the process of topography building in the overlying solid crust. For large effective viscosity of the MC ($>10^{12}$ Pa s), crustal deformations at MORs are thus attributed to the rheological conditions of the subcrustal magmas, rather than the buoyancy conditions in the MC.

3.6. Model Limitations

The present FSI model is designed to study the sole role of the viscosity of melt-rich regions in controlling the axial topography of mid-ocean ridges. However, as discussed in the Introduction, several other factors, e.g., the diking parameter (Liu and Buck, 2018), can influence the ridge topography. A large number of studies have recognized the spreading rate as a potential factor to modulate the axial high versus valley development. The exclusion of this factor obviously imposes a limitation on our modelling. However, this study sheds light in a new direction, showing that the viscosity changes of sub-crustal melt regions by $10^1 - 10^2$ order can alone bring a transition from flat to axial high topography in a MOR under the same spreading rate. Secondly, MORs generally undergo extensional faulting in the uppermost brittle crustal layer (Buck et al., 2005), which contributes to the development of high-order ocean floor morphology, such ridge parallel hills at MORs. Also, extensional stresses play a dominant role in forming axial valleys (Lin and Parmentier, 1989). The present model excludes such tectonic stress regimes at MOR and brittle failure in the elastic solid top layer as we focus on longer wavelength topography. The gradient in across-axis lithospheric thickness variation might have an additional influence in the axial topographic development. However, this factor excluded in this study to find independently the effects of sub-crustal mush complexes (MC) on the two end-members: flat and high axial topography.

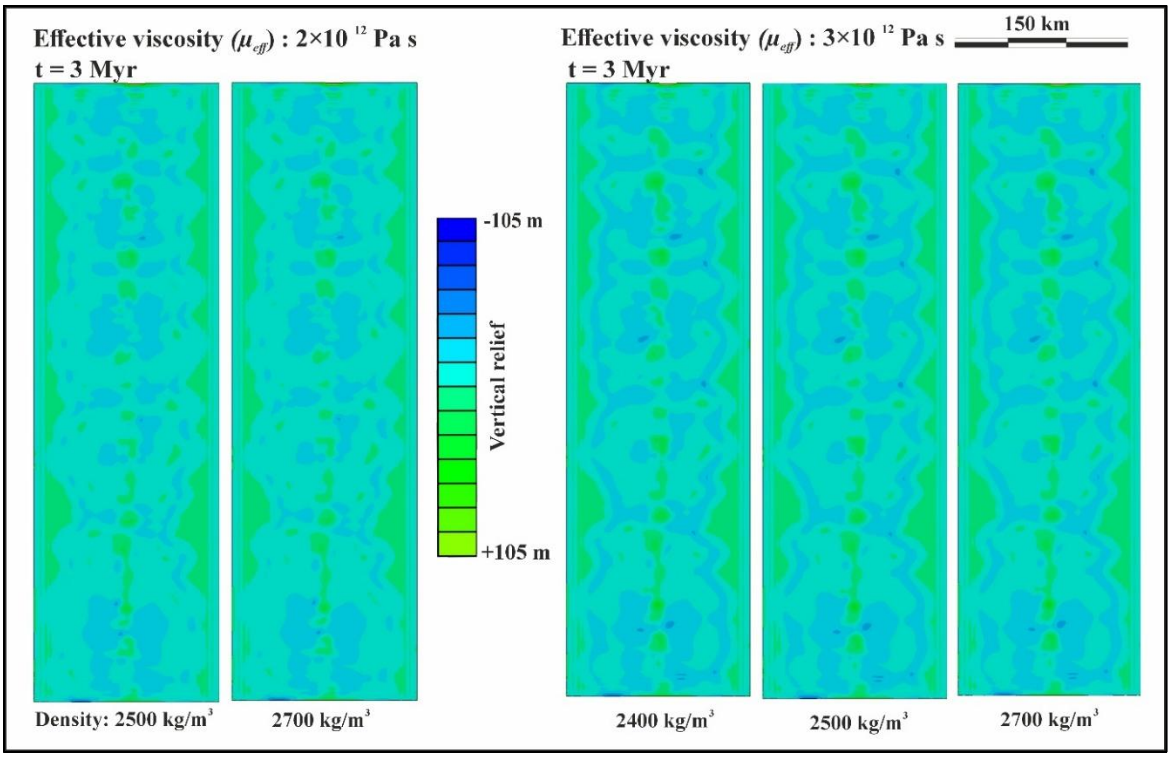

Figure 3.19 *Contour plots of axial relief as a function of the effective viscosity (μ_{eff}) of MC. a) and b) shows vertical displacement in varying density at $\mu_{eff} = 2x10^{12}$ Pa s and $\mu_{eff} = 3x10^{12}$ Pa s, respectively. Note that there is little or no fluctuation of topography as the density changes at particular viscosity.*

3.7. References

Alt, J. C. (2004). Alteration of the upper oceanic crust: mineralogy, chemistry, and processes. *Hydrogeology of the oceanic lithosphere*, *1*, 495-433.

Arnoux, G. M., Toomey, D. R., Hooft, E. E. E., & Wilcock, W. S. D. (2019). Seismic imaging and physical properties of the Endeavour segment: Evidence that skew between mantle and crustal magmatic systems governs spreading center processes. *Geochemistry, Geophysics, Geosystems*, *20*(3), 1319-1339. https://doi.org/10.1029/2018GC007978

Arnulf, A. F., Harding, A. J., Kent, G. M., & Wilcock, W. S. D. (2018). Structure, seismicity, and accretionary processes at the hot spot-influenced Axial Seamount on the Juan de Fuca Ridge. Journal of Geophysical Research: Solid Earth, 123(6), 4618-4646. https://doi.org/10.1029/2017JB015131

Bachmann, O., & Bergantz, G. W. (2004). On the origin of crystal-poor rhyolites: extracted from batholithic crystal mushes. *Journal of Petrology*, *45*(8), 1565-1582.https://doi.org/10.1093/petrology/egh019

Bachmann, O., & Huber, C. (2016). Silicic magma reservoirs in the Earth's crust. American Mineralogist, 101(11), 2377-2404. https://doi.org/10.2138/am-2016-5675

Badia, S., Nobile, F., & Vergara, C. (2008). Fluid–structure partitioned procedures based on Robin transmission conditions. *Journal of Computational Physics*, *227*(14), 7027-7051. https://doi.org/10.1016/j.jcp.2008.04.006

Baker, E. T., Hémond, C., Briais, A., Maia, M., Scheirer, D. S., Walker, S. L., ... & Chen, Y. J. (2014). Correlated patterns in hydrothermal plume distribution and apparent magmatic budget along 2500 km of the Southeast Indian Ridge. *Geochemistry, Geophysics, Geosystems*, *15*(8), 3198-3211.https://doi.org/10.1002/2014GC005344

Bazilevs, Y., Calo, V. M., Hughes, T. J., & Zhang, Y. (2008). Isogeometric fluid-structure interaction: theory, algorithms, and computations. Computational mechanics, 43(1), 3-37. https://doi.org/10.1007/s00466-008-0315-x

Belytschko, T. (1980). Fluid-structure interaction. Computers & Structures, 12(4), 459-469. https://doi.org/10.1016/0045-7949(80)90121-2

Bergantz, G. W., Schleicher, J. M., & Burgisser, A. (2015). Open-system dynamics and mixing in magma mushes. *Nature Geoscience*, *8*(10), 793-796. https://doi.org/10.1038/ngeo2534

Bernal, J. D., & Mason, J. (1960). Packing of spheres: co-ordination of randomly packed spheres. Nature, 188(4754), 910-911. https://doi.org/10.1038/188910a0

Braun, J. (2010). The many surface expressions of mantle dynamics. *Nature Geoscience*, *3*(12), 825-833.https://doi.org/10.1038/ngeo1020

Braun, M. G., Hirth, G., & Parmentier, E. M. (2000). The effects of deep damp melting on mantle flow and melt generation beneath mid-ocean ridges. *Earth and Planetary Science Letters*, *176*(3-4), 339-356.https://doi.org/10.1016/S0012-821X(00)00015-7

Buck, W. R. (2001). Accretional curvature of lithosphere at magmatic spreading centers and the flexural support of axial highs. *Journal of Geophysical Research: Solid Earth*, *106*(B3), 3953-3960.https://doi.org/10.1029/2000JB900360

Buck, W. R., Lavier, L. L., & Poliakov, A. N. (2005). Modes of faulting at mid-ocean ridges. *Nature*, *434*(7034), 719-723.https://doi.org/10.1038/nature03358

Canales, J. P., Detrick, R. S., Carbotte, S. M., Kent, G. M., Diebold, J. B., Harding, A., ... & Van Ark, E. (2005). Upper crustal structure and axial topography at intermediate spreading ridges: Seismic constraints from the southern Juan de Fuca Ridge. *Journal of Geophysical Research: Solid Earth*, *110*(B12). https://doi.org/10.1029/2005JB003630

Cannat, M., Sauter, D., Mendel, V., Ruellan, E., Okino, K., Escartin, J., ... & Baala, M. (2006). Modes of seafloor generation at a melt-poor ultraslow-spreading ridge. *Geology*, *34*(7), 605-608.

Carbotte, S. M., Marjanović, M., Arnulf, A. F., Nedimović, M. R., Canales, J. P., & Arnoux, G. M. (2021). Stacked magma lenses beneath mid-ocean ridges: insights from new seismic observations and synthesis with prior geophysical and geologic findings. *Journal of Geophysical Research: Solid Earth*, *126*(4), e2020JB021434. https://doi.org/10.1029/2020JB021434

Carbotte, S. M., Smith, D. K., Cannat, M., & Klein, E. M. (2016). Tectonic and magmatic segmentation of the Global Ocean Ridge System: a synthesis of observations. *Geological Society, London, Special Publications*, *420*(1), 249-295.https://doi.org/10.1144/SP420.5

Carbotte, Suzanne M., Adrien Arnulf, Marc Spiegelman, Michelle Lee, Alistair Harding, Graham Kent, Juan Pablo Canales, and Mladen Nedimović. Stacked sills forming a deep melt-mush feeder conduit beneath Axial Seamount. *Geology* 48, no. 7 (2020): 693-697. https://doi.org/10.1130/G47223.1

Caricchi, L., Burlini, L., Ulmer, P., Gerya, T., Vassalli, M., & Papale, P. (2007). Non-Newtonian rheology of crystal-bearing magmas and implications for magma ascent dynamics. Earth and Planetary Science Letters, 264(3-4), 402-419. https://doi.org/10.1038/188910a0

Caricchi, L., Pommier, A., Pistone, M., Castro, J., Burgisser, A., & Perugini, D. (2011). Strain-induced magma degassing: insights from simple-shear experiments on bubble bearing melts. Bulletin of volcanology, 73(9), 1245-1257. https://doi.org/10.1016/j.epsl.2007.09.032

Chadwick Jr, W. W., Nooner, S. L., Zumberge, M. A., Embley, R. W., & Fox, C. G. (2006). Vertical deformation monitoring at Axial Seamount since its 1998 eruption using deep-sea pressure sensors. *Journal of Volcanology and Geothermal Research*, *150*(1-3), 313-327. https://doi.org/10.1016/j.jvolgeores.2005.07.006

Chadwick, J., Perfit, M., Ridley, I., Jonasson, I., Kamenov, G., Chadwick, W., ... & Smith, M. (2005). Magmatic effects of the Cobb hot spot on the Juan de Fuca Ridge. *Journal of Geophysical Research: Solid Earth*, *110*(B3).https://doi.org/10.1029/2003JB002767.

Chang, C., & Powell, R. L. (1994). Effect of particle size distributions on the rheology of concentrated bimodal suspensions. Journal of rheology, 38(1), 85-98. https://doi.org/10.1122/1.550497

Chen, J., Olive, J. A., & Cannat, M. (2022). Thermal regime of slow and ultraslow spreading ridges controlled by melt supply and modes of emplacement. *Journal of Geophysical Research: Solid Earth*, *127*(4), https://doi.org/10.1029/2021JB023715.

Chen, Y., & Morgan, W. J. (1990). A nonlinear rheology model for mid‐ocean ridge axis topography. *Journal of Geophysical Research: Solid Earth*, *95*(B11), 17583-17604. https://doi.org/10.1029/JB095iB11p17583

Chenevez, J., P. Machetel, and A. Nicolas (1998), Numerical models of magma chambers in the Oman ophiolite, J. Geophys. Res., 103(B7), 15,443–15,455. *https://doi.org/10.1029/98JB00597*

Choi, E., & Buck, W. R. (2010). Constraints on shallow mantle viscosity from morphology and deformation of fast‐spreading ridges. *Geophysical research letters*, *37*(16). https://doi.org/10.1029/2010GL043681

Chong, J. S., Christiansen, E. B., & Baer, A. D. (1971). Rheology of concentrated suspensions. Journal of applied polymer science, 15(8), 2007-2021. https://doi.org/10.1002/app.1971.070150818

Coombs, M. L., & Gardner, J. E. (2004). Reaction rim growth on olivine in silicic melts: Implications for magma mixing. American Mineralogist, 89(5-6), 748-758. https://doi.org/10.2138/am-2004-5-608

Cordier, C., Benoit, M., Hémond, C., Dyment, J., Le Gall, B., Briais, A., & Kitazawa, M. (2010). Time scales of melt extraction revealed by distribution of lava composition across a ridge axis. Geochemistry, Geophysics, Geosystems, 11(7).https://doi.org/10.1029/2010GC003074

Costa, F., & Dungan, M. (2005). Short time scales of magmatic assimilation from diffusion modeling of multiple elements in olivine. Geology, 33(10), 837-840. https://doi.org/10.1130/G21675.1

Costa, F., & Dungan, M. (2005). Short time scales of magmatic assimilation from diffusion modeling of multiple elements in olivine. Geology, 33(10), 837-840. https://doi.org/10.1130/G21675.1

Desmond, K. W., & Weeks, E. R. (2014). Influence of particle size distribution on random close packing of spheres. Physical Review E, 90(2), 022204. https://doi.org/10.1103/PhysRevE.90.022204

Detrick, R. S., Buhl, P., Vera, E., Mutter, J., Orcutt, J., Madsen, J., & Brocher, T. (1987). Multi-channel seismic imaging of a crustal magma chamber along the East Pacific Rise. *Nature*, *326*(6108), 35-41. https://doi.org/10.1038/326035a0

Dick, H. J., Lin, J., & Schouten, H. (2003). An ultraslow-spreading class of ocean ridge. *Nature*, *426*(6965), 405-412.

Dunn, R. A., Lekić, V., Detrick, R. S., & Toomey, D. R. (2005). Three-dimensional seismic structure of the Mid-Atlantic Ridge (35 N): Evidence for focused melt supply and lower crustal dike injection. *Journal of Geophysical Research: Solid Earth*, *110*(B9). https://doi.org/10.1029/2004JB003473

Eberle, M. A., & Forsyth, D. W. (1998). An alternative, dynamic model of the axial topographic high at fast spreading ridges. *Journal of Geophysical Research: Solid Earth*, *103*(B6), 12309-12320.https://doi.org/10.1029/98JB00437

Edmonds, M., Cashman, K. V., Holness, M., & Jackson, M. (2019). Architecture and dynamics of magma reservoirs. *Philosophical Transactions of the Royal Society A*, *377*(2139), 20180298. https://doi.org/10.1098/rsta.2018.0298

Edmonds, M., Cashman, K. V., Holness, M., & Jackson, M. (2019). Architecture and dynamics of magma reservoirs. Philosophical Transactions of the Royal Society A, 377(2139), 20180298. https://doi.org/10.1098/rsta.2018.0298

Eilers, V. H. (1941). Die viskosität von emulsionen hochviskoser stoffe als funktion der konzentration. Kolloid-Zeitschrift, 97(3), 313-321.

Einstein, A., 1906. A new determination of molecular dimensions. *Ann. Phys.*, *19*, pp.289-306.

Escartín, J., Smith, D. K., Cann, J., Schouten, H., Langmuir, C. H., & Escrig, S. (2008). Central role of detachment faults in accretion of slow-spreading oceanic lithosphere. *Nature*, *455*(7214), 790-794. https://doi.org/10.1038/nature07333

Evans, R. L., Tarits, P., Chave, A. D., White, A., Heinson, G., Filloux, J. H., ... & Unsworth, M. J. (1999). Asymmetric electrical structure in the mantle beneath the East Pacific Rise at 17 S. *Science*, *286*(5440), 752-756.https://doi.org/10.1126/science.286.5440.752

Farris, R. J. (1968). Prediction of the viscosity of multimodal suspensions from unimodal viscosity data. Transactions of the Society of Rheology, 12(2), 281-301. https://doi.org/10.1007/BF01503023

Fernández, M. A., & Moubachir, M. (2005). A Newton method using exact Jacobians for solving fluid–structure coupling. Computers & Structures, 83(2-3), 127-142. https://doi.org/10.1016/j.compstruc.2004.04.021

Figueroa, C. A., Vignon-Clementel, I. E., Jansen, K. E., Hughes, T. J., & Taylor, C. A. (2006). A coupled momentum method for modeling blood flow in three-dimensional deformable arteries. Computer methods in applied mechanics and engineering, 195(41-43), 5685-5706. https://doi.org/10.1016/j.cma.2005.11.011

Figueroa, C. A., Vignon-Clementel, I. E., Jansen, K. E., Hughes, T. J., & Taylor, C. A. (2006). A coupled momentum method for modeling blood flow in three-dimensional deformable arteries. Computer methods in applied mechanics and engineering, 195(41-43), 5685-5706. https://doi.org/10.1016/j.cma.2005.11.011

Fontaine, F. J., Rabinowicz, M., & Cannat, M. (2017). Can high-temperature, high-heat flux hydrothermal vent fields be explained by thermal convection in the lower crust along fast-spreading M id-O cean R idges?. *Geochemistry, Geophysics, Geosystems*, *18*(5), 1907-1925. https://doi.org/10.1002/2016GC006737

Gale, A., Escrig, S., Gier, E. J., Langmuir, C. H., & Goldstein, S. L. (2011). Enriched basalts at segment centers: The Lucky Strike (37 17′ N) and Menez Gwen (37 50′ N) segments of the Mid-Atlantic Ridge. *Geochemistry, Geophysics, Geosystems*, *12*(6).

Gale, A., Laubier, M., Escrig, S., & Langmuir, C. H. (2013). Constraints on melting processes and plume-ridge interaction from comprehensive study of the FAMOUS and North Famous segments, Mid-Atlantic Ridge. *Earth and Planetary Science Letters*, *365*, 209-220.

Gerya, T. V. (2013). Three-dimensional thermomechanical modeling of oceanic spreading initiation and evolution. *Physics of the Earth and Planetary Interiors*, *214*, 35-52. https://doi.org/10.1016/j.pepi.2012.10.007

Glasstone, S., Laidler, K. J., & Eyring, H. (1941). *The theory of rate processes; the kinetics of chemical reactions, viscosity, diffusion and electrochemical phenomena* (No. 541.39). McGraw-Hill Book Company.

Gonnermann, H. M., & Manga, M. (2007). The fluid mechanics inside a volcano. Annu. Rev. Fluid Mech., 39, 321-356. https://doi.org/10.1146/annurev.fluid.39.050905.110207

Gonnermann, H. M., & Manga, M. (2007). The fluid mechanics inside a volcano. Annu. Rev. Fluid Mech., 39, 321-356. https://doi.org/10.1146/annurev.fluid.39.050905.110207

Goss, A. R., Perfit, M. R., Ridley, W. I., Rubin, K. H., Kamenov, G. D., Soule, S. A., ... & Fornari, D. J. (2010). Geochemistry of lavas from the 2005–2006 eruption at the East Pacific Rise, 9 46′ N–9 56′ N: Implications for ridge crest plumbing and decadal changes in magma chamber compositions. Geochemistry, Geophysics, Geosystems, 11(5). https://doi.org/10.1029/2009GC002977

Grindlay, N. R., Madsen, J. A., Rommevaux-Jestin, C., & Sclater, J. (1998). A different pattern of ridge segmentation and mantle Bouguer gravity anomalies along the ultra-slow spreading Southwest Indian Ridge (15° 30′ E to 25° E). *Earth and Planetary Science Letters*, *161*(1-4), 243-253.https://doi.org/10.1016/S0012-821X(98)00154-X

Gudmundsson, A. (2012). Magma chambers: Formation, local stresses, excess pressures, and compartments. *Journal of Volcanology and Geothermal Research*, *237*, 19-41. https://doi.org/10.1016/j.jvolgeores.2012.05.015

Gudmundsson, A., & Brenner, S. L. (2004). How mechanical layering affects local stresses, unrests, and eruptions of volcanoes. *Geophysical Research Letters*, *31*(16). https://doi.org/10.1029/2004GL020083

Hanan, B. B., Blichert-Toft, J., Hemond, C., Sayit, K., Agranier, A., Graham, D. W., & Albarède, F. (2013). Pb and Hf isotope variations along the Southeast Indian Ridge and the dynamic distribution of MORB source domains in the upper mantle. *Earth and Planetary Science Letters*, *375*, 196-208.

Head III, J. W., Wilson, L., & Smith, D. K. (1996). Mid-ocean ridge eruptive vent morphology and substructure: Evidence for dike widths, eruption rates, and evolution of eruptions and axial volcanic ridges. Journal of Geophysical Research: Solid Earth, 101(B12), 28265-28280. https://doi.org/10.1029/96JB02275

Hebert, L. B., & Montési, L. G. (2010). Generation of permeability barriers during melt extraction at mid-ocean ridges. *Geochemistry, Geophysics, Geosystems*, *11*(12). https://doi.org/10.1029/2010GC003270

Herzberg, C. (2004). Partial crystallization of mid-ocean ridge basalts in the crust and mantle. *Journal of Petrology*, *45*(12), 2389-2405. https://doi.org/10.1093/petrology/egh040

Herzberg, C. (2004). Partial crystallization of mid-ocean ridge basalts in the crust and mantle. *Journal of Petrology*, *45*(12), 2389-2405. https://doi.org/10.1093/petrology/egh040

Hewitt, I. J. (2010). Modelling melting rates in upwelling mantle. *Earth and Planetary Science Letters*, *300*(3-4), 264-274.https://doi.org/10.1016/j.epsl.2010.10.010

Hewitt, I. J. (2010). Modelling melting rates in upwelling mantle. Earth and Planetary Science Letters, 300(3-4), 264-274. https://doi.org/10.1016/j.epsl.2010.10.010

Hirth, G., & Kohlstedf, D. (2003). Rheology of the upper mantle and the mantle wedge: A view from the experimentalists. *Geophysical monograph-american geophysical union*, *138*, 83-106.

Hou, G., Wang, J., & Layton, A. (2012). Numerical methods for fluid-structure interaction—a review. *Communications in Computational Physics*, *12*(2), 337-377.https://doi.org/10.4208/cicp.291210.290411s

Ito, G., & Behn, M. D. (2008). Magmatic and tectonic extension at mid-ocean ridges: 2. Origin of axial morphology. *Geochemistry, Geophysics, Geosystems*, *9*(9). https://doi.org/10.1029/2008GC001970

Jian, H., Singh, S.C., Chen, Y.J. and Li, J., 2017. Evidence of an axial magma chamber beneath the ultraslow-spreading Southwest Indian Ridge. Geology, *45*(2), pp.143-146. https://doi.org/10.1130/G38356.1

Jokat, W., Ritzmann, O., Schmidt-Aursch, M. C., Drachev, S., Gauger, S., & Snow, J. (2003). Geophysical evidence for reduced melt production on the Arctic ultraslow Gakkel mid-ocean ridge. *Nature*, *423*(6943), 962-965.

Katz, R. F. (2010). Porosity-driven convection and asymmetry beneath mid-ocean ridges. *Geochemistry, Geophysics, Geosystems*, *11*(11). https://doi.org/10.1029/2010GC003282

Kavanagh, J. L., Burns, A. J., Hazim, S. H., Wood, E. P., Martin, S. A., Hignett, S., & Dennis, D. J. (2018). Challenging dyke ascent models using novel laboratory experiments: Implications for reinterpreting evidence of magma ascent and volcanism. Journal of Volcanology and Geothermal Research, 354, 87-101. https://doi.org/10.1016/j.jvolgeores.2018.01.002

Kelemen, P. B., Braun, M., & Hirth, G. (2000). Spatial distribution of melt conduits in the mantle beneath oceanic spreading ridges: Observations from the Ingalls and Oman ophiolites. *Geochemistry, Geophysics, Geosystems*, *1*(7). https://doi.org/10.1029/1999GC000012

Kelemen, P. B., Koga, K., & Shimizu, N. (1997). Geochemistry of gabbro sills in the crust-mantle transition zone of the Oman ophiolite: implications for the origin of the oceanic lower crust. Earth and Planetary Science Letters, 146(3-4), 475-488. https://doi.org/10.1016/S0012-821X(96)00235-X

Keller, T., Katz, R. F., & Hirschmann, M. M. (2017). Volatiles beneath mid-ocean ridges: Deep melting, channelised transport, focusing, and metasomatism. *Earth and Planetary Science Letters*, *464*, 55-68. https://doi.org/10.1016/j.epsl.2017.02.006

Kent, G. M., Harding, A. J., & Orcutt, J. A. (1993). Distribution of magma beneath the East Pacific Rise between the Clipperton transform and the 9 17′ N Deval from forward modeling of common depth point data. *Journal of Geophysical Research: Solid Earth*, *98*(B8), 13945-13969.

Kent, G. M., Harding, A. J., & Orcutt, J. A. (1993). Distribution of magma beneath the East Pacific Rise near the 9 03′ N overlapping spreading center from forward modeling of common depth point data. *Journal of Geophysical Research: Solid Earth*, *98*(B8), 13971-13995. https://doi.org/10.1029/93JB00706

Key, K., Constable, S., Liu, L., & Pommier, A. (2013). Electrical image of passive mantle upwelling beneath the northern East Pacific Rise. *Nature*, *495*(7442), 499-502. https://doi.org/10.1038/nature11932

Klein, E. M., & Langmuir, C. H. (1987). Global correlations of ocean ridge basalt chemistry with axial depth and crustal thickness. *Journal of Geophysical Research: Solid Earth*, *92*(B8), 8089-8115.

Klein, E. M., & Langmuir, C. H. (1987). Global correlations of ocean ridge basalt chemistry with axial depth and crustal thickness. *Journal of Geophysical Research: Solid Earth*, *92*(B8), 8089-8115. https://doi.org/10.1029/JB092iB08p08089

Klein, J., Mueller, S. P., Helo, C., Schweitzer, S., Gurioli, L., & Castro, J. M. (2018). An expanded model and application of the combined effect of crystal-size distribution and crystal shape on the relative viscosity of magmas. Journal of Volcanology and Geothermal Research, 357, 128-133. https://doi.org/10.1016/j.jvolgeores.2018.04.01

Krieger, I. M., & Dougherty, T. J. (1959). A mechanism for non-Newtonian flow in suspensions of rigid spheres. Transactions of the Society of Rheology, 3(1), 137-152. https://doi.org/10.1122/1.548848

Kundu, P., Cohen, I., Hu, G., & Dowling, D. (2015). Fluid mechanics 6th ed., waltham, ma.

Lange, A. E., Nielsen, R. L., Tepley III, F. J., & Kent, A. J. (2013). The petrogenesis of plagioclase-phyric basalts at mid-ocean ridges. *Geochemistry, Geophysics, Geosystems*, *14*(8), 3282-3296. https://doi.org/10.1002/ggge.20207

Lange, R. A., Frey, H. M., & Hector, J. (2009). A thermodynamic model for the plagioclase-liquid hygrometer/thermometer. American Mineralogist, 94(4), 494-506. https://doi.org/10.2138/am.2009.3011

Lin, J., & Parmentier, E. M. (1989). Mechanisms of lithospheric extension at mid-ocean ridges. *Geophysical Journal International*, *96*(1), 1-22. https://doi.org/10.1111/j.1365-246X.1989.tb05246.x

Lin, J., & Parmentier, E. M. (1990). A finite amplitude necking model of rifting in brittle lithosphere. *Journal of Geophysical Research: Solid Earth*, *95*(B4), 4909-4923. https://doi.org/10.1029/JB095iB04p04909

Lissenberg, C. J., MacLeod, C. J., & Bennett, E. N. (2019). Consequences of a crystal mush-dominated magma plumbing system: a mid-ocean ridge perspective. *Philosophical Transactions of the Royal Society A*, *377*(2139), 20180014. https://doi.org/10.1098/rsta.2018.0014

Liu, Z., & Buck, W. R. (2018). Magmatic controls on axial relief and faulting at mid-ocean ridges. *Earth and Planetary Science Letters*, *491*, 226-237. https://doi.org/10.1016/j.epsl.2018.03.045

Luttrell, K., & Sandwell, D. (2012). Constraints on 3-D stress in the crust from support of mid-ocean ridge topography. *Journal of Geophysical Research: Solid Earth*, *117*(B4). https://doi.org/10.1029/2011JB008765

Macdonald, K. C., & Fox, P. J. (1988). The axial summit graben and cross-sectional shape of the East Pacific Rise as indicators of axial magma chambers and recent volcanic eruptions. *Earth and Planetary Science Letters*, *88*(1-2), 119-131.

Macdonald, K. C., Fox, P. J., Miller, S., Carbotte, S., Edwards, M. H., Eisen, M., ... & Wilson, D. (1992). The East Pacific Rise and its flanks 8–18 N: History of segmentation, propagation and spreading direction based on SeaMARC II and Sea Beam studies. *Marine Geophysical Researches*, *14*, 299-344.

Macdonald, K. C., Fox, P. J., Perram, L. J., Eisen, M. F., Haymon, R. M., Miller, S. P., ... & Shor, A. N. (1988). A new view of the mid-ocean ridge from the behaviour of ridge-axis discontinuities. *Nature*, *335*(6187), 217-225.

Mahoney, J. J., Graham, D. W., Christie, D. M., Johnson, K. T. M., Hall, L. S., & Vonderhaar, D. L. (2002). Between a hotspot and a cold spot: isotopic variation in the Southeast Indian Ridge asthenosphere, 86 E–118 E. *Journal of Petrology*, *43*(7), 1155-1176. https://doi.org/10.1093/petrology/43.7.1155

Mainprice, D. (1997). Modelling the anisotropic seismic properties of partially molten rocks found at mid-ocean ridges. Tectonophysics, 279(1-4), 161–179. https://doi.org/10.1016/S0040-1951(97)00122-4

Mallows, C., & Searle, R. C. (2012). A geophysical study of oceanic core complexes and surrounding terrain, Mid-Atlantic Ridge 13° N–14° N. *Geochemistry, Geophysics, Geosystems*, *13*(6).https://doi.org/10.1029/2012GC004075

Mandal, N., Sarkar, S., Baruah, A., & Dutta, U. (2018). Production, pathways and budgets of melts in mid-ocean ridges: An enthalpy based thermo-mechanical model. *Physics of the Earth and Planetary Interiors*, *277*, 55-69.https://doi.org/10.1016/j.pepi.2018.01.008

Mandal, N., Sarkar, S., Baruah, A., & Dutta, U. (2018). Production, pathways and budgets of melts in mid-ocean ridges: An enthalpy based thermo-mechanical model. Physics of the Earth and Planetary Interiors, 277, 55-69. https://doi.org/10.1016/j.pepi.2018.01.008

Maron, S. H., & Pierce, P. E. (1956). Application of Ree-Eyring generalized flow theory to suspensions of spherical particles. Journal of colloid science, 11(1), 80-95. https://doi.org/10.1016/0095-8522(56)90023-X

Marsh, B. D. (1981). On the crystallinity, probability of occurrence, and rheology of lava and magma. Contributions to Mineralogy and Petrology, 78(1), 85-98. https://doi.org/10.1007/BF00371146

Martin, V. M., Pyle, D. M., & Holness, M. B. (2006). The role of crystal frameworks in the preservation of enclaves during magma mixing. Earth and Planetary Science Letters, 248(3-4), 787-799. https://doi.org/10.1016/j.epsl.2006.06.030

Martinez, F., Hey, R., & Höskuldsson, Á. (2020). Reykjanes Ridge evolution: Effects of plate kinematics, small-scale upper mantle convection and a regional mantle gradient. Earth-Science Reviews, 206, 102956.https://doi.org/10.1016/j.earscirev.2019.102956

McKenzie, D. A. N. (1984). The generation and compaction of partially molten rock. Journal of petrology, 25(3), 713-765. https://doi.org/10.1093/petrology/25.3.713

Mckenzie, D. A. N., & Bickle, M. J. (1988). The volume and composition of melt generated by extension of the lithosphere. Journal of petrology, 29(3), 625-679. https://doi.org/10.1093/petrology/29.3.625

Meyzen, C. M., Toplis, M. J., Humler, E., Ludden, J. N., & Mével, C. (2003). A discontinuity in mantle composition beneath the southwest Indian ridge. *Nature*, *421*(6924), 731-733.

Michael, P., Langmuir,C.et al. 2003. Magmatic and amagmatic seafloor generation at the ultraslowspreading Gakkel ridge: Arctic Ocean. Nature, 423, 956–961.

Moitra, P., & Gonnermann, H. M. (2015). Effects of crystal shape-and size-modality on magma rheology. Geochemistry, Geophysics, Geosystems, 16(1), 1-26. https://doi.org/10.1002/2014GC005554

Moitra, P., & Gonnermann, H. M. (2015). Effects of crystal shape-and size-modality on magma rheology. Geochemistry, Geophysics, Geosystems, 16(1), 1-26. https://doi.org/10.1002/2014GC005554

Moretti, R., & Errera, M. (2018, June). Comparison between Dirichlet-Robin and Neumann-Robin Interface Conditions in CHT Problems. In 5th International Conference of Fluid Flow, Heat and Mass Transfer (FFHMT'18).

Murphy, M. D., Sparks, R. S. J., Barclay, J., Carroll, M. R., & Brewer, T. S. (2000). Remobilization of andesite magma by intrusion of mafic magma at the Soufriere Hills Volcano, Montserrat, West Indies. Journal of petrology, 41(1), 21-42. https://doi.org/10.1093/petrology/41.1.21

Murton, B. J., & Rona, P. A. (2015). Carlsberg Ridge and Mid-Atlantic Ridge: Comparison of slow spreading centre analogues. Deep Sea Research Part II: Topical Studies in Oceanography, 121, 71-84. https://doi.org/10.1016/j.dsr2.2015.04.021

Newhall, C. G., & Self, S. (1982). The volcanic explosivity index (VEI) an estimate of explosive magnitude for historical volcanism. Journal of Geophysical Research: Oceans, 87(C2), 1231-1238. https://doi.org/10.1029/JC087iC02p01231

Nicolas, A., & Boudier, F. (2011). Structure and dynamics of ridge axial melt lenses in the Oman ophiolite. *Journal of Geophysical Research: Solid Earth*, *116*(B3). https://doi.org/10.1029/2010JB007934

Nobile, F., & Vergara, C. (2008). An effective fluid-structure interaction formulation for vascular dynamics by generalized Robin conditions. SIAM Journal on Scientific Computing, 30(2), 731-763. https://doi.org/10.1137/060678439

O'Hara, M. J., & Mathews, R. E. (1981). Geochemical evolution in an advancing, periodically replenished, periodically tapped, continuously fractionated magma chamber. Journal of the Geological Society, 138(3), 237-277. https://doi.org/10.1144/gsjgs.138.3.0237

Olive, J. A. (2023). Mid-ocean ridges: geodynamics written in the seafloor. In *Dynamics of plate tectonics and mantle convection* (pp. 483-510). Elsevier.

Olive, J. A., & Dublanchet, P. (2020). Controls on the magmatic fraction of extension at mid-ocean ridges. Earth and Planetary Science Letters, 549, 116541. https://doi.org/10.1016/j.epsl.2020.116541

Phipps Morgan, J., Parmentier, E. M., & Lin, J. (1987). Mechanisms for the origin of mid-ocean ridge axial topography: Implications for the thermal and mechanical structure of accreting plate boundaries. Journal of Geophysical Research: Solid Earth, 92(B12), 12823-12836. https://doi.org/10.1029/JB092iB12p12823

Picard, D., L. Arbaret, M. Pichavant, R. Champallier, and P. Launeau (2013), The rheological transition in plagioclase-bearing magmas, J. Geophys. Res. Solid Earth, 118, 1363–1377, doi:*10.1002/jgrb.50091.*

Pusok, A. E., Katz, R. F., May, D. A., & Li, Y. (2022). Chemical heterogeneity, convection and asymmetry beneath mid-ocean ridges. *Geophysical Journal International*, *231*(3), 2055-2078. https://doi.org/10.1093/gji/ggac309

Reverso, T., Vandemeulebrouck, J., Jouanne, F., Pinel, V., Villemin, T., Sturkell, E., & Bascou, P. (2014). A two-magma chamber model as a source of deformation at Grímsvötn Volcano, Iceland. *Journal of Geophysical Research: Solid Earth*, *119*(6), 4666-4683. https://doi.org/10.1002/2013JB010569

Reynolds, J. R., & Langmuir, C. H. (1997). Petrological systematics of the Mid-Atlantic Ridge south of Kane: Implications for ocean crust formation. *Journal of Geophysical Research: Solid Earth*, *102*(B7), 14915-14946.

Roche, O., & Carazzo, G. (2019). The contribution of experimental volcanology to the study of the physics of eruptive processes, and related scaling issues: A review. Journal of Volcanology and Geothermal Research, 384, 103-150. https://doi.org/10.1016/j.jvolgeores.2019.07.011

Roche, O., & Carazzo, G. (2019). The contribution of experimental volcanology to the study of the physics of eruptive processes, and related scaling issues: A review. Journal of Volcanology and Geothermal Research, 384, 103-150. https://doi.org/10.1016/j.jvolgeores.2019.07.011

Roegiers, M. (Sr.) & Roegiers, L.(1946). La viscositédes mélanges de fluides normaux, Sociétédes Huiles deCavel & Roegiers, S.A., Gand.

Roegiers, M. (Sr.) (1951). Discussion of the fundamental equation of viscosity, Industrial Lubrication and Tribology. 3(1951)27-29.

Roegiers, M., & Zhmud, B. (2011). Property blending relationships for binary mixtures of mineral oil and elektrionised vegetable oil: viscosity, solvent power, and seal compatibility index. Lubrication Science, 23(6), 263-278. https://doi.org/10.1002/ls.154

Roscoe, R. (1952). The viscosity of suspensions of rigid spheres. *British journal of applied physics*, *3*(8), 267. https://doi.org/10.1088/0508-3443/3/8/306

Rosenberg, C. L., & Handy, M. R. (2005). Experimental deformation of partially melted granite revisited: implications for the continental crust. *Journal of metamorphic Geology*, *23*(1), 19-28. https://doi.org/10.1111/j.1525-1314.2005.00555.x

Rowley, D. B., Forte, A. M., Rowan, C. J., Glišović, P., Moucha, R., Grand, S. P., & Simmons, N. A. (2016). Kinematics and dynamics of the East Pacific Rise linked to a stable, deep-mantle upwelling. Science advances, 2(12), e1601107. https://doi.org/10.1126/sciadv.1601107

Rubin, K. H., & Sinton, J. M. (2007). Inferences on mid-ocean ridge thermal and magmatic structure from MORB compositions. *Earth and Planetary Science Letters*, *260*(1-2), 257-276.

Rubin, K. H., Smith, M. C., Bergmanis, E. C., Perfit, M. R., Sinton, J. M., & Batiza, R. (2001). Geochemical heterogeneity within mid-ocean ridge lava flows: Insights into eruption, emplacement and global variations in magma generation. Earth and Planetary Science Letters, 188(3-4), 349-367. https://doi.org/10.1016/S0012-821X(01)00339-9

Sarkar, S., Baruah, A., Dutta, U., & Mandal, N. (2014). Role of random thermal perturbations in the magmatic segmentation of mid-oceanic ridges: Insights from numerical simulations. Tectonophysics, 636, 83-99. https://doi.org/10.1016/j.tecto.2014.08.008

Sarkar, S., Baruah, A., Dutta, U., & Mandal, N. (2014). Role of random thermal perturbations in the magmatic segmentation of mid-oceanic ridges: Insights from numerical simulations. Tectonophysics, 636, 83-99. https://doi.org/10.1016/j.tecto.2014.08.008

Sauter, D., Unternehr, P., Manatschal, G., Tugend, J., Cannat, M., Le Quellec, P., ... & Horn, B. W. (2016). Evidence for magma entrapment below oceanic crust from deep seismic reflections in the Western Somali Basin. Geology, 44(6), 407-410. https://doi.org/10.1130/G37747.1

Schubert, G., Anderson, J. D., Travis, B. J., & Palguta, J. (2007). Enceladus: Present internal structure and differentiation by early and long-term radiogenic heating. Icarus, 188(2), 345-355. https://doi.org/10.1016/j.icarus.2006.12.012

Searle, R. C., & Escartin, J. (2013). The rheology and morphology of oceanic lithosphere and mid-ocean ridges.

Searle, R. C., Keeton, J. A., Owens, R. B., White, R. S., Mecklenburgh, R., Parsons, B., & Lee, S. M. (1998). The Reykjanes Ridge: structure and tectonics of a hot-spot-influenced, slow-spreading ridge, from multibeam bathymetry, gravity and magnetic investigations. *Earth and Planetary Science Letters*, *160*(3-4), 463-478. https://doi.org/10.1016/S0012-821X(98)00104-6

Sempéré, J. C., & Cochran, J. R. (1997). The Southeast Indian Ridge between 88 E and 118 E: Variations in crustal accretion at constant spreading rate. Journal of Geophysical Research: Solid Earth, 102(B7), 15489-15505. https://doi.org/10.1029/97JB00511

Sempéré, J. C., Purdy, G. M., & Schouten, H. (1990). Segmentation of the Mid-Atlantic Ridge between 24 N and 30 40'N. *Nature*, *344*(6265), 427-431.Sauter, D., & Cannat, M. (2010). The ultraslow spreading Southwest Indian ridge. *Diversity of hydrothermal systems on slow spreading ocean ridges*, *88*, 153-173.

Seyler, M., Cannat, M., & Mevel, C. (2003). Evidence for major-element heterogeneity in the mantle source of abyssal peridotites from the Southwest Indian Ridge (52 to 68 E). *Geochemistry, Geophysics, Geosystems*, *4*(2).

Shapiro, A. P., & Probstein, R. F. (1992). Random packings of spheres and fluidity limits of monodisperse and bidisperse suspensions. Physical review letters, 68(9), 1422. https://doi.org/10.1103/PhysRevLett.68.1422

Shimizu, N., & Grove, T. L. (1998). Geochemical studies of olivine-hosted melt inclusions from ridges and arcs. Eos, 79, F1002.

Siebert, L., Cottrell, E., Venzke, E., & Andrews, B. (2015). Earth's volcanoes and their eruptions: an overview. The encyclopedia of volcanoes, 239-255.https://doi.org/10.1016/B978-0-12-385938-9.00012-2

Sim, S. J., Spiegelman, M., Stegman, D. R., & Wilson, C. (2020). The influence of spreading rate and permeability on melt focusing beneath mid-ocean ridges. *Physics of the Earth and Planetary Interiors*, *304*, 106486. https://doi.org/10.1016/j.pepi.2020.106486

Singh, S. C., Crawford, W. C., Carton, H., Seher, T., Combier, V., Cannat, M., ... & Miguel Miranda, J. (2006). Discovery of a magma chamber and faults beneath a Mid-Atlantic Ridge hydrothermal field. *Nature*, *442*(7106), 1029-1032. https://doi.org/10.1038/nature05105

Sinton, J. M., & Detrick, R. S. (1992). Mid-ocean ridge magma chambers. *Journal of Geophysical Research: Solid Earth*, *97*(B1), 197-216.

Sleep, N. H., & Rosendahl, B. R. (1979). Topography and tectonics of mid-oceanic ridge axes. Journal of Geophysical Research: Solid Earth, 84(B12), 6831-6839. https://doi.org/10.1029/JB084iB12p06831

Small, C. (1998). Global systematics of mid-ocean ridge morphology. Washington DC American Geophysical Union Geophysical Monograph Series, 106, 1-25. https://doi.org/10.1029/GM106p0001

Smith, D. K., & Cann, J. R. (1992). The role of seamount volcanism in crustal construction at the Mid-Atlantic Ridge (24°–30° N). *Journal of Geophysical Research: Solid Earth*, *97*(B2), 1645-1658. https://doi.org/10.1029/91JB02507

Smith,D.K.&Cann,J.R.1993.Building the crust at the Mid-Atlantic Ridge. Nature, 365, 707–715.

Sparks, R. S. J., Annen, C., Blundy, J. D., Cashman, K. V., Rust, A. C., & Jackson, M. D. (2019). Formation and dynamics of magma reservoirs. *Philosophical Transactions of the Royal society A*, *377*(2139), 20180019. https://doi.org/10.1098/rsta.2018.0019

Sparks, R. S. J., Annen, C., Blundy, J. D., Cashman, K. V., Rust, A. C., & Jackson, M. D. (2019). Formation and dynamics of magma reservoirs. Philosophical Transactions of the Royal society A, 377(2139), 20180019. https://doi.org/10.1098/rsta.2018.0019

Spiegelman, M., & McKenzie, D. (1987). Simple 2-D models for melt extraction at mid-ocean ridges and island arcs. *Earth and Planetary Science Letters*, *83*(1-4), 137-152. https://doi.org/10.1016/0012-821X(87)90057-4

Tolstoy, M. (2008). Seismological constraints on magmatic and hydrothermal processes at mid-ocean ridges. *Magma to Microbe: Modeling Hydrothermal Processes at Ocean Spreading Centers*, *178*, 75-96.

Toomey, D. R., Jousselin, D., Dunn, R. A., Wilcock, W. S., & Detrick, R. S. (2007). Skew of mantle upwelling beneath the East Pacific Rise governs segmentation. *Nature*, *446*(7134), 409-414. https://doi.org/10.1038/nature05679

Van der Molen, I., & Paterson, M. S. (1979). Experimental deformation of partially-melted granite. Contributions to Mineralogy and Petrology, 70(3), 299-318. https://doi.org/10.1007/BF00375359

Wanless, V. D., & Shaw, A. M. (2012). Lower crustal crystallization and melt evolution at mid-ocean ridges. *Nature Geoscience*, *5*(9), 651-655. https://doi.org/10.1038/ngeo1552

Ward, S. G., & Whitmore, R. L. (1950). Studies of the viscosity and sedimentation of suspensions Part 1.-The viscosity of suspension of spherical particles. British Journal of Applied Physics, 1(11), 286. https://doi.org/10.1088/0508-3443/1/11/303

Webb, S. L., & Dingwell, D. B. (1990). Non-Newtonian rheology of igneous melts at high stresses and strain rates: Experimental results for rhyolite, andesite, basalt, and nephelinite. Journal of Geophysical Research: Solid Earth, 95(B10), 15695-15701. https://doi.org/10.1029/JB095iB10p15695

West, M., Menke, W., & Tolstoy, M. (2003). Focused magma supply at the intersection of the Cobb hotspot and the Juan de Fuca ridge. Geophysical Research Letters, 30(14). https://doi.org/10.1029/2003GL017104

White, R. S., Bown, J. W., & Smallwood, J. R. (1995). The temperature of the Iceland plume and origin of outward-propagating V-shaped ridges. *Journal of the Geological Society*, *152*(6), 1039-1045. https://doi.org/10.1144/GSL.JGS.1995.152.01.26

White, W. M., & Schilling, J. G. (1978). The nature and origin of geochemical variation in Mid-Atlantic Ridge basalts from the Central North Atlantic. *Geochimica et Cosmochimica Acta*, *42*(10), 1501-1516.

Wilson, D. S. (1992). Focused mantle upwelling beneath mid-ocean ridges: Evidence from seamount formation and isostatic compensation of topography. Earth and Planetary Science Letters, 113(1-2), 41-55. https://doi.org/10.1016/0012-821X(92)90210-M

Xu, M., Pablo Canales, J., Carbotte, S. M., Carton, H., Nedimović, M. R., & Mutter, J. C. (2014). Variations in axial magma lens properties along the East Pacific Rise (9° 30′ N–10° 00′ N) from swath 3-D seismic imaging and 1-D waveform inversion. Journal of Geophysical Research: Solid Earth, 119(4), 2721-2744. https://doi.org/10.1002/2013JB010730

Zhang, C., Koepke, J., Kirchner, C., Götze, N., & Behrens, H. (2014). Rapid hydrothermal cooling above the axial melt lens at fast-spreading mid-ocean ridge. Scientific reports, 4(1), 1-9. https://doi.org/10.1016/j.chemgeo.2017.04.002

Zhang, W. Q., Liu, C. Z., & Dick, H. J. (2020). Evidence for multi-stage melt transport in the lower ocean crust: The Atlantis bank gabbroic massif (IODP Hole U1473A, SW Indian Ridge). Journal of Petrology, 61(9), egaa082. https://doi.org/10.1093/petrology/egaa082

Zhmud, B. (2014). Viscosity blending equations. Lube Mag, 121(93), 24-27.

Chapter 4 | 3D stress fields of mid-ocean ridge tectonics: a manifestation of sub-crustal mush dynamics

4.1. Previous studies: a survey

Mid-ocean ridges (MORs) are the most spectacular surface manifestations of the present-day divergent plate motion, dominated by ridge-axis normal tensile stresses. However, a range of morphological features, such as surface topography, transform faults and along-axis tectonic variations indicate that the stress fields are far more complex than a simple uniaxial tensional setting. Several studies have shown the occurrence of across-axis tension with synchronously acting along-axis tension, implying that MORs can evolve in a bi-axial stress regime. A range of tectonic models, such as bi-axial global extension (Gudmundsson, 1995), flexural stresses resulting from spreading direction changes (Pockalny et al., 1996), stresses from isostatic compensation of the long-wavelength topography (Neves et al., 2004), and thermal stresses due to slab cooling (Choi et al., 2008; Sandwell, 1986), have been proposed to explain the origin of such bi-axial stress fields. A parallel line of studies, in contrast, report along-axis compressional stress regimes. For example, Maia et al., 2016 have shown from earthquake focal mechanism solutions that the St Peter and St Paul islets, which represent parts of a major, 200 km long and 30 km wide submarine shear zone accommodate transpressive stresses along the northern transform fault of the St Paul system17, resulting in deep-crustal exhumation in this ridge segment. Similar ridge-parallel compressional stress regimes were reported earlier from the East Indian Ridge (Craddock et al., 2004). MORs often develop more complex heterogeneous stress fields, characterized by a close spatial association of along-axis compression and tension regimes (Parnell-Turner et al., 2017). All these observations suggest that MORs stresses can hardly be described by either an across-ridge uniaxial or a simple bi-axial tension model.

The stress activities in MOR systems generally persist far away from the ridge axes, forming characteristic off-axis stress regimes, which are reported from geological and geophysical investigations, e.g., borehole breakout stress studies (Mildren and Hillis, 2000; Newmark et al., 1984). The most widely documented stress field is ridge-parallel off-axis compressional fields, which are thought to originate from ridge-normal tension (Castillo et al., 1998; Newmark et al., 1984). Various mechanical models have been proposed to explain the origin of off-axis stress fields. For example, Parnell-Turner et al., (2017) developed a stress model based on the solutions of local micro-earthquakes originating from an active detachment at 13°20′N in the Mid-Atlantic Ridge. Their investigation recorded a remarkably high rate of seismic activity, with > 244,000 events detected along 25 km of the ridge axis and at depths of ~10 km below the seafloor, and recognized reverse-faulting events. Their stress model accounts for far-field horizontal forces (ridge-push or slab pull) at the plate extremities to explain the compressive stresses for reverse-faulting events within a global tensile regime. Intraplate earthquake focal mechanisms (Richardson et al., 1979; sites 92–94) also indicate a principal horizontal ENE-WSW trending compression zone within the Pacific plate. Similar off-axis compressional regimes are recorded from several other MORs (Moos and Zoback, 1990). In-situ borehole stress measurements near active spreading centers in the Ocean Drilling Program (ODP, Holes 504B and 765D, Newmark et al., 1984, DSDP Holes 504B and 395A, (Moos and Zoback, 1990) indicate that the maximum horizontal stress is compressive (>100 MPa), which is oriented normal to the spreading ridge axis.

The mechanical complexity of MORs is again manifested in their along-axis structural segmentation, often forming ridge transverse topographic morphologies (Macdonald et al., 1988). These transverse structures show stress intensification at the segment ends, which are explained in different ways, such as release of stress at the segment centres due to greater magmatic extension (Gràcia et al., 1999; Karson and Winters, 1992), variation in the properties of the elastic lithosphere (Behn and Ito, 2008; Dalton et al., 2014; Sibrant et al., 2018) and geometry of ridge-transform intersection (e.g., Morgan and Parmentier, 1984; Pollard and Aydin, 1984). Ridge-transverse structural segmentation is a reflection of across-axis shear stresses, further supported by strike-slip focal mechanisms. Step-like ridge geometry can explain such shear stress fields. Ridge axes often undergo transcurrent movement, which is revealed from earthquake focal spread across them (Abercrombie and Ekström, 2001).

A direction of mechanical modelling deals with the mechanics of stress development in the divergent tectonics of MORs. Lithospheric flexural bending is perhaps the most widely accepted model, but used to explain the origin of ridge normal uniaxial tension that gives rise to ridge parallel normal faulting. Sohn and Sims, (2005) described plate bending as another possible mechanism for stress generation at MORs. In their model, bending stress accumulates as the plate progressively moves off axis, leading to maximum magnitudes, reaching 1.8 GPa as a tensile stress at the upper part of the lithosphere and 4 GPa as a compressive stress at its lower part. However, the failure stresses at 1 km deep oceanic crust are estimated around 100 – 200 MPa (for E=200 Mpa, Moos and Zoback, 1990); the actual stresses can thus never attain such large values. Parnell-Turner et al., (2017) bending model also yields large compressive stresses in the footwall of detachment faults in the axial regions, which would initiate reverse-faulting before such high stress magnitudes were reached. However, the bending model does not account for either along-axis tension or compression, as discussed in the preceding paragraphs. Several authors have considered topographic relief as a factor to show the development of axial tension (Luttrell and Sandwell, 2012; Morgan and Parmentier, 1984). All these calculations attempt to explain individual stress fields, ridge normal or parallel tension. However, there is no unified model to combine all types of stress fields into a single dynamic setting, and such a model would resolve the long-standing problem of synchronous shear stress development in a biaxial stress regime of MORs.

The study presented in this chapter investigates the origin of stress complexities at the ridge axes taking into account the role of underlying mush dynamics in MORs. A thermo-mechanical model is developed to find the three-dimensional (3D) stress fields in the perspective of interactions between solid elastic crust and convecting melt-bearing mushy substrates, treated as fluid domains. This modelling approach allows to simulate the 3D stress fields, which is used to quantify the axial stresses, and across-ridge shear stresses. The model estimates are validated by using the morphological characteristics of MOR systems, such as segment, axial topography, abyssal hill, transform and other types of faults.

4.2. Computational Methods

4.2.1. Approach

Four fundamental physical processes are combined to conceptualize a representative model of the complex mid-ocean ridge systems. These are: 1) decompression melting at 60-30 km depth (Figure 4.1a), 2) convection at 30 km, extending up to the crustal depth (Figure 4.1c), and 3) fluid-solid interaction at the crustal base (4-5 km depth), (Figure 4.1b) and 4) stress versus topographic correlations in the solid crust. Each of them is treated with a distinctive theoretical consideration. Based on these four phenomena, the present theoretical framework accounts for a three-layer model architecture (Figure 4.1a) for the stress-field simulations of MORs.

4.2.2. Decompression melting

Considering the basic premises of decompression melting (explained in detail in Chapter 3), the present modelling takes into account a set of boundary conditions as described in Table 4.1. The model consists of a horizontal layer subjected to thermal perturbations at the base of the prismatic control volume (Numerical Domain), covering a horizontal distance of 15 km on either side of the MOR axis (Figure 4.1a). The model depth is fixed at 28 km from the seafloor, considering that it corresponds to the threshold depth at which decompression melting ceases. The thermal perturbations are randomized within a temperature bound between 500ºC to 1440ºC (Mandal et al., 2018; Sarkar et al., 2014; Sen et al., 2023), (Figure 4.1c) subject to a condition that the number of thermal points with temperatures above the liquidus must not exceed a threshold limit (20% of the total thermal points). This specific boundary condition is imposed to constrain the melt production in the model approximated to natural cases. (Figures 4.2 a-c)

4.2.3. Convection

The convection process starts to operate in the model following the decompression melting event, producing a critical amount of melts in the system to form mushy (solid + melt) materials in sub-ridge regions. It is noteworthy that the occurrence of mushy zones in sub-ridge mantle has been extensively reported in the earlier literature (e.g., Baines et al., 2009; Singh et al., 1998; Sinton and Detrick, 1992). Melts in the mushy regions set in buoyancy-driven convective circulations beneath the MOR (Figure 4.3a and 4.3b). A detailed description of the theoretical treatment of mushy flows is provided in Sarkar et al., (2014) and Mandal et al., (2018). The basic theoretical principles are used in the modelling of melt dynamics. The detailed explanation has been described in Chapter 3.

For the present problem, this study adopts the numerical method of heat and fluid flow simulation of Patankar (1980), utilizing the continuity equation, momentum equation and the energy equation in enthalpy form. Three source terms are introduced to these equations: a Darcy term and a buoyancy term in the momentum equation; and an enthalpy term in the energy equation (Brent et al., 1988; Voller and Prakash, 1987). After incorporating these source terms, the three governing equations: continuity, momentum and energy equations can be expressed respectively as:

$$\nabla . v = 0 \tag{4.1}$$

$$\rho \frac{\partial}{\partial t} v + \rho v . \nabla v = -\nabla p + \mu_{fd} \nabla^2 v + S_g + S_D \tag{4.2}$$

$$\frac{\partial}{\partial t}(\rho h) + \nabla . (\rho v h) = \nabla . (a \nabla h) - S_h, \tag{4.3}$$

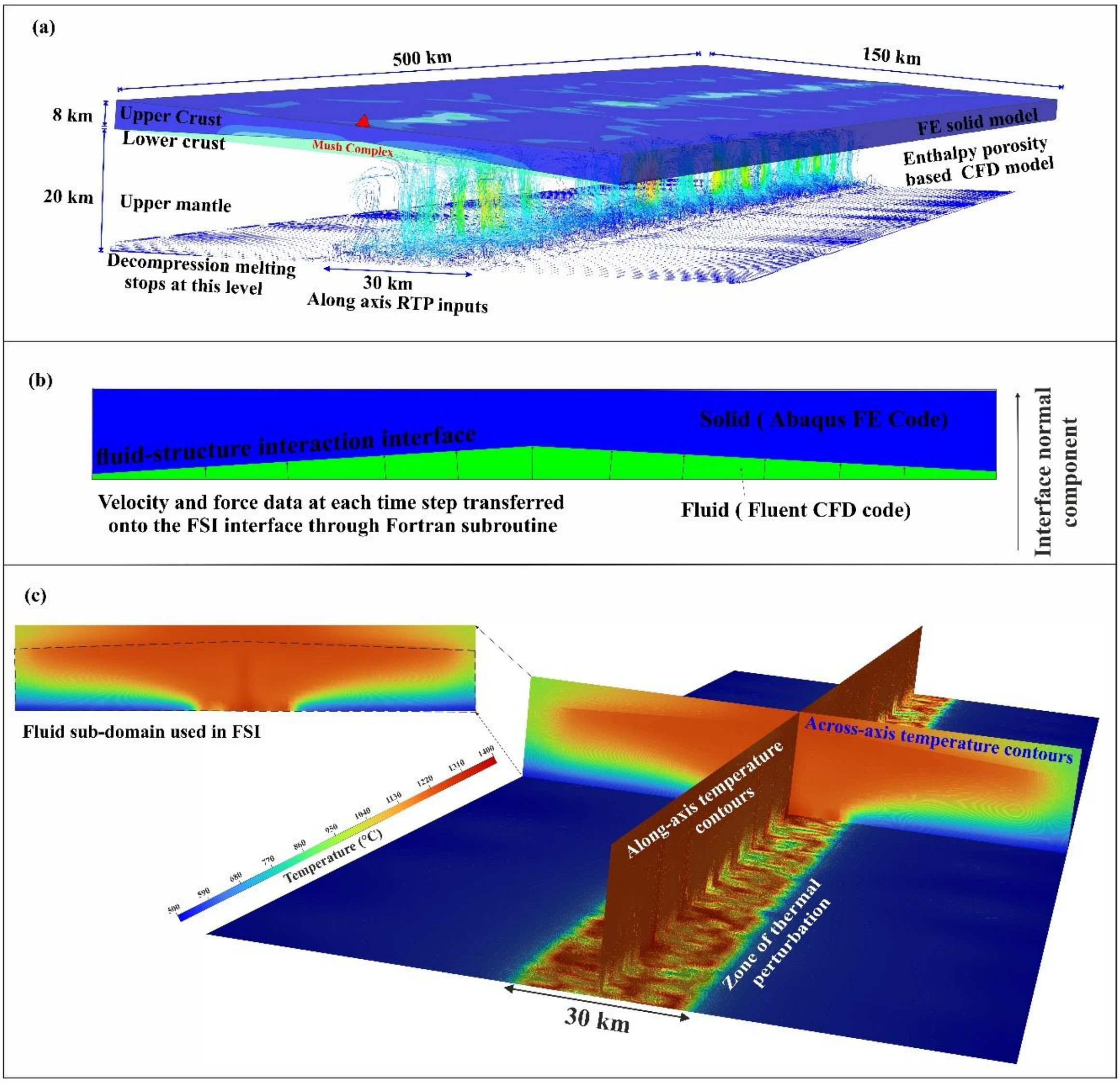

Figure 4.1 *A schematic diagram of the MOR model, showing upper-mantle convective upwelling beneath the crust. (a) A rectangular zone of melt 'points' that marks cessation of decompression melting and formation of random thermal perturbations (RTP), with a temperature fluctuation in the range 500^{0}C to 1400 ^{0}C (Sarkar et al., 2014). The RTP points act as initiation of convection in the shallower part of the mantle beneath the MOR, indicated by flow path lines. The lower crustal mush complex (MC) transfers motion and force to the crustal base, causing an elastic deformation in thin crust (Sen et al., 2023). (b) Diagrammatic explanation of the Fluid Structure Interaction (FSI) in the two-layer MOR model. (c) Along- and across-axis temperature profiles of the convective flows in the fluid simulation, showing temperature variations in the range 1000 °C to 1250 ^{0}C (solidus-liquidus) in the upwelling zones. The fluid subproblem is simulated with an overlying much viscous 'fluid' layer; however, the kinematic and dynamic states of the underlying layer (denoted by 'black' dotted line) are utilized for the FSI modelling*

where p, ρ and μ_{fd} denote pressure, density and viscosity of the fluid domain, respectively. T, h and a represent temperature, enthalpy, and thermal diffusivity ($a = k/\rho c$, k and c are the thermal conductivity and specific heat, respectively). The fluid velocity, v is chosen to vary linearly with the melt fraction ϕ. In this single-phase idealization, the domain viscosity μ_{fd} is chosen to vary with temperature in a power-law function (Sarkar et al., 2014; Yongshun Chen and Morgan, 1990). In the momentum equation (Equation 4.2) the source term S_D regulates the dominance of Darcy (i.e.porous) flows, whereas S_g implements the buoyancy factor through Boussinesque approximation. In the energy equation (Equation 4.3) the source term S_h acts as an enthalpy factor to incorporate the energy involved in the solid-melt phase transformation. The mathematical expressions of these source terms are,

$$S_D = -C\frac{(1-\phi)^2}{(\phi^3+\varepsilon)}v \qquad (4.4)$$

$$S_g = \rho g\theta \varDelta T \qquad (4.5)$$

$$S_h = \frac{\partial\rho\varDelta H}{\partial t} + \nabla.(\rho v\varDelta H). \qquad (4.6)$$

C and ε in Eq.4 are constants, whose values are taken as 1e5 and 0.001, (Sarkar et al., 2014). In Equation 4.5 $\varDelta T$ represents temperature fluctuations with respect to the reference temperature, and θ is the co-efficient of thermal expansion. In Equation 4.6, $\varDelta H$ is the mean latent heat content.

4.2.4. Fluid - Structure Interaction

Implementation of this partitioning procedure of FSI interaction in the present model has been carried out through a range of simplification and idealization. 1) As the model has relatively a thin solid domain, it is assumed that the structural dynamics does not significantly affect the fluid domain kinematics. In other words, this is a one-way FSI mechanical setting, where the fluid has been solved independently over a time frame of 7 Myr, and the velocity data of more than 100-time instances have been stored. 2) As the present CFD modelling considers an almost rigid fluid domain overlying crust, whose viscosity is greater than the underlying mantle mush by an order of six (Table 4.1). Under this condition the crust-mantle interface in the fluid model completely dampens the velocity. The velocity values of the next layer of cell nodes are averaged with those of the interface cell nodes, and stored them as the fluid velocity of FSI interface (see, Figure 4.1b). In the FSI implementation, the viscous stress part in equation 14 is a product of normal-to-surface component of strain rate and dynamic viscosity of the fluid. The present theory uses a dynamic viscosity of fluid for the Robin transmission condition different from that obtained from the CFD model. In a CFD model, a reference viscosity for mantle-mush is chosen in the order of 10^{15} Pa s, which decreases further with rise in temperature following a power-law, where the variation is limited within one order. But, for the Robin transmission condition in FSI, the fluid viscosity that affects the interface is

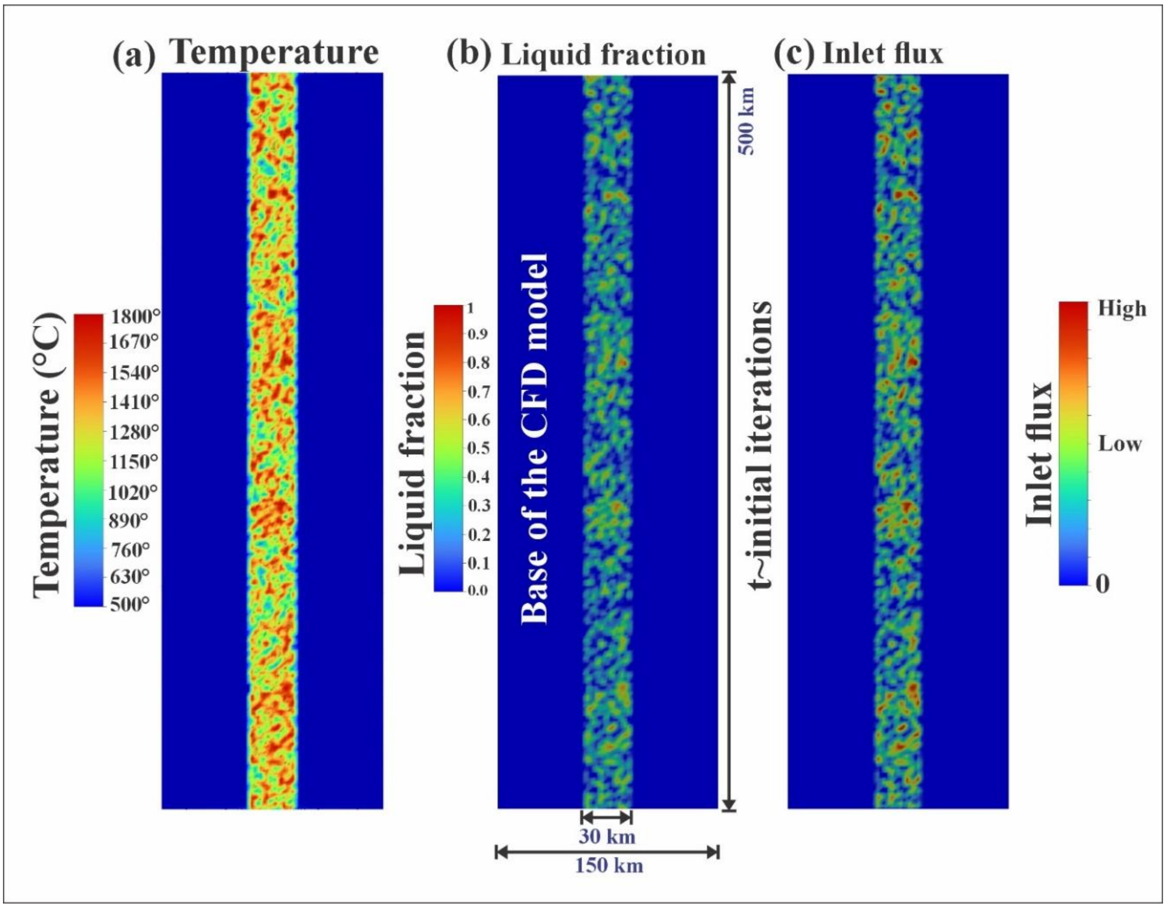

Figure 4.2 *Considerations of the inlet thermal and kinematic conditions at the base of the MOR system model: (a) temperature, (b) liquid fraction, and (c) inlet flux contours at initial iterations of the simulation. The central rectangular portion of the model base is subjected to random thermal perturbations (RTP) within a temperature range: 500 °C -1800 °C covering the entire range of solidus to liquidus temperatures in the underlying decompression melting zone. The upwelling velocity at the base is 6 cm/yr.*

equated with that of the top 10 km sub-crustal fluid domain. Its effective viscosity has been estimated in the order of 10^{13} to 10^{15} Pa s (Sen et al., 2023). 4) The normal-to-surface strain rate in describing the viscous stress part of equation 3.20 (*cf.* Chapter 3) has been idealized as the ratio of vertical fluid-velocity component of the interface nodes and the thickness of the fluid domain of the CFD model, which represents the total height of the convection loop. 5) The pressure part of equation 3.20 has been idealized as a combination of normal dynamic pressure utilizing the vertical velocity component and a constant hydrostatic pressure. 6) The essential part of the Robin transmission condition is the utilization of a scaled velocity component, as has been outlined in equation 3.19 (*cf.* Chapter 3) Numerical implementation of FSI is carried without this component (i.e., only Neumann), which produces a convex or concave crustal top surface each time without a narrow axial high or morphological complexity resembling MOR topography. But, implementation of the scaled velocity component (i.e., Robin transmission) in FSI gives rise to MOR topography. The scale factor has a positive and bounded value, which is set at 0.025. A trial with values ranging 2 to 0.005 has been carried out in order to ascertain its influence on the topography of the crustal top surface and the principal stresses. It is found that the choice of this scaling factor's value has little effect in the range of 0.1 to 0.01, on both topography and principal stresses. The FSI mechanism of 3D mid-oceanic ridge system is thoroughly discussed in Chapter 3. The sub-problem for the fluid domain was tackled using finite volume computational dynamics code Fluent (Ansys 2016), whereas that for the structural domain was solved with the help of a finite element code for solid mechanics, ABAQUS CAE (Abaqus 2016). This computational study implemented the FSI operations using an indigenous code based on FORTAN, linked through Abaqus user-subroutines. A detailed description of the computational procedures is given in Chapter 3.

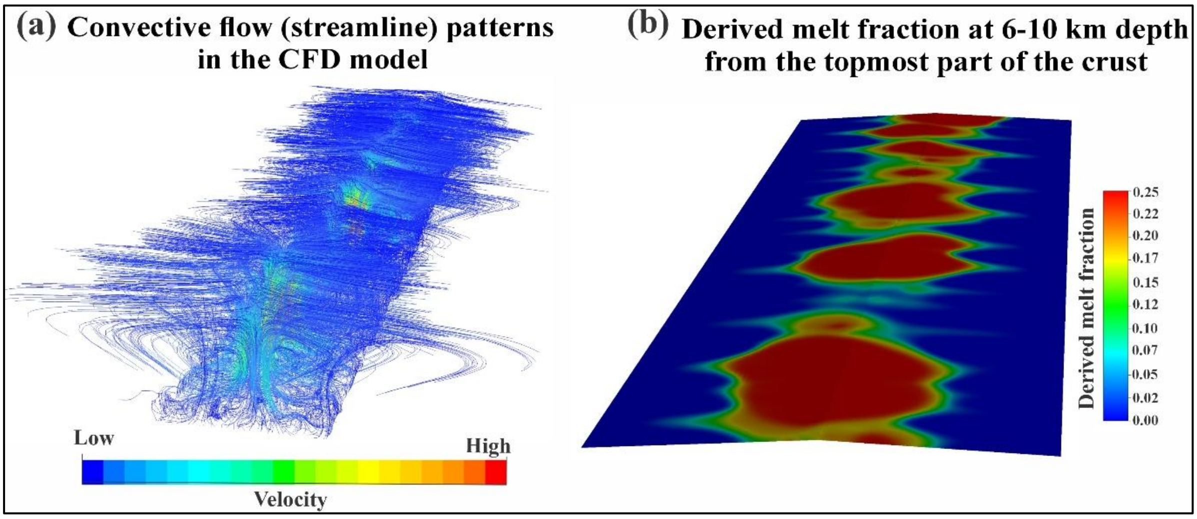

Figure 4.3 *(a) and (b) shows the resulting convective flows in the fluid domain, and subcrustal melt fraction contours derived from the liquid fraction, respectively.*

4.2.5. Elastic crustal deformations

Several authors (e.g., Buck et al., 2005) modelled the crust as a brittle layer to show shear failures (faults) in response to its extension and buckling. In contrast, the present approach considers a body matrix depicting a series of three-dimensional stress fields, which allow us to map an array of tensile and compressive stress concentration zones on the top surface as well as within the elastic crust. The crustal strength at the MOR system is a critical parameter, as pointed out by previous researchers in the stress modelling. Based on the available estimates from volcanic rock systems (Behn et al., 2002; Behn and Ito, 2008; Gudmundsson, 2003), the Young's modulus of the crustal layer is varied between 5 and100

Table 4.1 *Model parameters and boundary conditions used in FE-FSI-CFD modelling*

Model materials	Properties/Boundary conditions (BC)
FE Model of Upper Crust	***Material Properties:*** Model dimensions = $(48)km \times 150Km \times 500km$; Density ($\rho_s$) = 2400-2800 kg / m^3; Elastic modulus (E) = 10 GPa; Poisson's ratio (ν) = 0.26. ***Boundary Conditions:*** Upper surface = Free BC; Left and Right Wall = Not Constrained Front and Back Wall = Not Constrained; Bottom surface = interface.
FSI Interface	***Material Properties:*** Viscosity (μ_{eff}) = 1×10^{12} Pa s -1×10^{14} Pa s (Sen et al., 2023) Density (ρ_{eff}) = 2500 kg / m^3 ***Boundary Conditions:*** Dirichilet and Neumann conditions (Robin Transmission); No slip.
CFD model of Upper Mantle And lower crust	***Material Properties:*** Model dimensions = $(20-24)km \times 150Km \times 500km$ Viscosity of the upper-mantle (Single Phase Idealization; Temperature dependent) = 10^{15} Pa s {Viscosity of mantle rock = 10^{19} Pa s; Viscosity of melt = 10^{3} Pa s} Density of the upper mantle = 2500 kg / m^3 (Boussinesq); Thermal Expansion Co-efficient = 5×10^{-5} / ºC (Sim et al. 2020, Keller and Katz, 2016); Thermal diffusivity = 10^{-6} m^2/s; Reference Permeability = 10^{-5} - 10^{-6} m^2 (as approximated from Carman-Kozeny Parameter C in Eq. 5, e.g., Katz, 2008; Sarkar et el., 2014) Specific Heat = 1600 J / kg ºC; Solidus Temperature = 1000 ºC Liquidus Temperature = 1250 ºC Viscosity of lower crust = 10^{21} Pa s; Density of Lower Crust = 2500 kg / m^3 ***Boundary Conditions:*** Upper surface of lower crust: heat outflow = 0.001 w/m^2 Left and Right wall of the lower crust: No slip; Heat outflow = 0.001 w/m^2; $V_{divergence}$= 5cm/yr; Front and Back wall of the lower crust: No slip; Heat outflow = 0; Lower crust and upper mantle interface = kinematically coherent and thermally coupled; Left and right wall of the upper mantle: No slip; Heat outflow = 0.001w/m^2; Front and back wall of upper mantle = No slip; Heat Outflow = 0; Bottom surface of upper mantle: Inlet, Along axis random thermal perturbation (RTP) V_{inlet}= 6 cm/yr

GPa, finally keeping the E values in the line of recent studies (Olive and Dublanchet, 2020), where E is chosen in the order of 10 GPa for the overlying crust.

The 3D stress analysis of MORs focuses on the following three stress components with respect to the ridge axis. a) *Axial stresses*: These stresses in upper crust have been calculated in along- and across-axis directions, as well as in the vertical direction. b) *Shear stresses*: They represent horizontal shear stresses parallel and perpendicular to the ridge axis, calculated from the top computational layer of the upper crust. c) *von-Mises stress*: According to shear-energy theory (Barsanescu & Comanici, 2017), the second invariant of a deviatoric stress tensor reaches a critical value before a ductile material starts yielding. The second invariant of the deviatoric stress of a material (von-Mises stress) is expressed in terms of the three principal stresses as,

$$\sigma^{vm} = \{[(\sigma_1 - \sigma_2)^2 + (\sigma_2 - \sigma_3)^2 + (\sigma_1 - \sigma_3)^2]/2\}^{1/2} \tag{4.7}$$

4.3. Results: Stress tensor calculations

The numerical model produces three-dimensional convective melt flows in the middle layer, initially forming a series of along-axis spreading centres located at distances of ~ 10 km to ~ 40 km in the top layer. Their distributions maintain a first order periodicity with an average distance of ~ 25 km. In places, they are closely spaced to form a cluster of 3 to 6 centres in a 100 km length. The spreading centres often do not strictly maintain collinear arrangements, but show appreciable lateral offsetting with a magnitude of 5 km to 21 km. These initial spreading centres eventually coalesce with one another in course of time and form six major spreading centres in located at distances of 46-112 km (Figures 4.4-4.6). The multiple spreading centres that characterize a MOR setting give rise to a strongly heterogeneous 3D stress field in the elastic crust. Our model estimates reveal that the stresses generated in the crust is comparable to that derived from ocean floor topography or tectonic movements (Luttrell and Sandwell, 2012) The following sub-sections describe normal and shear stress components using 3D contour plots at simulation run times: 1, 3, 5, and 7 Myr (Figures 4.4-4.6). The descriptions adopt the symbol conventions of Luttrell and Sandwell, 2012; $\sigma^{\perp}$ and $\sigma^{\parallel}$ denote the normal stress components (σ_{xx} and σ_{zz} in the model Cartesian frame) perpendicular and parallel to the ridge axis, respectively, and $\sigma^{\uparrow}$ denote the vertical normal stress component (σ_{yy} in the model Cartesian frame). $\sigma^{\#}$ is used to express the horizontal shear stress component acting on a vertical plane perpendicular to the ridge axis (σ_{xz} in the model Cartesian frame). From a time-series analysis of the model runs, we investigate temporal and spatial variations of $\sigma^{\perp}$ and $\sigma^{\parallel}$ (Figures

Table 4.2 *Stress components and respective symbols, and their measurements from model simulations corresponding to 7 Myr.*

Model stresses		**Symbols**	**Stress Medians peak (in MPa)**	**Stress Medians (in MPa)**
Ridge perpendicular stress	Axial, top-crust	$\sigma^{\perp}_{ax,tc}$	231, -111	78, -38
	Axial, whole-crust	$\sigma^{\perp}_{ax,wc}$	273, -135	84, -47
	Off-axis, top-crust	$\sigma^{\perp}_{ox,tc}$	21, -63	21, -60
	Off-axis, whole-crust	$\sigma^{\perp}_{ox,wc}$	20, -81	20, -79
Ridge parallel stress	Axial, top-crust	$\sigma^{//}_{ax,tc}$	247, -192	89, -61
	Axial, whole-crust	$\sigma^{//}_{ax,wc}$	256, -228	98, -70
	Off-axis, top-crust	$\sigma^{//}_{ox,tc}$	25, -33	15, -25
	Off-axis, whole-crust	$\sigma^{//}_{ox,wc}$	25, -37	17, -34
Vertical Stress	Axial, top-crust	$\sigma^{\uparrow}_{ax,tc}$	10, -8.5	4, -1.2
	Axial, whole-crust	$\sigma^{\uparrow}_{ax,wc}$	50, -65	23, -14
	Off-axis, top-crust	$\sigma^{\uparrow}_{ox,tc}$	3.1, -3.7	1.7, -1
	Off-axis, whole-crust	$\sigma^{\uparrow}_{ox,wc}$	7.8, -27	4.8, -15
Horizontal Shear stresses	Axial, top-crust	$\sigma^{\#}_{ax,tc}$	147, -140	62, -57
	Off-axis, top-crust	$\sigma^{\#}_{ox,tc}$	21, -21	17, -16
Von-Misses stress	Axial, top-crust	$\sigma^{vm}_{ax,tc}$	500	200
	Axial, whole-crust	$\sigma^{vm}_{ax,wc}$	680	220
	Off-axis, top-crust	$\sigma^{vm}_{ox,tc}$	80	75
	Off-axis, whole-crust	$\sigma^{vm}_{ox,wc}$	125	109

4.4 and 4.5), with an objective to show the evolution of characteristic segmented MOR stress fields. $\sigma^{\#}$ mapping is utilized to study transversely segmented structures commonly observed in mid-ocean ridges. To examine vertical variations in the stress field, we calculate the stresses in the top 2 km thick crustal layer and the whole thickness of crust, denoted by subscripts, *tc* and *wc*, e.g., $\sigma^{\perp}_{\mathrm{tc}}$ and $\sigma^{\parallel}_{\mathrm{wc}}$ in their descriptions. The MOR model domain is subdivided broadly into two regions: axial zone (covering 15 km horizontal extent on either side of the axis) and off-axis region, and their stress fields are denoted as σ_{ax} and σ_{ox}, respectively. The symbolic presentation of various stress parameters used in this article is summarized in Table 4.2.

4.3.1. Ridge-perpendicular and -parallel compression and tension

Model MORs develop typically a heterogeneous across-axis tensile ($\sigma^{\perp}$) regime in the axial zone, consisting of multiple (9 – 10) segments of large $\sigma^{\perp}$ concentrations with separation distances of 20 to 60 km along the ridge axis (Figure 4.4a). Each segment persists down to the crustal base, albeit with their reducing size in the course of MOR evolution. The tensile axial regime is flanked by off-axis compressive belts on its either side, grossly running parallel to the ridge axis at approximately 2 Myr of the model run (Figure 4.4a). Along-axis stress $\sigma^{//}$ mapping reveals intense tensile and compressive stress localization, preferentially in ridge-normal narrow linear zones (Figure 4.5a). Tensile zones that localize higher stresses at the ridge axis grow in time, often coalescing with one another to form wide tensile regimes, separated by narrow, 10 to 30 km wide compressive zones. Their axial spacing varies between 40 km and 150 km with an average of >100 km to form a segmented structure of the MOR. The system initially develops numerous smaller segments, visibly marked by across-axis compressive zone (lengths < 50 km) and close spacing (20 – 40 km), which are asymmetrically distributed about the ridge axis. The tensile regimes in the top layer are stronger than those in the bottom crustal layer (Figure 4.5a).

Using the time-series FSI model results we performed box-plot analyses to study the temporal variation of stress fields in a MOR setting. The plots (Figure 4.4b) show that ridge-perpendicular stresses at axial zones remain predominantly tensile ($+ \sigma^{\perp}_{\mathrm{ax}}$), leaving the off-axis regions dominated by compressive stresses ($- \sigma^{\perp}_{\mathrm{ox}}$). In the top crustal layer both tensile and compressional $\sigma^{\perp}_{\mathrm{ax}}$ attain their respective peak values, + 231 MPa and -111 MPa at 1 Myr (Figure 4.4b), which steeply drops to +116 MPa and -36 MPa, respectively within 2.5 Myr. The median value of $+\sigma^{\perp}_{\mathrm{ax}}$ decreases to 78 MPa at 7 Myr, whereas that of $-\sigma^{\perp}_{\mathrm{ax}}$ remains almost steady at ~ -38 MPa (Figure 4.4b). The stress analysis for the whole crustal thickness reveals higher median peaks of tensile and compressional $\sigma^{\perp}_{\mathrm{ax}} = +273$ MPa and -135 MPa at 1 Myr,

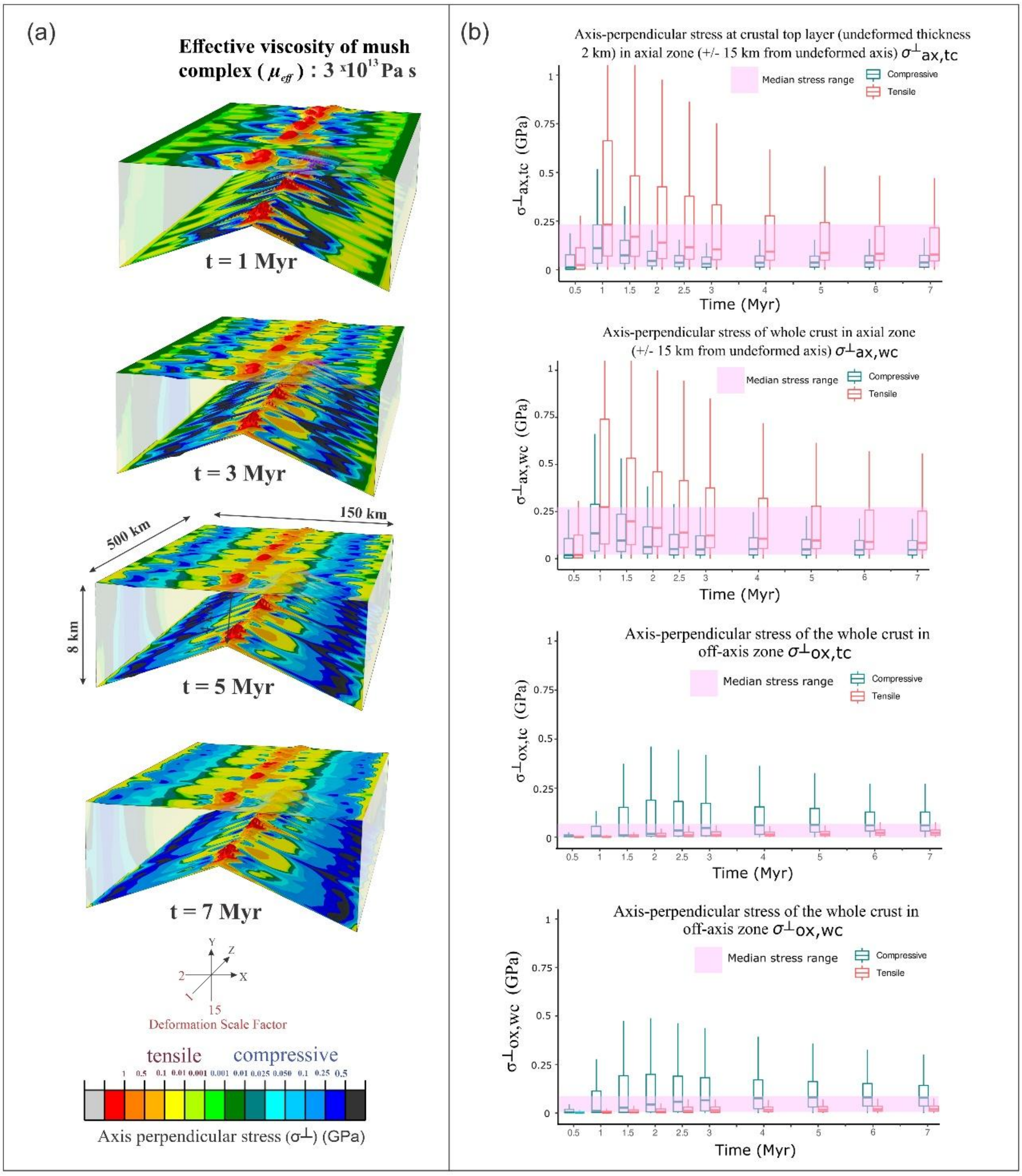

Figure 4.4 *Time series 3D contour plots for ridge-perpendicular stress and their statistical box-plots. (a) Ridge-perpendicular stress ($\sigma^{\perp}$) contours (σ_{xx} in Cartesian model settings) at 1, 3, 5, and 7 Myr (Spatial scales: vertical = 15, along-axis = 1, across-axis = 2). Transparent model views reveal the stress distributions in both top and bottom layers. (b) Statistical box-plots of the stresses in different crustal domains (axial zone, off-axis zone, top-crustal layer, whole-crust) with their medians and quartiles.*

which drop sharply to +138 MPa and -51 MPa at 2.5 Myr, and then moderately to +84 MPa and -47 MPa at 7 Myr (Figure 4.4b). The stress estimates show that the across-ridge median tensile and compressive stresses vary from the shallow to deep-crustal regions, but at unequal rates, as revealed from their contrasting ratios: $(\sigma^{\perp}_{\mathrm{ax}})_{\mathrm{WL}}/(\sigma^{\perp}_{\mathrm{ax}})_{\mathrm{TL}}$ = 1.18 at 1 Myr and 1.08 at 7 Myr for tensile stresses, and 1.22 and 1.24 for compressional stresses (Figure 4.4b). The axial zones of a mature MOR develop depth-wise more uniformly ridge-perpendicular tensile stresses regime in the crust, but heterogeneous compressive stresses at a greater crustal depth.

The off-axis stress ($\sigma^{\perp}_{\mathrm{ox}}$) fields (+/- 15 km to +/- 75 km from the ridge axis) differ significantly from those in the axial regions in the dominance of compressive stresses over tensile stresses (Figure 4.4b). The median compressional $\sigma^{\perp}_{\mathrm{ox}}$ in the top layer, however, defines a blunt peak with a magnitude of 63 MPa at 4 Myr, decreasing to an almost steady value of ~ 60 MPa at 5 Myr. The off-axis regions develop minor tensile peaks of ~ 21 MPa at 6 Myr, remaining steady with time (Figure 4.4b). The whole-crust $\sigma^{\perp}_{\mathrm{ox}}$ fields show a median compressive stress of 81 MPa at 5 Myr, slightly decreasing to 79 MPa at 7 Myr, and a much lower median tensile stresses of 17 MPa at 5 Ma, increasing to 20 MPa at 7 Myr (Figure 3b). The ratio of compressional $\sigma^{\perp}_{\mathrm{ox}}$ between the crustal top and bottom layers is 1.28 at 5 Myr and 1.32 at 7 Myr, whereas the ratio in the tensile zones is 0.88 at 6 Myr and 0.93 at 7 Myr. Evolved mid-ocean ridges develop the highest whole-crust ridge-normal tensile stresses in their axial zones (+84 MPa) and the highest compressive stresses (-79 MPa) in the off-axis regions (Figure 4.4b).

The FSI models develop ridge parallel compressive as well as tensile stresses ($\sigma^{\parallel}$) in the axial zones of MORs, but with unequal magnitudes. Tensile $\sigma^{\parallel}$ in the top crustal layer attains a median peak of 247 MPa at 1 Myr, significantly higher than the compressional median peak (192 MPa). With time both the median peaks drop to 109 MPa and 91 MPa, respectively at 2.5 Myr, and further to 89 MPa and 61 MPa, respectively at 7 Myr (Figure 4.5b). The whole-crust stress estimates yield their lower differences, e.g., 256 MPa and 228 MPa at 1 Myr, dropping to 123 MPa and 100 MPa at 2.5 Myr, and further to 98 MPa and 70 MPa at 7 Myr (Figure 4.5b). The model results suggest that an evolved (7 Myr) MOR always develops along-axis compressive stresses significantly higher than the corresponding tensile stresses, as evident from their median ratios, 1.6 and 1.5 in the top and the whole crustal layers, respectively. However, there are secondary bi-axial tensile regions with axis-parallel tensile stresses more than that across the axis, where their median ratios are 1.14 and 1.17 in the top and the whole crustal layer, respectively at 7 Myr (Figure 4.5b). Off-axis $\sigma^{\parallel}$ fields in the top crustal layer develops lower ridge parallel tension and compression with their median peaks: 25 MPa and

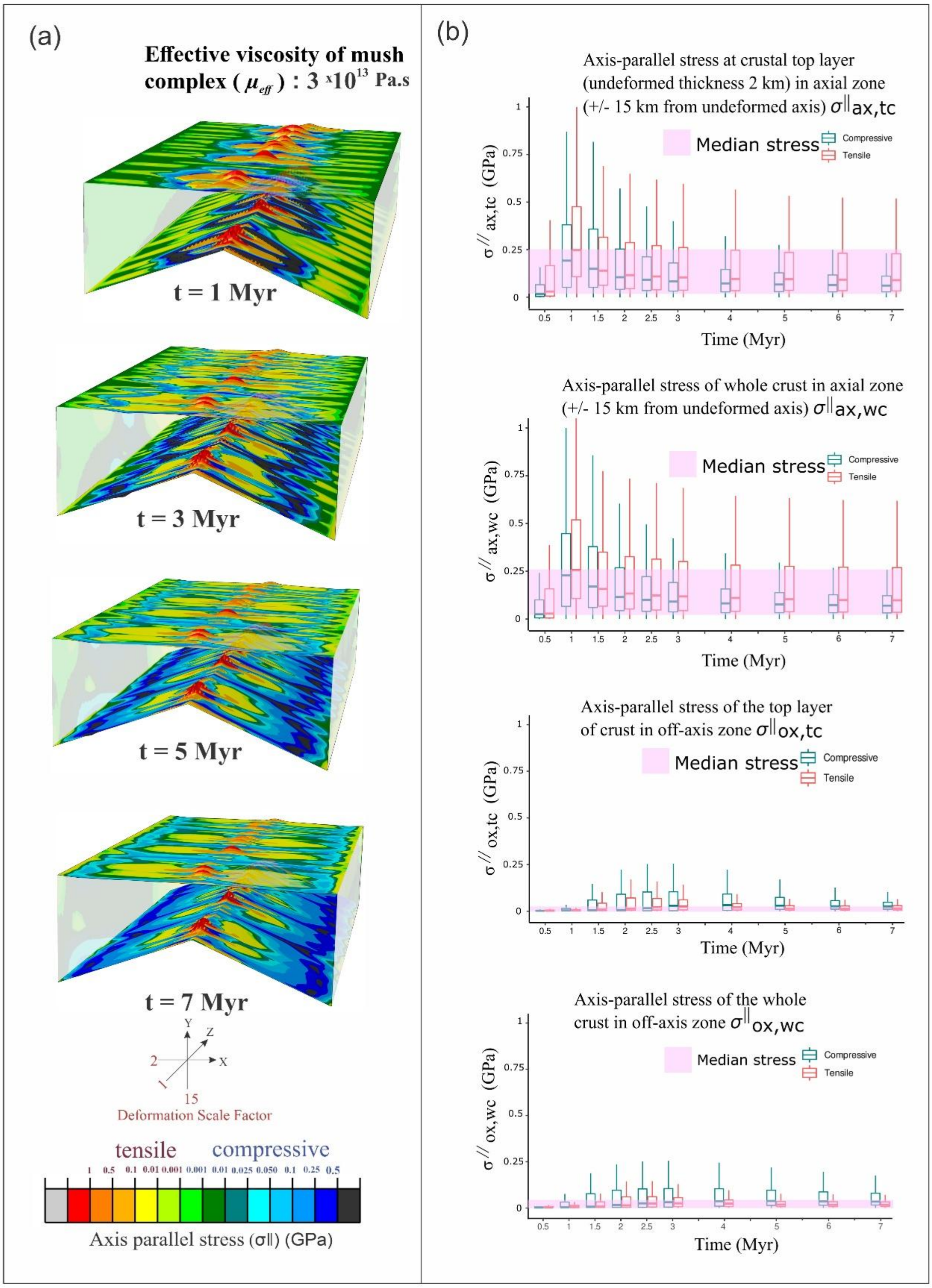

Figure 4.5 *3D contour plots of ridge-parallel stress ($\sigma^{\parallel}$) fields and their statistical (box-plots) representations. (a) Ridge-parallel stress ($\sigma^{\parallel}$)contours (σ_{zz} in Cartesian model frame) in model runs at 1, 3, 5, and 7 Myr. (b) Their statistical box-plots with the stress medians and quartiles.*

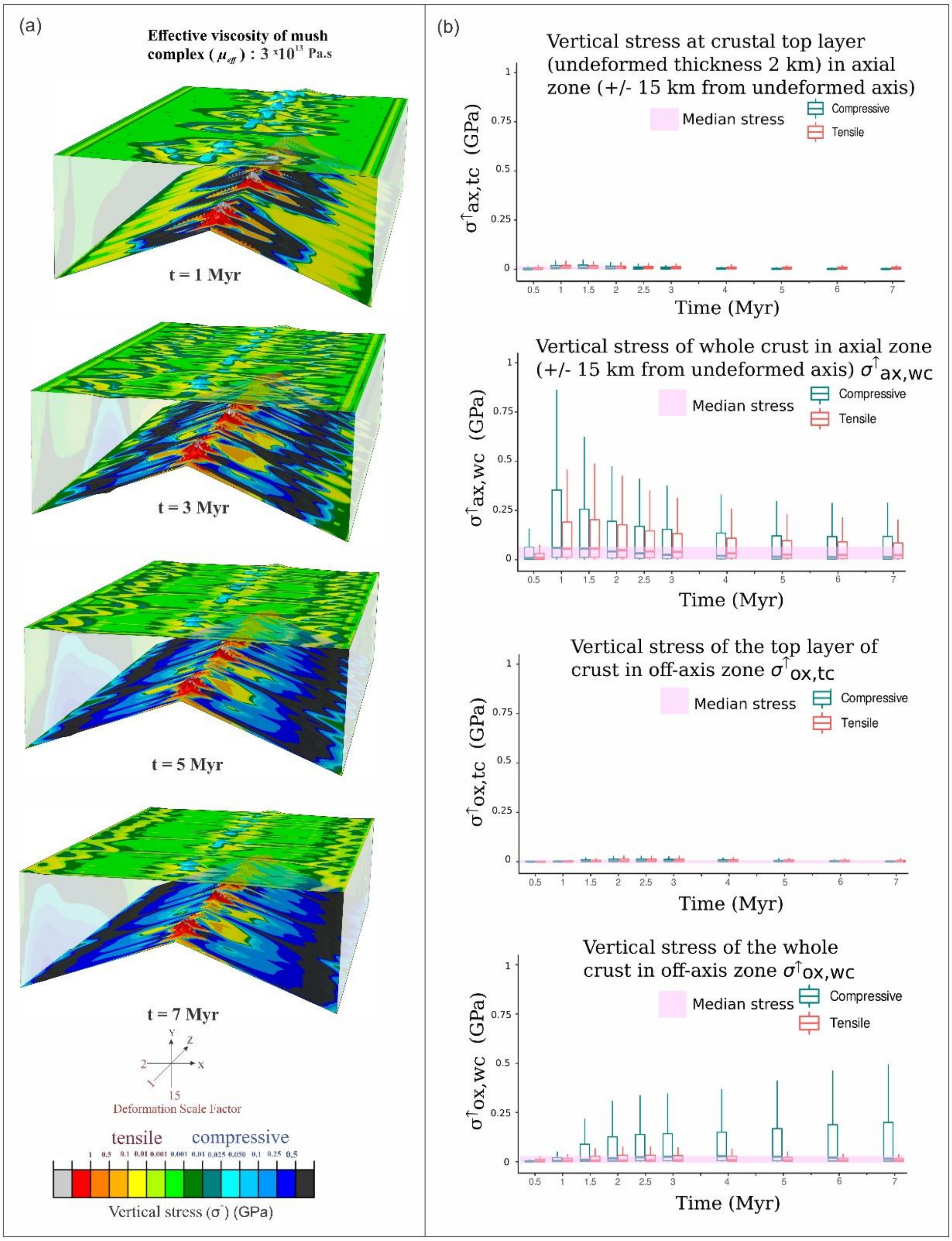

Figure 4.6 *A time series 3D analysis of the vertical stress and their statistical box-plots for different zones in Mid-Oceanic ridge. (a) Vertical stress ($\sigma^{\uparrow}$) contour (σ_{yy} in Cartesian model settings) plots from model runs at 1, 3, 5 and 7 Myr model run time (Model scales: vertical = 15, along-axis = 1, across-axis = 2) and transparent model views for visualization of the stress fields in both top and bottom layers. (b) Statistical box-plots of stresses in the axial zone, off axis zone, top-crustal layer, and whole-crust, showing their medians and quartiles.*

33 MPa, respectively at 3 – 4 Myr (Figure 4.5b). The whole-crust calculations yield a similar trend of tensile and compressional $\sigma^{//}$ in the off-axis regions with their peak values, 25 MPa and 37 MPa, gradually decreasing to 17 MPa and 34 MPa, respectively at 7 Myr. To summarize, the off-axis regions of a mature MOR concentrate along-axis compressive stress more in the deep-crustal layer than that in the top crustal layer, reflected from their median ratio, 1.36 at 7 Myr (Figure 4.5b).

The FSI model is used to also estimate the vertical stress ($\sigma^{\uparrow}$) component, controlled by both the MOR topography and the underlying mush flow dynamics. The magnitude of $\sigma^{\uparrow}$ is found to largely vary from the top to the bottom crustal boundary, setting in a steep stress gradient with depth in the crust. In the axial zones its median values for the top crustal layer show similar variations with time (Figure 4.6a): tensile $\sigma^{\uparrow} = +10$ MPa at 1 Myr and compressional $\sigma^{\uparrow} = -8.5$ MPa at 1.5 Myr, dropping to: +6.7 MPa and -4 MPa at 2.5, and further to +4 MPa and -1.2 MPa at 7 Myr), respectively. The whole crustal layer produces remarkably higher vertical stress (+50 MPa and -60 MPa at 1 Myr, decreasing with time to +42 MPa and -32 MPa at 2.5 Myr and further to +23 MPa and -14 MPa at 7 Myr). The variation of vertical stress with depth is exceptionally strong, as evident from the stress ratio between the top and the bottom boundaries (7 at 1 Myr and 5.7 at 7 Myr for tensile stress, and 7 at 1-1.5 Myr and 12 at 7 Myr for compressive stress), implying that the elastic crust completely attenuates the vertical stress within crust (Figure 4.6b). The off-axis regions develop a peak of the median of vertical stresses at around 3 Myr and thereafter stabilizes $\sigma^{\uparrow}$. In the top crustal layer, the median of the off-axis stress field is lower (+3.1 MPa and -3.7 MPa at 3 Myr, dropping down to +1.7 MPa and -1 MPa at 7 Myr) than that in the axial zones (Figure 4.6b). For the whole crustal layer, the stress medians show similar temporal variations (+7.8 MPa and -27 MPa at 4 Myr, decreasing to +4.8 MPa and -15 MPa at 7 Myr), and stress ratios between the top and the whole crustal layer (tensile $\sigma^{\uparrow}$: 2.5 at 3-4 Myr to 2.8 at 7 Myr, and compression $\sigma^{\uparrow}$: 7.3 at 4 Myr to 15 at 7 Myr) (Figure 4.6b).

The model shows several off-axis, deep-crustal regions with compressive vertical stresses significantly greater than the vertical tensile stress, which is evident from the high 75th percentiles in boxplots (Figure 4.6b). The axial zones in the top crustal layer contain discrete high compressive zones corresponding to hill topography, which is replaced by high tensile stress concentrations in the bottom layer beneath the hills. There are some across-axis narrow zones of compressive stress fields, separated by broad low stress zones in both top and bottom layers of the crust (Figure 4.6b), which signify segment boundaries in the MOR setting.

4.3.2. Ridge-transverse shear stress fields

Horizontal shear stresses ($\sigma^{\#}$) on across-ridge vertical planes reverse their shear sense periodically in the axial direction, forming alternate band structures of clockwise (dextral) and counter clockwise (sinistral) shear concentrations. Both the dextral and sinistral shear bands develop at an angle of around 45° to the ridge axis (Figures 4.7a-b), appearing mostly in the axial regions at initial stages of the model run. They retain their band structures with time, but reorient themselves at angles varying from 30° to 60° to the ridge axis, which further widen

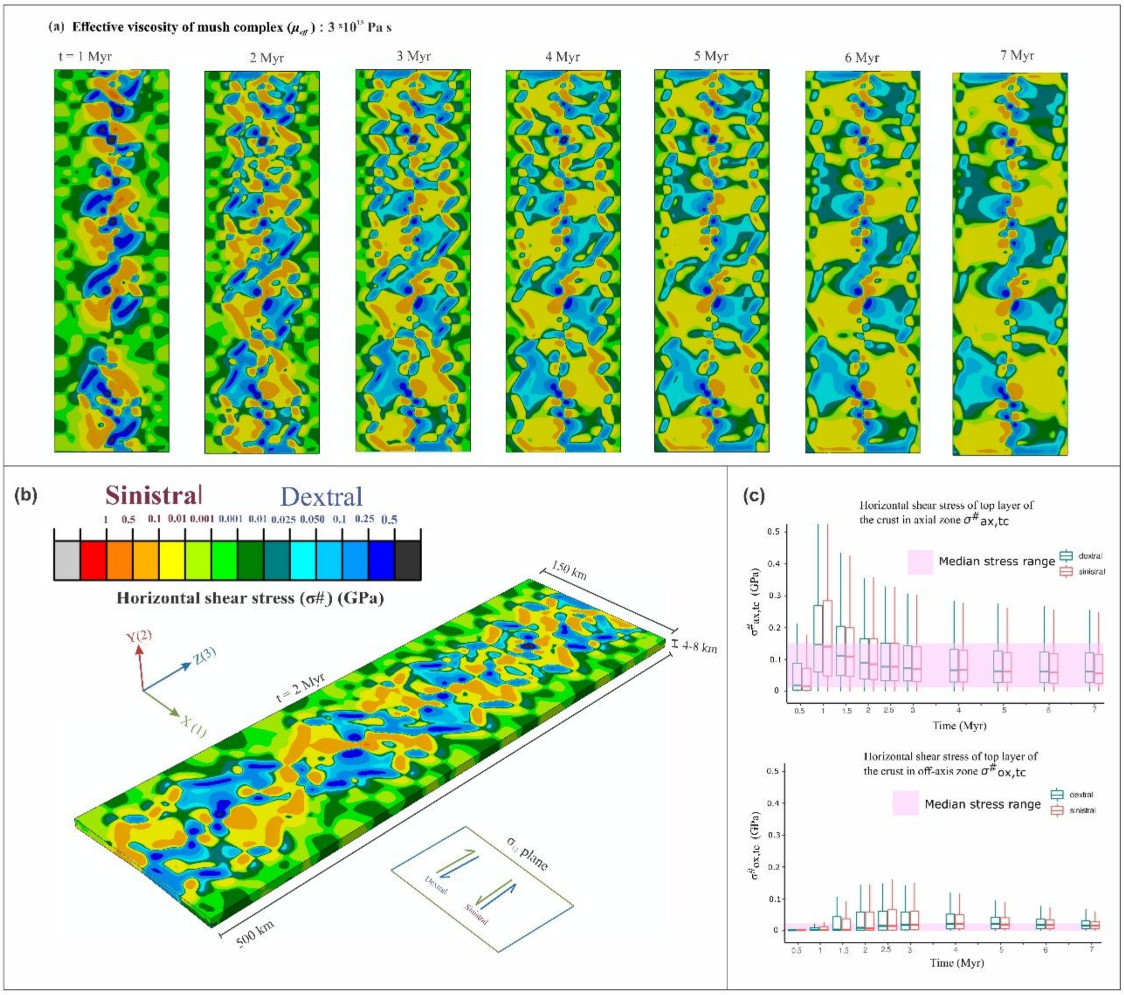

Figure 4.7 *A series of contour plots showing horizontal shear stresses ($\sigma^{\#}$) in MOR and their corresponding box-plot presentation. (a) Horizontal shear stress contours (σ_{xz} in Cartesian model settings) at 1, 2, 3, 4, 5, 6, and 7 Myr. Note counterclockwise (sinistral) and clockwise (dextral) stress patterns. (b) Three-dimensional presentations of the sinistral and dextral horizontal shear. (c) Statistical box-plots, showing the median values and their quartiles in the shear stress fields.*

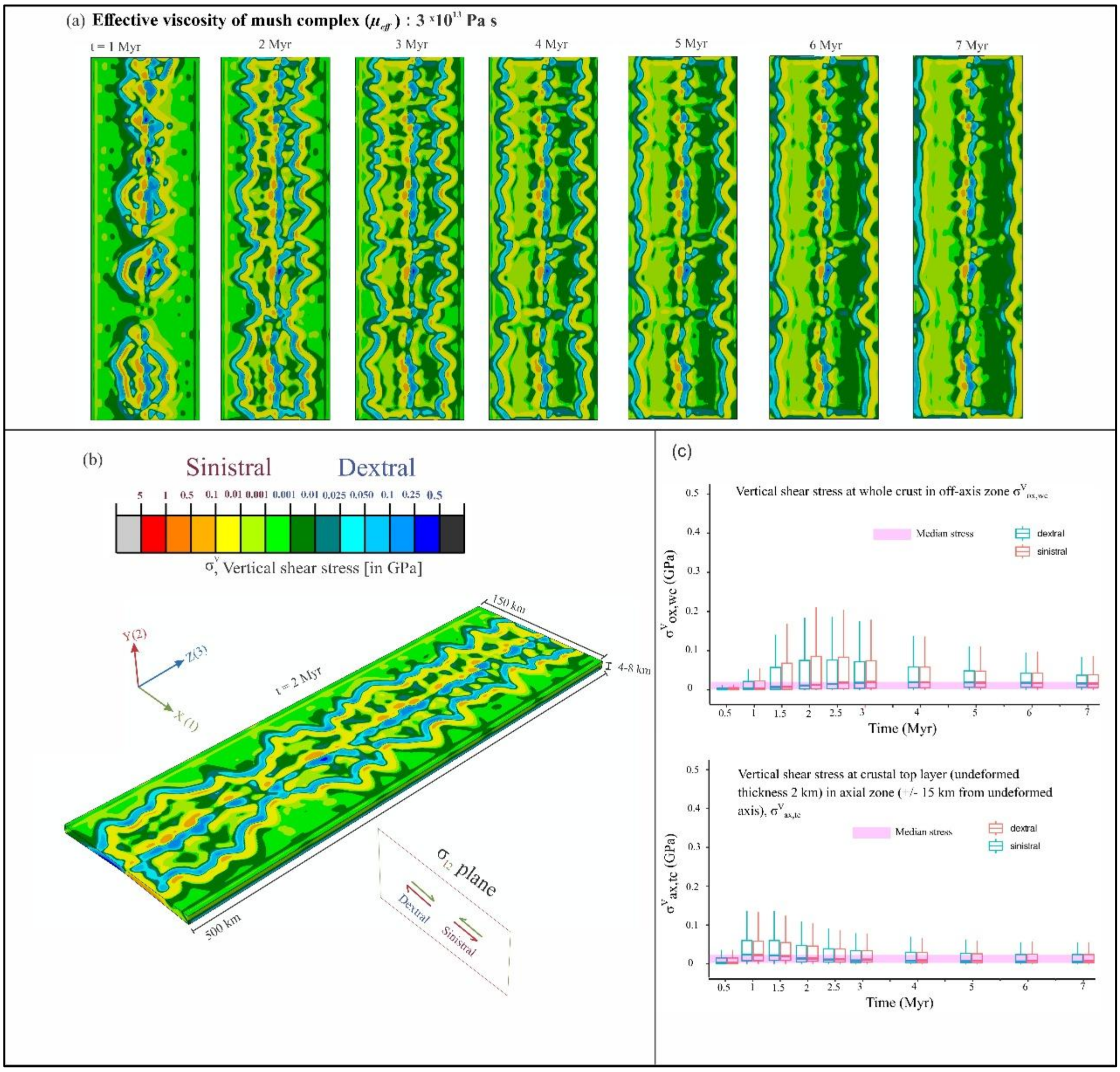

Figure 4.8 *Contour plots of the vertical shear stresses and the box-plots of the stresses in MOR. (a) Vertical shear stress (σ^V) contours (σ_{xy} in Cartesian model settings) obtained from model runs at 1, 2, 3, 4, 5, 6, and 7 Myr, with counterclockwise (sinistral) and clockwise (dextral) mapping to depict the dynamic evolution of vertical shear in the crust. (b) A contour plot in the three-dimensional model view at 2 Myr, showing sinistral and dextral vertical shear in a Cartesian model frame. (c) Corresponding statistical box-plots with the median stress values and their quartiles.*

this range to 20° -70°, especially in the off-axis regions (Figure 4.7a-b). Some of the shear bands transgress the ridge axis, keeping their lateral continuity on either side of the axis (Figure 4.7a). The boundaries between sinistral and dextral shear domains (marked by light green contours) are orthogonal to the ridge axis, giving rise to kinematic segmentation, which resembles those produced by transform faulting in natural MOR settings. Time-series model results show that the dextral and sinistral shear-stress domains in a young, 1 Myr old MOR are strongly heterogeneous in their size distributions, which evolves with time to reduce the heterogeneity, forming large shear domains at the cost of small ones at 7 Myr (Figure 4.7a).

Figure 4.7c presents a boxplot analysis to demonstrate varying dextral (positive) and sinistral (negative) shear stress magnitudes in the axial and off-axis regions obtained from the model runs. In the top crustal layer, their medians at the axial zone describe peaks values: +147 MPa and -140 MPa at 1 Myr, which progressively reduce to stable values: + 62 MPa and – 57 MPa at 7 Myr (Figure 4.7c). On the other hand, the off-axis regions show their lower peak values: +21 MPa and -21 MPa at 4 Myr, subsequently decreasing further to +17 MPa and +16 MPa at 7 Myr. A separate representation for vertical shear (σ^{v}) contours and boxplots is provided in Figure 4.8.

4.3.3. von-Mises stress analysis

von-Mises stress (σ^{vm}) in the upper crustal layer is calculated to show cumulative contributions of the three-dimensional stresses to MOR segmentation. The σ^{vm} contours in the axial region reveals a median with peaks at 500-700 MPa, which gradually drops to stable values of around 230-250 MPa at 7 Myr (Figure 4.9a). The σ^{vm} medians in off axis regions are significantly low (80-125 MPa). The stress median at axial zones reaches their peaks at 1 Myr (500 MPa at top-crustal layer and 680 MPa for the whole crust) and attain a steady state at 7 Myr (200 MPa at top-crustal layer and 220 MPa in case of whole crust) (Figure 4.9b). On the other hand, von-Mises stress Median at off axis zones peak at 3 Myr (80 MPa for the top crustal layer and 125 MPa for whole crust) and decrease nominally (75 MPa for top crustal layer and 109 MPa for whole crust) in the course of time (Figure 4.9b). Overall, von-Mises stresses contours suggest that axial zones failure could be generated by magmatic activity alone while off axis features could be triggered by magmatic activity, but associate plate movements may be needed to trigger faulting. It can also be inferred that cumulative shear is responsible for ridge-transverse orthogonal lengthy failures, as high von-Mises stress strip occurs in off axis regions away from the MOR axis.

4.3.4. Effect of crustal density on the stress distributions

This study investigated the influence of crustal density in controlling the stress distribution and topography of mid-ocean ridges (MOR). The crustal density was varied between 2400 and 2800 kg/m^3 to assess its impact on both stress distribution and ridge morphology. The von-Mises stress contours at 7 Myr of the top layer from our numerical simulations (Figure 4.10) revealed that the density variation in this range had negligibly small effects on the stress distributions and ridge structure. The findings suggest that the relationship between crustal density variation and von Mises stress is weak. The stress distribution and ridge

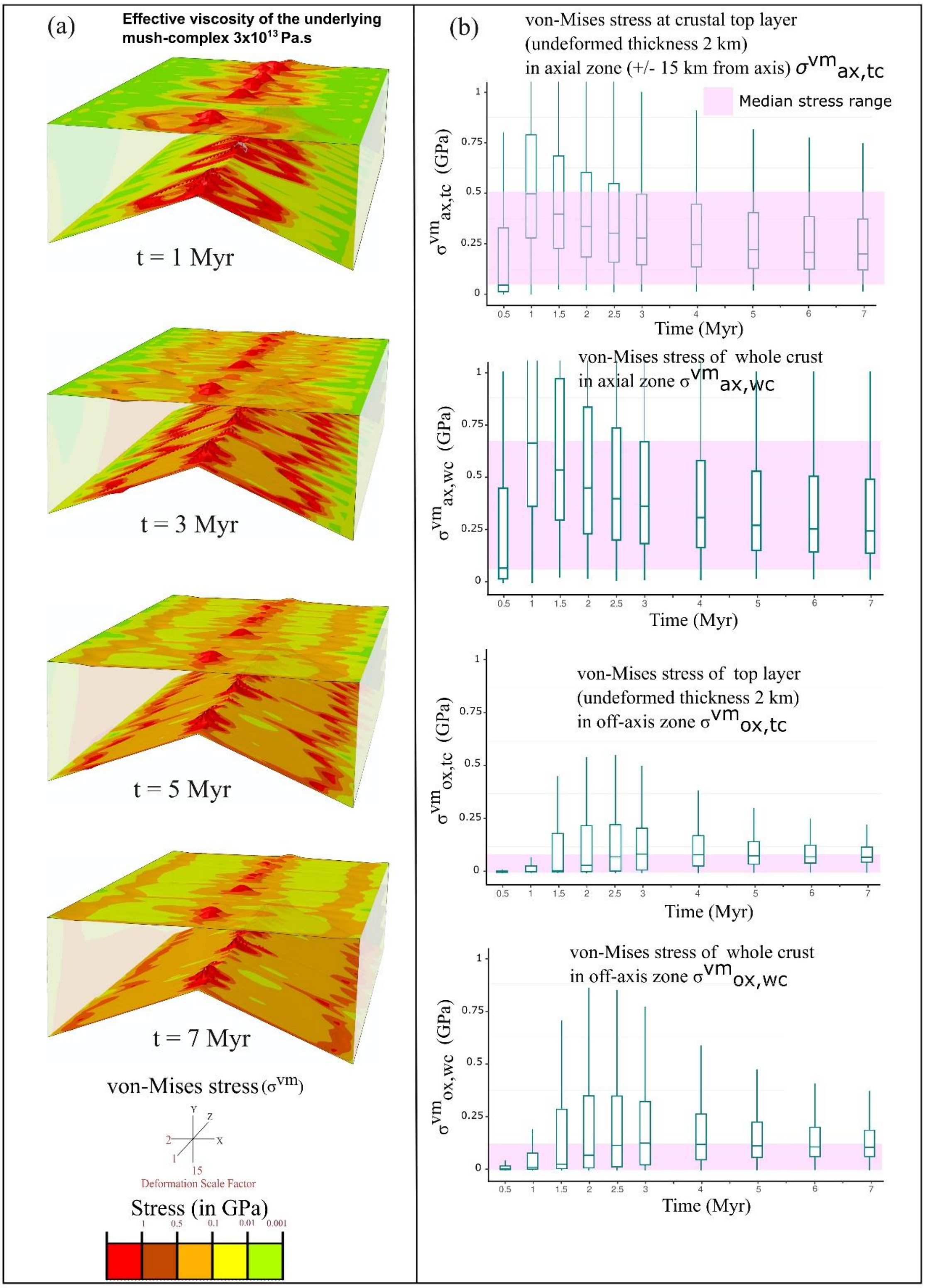

Figure 4.9 *A time series 3D contour plots for von-Misses stress and their statistical box-plots for different model MOR regimes. (a) von-Misses stress (σ^{vm}) contours for 1, 3, 5, and 7 Myr (Model scales: vertical = 15, along-axis = 1, across-axis = 2) and corresponding transparent representation, showing the stress fields in both the top and bottom layers. (b) Statistical box-plots of stresses in the axial zone, off-axis zone, top-crustal layer, and whole-crust, along with their medians and quartiles.*

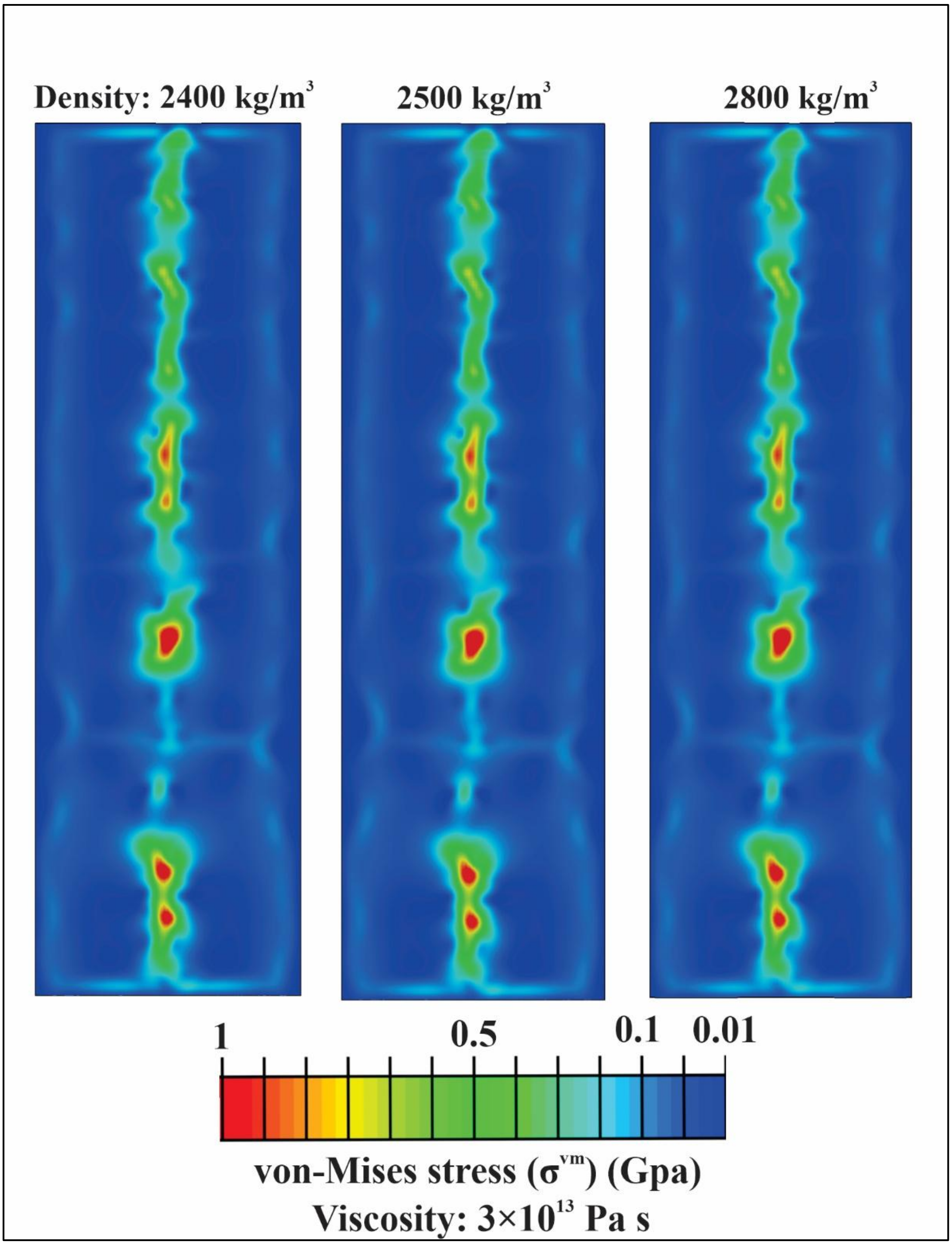

Figure 4.10 *von-Misses stress comparison between model simulations with three different crustal densities at 7 Myr. Contours show no significant differences.*

morphology is dominantly controlled by thermo-mechanical factors, such as mush convection, rather than the buoyancy forces related to density variations (detailed discussed in Chapter 3).

4.3.5. Model limitations

1) This fluid-solid interaction model excludes any thermal connection between the upper crust and the underlying mushy layer, which poses a limitation in this study. However, the effect of thermal stresses onto the overlying crust are likely to be effective in the short-wavelength morphological features, as indicated by earlier studies (e.g., Luttrel and Sandwell, 2012), or onset of features like transform faults (Choi et al., 2008). 2) The lateral boundaries of the model upper crust are set at large distances from the ridge axis, and any BC imposed thereby does not account for a given far-field influence, e.g., slab pull in the present model. 3) The fluid simulation incorporated a global divergence velocity, which is transmitted through the Neumann condition at the bottom of the overlying solid crust. However, the present modelling approach excludes any additional basal traction, e.g., localized slip to the crustal layer. The effect of such basal condition needs further investigation. 4) This study models the stress fields at MORs entirely within a mechanical framework, and does not account for any thermal effects of the underlying melt-bearing mushy zones on the physical properties of the crustal materials, which is another limitation of the present model results. Despite all these limitations, our mush-based model provides first-hand estimates of the 3D stress fields in MORs.

4.4. References

Abercrombie, R.E., Ekström, G., 2001. Earthquake slip on oceanic transform faults. Nature 410. https://doi.org/10.1038/35065064

Badia, S., Nobile, F., Vergara, C., 2008. Fluid-structure partitioned procedures based on Robin transmission conditions. J Comput Phys 227. https://doi.org/10.1016/j.jcp.2008.04.006

Baines, A.G., Cheadle, M.J., John, B.E., Grimes, C.B., Schwartz, J.J., Wooden, J.L., 2009. SHRIMP Pb/U zircon ages constrain gabbroic crustal accretion at Atlantis Bank on the ultraslow-spreading Southwest Indian Ridge. Earth Planet Sci Lett 287. https://doi.org/10.1016/j.epsl.2009.09.002

Barsanescu, P.D. and Comanici, A.M., 2017. von Mises hypothesis revised. Acta Mechanica, 228, pp.433-446. DOI : 10.1007/s00707-016-1706-2

Behn, M. D., & Grove, T. L. (2015). Melting systematics in mid-ocean ridge basalts: Application of a plagioclase-spinel melting model to global variations in major element chemistry and crustal thickness. *Journal of Geophysical Research: Solid Earth*, *120*(7). https://doi.org/10.1002/2015JB011885

Behn, M.D., Ito, G., 2008. Magmatic and tectonic extension at mid-ocean ridges: 1. Controls on fault characteristics. Geochemistry, Geophysics, Geosystems 9. https://doi.org/10.1029/2008GC001965

Behn, M.D., Lin, J., Zuber, M.T., 2002. Mechanisms of normal fault development at mid-ocean ridges. J Geophys Res Solid Earth 107. https://doi.org/10.1029/2001jb000503

Belytschko, T., 1980. Fluid-structure interaction. Comput Struct 12. https://doi.org/10.1016/0045-7949(80)90121-2

Bicknell, J.D., Sempere, J.C., Macdonald, K.C., Fox, P.J., 1987. Tectonics of a fast spreading center: A Deep-Tow and sea beam survey on the East Pacific rise at 19°30′ S. Mar Geophys Res (Dordr) 9. https://doi.org/10.1007/BF00338249

Brent, A.D., Voller, V.R., Reid, K.J., 1988. Enthalpy-porosity technique for modeling convection-diffusion phase change: Application to the melting of a pure metal. Numerical Heat Transfer 13. https://doi.org/10.1080/10407788808913615

Bruguier, N.J., Minshull, T.A., Brozena, J.M., 2003. Morphology and tectonics of the Mid-Atlantic Ridge, 7°-12°S. J Geophys Res Solid Earth 108. https://doi.org/10.1029/2001jb001172

Buck, W.R., Lavier, L.L., Poliakov, A.N.B., 2005. Modes of faulting at mid-ocean ridges. Nature 434. https://doi.org/10.1038/nature03358

Carbotte, S., Welch, S.M., MacDonald, K.C., 1991. Spreading rates, rift propagation, and fracture zone offset histories during the past 5 my on the Mid-Atlantic Ridge; 25°-

27°30′ S and 31°-34°30′ S. Mar Geophys Res (Dordr) 13. https://doi.org/10.1007/BF02428195

Castillo, P.R., Natland, J.H., Niu, Y., Lonsdale, P.F., 1998. Sr, Nd and Pb isotopic variation along the Pacific-Antarctic risecrest, 53-57°S: Implications for the composition and dynamics of the South Pacific upper mantle. Earth Planet Sci Lett 154. https://doi.org/10.1016/s0012-821x(97)00172-6

Cherkaoui, A.S., Wilcock, W.S., Dunn, R.A. and Toomey, D.R., 2003. A numerical model of hydrothermal cooling and crustal accretion at a fast spreading mid-ocean ridge. Geochemistry, Geophysics, Geosystems, 4(9). DOI: 10.1029/2001GC000215

Choi, E. seo, Lavier, L., Gurnis, M., 2008. Thermomechanics of mid-ocean ridge segmentation. Physics of the Earth and Planetary Interiors 171. https://doi.org/10.1016/j.pepi.2008.08.010

Cordery, M.J. and Morgan, J.P., 1993. Convection and melting at mid-ocean ridges. Journal of Geophysical Research: Solid Earth, 98(B11), pp.19477-19503. DOI : 10.1029/93JB01831

Craddock, J.P., Farris, D.W., Roberson, A., 2004. Calcite-twinning constraints on stress-strain fields along the Mid-Atlantic Ridge, Iceland. Geology 32. https://doi.org/10.1130/G19905.1

Crowley, J.W., Katz, R.F., Huybers, P., Langmuir, C.H., Park, S.H., 2015. Glacial cycles drive variations in the production of oceanic crust. Science (1979) 347. https://doi.org/10.1126/science.1261508

Dalton, C.A., Langmuir, C.H., Gale, A., 2014. Geophysical and geochemical evidence for deep temperature variations beneath mid-ocean ridges. Science (1979) 344. https://doi.org/10.1126/science.1249466

DeMets, C., Gordon, R.G., Argus, D.F., Stein, S., 1994. Effect of recent revisions to the geomagnetic reversal time scale on estimates of current plate motions. Geophys Res Lett 21. https://doi.org/10.1029/94GL02118

Dilek, Y., Furnes, H., 2011. Ophiolite genesis and global tectonics: Geochemical and tectonic fingerprinting of ancient oceanic lithosphere. Bulletin of the Geological Society of America 123. https://doi.org/10.1130/B30446.1

Eberle, M. A., & Forsyth, D. W. (1998). An alternative, dynamic model of the axial topographic high at fast spreading ridges. *Journal of Geophysical Research: Solid Earth*, *103*(6). https://doi.org/10.1029/98jb00437

Edmonds, M., Cashman, K. V., Holness, M., & Jackson, M. (2019). Architecture and dynamics of magma reservoirs. In *Philosophical Transactions of the Royal Society A: Mathematical, Physical and Engineering Sciences* (Vol. 377, Issue 2139). https://doi.org/10.1098/rsta.2018.0298

Faul, U.H., 2001. Melt retention and segregation beneath mid-ocean ridges. Nature, 410(6831), pp.920-923.

Fernández, M. A., & Moubachir, M. (2005). A Newton method using exact jacobians for solving fluid-structure coupling. *Computers and Structures*, *83*(2–3). https://doi.org/10.1016/j.compstruc.2004.04.021

Forsyth, D. W., Scheirer, D. S., Webb, S. C., Dorman, L. M., Orcutt, J. A., Harding, A. J., Blackman, D. K., Phipps Morgan, J., Detrick, R. S., Shen, Y., Wolfe, C. J., Canales, J. P., Toomey, D. R., Sheehan, A. F., Solomon, S. C., & Wilcock, W. S. D. (1998). Imaging the deep seismic structure beneath a mid-ocean ridge: The MELT experiment: The MELT seismic team. *Science*, *280*(5367). https://doi.org/10.1126/science.280.5367.1215

Fox, P.J., Grindlay, N.R., MacDonald, K.C., 1991. The Mid-atlantic Ridge (31°S-34°30′S): Temporal and spatial variations of accretionary processes. Mar Geophys Res (Dordr) 13. https://doi.org/10.1007/BF02428193

Freund, R., Merzer, M., 1976. The formation of rift valleys and their zigzag fault patterns. Geol Mag 113. https://doi.org/10.1017/S0016756800041315

Gartling, D.K., 1978. Finite element analysis of convective heat transfer problems with change of phase (No. SAND-77-2037C; CONF-780712-2). Sandia Labs., Albuquerque, N. Mex.(USA). OSTI ID:675873

Gerya, T.V., 2013. Three-dimensional thermomechanical modeling of oceanic spreading initiation and evolution. *Physics of the Earth and Planetary Interiors*, *214*, pp.35-52. https://doi.org/10.1016/j.pepi.2012.10.007

Giordano, D., Russell, J. K., & Dingwell, D. B., 2008**.** Viscosity of magmatic liquids: A model. *Earth and Planetary Science Letters*, 271(1-4), 123-134. DOI: 10.1016/j.epsl.2008.03.038

Goff, J.A., 1991. A global and regional stochastic analysis of near-ridge abyssal hill morphology. J Geophys Res 96. https://doi.org/10.1029/91jb02275

Gràcia, E., Bideau, D., Hekinian, R., Lagabrielle, Y., 1999. Detailed geological mapping of two contrasting second-order segments of the Mid-Atlantic Ridge between Oceanographer and Hayes fracture zones (33°30°N-35°N). J Geophys Res Solid Earth 104. https://doi.org/10.1029/1999jb900161

Grindlay, N.R., Fox, P.J., MacDonald, K.C., 1991. Second-order ridge axis discontinuities in the south Atlantic: Morphology, structure, and evolution. Mar Geophys Res (Dordr) 13. https://doi.org/10.1007/BF02428194

Gudmundsson, A., 1995. Stress fields associated with oceanic transform faults. Earth Planet Sci Lett 136. https://doi.org/10.1016/0012-821X(95)00164-8

Gudmundsson, A., 2003. Surface stresses associated with arrested dykes in rift zones. Bull Volcanol 65. https://doi.org/10.1007/s00445-003-0289-7

Hirth, G. & Kohlstedt, D. L., 1996. Water in the oceanic upper mantle: Implications for rheology, melt extraction, and the evolution of the lithosphere. *Earth and Planetary Science Letters*, 144(1-2), 93-108. DOI: 10.1016/0012-821X(96)00154-9

Hou, G., Wang, J., & Layton, A. (2012). Numerical methods for fluid-structure interaction - A review. In *Communications in Computational Physics* (Vol. 12, Issue 2). https://doi.org/10.4208/cicp.291210.290411s

Johan Lissenberg, C., MacLeod, C. J., & Bennett, E. N. (2019). Consequences of a crystal mush-dominated magma plumbing system: A mid-ocean ridge perspective. *Philosophical Transactions of the Royal Society A: Mathematical, Physical and Engineering Sciences*, *377*(2139). https://doi.org/10.1098/rsta.2018.0014

Karato, S.-i., & Wu, P., 1993. Rheology of the upper mantle: A synthesis. *Science*, 260(5109), 771-778. DOI: 10.1126/science.260.5109.771

Karson, J.A., Winters, A.T., 1992. Along-axis variations in tectonic extension and accommodation zones in the MARK Area, Mid-Atlantic Ridge 23°N latitude. Geol Soc Spec Publ 60. https://doi.org/10.1144/GSL.SP.1992.060.01.06

Katz, R.F., Spiegelman, M. and Langmuir, C.H., 2003. A new parameterization of hydrous mantle melting. Geochemistry, Geophysics, Geosystems, 4(9). DOI: 10.1029/2002GC000433

Keller, T. and Katz, R.F., 2016. The role of volatiles in reactive melt transport in the asthenosphere. *Journal of Petrology*, *57*(6), pp.1073-1108. DOI : 10.1093/petrology/egw030

Keller, T. and Katz, R.F., 2016. The role of volatiles in reactive melt transport in the asthenosphere. *Journal of Petrology*, *57*(6), pp.1073-1108. DOI : 10.1093/petrology/egw030

Kühn, D., Dahm, T., 2004. Simulation of magma ascent by dykes in the mantle beneath mid-ocean ridges. J Geodyn 38. https://doi.org/10.1016/j.jog.2004.06.002

Kuo, B.Y., Forsyth, D.W., 1988. Gravity anomalies of the ridge-transform system in the South Atlantic between 31 and 34.5° S: Upwelling centers and variations in crustal thickness. Mar Geophys Res (Dordr) 10. https://doi.org/10.1007/BF00310065

Langmuir, C.H., Klein, E.M. and Plank, T., 1992. Petrological systematics of mid-ocean ridge basalts: constraints on melt generation beneath ocean ridges. *Geophysical monograph series*, *71*, pp.183-280. DOI : 10.1029/GM071p0183

Lissenberg, C.J., MacLeod, C.J. and Bennett, E.N., 2019. Consequences of a crystal mush-dominated magma plumbing system: a mid-ocean ridge perspective. Philosophical

Transactions of the Royal Society A, 377(2139), p.20180014. DOI : 10.1098/rsta.2018.0014

Lonsdale, P., 1994. Geomorphology and structural segmentation of the crest of the southern (Pacific-Antarctic) East Pacific Rise. J Geophys Res 99. https://doi.org/10.1029/93JB02756

Luttrell, K., Sandwell, D., 2012. Constraints on 3-D stress in the crust from support of mid-ocean ridge topography. J Geophys Res Solid Earth 117. https://doi.org/10.1029/2011JB008765

Macdonald, K.C., 1977. Near-bottom magnetic anomalies, asymmetric spreading, oblique spreading, and tectonics of the Mid-Atlantic Ridge near lat 37°N. Bulletin of the Geological Society of America 88. https://doi.org/10.1130/0016-7606(1977)88<541:NMAASO>2.0.CO;2

Macdonald, K.C., Fox, P.J., Perram, L.J., Eisen, M.F., Haymon, R.M., Miller, S.P., Carbotte, S.M., Cormier, M.H., Shor, A.N., 1988. A new view of the mid-ocean ridge from the behaviour of ridge-axis discontinuities. Nature. https://doi.org/10.1038/335217a0

Maia, M., Sichel, S., Briais, A., Brunelli, D., Ligi, M., Ferreira, N., Campos, T., Mougel, B., Brehme, I., Hémond, C., Motoki, A., Moura, D., Scalabrin, C., Pessanha, I., Alves, E., Ayres, A., Oliveira, P., 2016. Extreme mantle uplift and exhumation along a transpressive transform fault. Nat Geosci 9. https://doi.org/10.1038/ngeo2759

Mandal, N., Sarkar, S., Baruah, A., Dutta, U., 2018. Production, pathways and budgets of melts in mid-ocean ridges: An enthalpy based thermo-mechanical model. Physics of the Earth and Planetary Interiors 277. https://doi.org/10.1016/j.pepi.2018.01.008

Mckenzie, D. (1984). The generation and compaction of partially molten rock. *Journal of Petrology*, *25*(3). https://doi.org/10.1093/petrology/25.3.713

Mckenzie, D., & Bickle, M. J. (1988). The volume and composition of melt generated by extension of the lithosphere. *Journal of Petrology*, *29*(3). https://doi.org/10.1093/petrology/29.3.625

Mildren, S.D., Hillis, R.R., 2000. In situ stresses in the southern Bonaparte Basin, Australia: Implications for first- and second-order controls on stress orientation. Geophys Res Lett 27. https://doi.org/10.1029/2000GL011537

Moos, D., Zoback, M.D., 1990. Utilization of observations of well bore failure to constrain the orientation and magnitude of crustal stresses: application to continental, Deep Sea Drilling Project, and Ocean Drilling Program boreholes. J Geophys Res 95. https://doi.org/10.1029/JB095iB06p09305

Morgan, J.P., Parmentier, E.M., 1984. Lithospheric stress near a ridge-transform intersection. Geophys Res Lett 11. https://doi.org/10.1029/GL011i002p00113

Neves, M.C., Bott, M.H.P., Searle, R.C., 2004. Patterns of stress at midocean ridges and their offsets due to seafloor subsidence. Tectonophysics 386. https://doi.org/10.1016/j.tecto.2004.06.010

Newmark, R.L., Zoback, M.D., Anderson, R.N., 1984. Orientation of in situ stresses in the oceanic crust. Nature 311. https://doi.org/10.1038/311424a0

Niu, Y., 1997. Mantle melting and melt extraction processes beneath ocean ridges: evidence from abyssal peridotites. *Journal of Petrology*, *38*(8), pp.1047-1074.

Nobile, F., & Vergara, C. (2007). An effective fluid-structure interaction formulation for vascular dynamics by generalized Robin conditions. *SIAM Journal on Scientific Computing*, *30*(2). https://doi.org/10.1137/060678439

Oldenburg, D.W., 1975. A Physical Model for the Creation of the Lithosphere. Geophysical Journal of the Royal Astronomical Society 43. https://doi.org/10.1111/j.1365-246X.1975.tb00642.x

Olive, J.A., Dublanchet, P., 2020. Controls on the magmatic fraction of extension at mid-ocean ridges. Earth Planet Sci Lett 549. https://doi.org/10.1016/j.epsl.2020.116541

Ondréas, H., Aslanian, D., Géli, L., Olivet, J.L., Briais, A., 2001. Variations in axial morphology, segmentation, and seafloor roughness along the Pacific-Antarctic Ridge between 56°S and 66°S. J Geophys Res Solid Earth 106. https://doi.org/10.1029/2000jb900394

Parnell-Turner, R., Sohn, R.A., Peirce, C., Reston, T.J., MacLeod, C.J., Searle, R.C., Simão, N.M., 2017. Oceanic detachment faults generate compression in extension. Geology 45. https://doi.org/10.1130/G39232.1

Patankar, S. V., 1980. Numerical heat transfer and fluid flow. https://doi.org/10.13182/nse81-a20112

Persaud, P., Tan, E., Contreras, J., Lavier, L., 2017. A bottom-driven mechanism for distributed faulting in the Gulf of California rift. Tectonophysics 719–720. https://doi.org/10.1016/j.tecto.2016.11.024

Pockalny, R.A., Gente, P., Buck, R., 1996. Oceanic transverse ridges: A flexural response to fracture-zone-normal extension. Geology 24. https://doi.org/10.1130/0091-7613(1996)024<0071:OTRAFR>2.3.CO;2

Pollard, D.D., Aydin, A., 1984. PROPAGATION AND LINKAGE OF OCEANIC RIDGE SEGMENTS. J Geophys Res 89. https://doi.org/10.1029/JB089iB12p10017

Presnall, D. C., Gudfinnsson, G. H., & Walter, M. J. (2002). Generation of mid-ocean ridge basalts at pressures from 1 to 7 GPa. *Geochimica et Cosmochimica Acta*, *66*(12). https://doi.org/10.1016/S0016-7037(02)00890-6

Ricard, Y., Šrámek, O., Dubuffet, F., 2009. A multi-phase model of runaway core-mantle segregation in planetary embryos. Earth Planet Sci Lett 284. https://doi.org/10.1016/j.epsl.2009.04.021

Richardson, R.M., Solomon, S.C., Sleep, N.H., 1979. Tectonic stress in the plates. Reviews of Geophysics. https://doi.org/10.1029/RG017i005p00981

Rundquist, D. V., Sobolev, P.O., 2002. Seismicity of mid-oceanic ridges and its geodynamic implications: A review. Earth Sci Rev. https://doi.org/10.1016/S0012-8252(01)00086-1

Sandwell, D.T., 1986. Thermal stress and the spacings of transform faults. J Geophys Res 91. https://doi.org/10.1029/jb091ib06p06405

Sarkar, S., Baruah, A., Dutta, U., Mandal, N., 2014. Role of random thermal perturbations in the magmatic segmentation of mid-oceanic ridges: Insights from numerical simulations. Tectonophysics 636. https://doi.org/10.1016/j.tecto.2014.08.008

Sen, J., Sarkar, S., & Mandal, N. (2023). Control of mush complex viscosity on mid-ocean ridge topography: A fluid–structure model analysis. *Physics of Fluids*, *35*(6). https://doi.org/10.1063/5.0152667

Sibrant, A.L.R., Mittelstaedt, E., Davaille, A., Pauchard, L., Aubertin, A., Auffray, L., Pidoux, R., 2018. Accretion mode of oceanic ridges governed by axial mechanical strength. Nat Geosci 11. https://doi.org/10.1038/s41561-018-0084-x

Sim, S.J., Spiegelman, M., Stegman, D.R. and Wilson, C., 2020. The influence of spreading rate and permeability on melt focusing beneath mid-ocean ridges. *Physics of the Earth and Planetary Interiors*, *304*, p.106486. DOI:10.31223/osf.io/uw7dn

Singh, S. C., Crawford, W. C., Carton, H., Seher, T., Combier, V., Cannat, M., Canales, J. P., Düsünür, D., Escartin, J., & Miranda, J. M. (2006). Discovery of a magma chamber and faults beneath a Mid-Atlantic Ridge hydrothermal field. *Nature*, *442*(7106). https://doi.org/10.1038/nature05105

Singh, S.C., Kent, G.M., Collier, J.S., Harding, A.J., Orcutt, J.A., 1998. Melt to mush variations in crustal magma properties along the ridge crest at the southern East Pacific Rise. Nature 394. https://doi.org/10.1038/29740

Sinton, J. M., & Detrick, R. S. (1992). Mid-ocean ridge magma chambers. *Journal of Geophysical Research*, *97*(B1). https://doi.org/10.1029/91JB02508

Sohn, R.A., Sims, K.W.W., 2005. Bending as a mechanism for triggering off-axis volcanism on the East Pacific Rise. Geology 33. https://doi.org/10.1130/G21116.1

Solomon, S.C., Huang, P.Y., Meinke, L., 1988. The seismic moment budget of slowly spreading ridges. Nature 334. https://doi.org/10.1038/334058a0

Sparks, R. S. J., Annen, C., Blundy, J. D., Cashman, K. V., Rust, A. C., & Jackson, M. D. (2019). Formation and dynamics of magma reservoirs. In *Philosophical Transactions of the Royal Society A: Mathematical, Physical and Engineering Sciences* (Vol. 377, Issue 2139). https://doi.org/10.1098/rsta.2018.0019

Turcotte, D.L., 1974. Are transform faults thermal contraction cracks? J Geophys Res 79. https://doi.org/10.1029/jb079i017p02573

Turner, A.J., Katz, R.F., Behn, M.D., 2015. Grain-size dynamics beneath mid-ocean ridges: Implications for permeability and melt extraction. Geochemistry, Geophysics, Geosystems 16. https://doi.org/10.1002/2014GC005692

Voller, V.R., Prakash, C., 1987. A fixed grid numerical modelling methodology for convection-diffusion mushy region phase-change problems. Int J Heat Mass Transf 30. https://doi.org/10.1016/0017-9310(87)90317-6

Yongshun Chen, Morgan, W.J., 1990. A nonlinear rheology model for mid-ocean ridge axis topography. J Geophys Res 95. https://doi.org/10.1029/jb095ib11p17583

Chapter 5 | First-order surface topography of Peninsular India: a dynamic analysis

5.1. Preamble

Surface topography and associated drainage patterns in continents result from a combination of endogenous (e.g., crustal deformations) and exogenous (e.g., surface erosion) Earth processes operating across a wide range of geological time scales (from kilo to million years). These processes typically manifest in large-scale, first-order physiographic features with distinctive river systems, as observed in Peninsular India (IP) (Figure. 5.1). Understanding how topography responds to tectonic forces is thus a crucial concern in interpreting the surface architecture of large continents like India that controls their long-term landscape evolution, drainage patterns, and sediment accumulation in basins (Bishop, 2007; Ellis et al., 1999; Kirby and Whipple, 2012; Mandal et al., 2015; Minár et al., 2020; Ruetenik et al., 2016; Stolar et al., 2007; Tucker, 2015; Tucker and Hancock, 2010; Whipple and Meade, 2004; Whipple, 2009). Recent studies have developed various tectonic models to explain the evolution of major continental-scale topographic elements, such as mountain ranges, elevated plateaus, foreland basins, fore-arcs, and deep oceanic trenches, as surface expressions of plate kinematics. A well-established example is the Tibetan Plateau, one of Earth's most significant planetary features, which has grown to attain an average elevation of about 5 km in course of the ongoing India-Asia convergence (DeCelles et al., 2007; Ding et al., 2022; Fang et al., 2020; Maiti et al., 2021). This convergence also led to the rise of the Himalayan Mountain range, setting in a southward topographic slope of approximately 3° in the extra-Peninsular region of India (Copley and Mckenzie, 2007; Houseman and England, 1993; Mandal et al., 2015). While substantial progress has taken place in tectonic modeling of the Himalaya-Tibet Mountain system, the vast Peninsular Plateau, covering much of the southern part of India, has remained largely unexplored from a geodynamical perspective. This plateau lies in a tectonically stable region, as indicated by the low frequency of seismic activity in the present day as well as geologically recent past (Asish et al., 2016; Chandra, 1977; Jaiswal and Sinha, 2007; Rao and Rao, 1984). Its geographical features: a pronounced eastward topographic slope and a spectacular eastward drainage flow, present an intriguing scenario (Figure. 5.1). Interestingly, the eastward surface slope appears largely independent of the N-S India-Asia convergence tectonics. The origin of this continental-scale topographic tilt remains unclear, although several hypotheses, diverse in their conceptual frameworks, have been proposed (Campanile et al., 2008; Collier et al., 2008; Cox, 1989; Gunnell andFleitout, 1998; Kailasam, 1975; Mandal et al., 2015; Pandey et al., 1996; Radhakrishna, 1993; Richards et al., 2016; Valdiya, 2001; Vita-Finzi, 2004; Watts and Cox, 1989; White and McKenzie, 1989; Whiting et al., 1994).

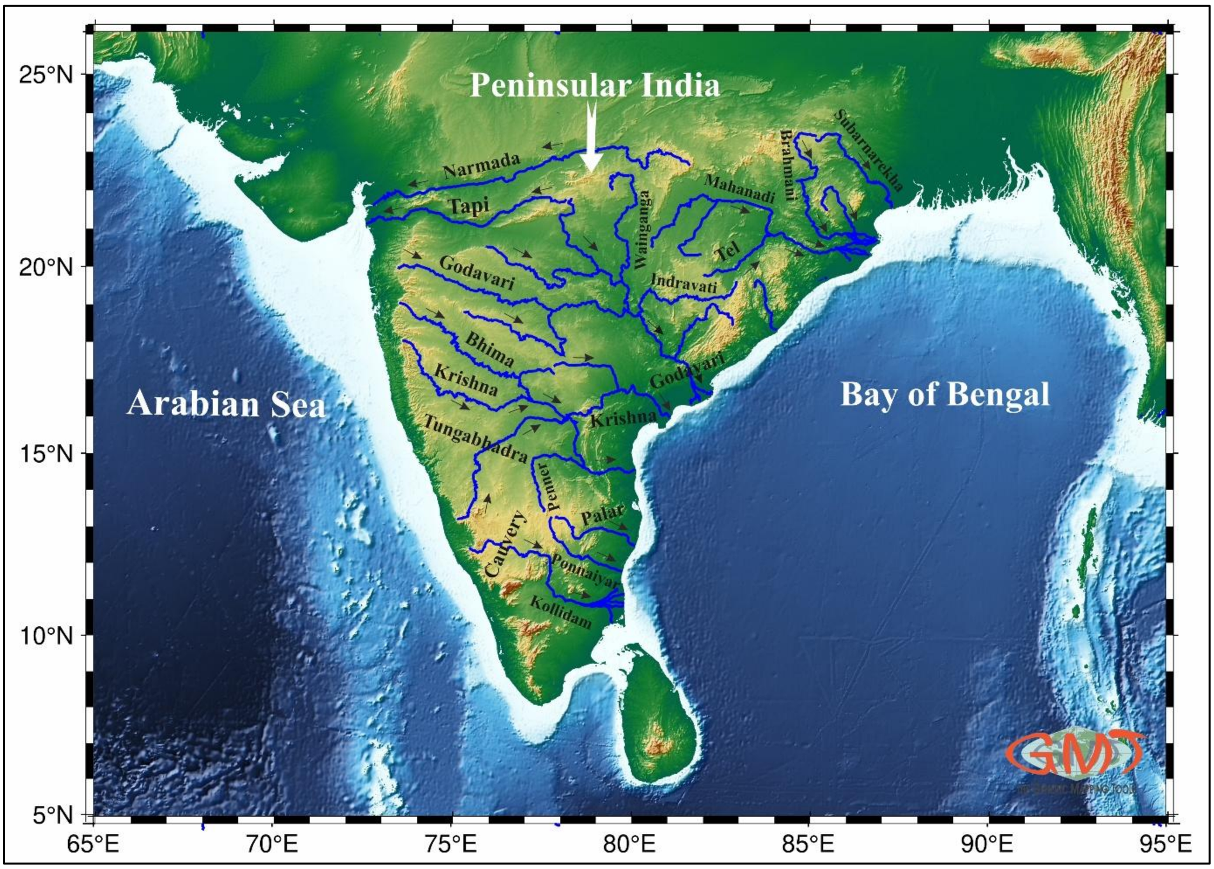

Figure 5.1 *Eastward River flow patterns in Indian peninsula (IP). The major rivers shown here include Narmada (Nar), Tapi (Tap), Godavari (God), Bhima (Bhi), Krishna (Kri), Tungabhadra (Tun), Cauvery (Cau), Ponnaiyar (Pon), Palar (Pal), Mahanadi (Mah), Tel (Tel), Indravati (Ind), Bhavani (Bha), Pennar (Pen), and Kollidam (Kol). The river system extends from the Arabian Sea on the west to the Bay of Bengal on the east, constituting the main regional water resources in IP. The eastward decrease in topographic elevation grossly conforms to the river flow directions. The drainage system depicted in the map excludes extra peninsular rivers. The map is developed by using the Generic Mapping Tools (GMT).*

The distinctive asymmetric topography of the Indian peninsular plateau has sparked an ongoing debate, primarily focused on its age and the factors responsible for the persistent eastward slope. One of the most influential propositions in this discussion claims that the Western Ghats escarpment is the remnant of a past rifting and magmatic event around 65 million years ago, which subsequently formed a passive continental margin that presently defines the ~1600 km long Western boundary of the Peninsular Indian landmass (Cox, 1989; Pandey et al., 1996; White and McKenzie, 1989). In contrast, an alternative perspective, based on tectonic evidence, attributes the current asymmetric physiography to more recent neotectonic activities (Valdiya, 2001; Vita-Finzi, 2004). Continued research for exploring the mechanisms of this landscape topography deepen the intriguing issues further. Some authors have proposed a flexural response model, claiming that the elevation at the western coastline could be a consequence of combined onshore denudation and offshore sedimentary loading (Campanile et al., 2008; Gunnell et al., 2003; Gunnell and Fleitout, 1998; White and McKenzie, 1989; Whiting et al., 1994). Another hypothesis posits that regional epirogenic uplift, driven by thermal anomalies in the convecting mantle, could be a contributing factor (Kailasam, 1975; Radhakrishna, 1993; Richards et al., 2016). These competing theories lead to divergent views on the temporal and spatial dimensions of uplift and tilting, though none provides a comprehensive explanation that lines up with the broader geodynamic context of peninsular India.

The problem of the eastwardly tilted peninsular topographic development, with an about 1,500 meters elevation at the Western Ghats escarpment (Richards et al., 2016), opened up geodynamic studies from the perspective of Indian plate reconstructions. From residual depth anomaly measurements, it has been shown that the tilt extends into the adjacent oceanic part of the plate, resulting in residual depths at the east lower than that at the west (Hoggard et al., 2016; Richards et al., 2016). This analysis finds this tilt as a remarkably long-wavelength topographic feature extending over 2,000 kilometers. Cox (1989) suggested that the long-wavelength topography and its resulting drainage pattern in the Indian subcontinent took their shapes during the Paleogene era when the Seychelles region separated from the western margin due to a mantle plume. However, more recent data suggest that any elevated terrain formed during the Deccan volcanic activity underwent rapid denudation, leading to a much-reduced topographic relief by the beginning of the Neogene period (Dole et al., 2022). During the Eocene and Oligocene epochs, extensive lateritic deposits were formed along both the continental margins, as reported by Bonnet et al., (2014), (2016), and others. This laterite formation, in conjunction with evidence from paleoclimatic proxies, points to a low-relief, wet, and tropical climate in peninsular India during this time (Chatterjee et al., 2013; Kent and Muttoni, 2008; Thorne et al., 2012). These findings are further supported by shifts in laterite formation patterns and sedimentation types, suggesting the denudation event approximately 23 million years ago (Raju, 2008). An alternative hypothesis accounts for the relative horizontal motion between the Indian plate and its underlying mantle as a possible factor controlling the long-wavelength tilting. Notably, some studies (Morgan and Smith, 1992; Russo and Silver, 1994) consider the role of subducting slab-driven westward return flows in the asthenosphere

(Becker, 2017), covering 2,000 kilometers from the Sunda trench at the eastern extremity of the Indian plate (Steckler et al., 2016). This proposition is supported by station-averaged SKS splits (Becker et al., 2012), claiming that an SSW-directed asthenospheric flow sets in the topographic gradient in peninsular India. In contrast, several geophysical studies report NNE-SSW oriented seismic mantle anisotropy, which is interpreted to be a consequence of the northward mantle flow beneath peninsular India (Heintz et al., 2009; Illa et al., 2021; Kumar et al., 2015; Mandal, 2011; Roy et al., 2024; Roy et al., 2012). This kinematic condition, however, appears to have little impact on the eastward topographic tilt. On the other hand, the role of active tectonic deformations in the development of this topographic tilt remains uncertain for several reasons. First, the level of background seismic activity in the region is relatively low, with large-magnitude earthquakes ($Mb \geq 6$) being infrequent (Gangrade and Arora, 2000; Jaiswal and Sinha, 2007; Maurya et al., 2016; Saha et al., 2020). Moreover, seismic events tend to localize in the Proterozoic mobile belts, which are obliquely oriented relative to the tilt axis (Copley et al., 2014; Valdiya, 2001; Veeraswamy and Raval, 2005; Widdowson and Mitchell, 1999). Focal mechanisms along the western seaboard typically exhibit extensional characteristics, while those along the continental interior and eastern seaboard suggest strike-slip dynamics (Müller et al., 2015; Yamato et al., 2013). Taken together, these various lines of evidence suggest that the origin of the eastward topographic tilt in peninsular India remains an unresolved question, especially in the perspective of a geodynamic issue.

This chapter embarks on this topographic problem of peninsular India in light of isostatic dynamics, integrating a detailed analysis of the E-W topographic profiles and those obtained from a geodynamic model of the Indian plate tectonic setting. It is demonstrated from model simulations that the contrasting physical properties of the oceanic lithospheres below the Bay of Bengal and the Arabian Sea on the eastern and the western flanks of peninsular India have modulated the eastward-sloping asymmetric topographic development in peninsular India. This topographic gradient has driven all the major peninsular rivers to drain across the entire continental craton and ultimately fall into the Bay of Bengal.

5.2. Indian Peninsular Plateau

5.2.1. Geology of Peninsular India

Indian peninsular landmass comprises several Precambrian cratons, including the Dharwar, Singhbhum, Bundelkhand, and Bastar, which stabilized during the Archaean time through repeated tectonic cycles of magmatism, metamorphism, and crustal differentiation (Dey and Moyen, 2020; Jayananda et al., 2020, 2023; Saha and Mazumder, 2012) (Figure. 5.2). The Dharwar Craton (DC), which is one of the oldest, geologically significant cratonic blocks is constituted by Archean rocks of ages spanning from 3.6 to 2.5 Ga (Chadwick et al., 2000; Brian Chadwick et al., 1997; Krapež et al., 2020; Prabhakar et al., 2009). The DC is divided into two parts: the Western Dharwar Craton (WDC) and the Eastern Dharwar Craton (EDC), separated by the Chitradurga shear zone (Figure. 5.2). The WDC consists of low-grade greenstone belts, including volcanic and sedimentary sequences, and tonalite-trondhjemite-granodiorite (TTG) gneisses, which represent some of the Earth's earliest crust (Boraiaha, 2022; Ranjan et al., 2020; Wang et al., 2023). The EDC, in contrast, features high-grade gneisses, granitoids, and younger supracrustal rocks, indicating a more dynamic and thermally active evolution (Goswami et al., 2023; Mohan et al., 2020, 2013; Talukdar et al., 2018). The tectono-metamorphic history of the DC evolved through multiple episodes of crustal growth, accretion, and stabilization (Chadwick et al., 2000; Krapež et al., 2020; Prabhakar et al., 2009). The Singhbhum Craton (SC) is a spectacular Archaean block in eastern India, which is a mosaic of granitoids, greenstone belts, and banded iron formations (BIFs) belonging to the Iron Ore Group (Figure. 5.2). The SC show evidence of tectonic and magmatic processes during the Mesoarchaean to Neoarchaean periods (Hofmann et al., 2022). The Bastar Craton (BC) in central India is an adjoining Precambrian craton, bordered by the Satpura Mobile Belt and the Eastern Ghats (Figure. 5.2). The BC hosts ancient supracrustal sequences, such as the Sakoli and Sausar groups (Mohanty, 2021; Mondal et al., 2006; Saha and Deb, 2014), which have undergone significant metamorphism and deformation (Mohanty, 2021; Mondal et al., 2006; Saha and Deb, 2014).

These cratons collectively form the spatially vast basement of Indian Peninsula, intervened by isolated Proterozoic sedimentary basins, which are correlated with the rifting during breakup of the supercontinents: Columbia, Rodinia, and Gondwana. The Vindhyan, Cuddapah, and Chhattisgarh basins, known as "Purana basins", (Figure. 5.2) hold sedimentary sequences deposited in rift-controlled environments (Bose et al., 2015; Miall et al., 2015; Singh and Mishra, 2002). The Vindhyan Basin, for instance, records over a billion years of sedimentation, including fluvial and shallow marine deposits, reflecting tectonic stability and prolonged sediment accumulation during the Mesoproterozoic to Neoproterozoic (Bose et al., 2015; Miall et al., 2015). The Eastern Ghats Mobile Belt (EGMB) represents one of the most tectonically active regions of Peninsular India (Figure. 5.2), comprising high-grade metamorphic rocks, such as charnockites, khondalites, and granulites. The EGMB preserves

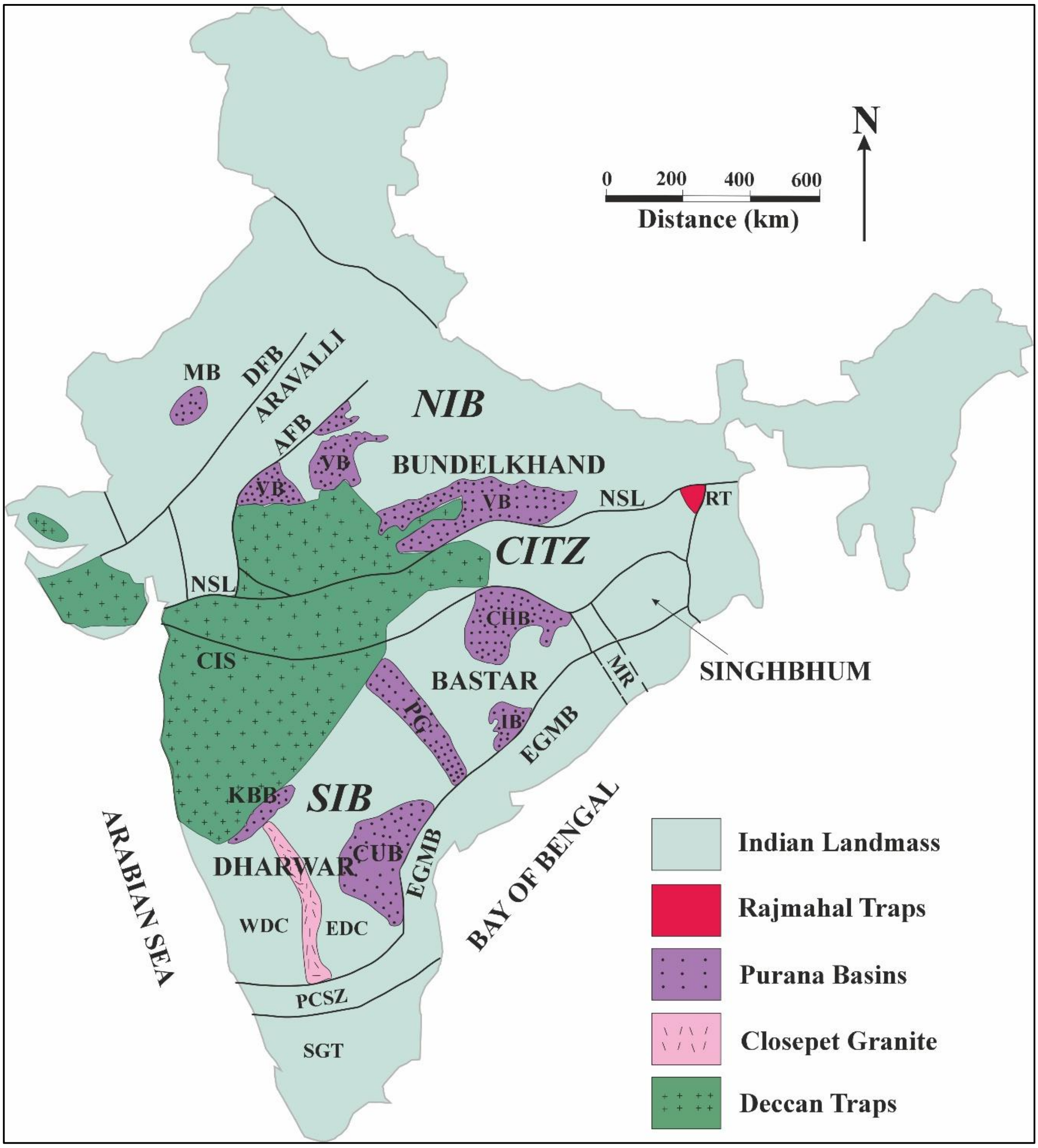

Figure 5.2 *A simplified geological map (Meert and Pandit, 2015) of Peninsular India (IP) showing major Precambrian cratons, Proterozoic mobile belts, Sedimentary basins and Volcanic provenances. The abbreviation are as follows- NIB: North Indian Block; SIB: South Indian Block; AFB: Aravalli Fold Belt; DFB: Delhi Fold Belt; EGMB: Eastern Ghat Mobile Belt; SMB: Satpura Mobile Belt; NSL: Narmada Son Lineament; CIS: Central Indian Suture; PCSZ: Palghat-Cauvery Shear Zone; DT: Deccan Traps; RT: Rajmahal Trap; IB: Indravati Basin; MB: Marwar Basin; VB: Vindhyan Basin; PG: Pranhita-Godavari Basin; CUB: Cuddapah Basin; KBB: Kaladgi-Bhima Basin; CHB: Chhattisgarh Basin; EDC: Eastern Dharwar Craton; WDC: Western Dharwar Craton; SGT: Southern Garnulites Terrain.*

evidence of Proterozoic collision and crustal reworking (Biswal and Sinha, 2004; Chetty and Murthy, 1994; Singh and Mishra, 2002). Geochronological studies suggest that the EGMB underwent significant tectonothermal events during the Mesoproterozoic and Neoproterozoic, linked to the assembly of Rodinia and Gondwana (Biswal and Sinha, 2004; Chetty and Murthy, 1994; Powell et al., 1988; Singh and Mishra, 2002). Its evolution is marked by the intrusion of granitic bodies and the development of shear zones, emphasizing its role in the tectonic reconfiguration of the Indian Peninsula. The Western Ghats, a prominent feature of the peninsular landscape, is primarily composed of the Deccan Traps, a vast flood basalt province formed during the Late Cretaceous (~65 Ma) (Figure. 5.2) (Allègre et al., 1999; Mahoney et al., 2002; Mitchell and Widdowson, 1991; Sangode et al., 2022). The traps, linked to the Reunion mantle plume, cover a significant portion of western and central India. These basaltic flows are interbedded with sedimentary layers and laterite soils, which provide critical evidence of weathering and paleoclimatic conditions during and after the volcanic episodes. The structural orientation of the Western Ghats reflects rift-flank uplift associated with the breakup of Gondwana and the subsequent opening of the Indian Ocean (Kale et al., 2017; Widdowson, 1997). Their steep western escarpments are indicative of tectonic uplift and erosional processes, while the eastern slopes grade gently into the Deccan Plateau.

The Southern Granulite Province in Tamil Nadu and Kerala is a major metamorphic belt in Indian peninsula (Figure. 5.2), comprising high-grade metamorphic rocks, including mafic granulites, charnockites, and khondalites. This province has been pivotal in reconstructions of East Gondwana (Dev and Tomson, 2024; Plavsa et al., 2015; Tomson and Dev, 2024). Geochronological studies indicate that granulite facies metamorphism occurred around 2.5 Ga (Plavsa et al., 2015; Tomson and Dev, 2024), followed by Pan-African reworking during the late Neoproterozoic to Cambrian periods. In northwestern part of peninsular India, the Aravalli-Banded Gneiss Complex and Bundelkhand Craton record (Figure. 5.2) the interplay of Archaean and Proterozoic tectonics (Hahn et al., 2020; Kaur et al., 2024; Mohanty, 2023; Singh et al., 2020). The Aravalli Supergroup comprises sedimentary and volcanic sequences, which were deposited in fault-controlled basins and later deformed during Proterozoic orogenesis. The Bundelkhand Craton, dominated by granitoids and mafic dyke swarms, stabilized in the Late Archaean, serving as the basement for the Vindhyan sediments (Gokarn et al., 2013; Singh et al., 2021).

5.2.2. Evolution of the Indian Plate tectonic setting

The 160 million years tectonic history of the Indian plate begins with its separation from the Gondwanaland in the southern hemisphere, and records a complex interplay of plate movements, interaction with mantle plumes, magmatism, and collisions with Eurasia. Its breakup from the Gondwana Supercontinent in Late Jurassic (~167 Ma) (Norton and Sclater, 1979; Raval and Veeraswamy, 2003) led to opening of a nascent ocean basin that separated East Gondwana—comprising India, Madagascar, Antarctica, and Australia from West Gondwana, comprising Africa and South America (Figure. 5.3). This opening event initiated the Southwest Indian Ridge (SWIR) as a divergent plate boundary. By the Early Cretaceous (~130 Ma), the Indian plate separated from Antarctica and Australia, forming the Southeast Indian Ridge (SEIR) (Figure. 5.3) (Gaina et al., 2007; Johnson et al., 1980; Powell et al., 1988; Weissel et al., 1977) . During this period, Sri Lanka also experienced limited rifting from India, but ultimately remained attached to the Indian plate (Desa et al., 2018; Katz, 2000; Ratheesh-Kumar et al., 2020). An equally critical phase in the Indian plate's tectonic evolution occurred around 70 Ma with the separation of the Laxmi Ridge (Mishra et al., 2020; Talwani and Reif, 1998). Located in the Arabian Sea, the Laxmi Ridge represents a microcontinental fragment that was initially part of the Indian plate. Its rifting and subsequent isolation were closely associated with mantle plume activity, particularly from the Reunion plume (Figure. 5.3) (Mishra et al., 2018; Singh, 1999). The separation of the Laxmi Ridge created the Laxmi Basin, which further lengthened the western margin of the Indian plate. This tectonic reorganization also contributed to the development of the Carlsberg Ridge, a major spreading center in the Indian Ocean (Figure. 5.3) (Bohannon et al., 1989; Dyment, 1998; Illarionov and Boyko, 2018).

Following the rifting of Madagascar, the Indian plate experienced a period of unprecedented northward acceleration, with velocities reaching up to 20 cm/year during the Late Cretaceous period (~67 Ma) (Ghosh and Sengupta, 2020; Powell et al., 1988; Raval and Veeraswamy, 2003). This rapid motion is thought to be a consequence of slab pull forces, exerted by the subducting Tethyan lithosphere beneath Eurasia (Eagles and Hoang, 2014; Van Hinsbergen et al., 2011; McKenzie and Sclater, 1971; Peirce, 1978) . This rapid movement coincided with one of Earth's most significant volcanic events: the eruption of the Deccan Traps around 65 Ma (Allègre et al., 1999; Mitchell and Widdowson, 1991; Sen, 2001; Watts and Cox, 1989), which is linked to the Reunion plume activities (Figure. 5.3) (Mahoney et al., 2002; Melluso et al., 2006; O'Neill et al., 2003; Tiwari et al., 2007). As the Indian plate continued its northward migration, it encountered the Kohistan-Ladakh Arc (~85 Ma) (Burg, 2011; Clift et al., 2002; Gibbons et al., 2015; Jagoutz et al., 2019; Martin et al., 2020; Rehman et al., 2011; Sharma, 1987; Sun et al., 2016), a volcanic island arc system located along the southern margin of the Asian plate (Figure. 5.3). This collision, which occurred along the Indus Suture Zone, marked the beginning of India's interaction with Eurasia. The accretion of the Kohistan-Ladakh Arc to the Indian plate reflects the progressive narrowing of the Neotethys Ocean (Figure. 5.3) (Burg, 2011; Gibbons et al., 2015; Jagoutz et al., 2019; Martin et al., 2020; Rehman et al., 2011). The culmination of the Indian plate tectonics occurred in the Early Eocene (~50 Ma)(Burg, 2011; Khan et al., 2009; Peltzer and Tapponnier, 1988; Sharma, 1987) when it collided with the Eurasian continent, resulting in complete closure of the Tethys Ocean and the rise of the Himalaya(Flesch et al., 2001; Larson et al., 1999; Patriat and Achache, 1984; Zahirovic et al., 2012; Zheng et al., 2017). At this stage the northward velocity reduced to about 5 cm/year (Flesch et al., 2001; Patriat and Achache, 1984; Zahirovic et al., 2012). The continued convergence during 21 Ma to the present (Larson et al., 1999; Zheng et al., 2017)

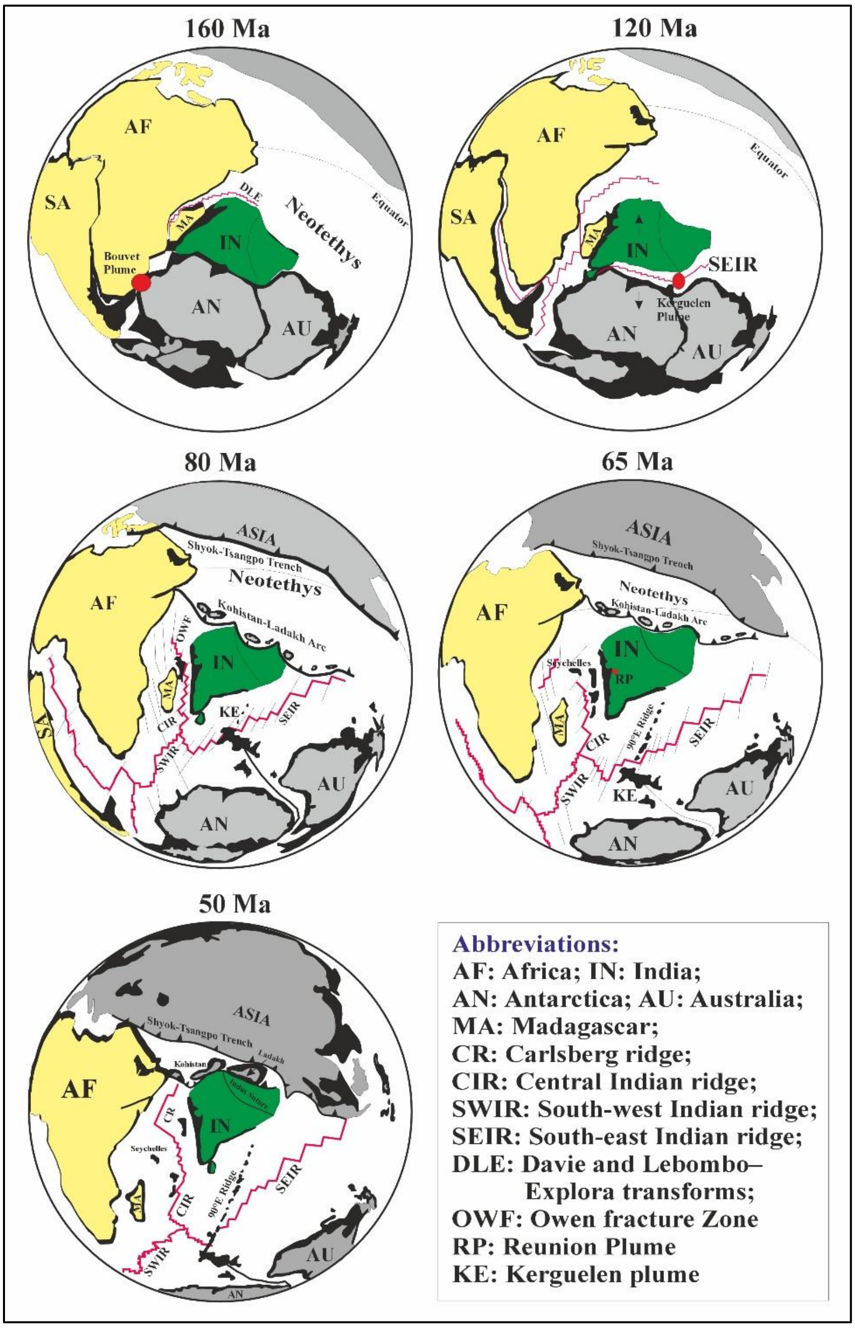

Figure 5.3 *A cartoon illustrating break-up of Gondwanaland, subsequent dispersion of the constituting continents, formation of plate boundaries and opening of the major sea from 160 Ma to 50 Ma*

gave rise to the foreland basins and thrust belts, which are the characteristic tectonic features of the present-day Himalayas.

The formation of the Bay of Bengal can be traced back to the Late Jurassic and Early Cretaceous (~160 – 130 Ma) during the fragmentation of Gondwana (Biswas and Majumdar, 1997; Curray and Moore, 1974; Rao et al., 1997; Talwani et al., 2016) . The rifting between East and West Gondwana marked the initiation phase of this ocean basin (Figure. 5.3) (Krishna et al., 2009; Mukherjee et al., 2009; Ramana et al., 1994) . This process was facilitated by the activation of the Southeast Indian Ridge (SEIR) (Figure. 5.3), which began spreading and creating the Indian Ocean (Biswal and Sinha, 2004; Gaina et al., 2007; K. S. Krishna et al., 2009). During this time, the eastern margin of the Indian plate evolved as a passive continental margin, experiencing significant extensional tectonics and lithospheric thinning. As the plate moved, the eastern margin of the Indian subcontinent became a major depositional site, capturing massive volumes of sediment transported by ancient river systems such as the paleo-Ganges and paleo-Brahmaputra (Curray and Moore, 1974; P. K. Mohanty et al., 2008; Mukhopadhyay et al., 2010; Rao et al., 1997). These sediments were derived from the weathering of Gondwana terrains and volcanic materials, resulting in extensive sedimentary sequences along the margin.

The ongoing subduction of Indian plate beneath the Burma microplate led to the formation of accretionary prisms, deep-sea trenches, and active fault systems, creating a complex tectonic and depositional environment in the eastern Bay of Bengal. The tectonic evolution of the Bay of Bengal is also linked to the dynamics of the Ninety East Ridge, a prominent submarine feature extending north-south through the Bay (Figure. 5.3) (Krishna et al., 2012; Levchenko et al., 2021; Mahoney et al., 1983; Nobre Silva et al., 2013; Subrahmanyam et al., 2008; Sushchevskaya et al., 2016). This ridge represents the hotspot trace of the Kerguelen plume (Figure. 5.3), formed during the northward drift of the Indian plate. Its alignment and magmatic history provide evidence of the plate's movement and interactions with underlying mantle dynamics. The Ninety East Ridge has also acted as a barrier to sediment transport, influencing the depositional patterns within the Bay. Modern tectonic activity in the Bay of Bengal is characterized by active subduction at the Sunda Trench and strike-slip faulting along the Andaman-Nicobar Islands (Curray, 2005; Jacob et al., 2021; Singh et al., 2013). The ongoing convergence between the Indian plate and the Burma microplate contributes to seismic activity (Cochran, 2010; McCaffrey, 2009; Mohanty et al., 2024; Panda et al., 2020; Satyabala, 2003; Sloan et al., 2017), with significant implications for regional tectonics and tsunami generation.

Rifting along the Southwest Indian Ridge led to the formation of the proto-Arabian Sea, characterized by extensional tectonics and lithospheric thinning. A major tectonic phase occurred during the Late Cretaceous (~90 Ma) (Figure. 5.3) (Ghosh and Sengupta, 2020; Raval and Veeraswamy, 2003) when the Indian plate rifted from Madagascar, creating the Mascarene Basin and marking the initiation of the Laxmi Ridge as a distinct microcontinental fragment(Pandey et al., 1995; Talwani and Reif, 1998). The Marion mantle plume (Figure. 5.3) is held responsible for this separation, triggering volcanism and shaping tectonic structures, such as the Laxmi Basin (Mishra et al., 2018; Pandey et al., 1995; Singh, 1999). By ~70 Ma, the Reunion mantle plume activated, causing the separation of the Laxmi Ridge from the Indian plate and initiating seafloor spreading at the Carlsberg Ridge, which continued to remain an active mid-ocean ridge in the Present day (Figure. 5.3). The eruption of the Deccan Traps (~65 Ma), associated with this plume, profoundly influenced the region, contributing volcanic material to the Arabian Sea and aiding in the rapid northward drift of the Indian plate (Mitchell and Widdowson, 1991; Sangode et al., 2022; Watts and Cox, 1989).The collision of the Indian plate with Eurasia in the Early Eocene (~50 Ma) reshaped the northern Arabian Sea margins (Figure. 5.3), forming subduction at the Makran Trench. Concurrently, the Owen Fracture Zone emerged as a major transform fault (Figure. 5.3), delineating the boundary between the Indian and Arabian plates and adding complexity to the region's tectonic framework.

5.2.3. Geodynamic settings of the Peninsular India

The Indian plate forms a complex geological relationship with its neighbouring tectonic plates, each significantly influencing the topography of the Indian subcontinent. Its northern boundary with the Eurasian Plate is marked by the remarkable Himalayan Mountain range and the vast Tibetan Plateau, both of which have developed over the past 50 million years as a result of the India-Asia continental collision (Ding et al., 2022; Royden et al., 2008). Their current topography reflects the interplay of decreasing convergence rates and isostatic adjustments, continuously reshaping elevations over time (Maiti et al., 2021). In contrast, Peninsular India (PI), illustrated in Figure. 5.4, represents a stable Precambrian craton characterized by minimal recent tectonic activity (Gerya, 2014). A significant portion of IP is dominated by the Deccan volcanic province (Ghosh et al., 2024; Mittal et al., 2021; Mittal and Richards, 2021), flanked by the prominent Western and Eastern Ghats (its geological constitution is elaborated in S1;

Figure. 5.2). The continental lithosphere of IP interfaces with oceanic plates of varying sea-floor ages (Figure. 5.4). In the Arabian Sea, the Carlsberg Ridge marks a divergent plate boundary, with lithospheric ages progressively increasing away from it. Conversely, the oceanic lithosphere of the Bay of Bengal (BOB), situated to the east of PI, is considerably older (Age ~ 140 Ma) than that of the Arabian Sea (Age ~ 60 Ma) (Figure. 5.4). The BOB lithosphere ultimately meets the Sunda Trench, where the Indian Plate subducts beneath the Sunda and Burma plates (Steckler et al., 2016). Geophysical data indicate substantial variations in lithospheric thickness across the Bay of Bengal, with central regions exhibiting a thinner lithosphere of approximately 50-60 km compared to other areas (Dubey and Tiwari, 2022; Rao et al., 2016; Saha et al., 2021). These variations may stem from ongoing rifting and subsidence, influenced by mantle upwelling (Roy and Chatterjee, 2015). At the north-eastern margin of the Bay of Bengal, the Indian Plate establishes a convergent boundary with the Burmese Plate resulting in significant lithospheric deformation and high seismicity in the region (Steckler et al., 2016) (Figure. 5.4).

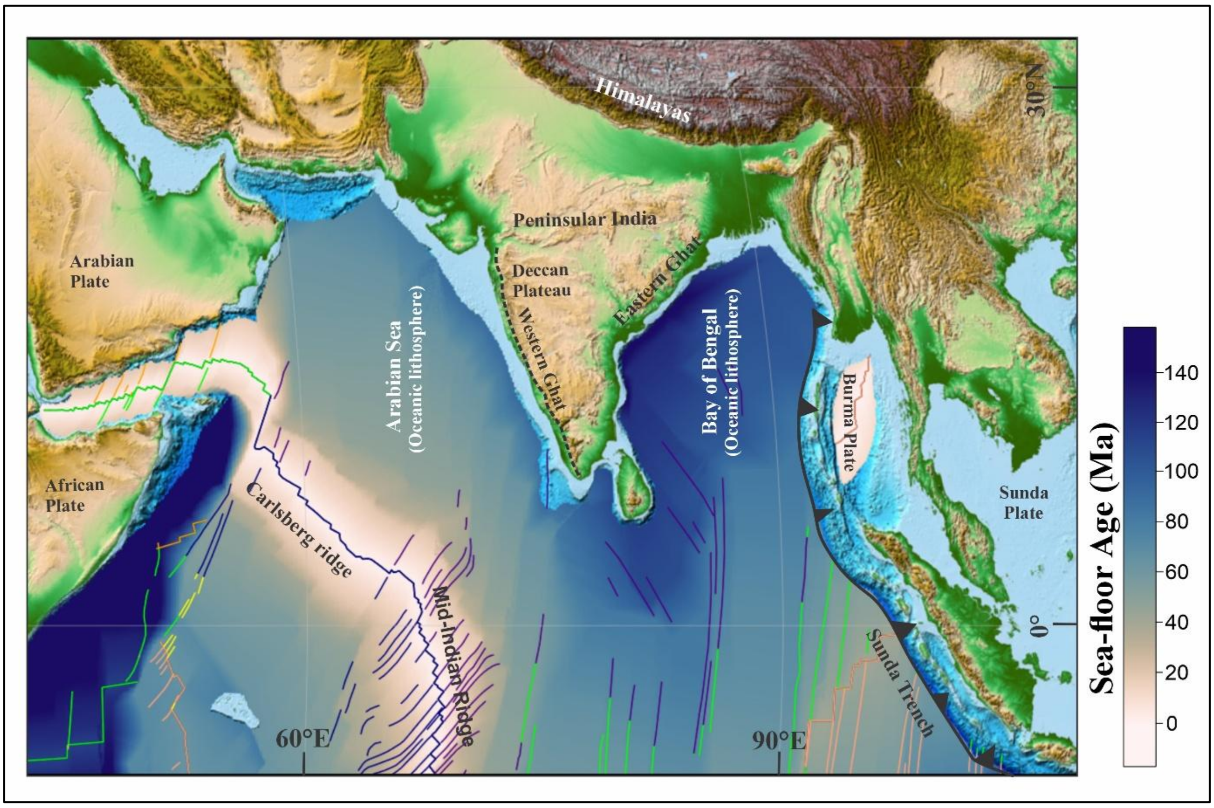

Figure 5.4 *Tectonic setting of the Indian Peninsular (IP) landmass, constituted by major tectonic plates: the Indian Plate, surrounded by the Arabian Plate to the west, the Eurasian Plate to the north, and the Indo-Australian Plate to the east, and the plate boundaries: the Carlsberg Ridge, the Mid-Indian Ridge, and the Sunda Trench. The IP continental craton consists of large-scale geomorphic elements: the Western Ghats, the Eastern Ghats Mountain ranges, and the Deccan Plateau. Seafloor age data indicates contrasting ages of oceanic lithosphere beneath the Bay of Bengal (~140 Ma) and the Arabian Sea (~ 40 Ma).*

The Eastern Continental Margin (ECM) of Peninsular India, stretching approximately 2,600 km presently occurs as a passive continental margin. Current tectonic models suggest that the ECM originated from a rifting event during the Late Jurassic to Early Cretaceous period, when India, Antarctica, and Australia separated from the Gondwanaland (Ali and Aitchison, 2008; Chatterjee et al., 2013; Gibbons et al., 2012). This is evidenced by rift-related grabens and sags near the shelf and the offshore basins. The processes of continental breakup have left geological signatures, such as the truncation of the northwest-southeast trending Godavari and Mahanadi rift valleys against the ECM (Biswas, 2003; Mishra et al., 1999, 1989). The ECM features the Eastern Ghats Proterozoic mobile belt (EGMB) as the principal physiographic element (Figure. 5.2), approximately 1,500 km long, extending from India's eastern coast to the southern tip of IP (Chetty and Murthy, 1994; Mishra et al., 1999). The tectonics of the Gondwanaland breakup during the Mesozoic Era also led to the formation of several continental-scale intra-cratonic sedimentary basins, including the Krishna-Godavari and Mahanadi basins in IP (Chatterjee et al., 2013).

On the western side of IP, the Western Continental Margin (WCM) extends north-south for about 2,200 km and includes diverse geological formations, such as Precambrian granitic belts, Mesozoic sedimentary layers, the Deccan volcanic province, and Paleocene to Recent sediments (Crawford, 1969; Kale, 2002; Meert and Pandit, 2015; Subrahmanyam and Chand, 2006). This margin is crucial for understanding the geodynamic evolution of the Arabian Sea and is considered a passive continental margin that formed during the Gondwanaland breakup in the Cretaceous period. The supercontinent separated the Indian subcontinent from Africa and Madagascar, subsequently leading to the opening of the Arabian Sea through the initiation of the Carlsberg Ridge (Chatterjee et al., 2013, 2017; Subrahmanyam and Chand, 2006) (Figure. 5.3). The WCM displays geological evidence of extensional tectonics, including rifted and faulted blocks, indicative of lithospheric stretching during the early stages of continental breakup. This extensional tectonics has facilitated the accumulation of sediments, presently preserved at the continental margin (Kale, 2002; Subrahmanyam and Chand, 2006). Geological studies suggest that the Arabian Sea began to open in the Late Jurassic to Early Cretaceous period (around 150 Ma) due to rifting between the Indian and African plates, followed by seafloor spreading in the oceanic lithosphere (Chatterjee et al., 2013; Gaina et al., 2015) (Figure. 5.3). The lithosphere beneath Arabian sea gradually thins towards the mid-ocean ridge system, particularly at the Carlsberg Ridge, which is a part of the larger Indian Ocean Ridge system (Chatterjee et al., 2013; Gaina et al., 2015) (Figure. 5.3). The geological evolution of the Arabian Sea is further complicated by the interaction between the Indian Plate and the Eurasian Plate, which has activated ridge-push forces from the Carlsberg Ridge.

The geological setting of the WCM has been significantly influenced by the Deccan Traps, formed during the late Cretaceous period, around 66 Ma ago. The extensive outpouring of flood basalts associated with the breakup of the Indian plate from the African plate is linked to the Réunion hotspot beneath the Indian lithosphere (Figure. 5.3) (Chatterjee et al., 2013). Geomorphologically, the Deccan Traps exhibit a step-like topography characterized by thick basaltic lava flows covering over 500,000 square kilometers in west-central India. Some studies suggest that the underlying domal structure, resulting from the interaction of the Réunion plume with the lithosphere, has shaped the current plateau's topography (Cox, 1989; Radhakrishna, 1993). The WCM features the Western Ghats, a prominent mountain range along India's western coast. The formation of the Western Ghats is closely associated with the development of the western continental margin due to India's separation from Madagascar at around 90 Ma (Chatterjee et al., 2013, 2017). Its tectonic studies indicate that the range itself represents a fault escarpment formed by uplift and erosion rather than tectonic folding or orogeny (Chatterjee et al., 2013). The timing of uplift in the Western Ghats remains debated, with estimates ranging from the Late Cretaceous to the Early Cenozoic; this uplift is thought to have been influenced by both the thermal effects of Deccan volcanism and tectonic forces related to the rifting of the Indian plate (Cochran, 1983; Cox, 1980; Devey and Lightfoot, 1986; Gunnell et al., 2003; Gunnell and Fleitout, 1998; McKenzie, 1978; Roger Buck, 1986; Tiwari et al., 2006; Weissel and Karner, 1989; Widdowson and Cox, 1996). Geophysical studies suggest that the lithospheric thickness beneath the Western Ghats is relatively high, ranging from 100-120 km, indicating a stable cratonic region that has experienced minimal lithospheric thinning (Dubey and Tiwari, 2018; Gupta et al., 2018; Radha Krishna et al., 2002; Tiwari et al., 2006). The Western Ghats exhibit a variety of geological features, including rifted margins, escarpments, and deeply incised valleys. The region's high topographic relief is generally attributed to a combination of tectonic uplift and differential erosion over millions of years (Mandal et al., 2015; Mandal et al., 2015).

5.3. Topography and drainage system of Indian Peninsula

5.3.1. Drainage Patterns

I studied the large-scale drainage patterns in peninsular India as they directly respond to the first-order topographic slopes in the continental region. All the major rivers show a common characteristic feature; they originate at the plateau's extreme western edge, a few kilometers away from the Arabian Sea coast and drain through the entire transect of peninsular plateau to finally fall into the Bay of Bengal (BOB) on the East. For example, the Godavari, Krishna, and Kaveri, which are the three longest rivers in this region, find their sources at the crest line in the Western Ghats and subsequently flow eastward to meet the BOB by cutting the Eastern Ghats Mountain barriers (Figure. 5.1). Their east-directed courses clearly indicate an overall eastward tilt of the peninsular plateau.

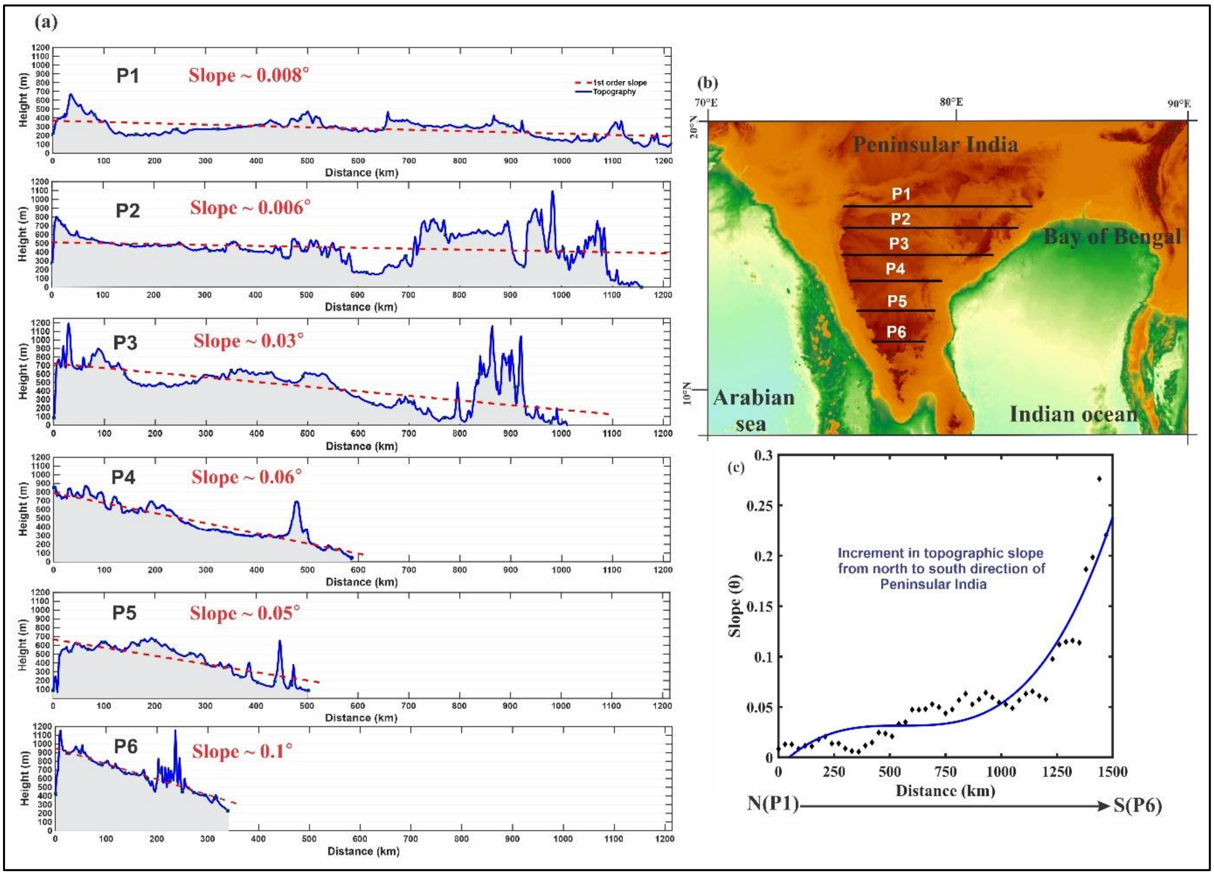

Figure 5.5 *(a) A set of topographic profiles (P1–P6) across the Indian Peninsular landmass, displaying eastward decrease in topographic elevations (in meters), forming first-order surface slopes to east (red dashed line). It is noteworthy that the surface slope varies from 0.008° to 0.1° in the south direction. The profile locations: P1–P6 are shown in (b). (c) DEM model calculated plot showing a steep increase in the topographic slopes from north to south.*

The East coast of peninsular India stretches for about 2600 km, starting from the Sundarbans and ending at Kanyakumari (Figure. 5.1; Figure. 5.4), intervened by various physiographic features, such as river delta systems, vast coastal plains and extensively sediment deposits. The river systems in peninsular India are divided by the westward-flowing Narmada River. On the north of this river, the Ganga and associated rivers constitute the river system that collectively drains to south-west and then takes a sharp turn to south, eventually to fall into the BOB, forming the Sundarbans Delta, the largest delta in the world (Rogers and Goodbred, 2014). On south of the Narmada River, the peninsular plateau is drained by four major rivers: Mahanadi, Godavari, Krishna and Cauvery and associated minor rivers, e.g., Pennar and Palar and Thamirabarani and Vaigai; all of them flow into the BOB, producing isolated deltaic platforms at their mouths on the East coast (Figure. 5.1).

The western coast of the Indian Peninsula broadly follows the Western Ghat Escarpments (WGE), a spectacular orographic feature that constitutes a linear relief at the western edge of the peninsular plateau, stretching for about 1600 km from the Tapi valley on north of Mumbai to the southern tip at Kanyakumari. All the major peninsular rivers discussed above originate from the WGE relief, on average, of 1200 m, and flow eastward over the plateau with elevations of more than 800 m. The escarpment shows west-directed embayment lines, formed due to intense erosion by westerly-flowing streams. The WGE serves as a N-S divide between eastward-flowing river systems (e.g., Godavari, Krishna and Cauvery) (Figure. 51) and the westward-flowing short-range streams. Due to the paucity of rivers in the Arabian sea, the sedimentary thickness in the Arabian Sea is substantially thinner than that of the BOB.

5.3.2. Topographic Analysis

Using digital elevation maps (DEM) I prepared a series of E-W topographic profiles (Figure. 5.5a-5.5b), covering the entire E-W stretch from the WGE crest line to the eastern flank of the Eastern Ghat Mountain ranges. The profiles were taken at a close interval (~ 180-200 km) to cover a N-S horizontal distance of 350-1200 km, as illustrated in Figure. 5.5a-5.5b. They reveal topographic undulations in multiple wavelengths, which evidently reflect involvement of multiple factors, such as tectonic uplift, surface erosion, and rock types, in shaping the surface topography. In this study, I focus on the long-wavelength (first-order) topography (red colour in Figure. 5.5a), considering it as a direct proxy of the lithospheric scale dynamics (Beaumont et al., 2001; Clark and Royden, 2000; Copley et al., 2011; Copley and Mckenzie, 2007; Maiti et al., 2021; Mandal et al., 2015; Neuharth et al., 2022; Neuharth et al., 2022; Pons et al., 2022). The first-order topography at any E-W transect in the peninsular plateau forms a recognizable eastward slope, with its elevations declining from ~800 meters on the WGE crest to ~200 meter at the extreme eastern edge (Figure. 5.5a). The serial topographic profiles reveal a consistent change in the maximum WGE elevations from north to south, varying from ~380 meter and to ~950 meter (Figure. 3a). On the eastern flank of the plateau the maximum elevation varies between ~198 meter and ~390 meter (Figure. 5.5a).

The peninsular plateau shows internal topographic heterogeneities on relatively smaller wavelengths, as illustrated in Figure. 3a, where the surface topography forms a few elevation spikes in its central region, which die out in both the west and east directions. In contrast, the eastern flank of the plateau has markedly a gentler gradient. It is important to note that the plateau topography varies significantly from north to south, both along the Western and Eastern Ghat Mountain ranges. In the Western Ghats, the average elevation ranges from approximately 500 to 600 meters, while in the Eastern Ghats region, it averages around 375 meters, as depicted in Figure. 3a. The topographic profile exhibits a sharp increase in elevation with steep slopes (average ~75°) along the western side of the WGE mountain range, followed by gentle slopes (average ~25°) on its eastern flank (Figure. 5.6). The maximum elevation in the Western Ghats region reaches approximately 800 meters, whereas in the eastern part, it lies at around 650 meters (Figure. 4). The height, however, increases sharply to form a narrow, about 100 km wide peak in the Eastern Ghats region (Figure. 5.5a).

To calculate the topographic slope along a given, transect in the peninsular terrain, the present analysis uses a first-order polynomial fit to the elevation data obtained from the corresponding digital elevation maps (DEM). This method ensures accurate quantification of the first-order topographic slope from a linear regression, which captures the general inclination of the landscape by filtering out higher-order (local) topographic fluctuations. The elevation profile in peninsular topography is expressed as:

$$z = mx + c \tag{5.1}$$

where z represents elevation, x is the horizontal distance, $m$is the slope (rate of elevation change with respect to distance), and c is the intercept, representing the elevation where the horizontal distance x is zero. The slope, m, is the primary parameter of interest as it quantifies the steepness of the terrain. Using the least-squares method, the slope m is determined by minimizing the sum of squared residuals between observed elevations and those predicted by the polynomial model. The least-squares solution for m is given by:

$$m = \frac{\sum x_i z_i - \sum x_i \sum z_i}{n \sum x_i{}^2 - (\sum x_i)^2} \tag{5.2}$$

Here, n is the total number of data points, $\sum x_i$ is the sum of horizontal distances, $\sum z_i$ is the sum of elevation values, $\sum x_i \sum z_i$ is the sum of the products of distances and elevations, and $\sum {x_i}^2$ is the sum of squared distances. The intercept c can be subsequently computed as:

$$c = \frac{\sum z_i - m \sum x_i}{n} \tag{5.3}$$

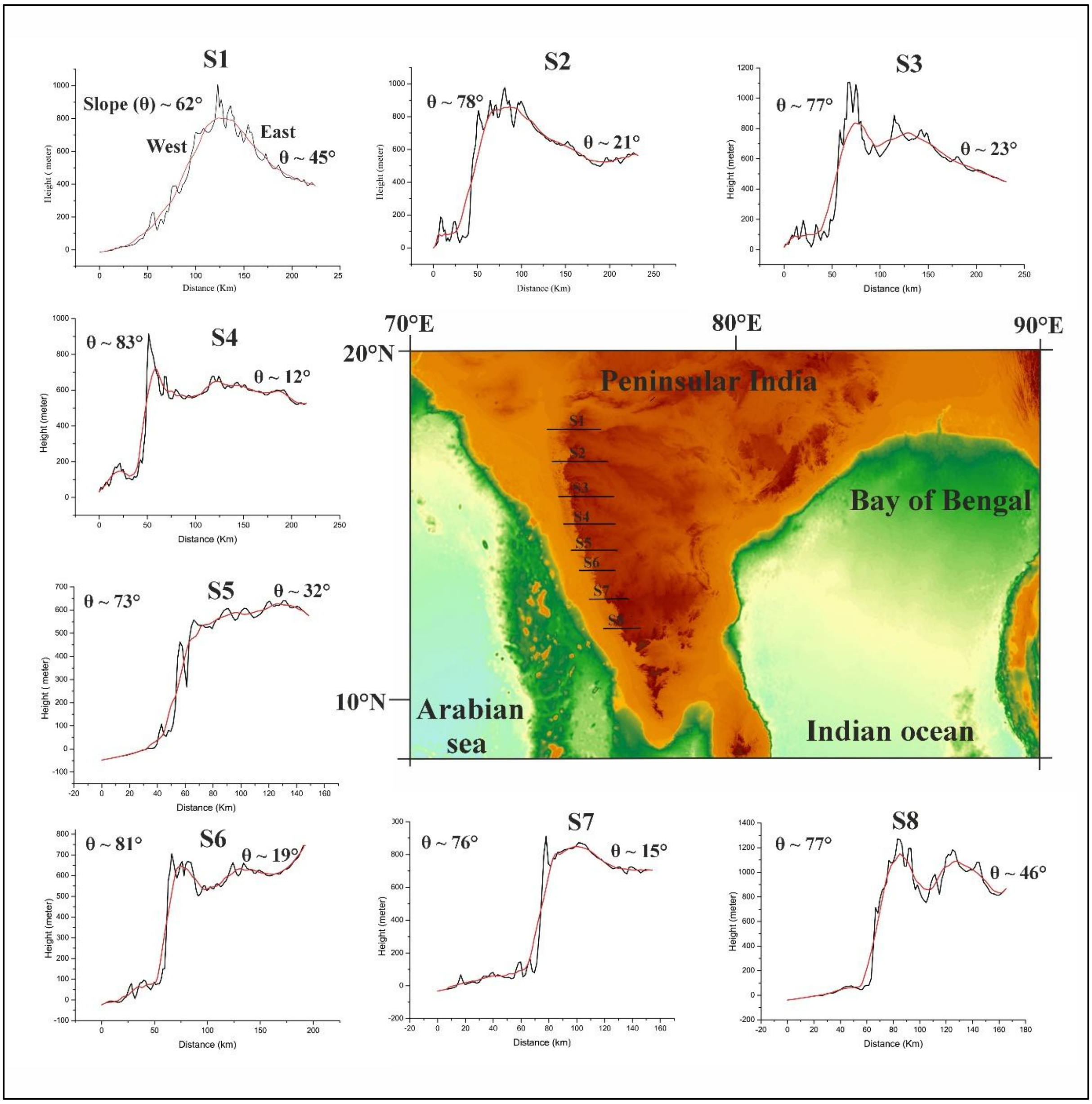

Figure 5.6 *Strongly asymmetric topographic profiles (S1–S8) across the Western Ghats escarpment. The escarpment exhibit elevation drops of more than 1000 m, forming steep slopes (70° to 82°) to west, and a much gentler eastward slope (40° to 15°) on the other side.*

In peninsular topography, an E-W transect often spans across gently sloping plateaus, dissected river valleys, or escarpments, which are characteristic features of such landscapes.

The slope derived from this method provides a representative measure of the terrain's inclination, capturing the overall topographic gradient. The polynomial fitting process is implemented in MATLAB, a computational environment that efficiently handles matrix operations and performs least-squares regression (Kiusalaas, 2015; Chen et al., 2005). The input data comprise horizontal distances x_i and corresponding elevation values $z_i$sampled along transects from digital elevation models (DEMs) of peninsular regions. The derived slope values were cross-validated against known geological gradients to ensure consistency and reliability.

The method of a first-order polynomial fit to peninsular topography provides several advantages. It allows for the simplification of complex terrain into a linear model that is easy to interpret and compare across regions. Moreover, it highlights larger-scale topographic trends that are crucial for understanding geological processes such as erosion, sediment transport, and tectonic uplift. By focusing on the overall slope, the method effectively excludes local topographic gradients due to various geomorphic elements, such as minor ridges and valleys, which are not important in the present topographic analysis.

To evaluate the eastward tilt in the plateau, the overall first-order topographic slopes were calculated from each E-W section, which are found to range from 0.008° to 0.3° (Figure. 5.5a-5.5c). In the northern sector the plateau forms a topographic slope of ~ 0.008°- 0.006° (see Figure. 5.5a) towards the BOB. The slope increases to 0.03° - 0.05° in the central sector of the peninsula. The southern part of the peninsula yields locally an eastward topographic slope of 0.1° (Figure. 5.5a). The overall first-order slopes were estimated from a histogram analysis of the slope data. The most dominant topographic slope is found to be 0.05° in the far north and the central region of the Peninsula, which increases to ~ 0.1°-0.3° in the south (Figure. 5.5c). The comprehensive topographic slope analysis clearly suggests that the Indian Peninsular plateau maintains an overall eastward slope in the entire craton, spanning from north to south.

5.4. Model topography of Indian Peninsula

5.4.1. Approach

Numerical simulations were implemented based on a finite element method (FEM) approach to model the topographic evolution of the Indian Peninsula (IP), including the oceanic lithospheres beneath the Bay of Bengal (BOB) to the east and the Arabian Sea (AS) to the west of the IP (Figure. 5.4). As discussed previously (section 5.2.3), the Arabian oceanic lithosphere is modeled with an age of 60 million years at the western IP passive margin, with its density varying as a function of lithospheric temperature. The BOB lithosphere, on the other hand, is assigned an average age of 140 million years, and its density is modelled with a constant average value of 3460 kg/m³ (see supplementary section in Afonso et al., 2007; Dasgupta et al., 2021), given the absence of an active ridge or significant variation in lithospheric age in this region.

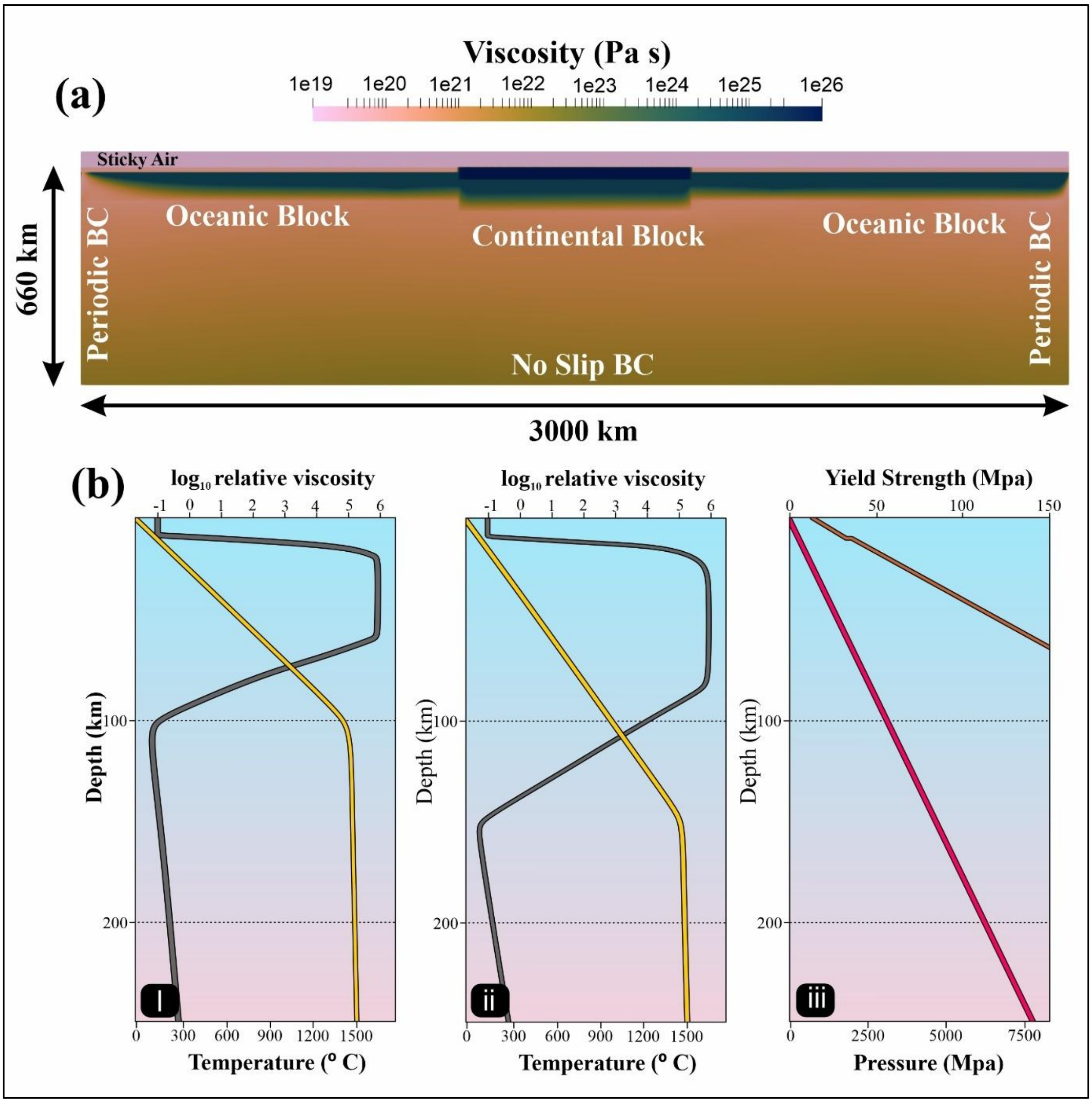

Figure 5.7 (*a*) *Two-dimensional thermo-mechanical model setup that represents an E-W vertical section of Indian peninsula. The model consists of a continental block, flanked by oceanic blocks and a sticky air layer at the top. Periodic boundary conditions are imposed at the lateral walls, while a no-slip boundary condition at the model base. The colour scale indicates the viscosity distribution. (b) Depth-dependent variations of temperature (yellow) and viscosity (gray) of (i) oceanic, and (ii) continental lithosphere, and (iii) the yield strength considered in this model. It is to be noted that the temperature*

increases with depth, reaching ~1500°C at the lithospheric base, accompanied by a significant viscosity decrease in the asthenosphere.

The initial model setup and boundary conditions are illustrated in Figure. 5.7. To capture topographic variations in the IP in the north-south direction, a series of east-west cross-sections across the IP (Figure. 5.8) was considered. For a detailed analysis, this study focus on three specific sections: AB (IP length = 900 km), CD (IP length = 750 km), and EF (IP length = 600 km), which represent the northern, central, and southern segments of the IP, respectively (Figure. 5.8). The E-W lithospheric stretches of the BOB and AS are also varied in the models accordingly, while maintaining a constant model domain length.

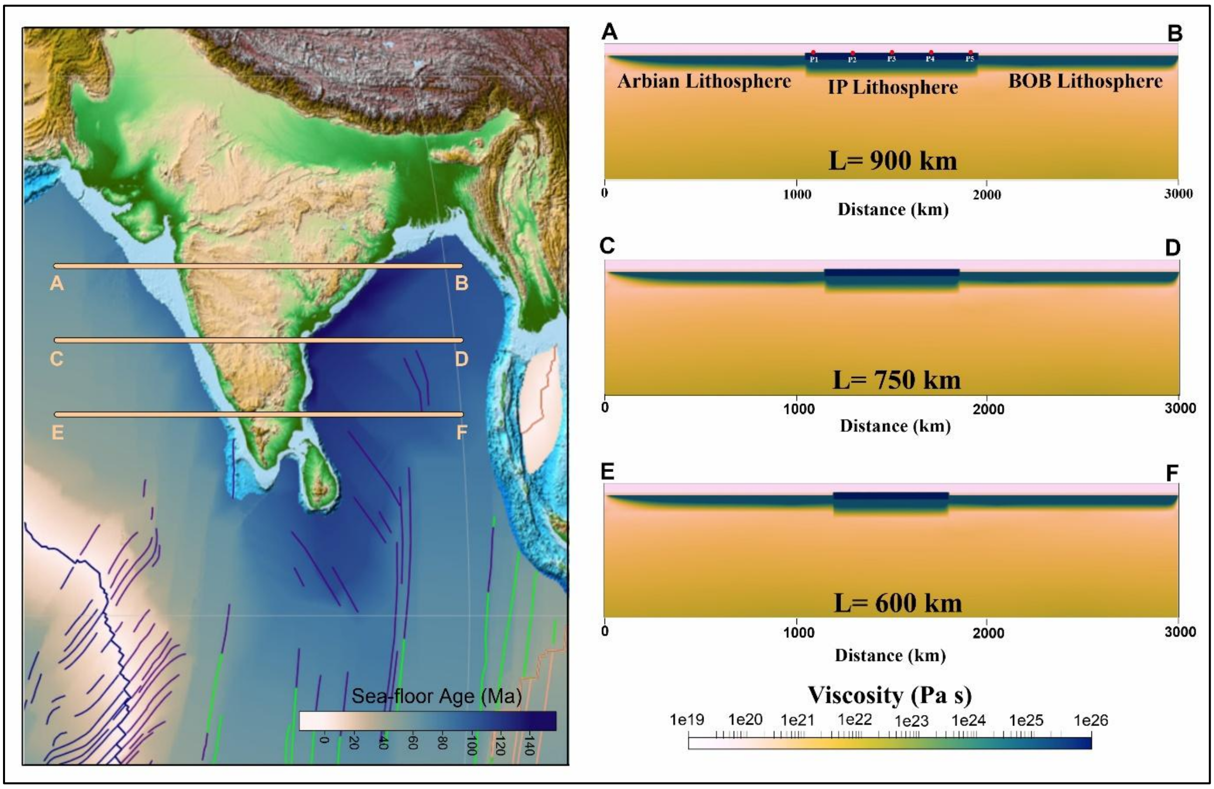

Figure 5.8 *Topographic map of the Indian subcontinent, including the Arabian Sea and the Bay of Bengal (BOB) of varying sea-floor ages (in millions of years, Ma). The colour bar denotes the age spectrum, ranging from 0 Ma (recent) to over 140 Ma (oldest). It is noteworthy that the oceanic lithosphere beneath the BOB is significantly older than that beneath the Arabian Sea. Horizontal lines (A–B, C–D, and E–F) represent the cross-sections of varying continental width (L) considered for the thermomechanical model simulations (right panels). Colour bar shows viscosity values on a logarithmic scale chosen in the model. P_1-P_5 are the positions of the tracers at the surface of the lithospheric block, which are used to track the surface displacement.*

The mantle rheology is modelled using a composite creep law that combines diffusion (η_{diff}) and dislocation (η_{disl}) creep processes. The creep laws for mantle silicates are described by an Arrhenius function for temperature and pressure dependence of the activation volume

(V) and activation energy (E) (Hirth and Kohlstedt, 2003). The resulting diffusion- and dislocation-controlled viscosity is expressed as:

$$\eta_{diff/disl} = A^{\frac{-1}{n}} \dot{\varepsilon}^{\frac{1-n}{n}} exp\left(\frac{E+PV}{nRT}\right), \tag{5.4}$$

where A is a pre-factor, n is the stress exponent ($n = 1$ and 3.5 for diffusional and dislocation creep, respectively), R is the gas constant and P is the lithostatic pressure. A harmonic mean of the two types of viscosity is considered to find an effective model viscosity (η_{eff}),

$$\frac{1}{\eta_{eff}} = \frac{1}{\eta_{diff}} + \frac{1}{\eta_{disl}}. \tag{5.5}$$

The activation volumes (V) and activation energies (E) used in our modelling (details in Table 1) are consistent with experimental estimates for dry olivine (Karato and Wu, 1993). The pre-factor A for the upper mantle is chosen to satisfy two key observations: 1) an effective viscosity of approximately 10^{20} Pa s in the shallow part of the upper mantle (Hager, 1991), and 2) seismic anisotropy, which suggests that dislocation creep dominates in the upper mantle (Becker, 2017). In our model, the top crustal layer is assigned a constant viscosity of 1×10^{26} Pa s. The strength of the mantle lithosphere is determined by the upper viscosity cut-off value (1×10^{26} Pa s) (Gerya et al., 2008). The present modelling treats the crust and lithosphere as single, uniform layers without internal rheological stratification.

This study numerically simulate the isostatic dynamics of IP in a time-evolving, dynamically consistent thermomechanical model. The model is developed in 2-D Cartesian domains within a theoretical framework of computational fluid dynamics (CFD) using the *Underworld2* code (Beucher et al., 2019; Cooper et al., 2017; Mansour et al., 2020; Sandiford et al., 2019; Sandiford and Moresi, 2019). This CFD simulation study assumes an incompressible Boussinesq fluid flow at low Reynolds Number, approximating the million-year scale kinematic state of Earth's mantle (Roy et al., 2024). The mathematical treatment uses two governing equations: the continuity equation and the momentum conservation equation to describe the spontaneous flows in the model. Their respective expressions are as follows:

$$\frac{\partial v_i}{\partial x_i} = 0 \tag{5.6}$$

Table 1: *Model parameters used in thermo-mechanical model*

Description	Symbol	Unit	Default Values
Thermal expansion coefficient	α	K^{-1}	3×10^5
Thermal diffusivity	κ	m^2 s^{-1}	10^{-6}
Reference density	ρ_0	kg m^{-3}	3300
Surface temperature	T_s	K	273
Potential temperature	T_m	K	1673
Adiabatic temperature gradient	dT/dz	K km^{-1}	0.37
Gravitational acceleration	g	m s^{-2}	9.81
Maximum viscosity	η_{max}	Pa s	1.0×10^{26}
Minimum viscosity	η_{min}	Pa s	1.0×10^{19}
Crust viscosity	η_C	Pa s	1.0×10^{26}
Dislocation creep (Upper Mantle)			
Activation energy	E	kJ mol^{-1}	540
Activation volume	V	cm^3 mol^{-1}	10
Pre-factor	A	Pa^n s^1	4.1×10^{15}
Exponent	n	-	3.5
Diffusion creep (Upper and Lower mantle)			
Activation energy	E	kJ mol^{-1}	300 (UM & LM)
Activation volume	V	cm^3 mol^{-1}	4.5 (UM), 1.58 (LM)
Pre-factor	A	Pa^1 s^1	1.87×10^9 (UM)
			1.77×10^{14} (LM)
Exponent	n	-	1

$$-\frac{\partial P}{\partial x_i} + \frac{\partial \sigma_{ij}}{\partial x_j} + \rho g_i = 0, \tag{5.7}$$

where v_i is the velocity vector. In equation (4) inertial forces are negligible, as applicable to long term flows in the mantle. Applying the model boundary conditions (Figure. 5.7), equations (5.6) and (5.7) are numerically solved to find the velocity and pressure in the model domain, as described in the preceding paragraph. The thermal evolution in the geodynamic model is determined by combining advective heat transfer, thermal diffusion, and heat sources/sinks in the system.

Applying Boussinesq approximation, the model uses the following heat equation:

$$\frac{\partial T}{\partial t} + \boldsymbol{v}.\nabla T' = \kappa \nabla^2 T' + \frac{Q}{C_p}, \tag{5.8}$$

where $\kappa = \frac{k}{\rho C_p}$, which represents the thermal diffusivity. T' is replaced by the adiabatic temperature (T) of the system as a function of depth (z) obtained from the relation:

$$T = T' + z\left(\frac{\partial T}{\partial z}\right) = T' + z\left(\frac{\alpha g T_p}{C_p}\right), \tag{5.9}$$

where T_p is the mantle potential temperature and α is the coefficient of thermal expansion, which was set at a value of 3×10^{-5} K^{-1} (Roy et al., 2024). Considering C_p = 1260 J/kg/K for Earth's mantle (Roy et al., 2024), a resultant adiabatic temperature gradient of 0.4 K/km is added to the nonadiabatic mantle temperature. Constant (Dirichlet) and zero-flux (Neumann) temperature conditions are imposed on the top and bottom model boundaries, respectively to solve the energy equation. The initial model surface and bottom temperatures are set at 0°C and 1300°C, respectively.

To solve the governing equations, the 2D FEM domain (3000 km × 660 km) is meshed by smaller quadrilateral elements with a mesh resolution of 320 elements in the vertical direction, which provides an element width of ~2 km, and a particle density of 50 tracers per element (Sandiford and Moresi, 2019). A set of passive tracers (P_1, P_2, P_3, P_4, and P_5) in the compositional field is introduced to track the plate motion and deformation in the model simulations at five different locations in the numerical models (Figure. 5.7).

5.4.2. Model Results

5.4.2.1 The IP topography: a model analysis

The FE model simulations show an asymmetric topographic evolution in peninsular India, forming consistently eastward surface slopes on E-W transects from north to south. The following descriptions considers specifically three IP transects: (i) AB, (ii) CD and (iii) EF (Figure. 5.8) to elaborate the asymmetric topographic elements in the northern, central and southern segments of the continental mass.

The numerical model, representing the northern segment of the Indian Peninsula (NIP), consists of a continental lithospheric block (AB) with a horizontal extent of 900 km and a vertical thickness of 120 km (Figure. 5.9a). At time $t = 0$, the model shows a uniform horizontal topography with no distinct surface slope ($\theta = 0°$) (Figure. 5.9b). As the simulation progresses to 0.1 Ma, the NIP lithospheric complex begins to dynamically adjust, producing an asymmetric first-order topography with an overall eastward slope of approximately 0.2°. By $t = 0.21$ Ma, the model surface in the continental region undergoes significant vertical uplift, as evidenced by the increasing elevations of passive markers (P2, P3, and P4) (Figure. 5.9b). At P1 (western side), the NIP topography attains a height of approximately 5.65 km, which

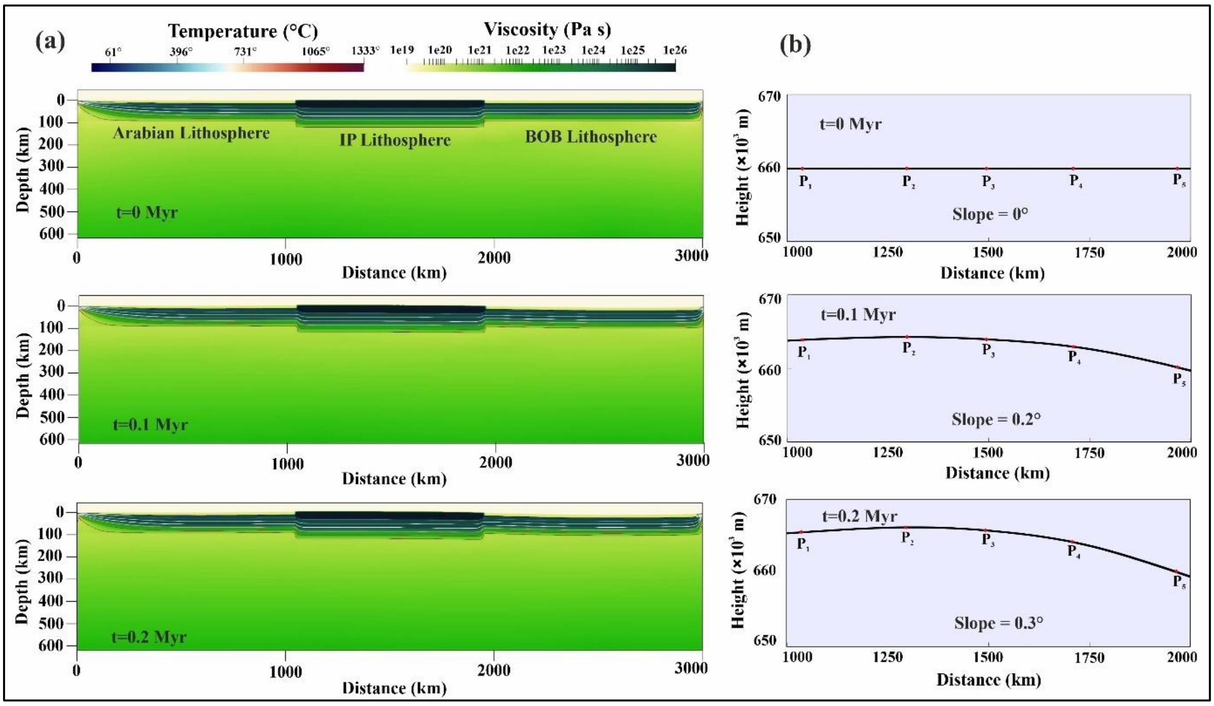

Figure 5.9 *(a) A time series presentation of the thermo-mechanical model simulations for the E-W transect (A-B) in the northern segment of Indian peninsula (NIP). The isotherms reveal variations in temperatures in the NIP model lithosphere, including the Arabian Sea (AS), and the Bay of Bengal (BOB). (b)Topographic evolution in the same model simulation by differential surface uplift. The topography is reconstructed from progressive vertical displacements of five tracer points: P_1 to P_5, as explained in the caption of Figure. 5.8. At t = 0 Myr, the topography is flat, which gains slopes of 0.2° and 0.3° at model run times: t = 0.1 Myr and 0.2 Myr, respectively.*

increases to a maximum of 6.29 km at P2 (eastern side). However, at P4 and P5, the maximum elevations are ~3.87 km and 0.55 km, respectively (Figure. 5.9b). This east–west variation in elevation results in a first-order eastward topographic slope of 0.33°, which is notably steeper than the topographic gradients observed in the corresponding digital elevation map of peninsular India. At t = 0.54 Ma, the topography of the NIP region continues to rise, with elevations of 8.47 km, 7.96 km, and 5.59 km at P2, P3, and P4, respectively. During this period, the eastward topographic slope steepens further to 0.37°. The representative model for the Central Indian Peninsula (CIP) segment consists of a 120 km thick continental lithospheric block (CD) that extends 750 km in length (Figure. 5.10a). This block is situated between two oceanic lithospheres, corresponding to the Bay of Bengal and the Arabian Sea. At the initial simulation time (t = 0 Ma), the model maintains a uniform, horizontal surface topography with a slope of θ = 0° (Figure. 5.10b). As the simulation progresses, the CIP lithospheric block begins to dynamically adjust, forming asymmetric topography with a consistent eastward slope (Figure. 5.10b), analogous to the trends observed in the NIP model. By t = 0.11 Ma, the CIP topography shows substantial elevation changes, as indicated by the positions of passive

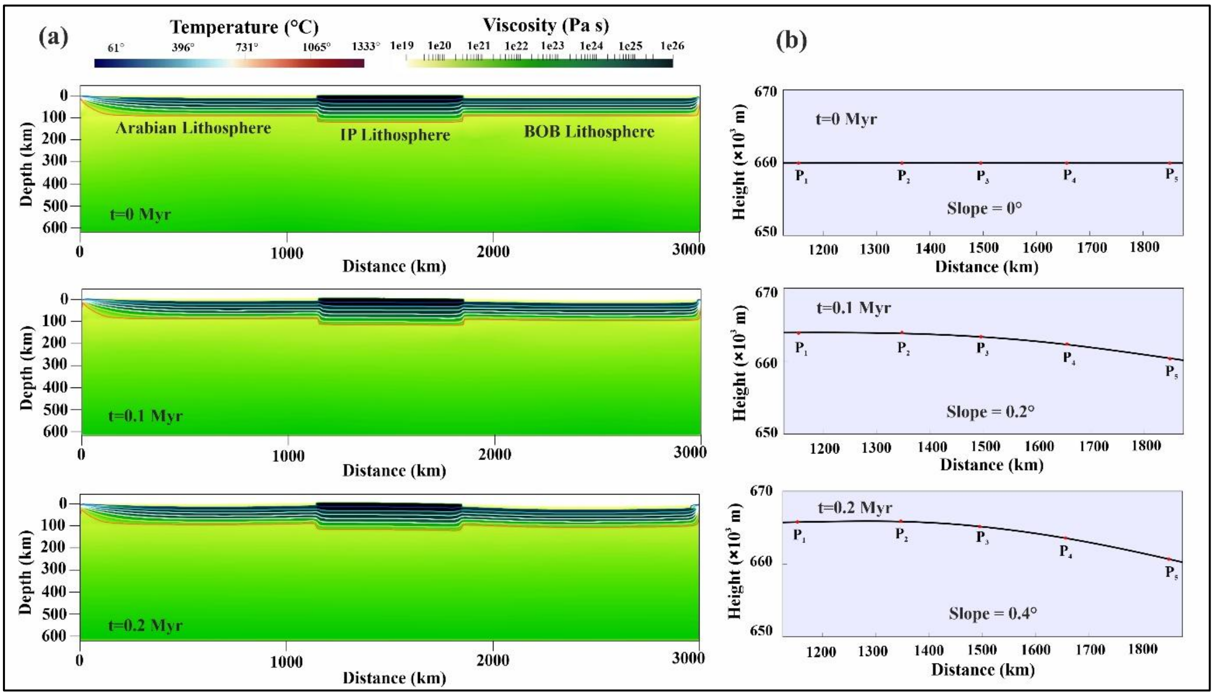

Figure 5.10 *(a) Thermo-mechanical model simulations for the Central Peninsular India (CIP) (L = 750 km), including the adjoining Arabian Sea (AS) and Bay of Bengal (BOB). The isotherm concentrations indicate varying thermal gradients in the continental and oceanic lithosphere. (b) Topographic evolution in the IP continental lithosphere. The initially (t = 0) flat model surface undergoes differential uplift to produce slopes of 0.2°, and 0.4° at model run times: t = 0.1, and 0.2 Myr.*

markers P2, P3, and P4 on the initial surface. At P2, the elevation (h) reaches a maximum of approximately 3.93 km, after which it decreases eastward to 3.34 km at P3. The elevation continues to decline further east after crossing a high of 2.34 km at P4 (Figure. 5.10b). This lateral variation in elevation results in an eastward topographic slope of $\theta = 0.29°$, which is consistent with observed natural landscape profiles (Figure. 5.10b and Figure. 5.5c). By t = 0.63 Ma, the surface topography of the CIP continues to rise, with elevations at passive markers P2 (h = 8.31 km), P3 (h = 7.6 km), and P4 (h = 5.61 km) showing significant increases. At this stage of the simulation, the calculated θ increases to 0.51° and maintains an eastward trend across the CIP (Figure. 5.10b).

The representative numerical model of the Southern India Peninsular (SIP) topography consists of a 120 km thick and 600 km long continental lithospheric block (EF), sandwiched between two oceanic lithospheres of contrasting ages: 40 Ma and 140 Ma in the Arabian Sea and the BOB east, respectively (Figure. 5.11a). The simulation run at t = 0 Ma shows flat topography with horizontal surface ($\theta = 0°$) (Figure. 5.11b), which on dynamic adjustments evolves to an asymmetrically elevated topography at t = 0.11 Ma. To describe the topographic

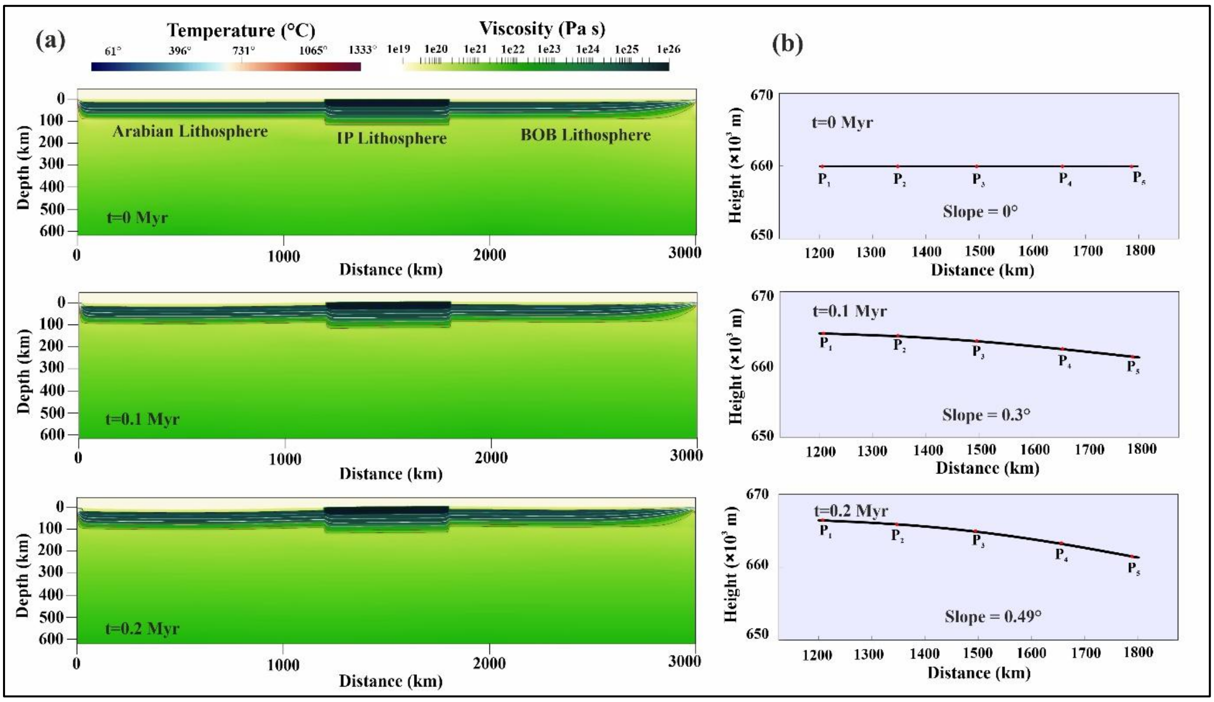

Figure 5.11 *(a) Thermo-mechanical model simulations for the Southern Indian peninsula (SIP) (L= 600 km). (b) Topographic evolution in the PI lithospheric block. It is to be noted that the model produces significantly steeper eastward surface slopes: 0.3° to 0.49° than the NIP and CIP models at the model run times: 0.1 Myr, and 0.2 Myr, respectively. In addition, the topography becomes more asymmetric.*

evolution, I choose three passive markers (P_2, P_3, P_4) on the surface of the initial model (Figure. 5.11b). On the western side (P_1) the SIP gains a maximum height (h) of about 4.27 km, which continuously decreases to attain an elevation, $h = 3.12\ km$ at P_3, and ultimately decreases to a height of about $h = 2.02\ km$ at P_4. The differential elevation changes give rise to asymmetric surface topography that consistently slopes ($\theta = 0.32^\circ$) towards east (Figure. 5.11b). A steep rise of topographic elevations occurs on the western side of the SIP section to produce a strong asymmetry of the surface topography with a large eastward slope ($\theta = 0.48^\circ$) at t = 0.22 Ma (Figure. 5.11b) which further increases to $\theta = 0.58^\circ$ at t = 0.69 Ma.

5.4.2.2 Mantle flow patterns and surface dynamics

The BOB lithospheric subsidence sets in large-scale, westward sublithospheric mantle flows, which play the most crucial role in controlling the geodynamics of IP topography (Figure. 5.12a, 5.12b, and 5.12c). The flows originate from a sublithospheric region beneath the central part of the BOB and follow curvilinear paths with predominantly horizontal velocity components. They eventually upwell at the western margin of IP. The west-ward flow is complemented by east-directed sub-lithospheric flows beneath the Arabian Sea, but significantly weaker than the westward counterparts. The two oppositely-directed mantle flows converge to form a focused upwelling zone beneath the western IP margin (Figure. 5.12a, 5.12b, and 5.12c).

The velocity fields exhibit a striking contrast in the mantle regions beneath the eastern and western flanks of the IP lithosphere. In the eastern flank, a highly subdued flow regime develops, characterized by a stagnation zone within the lithosphere (Figure. 5.12a, 5.12b, and 5.12c), indicating that the eastern IP lithosphere behaves as a relatively stable region. For instance, the sublithospheric velocity field in the NIP model (AB-section) shows strong horizontal flows (U_H = 3.23 cm/yr), with much smaller vertical components (U_V = 1.37 cm/yr) (Figure. 5.12a). In contrast, the velocity field at the western margin is dominated by large vertical velocity components (U_V = 2.61 cm/yr). This westward gradient in vertical velocity (U_V) induces a rotational motion of the IP lithosphere, leading to the eastward tilting of the IP plateau. These velocity field patterns suggest that the eastward topographic tilt is primarily driven by upwelling mantle dynamics, localized at the western flank of the IP lithosphere.

Serial model simulations reveal a systematic variation in sublithospheric mantle flow patterns from the northern to the southern transects of the IP (Figure. 5.12a, 5.12b, and 5.12c). As the E-W continental width of the IP decreases southward, the west-directed mantle flows extend beyond the western IP margin, encountering the weaker east-directed sublithospheric flows beneath the Arabian Sea. This interaction forms an upwelling zone at the ocean-continent boundary, resulting in the highest uplift velocities (U_V = 3.93 cm/yr) along the western margin of the IP (Figure 5.12b). Moving south, the location of this upwelling zone shifts eastward (Figure 5.12c), strengthening the upwelling dynamics and amplifying the rotational motion of the IP lithosphere. This shift is reflected in larger tilts of the topographic plateau in the southern sector of the IP (Figure 5.12c).

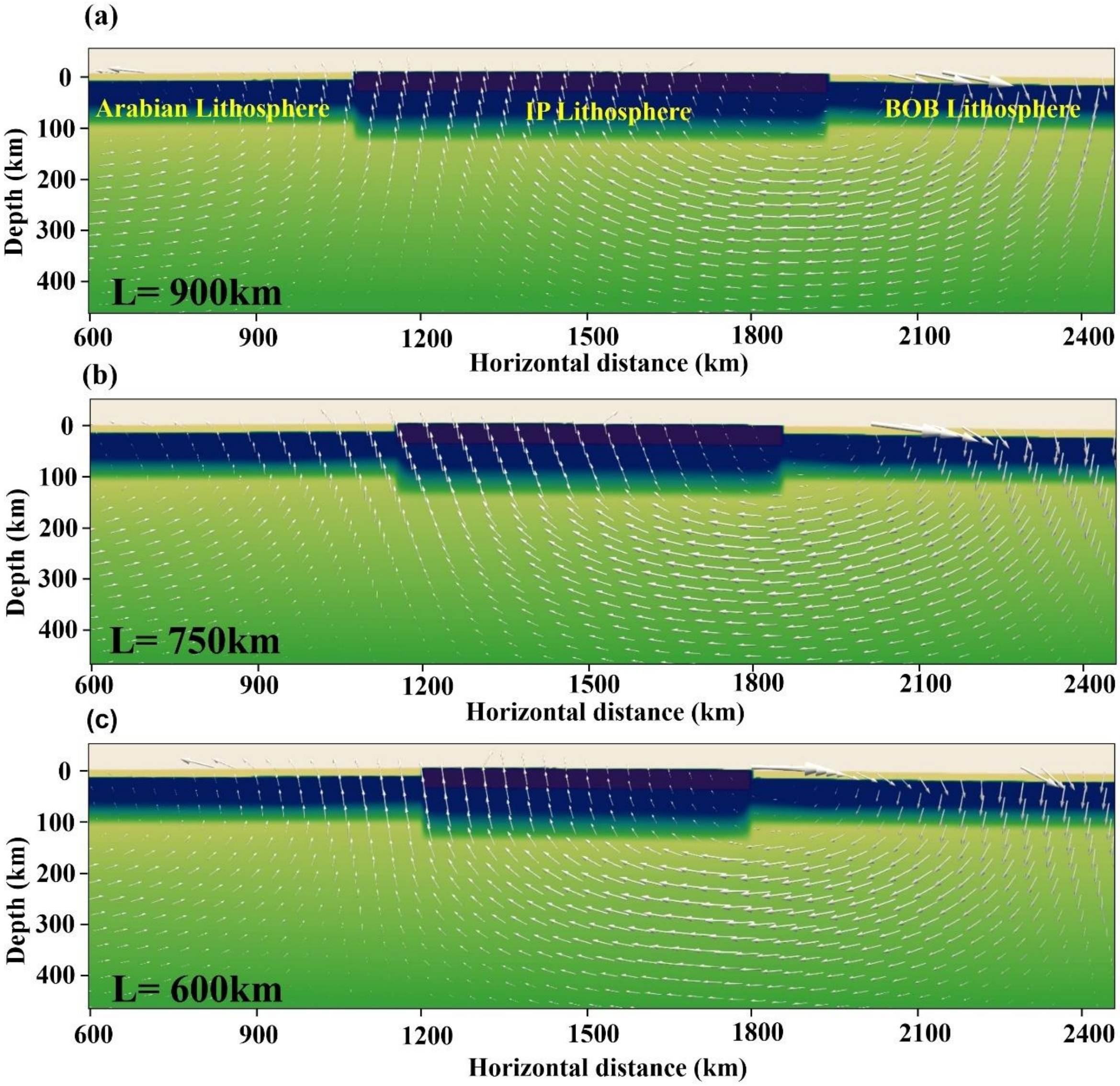

Figure 5.12 *IP model simulations showing sublithospheric mantle flow patterns and their interactions with the overlying lithosphere along three E-W transects: (a) NIP section, (b) CIP section, and SIP section. The models produce prominent westward sublithospheric flows, originated beneath the BOB, which eventually encounters the eastward flows originated beneath the AS, forming distinct upwelling zones at the western flank of the IP lithosphere. The reducing E-W continental width from north to south*

facilitates rotation of the continental lithospheric block, giving rise to greater topographic tilts in the southern sector.

5.4.2.3 Synthesis of model and observed IP topography

The topographic analysis of the E-W serial sections clearly suggests a steady increase in topographic asymmetry from the northern to the southern regions of IP, reflecting a notable enhancement in the eastward slopes moving towards south. For Example, our NIP model (AB section) estimates that the northern peninsular region develops an eastward topographic slope ($\theta = 0.37^{\circ}$), which multiplies to attain a substantially larger value ($\theta = 0.58^{\circ}$) in the EF section considered in our SIP model. This striking increase in the first-order topographic slope of peninsular India is a convincing indication of the geodynamic forces driving this asymmetry becoming stronger at the southern region of IP, which is evident from the sub-lithospheric mantle flow pattern described in the preceding section. The model simulations show that the initial E-W horizontal extent of the Indian continent lithosphere (L) determines the upwelling location of westward sublithospheric mantle flows (Figure. 10). Southwardly reducing θ allows the westward mantle flows to dominate over the eastward flow and upwells right at the ocean-continent lithospheric boundary. The upwelling thereby exerts vertical forces on the entire IP lithospheric stretch to the west, setting a favourable mechanical condition to facilitate the lithospheric rotation.

5.4.2.4 Synthesis of model and observed IP topography

The present modelling approach simplifies the geodynamic setting of the Indian Plate (IP) by excluding additional tectonic factors, such as the northward motion of the Indian plate, far-field effects from the Sumatra Trench subduction zone, and the synkinematic infilling of sediments in ocean basins. While this simplification aids in the modelling treatments, it limits the quantitative accuracy of the results. Moreover, the current 2D model assumes that gravity-driven sublithospheric mantle flows occur entirely on east-west (E-W) vertical planes, with minimal or no north-south (N-S) flow components. However, seismic anisotropy reveals significant azimuthal variations in mantle flow, suggesting directional variability that is not captured in this 2D framework. Consequently, the effects of non-planar mantle flows remain unaddressed in the current model. To address this limitation, future studies would benefit from incorporating 3D modelling to capture the full complexity of mantle dynamics. In the present model, the Indian continental lithosphere is represented as a two-layer continuum using a thinsheet approximation. This simplification reduces computational complexity but does not account for smaller-scale heterogeneities that may play a significant role in localized tectonic and geomorphological processes (Kale et al., 2017; Kumar et al., 2013; Saha et al., 2020). Despite this, the model provides valuable insights into the first-order topographic features of the Indian Peninsula, which appear to be primarily controlled by large-scale sublithospheric mantle flows. The main objective of this study is to explore the dynamics responsible for the eastward tilting of the Indian Peninsular topography. To achieve this, I focused on a relatively short time span, sufficient to capture the immediate lithospheric and mantle responses to tectonic and gravitational forces. This approach allows us to identify the specific mechanisms responsible for the observed topographic slopes.

5.5. References

Afonso, J.C., Ranalli, G., Fernàndez, M., 2007. Density structure and buoyancy of the oceanic lithosphere revisited. Geophys Res Lett 34. https://doi.org/10.1029/2007GL029515

Ali, J.R., Aitchison, J.C., 2008. Gondwana to Asia: Plate tectonics, paleogeography and the biological connectivity of the Indian sub-continent from the Middle Jurassic through latest Eocene (166–35 Ma). Earth Sci Rev 88, 145–166. https://doi.org/10.1016/J.EARSCIREV.2008.01.007

Allègre, C.J., Birck, J.L., Capmas, F., Courtillot, V., 1999. Age of the Deccan traps using 187Re–187Os systematics. Earth Planet Sci Lett 170, 197–204. https://doi.org/10.1016/S0012-821X(99)00110-7

Amal Dev, J., Tomson, J.K., 2024. U-Pb geochronology of rutiles from Southern granulite Terrane, India: Implications for the cooling and exhumation of East Gondwanan terranes. Precambrian Res 407, 107408. https://doi.org/10.1016/J.PRECAMRES.2024.107408

Asish, L.C., Parvez, I.A., Kühn, D., 2016. Probabilistic earthquake hazard assessment for Peninsular India. J Seismol 20, 629–653. https://doi.org/10.1007/S10950-015-9548-2/METRICS

Beaumont, C., Jamieson, R.A., Nguyen, M.H., Lee, B., 2001. Himalayan tectonics explained by extrusion of a low-viscosity crustal channel coupled to focused surface denudation. Nature 414, 738–742. https://doi.org/10.1038/414738a

Becker, T.W., 2017. Superweak asthenosphere in light of upper mantle seismic anisotropy. Geochemistry, Geophysics, Geosystems 18, 1986–2003. https://doi.org/10.1002/2017GC006886

Becker, T.W., Lebedev, S., Long, M.D., 2012. On the relationship between azimuthal anisotropy from shear wave splitting and surface wave tomography. J Geophys Res Solid Earth 117. https://doi.org/10.1029/2011JB008705

Beucher, R., Moresi, L., Giordani, J., Mansour, J., Sandiford, D., Farrington, R., Mondy, L., Mallard, C., Rey, P.P., Duclaux, G., Kaluza, O., Laik, A., Morón, S., 2019. UWGeodynamics: A teaching and research tool for numerical geodynamic modelling. J Open Source Softw 4, 1136. https://doi.org/10.21105/JOSS.01136

Bishop, P., 2007. Long-term landscape evolution: linking tectonics and surface processes. Earth Surf Process Landf 32, 329–365. https://doi.org/10.1002/ESP.1493

Biswal, T.K., Sinha, S., 2004. Fold-Thrust-Belt Structure of the Proterozoic Eastern Ghats Mobile Belt: A Proposed Correlation Between India and Antarctica in Gondwana. Gondwana Research 7, 43–56. https://doi.org/10.1016/S1342-937X(05)70305-1

Biswas, S., Majumdar, R.K., 1997. Seismicity and tectonics of the Bay of Bengal: Evidence for intraplate deformation of the northern Indian plate. Tectonophysics 269, 323–336. https://doi.org/10.1016/S0040-1951(96)00168-0

Biswas, S.K., 2003. Regional tectonic framework of the Pranhita–Godavari basin, India. J Asian Earth Sci 21, 543–551. https://doi.org/10.1016/S1367-9120(02)00145-1

Bohannon, R.G., Naeser, C.W., Schmidt, D.L., Zimmermann, R.A., 1989. The timing of uplift, volcanism, and rifting peripheral to the Red Sea: A case for passive rifting? J Geophys Res Solid Earth 94, 1683–1701. https://doi.org/10.1029/JB094IB02P01683

Bonnet, N.J., Beauvais, A., Arnaud, N., Chardon, D., Jayananda, M., 2016. Cenozoic lateritic weathering and erosion history of Peninsular India from 40Ar/39Ar dating of supergene K–Mn oxides. Chem Geol 446, 33–53. https://doi.org/10.1016/J.CHEMGEO.2016.04.018

Bonnet, N.J., Beauvais, A., Arnaud, N., Chardon, D., Jayananda, M., 2014. First 40Ar/39Ar dating of intense Late Palaeogene lateritic weathering in Peninsular India. Earth Planet Sci Lett 386, 126–137. https://doi.org/10.1016/J.EPSL.2013.11.002

Boraiaha, C.K., 2022. Geochemistry of the Precambrian mafic dykes in and around the Western Ghats greenstone belt, Western Dharwar Craton. Journal of Earth System Science 131, 1–19. https://doi.org/10.1007/S12040-022-01865-6/FIGURES/8

Bose, P.K., Sarkar, S., Das, N.G., Banerjee, S., Mandal, A., Chakraborty, N., 2015. Proterozoic Vindhyan Basin: Configuration and evolution. Geological Society Memoir 43, 85–102. https://doi.org/10.1144/M43.6

Burg, J.P., 2011. The Asia–Kohistan–India Collision: Review and Discussion. Frontiers in Earth Sciences 4, 279–309. https://doi.org/10.1007/978-3-540-88558-0_10

Campanile, D., Nambiar, C.G., Bishop, P., Widdowson, M., Brown, R., 2008. Sedimentation record in the Konkan-Kerala Basin: Implications for the evolution of the Western Ghats and the Western Indian passive margin. Basin Research 20, 3–22. https://doi.org/10.1111/J.1365-2117.2007.00341.X/CITE/REFWORKS

Catherine, J.K., Gahalaut, K., Gahalaut, V.K., 2007. Role of flexure in earthquake triggering along the Western Ghat escarpment, India. J Asian Earth Sci 31, 104–111. https://doi.org/10.1016/J.JSEAES.2007.04.005

Chadwick, B., Vasudev, V.N., Hegde, G. V., 2000. The Dharwar craton, southern India, interpreted as the result of Late Archaean oblique convergence. Precambrian Res 99, 91–111. https://doi.org/10.1016/S0301-9268(99)00055-8

Chadwick, B., Vasudev, V.N., Hegde, G. V., 1997. The dharwar craton, southern india, and its late archaean plate tectonic setting: current interpretations and controversies. Proceedings of the Indian Academy of Sciences, Earth and Planetary Sciences 106, 249–258. https://doi.org/10.1007/BF02843452

Chandra, U., 1977. Earthquakes of peninsular India—a seismotectonic study. Bulletin of the Seismological Society of America 67, 1387–1413. https://doi.org/10.1785/BSSA0670051387

Chatterjee, S., Goswami, A., Scotese, C.R., 2013. The longest voyage: Tectonic, magmatic, and paleoclimatic evolution of the Indian plate during its northward flight from

Gondwana to Asia. Gondwana Research 23, 238–267. https://doi.org/10.1016/J.GR.2012.07.001

Chatterjee, S., Scotese, C.R., Bajpai, S., 2017. The Restless Indian Plate and Its Epic Voyage from Gondwana to Asia: Its Tectonic, Paleoclimatic, and Paleobiogeographic Evolution. Geological Society of America. https://doi.org/10.1130/2017.2529(A)

Chetty, T.R.K., Murthy, D.S.N., 1994a. Collision tectonics in the late Precambrian Eastern Ghats Mobile Belt: mesoscopic to satellite-scale structural observations. Terra Nova 6, 72–81. https://doi.org/10.1111/J.1365-3121.1994.TB00635.X

Chetty, T.R.K., Murthy, D.S.N., 1994b. Collision tectonics in the late Precambrian Eastern Ghats Mobile Belt: mesoscopic to satellite-scale structural observations. Terra Nova 6, 72–81. https://doi.org/10.1111/J.1365-3121.1994.TB00635.X

Clark, M. k, Royden, L.H., 2000. Topographic ooze: Building the eastern margin of Tibet by lower crustal flow. Geology 28(8), 703–706. https://doi.org/https://doi.org/10.1130/0091-7613(2000)28%3C703:TOBTEM%3E2.0.CO;2

Clift, P.D., Hannigan, R., Blusztajn, J., Draut, A.E., 2002. Geochemical evolution of the Dras–Kohistan Arc during collision with Eurasia: Evidence from the Ladakh Himalaya, India. Island Arc 11, 255–273. https://doi.org/10.1046/J.1440-1738.2002.00371.X

Cochran, J.R., 2010. Morphology and tectonics of the Andaman Forearc, northeastern Indian Ocean. Geophys J Int 182, 631–651. https://doi.org/10.1111/J.1365-246X.2010.04663.X/2/182-2-631-FIG018.JPEG

Cochran, J.R., 1983. Effects of finite rifting times on the development of sedimentary basins. Earth Planet Sci Lett 66, 289–302. https://doi.org/10.1016/0012-821X(83)90142-5

Collier, J.S., Sansom, V., Ishizuka, O., Taylor, R.N., Minshull, T.A., Whitmarsh, R.B., 2008. Age of Seychelles–India break-up. Earth Planet Sci Lett 272, 264–277. https://doi.org/10.1016/J.EPSL.2008.04.045

Cooper, C.M., Miller, M.S., Moresi, L., 2017. The structural evolution of the deep continental lithosphere. Tectonophysics 695, 100–121. https://doi.org/10.1016/j.tecto.2016.12.004

Copley, A., Avouac, J.P., Wernicke, B.P., 2011. Evidence for mechanical coupling and strong Indian lower crust beneath southern Tibet. Nature 472, 79–81. https://doi.org/10.1038/nature09926

Copley, A., Mckenzie, D., 2007. Models of crustal flow in the India-Asia collision zone. Geophys J Int 169, 683–698. https://doi.org/10.1111/J.1365-246X.2007.03343.X/2/M_169-2-683-TBL001.JPEG

Copley, A., Mitra, S., Sloan, R.A., Gaonkar, S., Reynolds, K., 2014. Active faulting in apparently stable peninsular India: Rift inversion and a Holocene-age great earthquake on the Tapti Fault. J Geophys Res Solid Earth 119, 6650–6666. https://doi.org/10.1002/2014JB011294

Cox, K.G., 1989. The role of mantle plumes in the development of continental drainage patterns. Nature 342, 873–877. https://doi.org/10.1038/342873A0

Cox, K.G., 1980. A Model for Flood Basalt Vulcanism. Journal of Petrology 21, 629–650. https://doi.org/10.1093/PETROLOGY/21.4.629

Crawford, A.R., 1969. Reconnaissance Rb-Sr Dating of the Precambrian Rocks of Southern Peninsular India. Journal of the Geological Society of India 10, 117–166. https://doi.org/10.17491/JGSI/1969/100201

Curray, J.R., 2005. Tectonics and history of the Andaman Sea region. J Asian Earth Sci 25, 187–232. https://doi.org/10.1016/J.JSEAES.2004.09.001

Curray, J.R., Moore, D.G., 1974. Sedimentary and Tectonic Processes in the Bengal Deep-Sea Fan and Geosyncline. The Geology of Continental Margins 617–627. https://doi.org/10.1007/978-3-662-01141-6_45

Dasgupta, R., Sen, J., Mandal, N., 2021. Bending curvatures of subducting plates: old versus young slabs. Geophys J Int 225, 1963–1981. https://doi.org/10.1093/GJI/GGAB070

DeCelles, P.G., Quade, J., Kapp, P., Fan, M., Dettman, D.L., Ding, L., 2007. High and dry in central Tibet during the Late Oligocene. Earth Planet Sci Lett 253, 389–401. https://doi.org/10.1016/J.EPSL.2006.11.001

Desa, M.A., Ismaiel, M., Suresh, Y., Krishna, K.S., 2018. Oblique strike-slip motion off the Southeastern Continental Margin of India: Implication for the separation of Sri Lanka from India. J Asian Earth Sci 156, 111–121. https://doi.org/10.1016/J.JSEAES.2018.01.015

Devey, C.W., Lightfoot, P.C., 1986. Volcanological and tectonic control of stratigraphy and structure in the western Deccan traps. Bull Volcanol 48, 195–207. https://doi.org/10.1007/BF01087674/METRICS

Dey, S., Moyen, J.F., 2020. Archean granitoids of India: Windows into early earth tectonics – an introduction. Geol Soc Spec Publ 489, 1–13. https://doi.org/10.1144/SP489-2020-155/ASSET/77FD8629-9782-4093-B89C-02A1EBEB23BE/ASSETS/GRAPHIC/01_GSLSPECPUB2020-155F04.JPEG

DiBiase, R.A., Whipple, K.X., 2011. The influence of erosion thresholds and runoff variability on the relationships among topography, climate, and erosion rate. J Geophys Res Earth Surf 116. https://doi.org/10.1029/2011JF002095

Ding, L., Kapp, P., Cai, F., Garzione, C.N., Xiong, Z., Wang, H., Wang, C., 2022. Timing and mechanisms of Tibetan Plateau uplift. Nature Reviews Earth & Environment 2022 3:10 3, 652–667. https://doi.org/10.1038/s43017-022-00318-4

Dole, G., Das, S., Kale, V.S., 2022. Tectonic framework of geomorphic evolution of the Deccan Volcanic Province, India. Earth Sci Rev 228, 103988. https://doi.org/10.1016/J.EARSCIREV.2022.103988

Dubey, C.P., Tiwari, V.M., 2022. Lithospheric-mantle modification beneath the thick sedimentary fan of Bay of Bengal: Inference from the 3D gravity model. Tectonophysics 826, 229253. https://doi.org/10.1016/J.TECTO.2022.229253

Dubey, C.P., Tiwari, V.M., 2018. Gravity Anomalies and Crustal Thickness Variations over the Western Ghats. Journal of the Geological Society of India 92, 517–522. https://doi.org/10.1007/S12594-018-1059-7/METRICS

Dyment, J., 1998. Evolution of the Carlsberg Ridge between 60 and 45 Ma: Ridge propagation, spreading asymmetry, and the Deccan-Reunion hotspot. J Geophys Res Solid Earth 103, 24067–24084. https://doi.org/10.1029/98JB01759

Eagles, G., Hoang, H.H., 2014. Cretaceous to present kinematics of the Indian, African and Seychelles plates. Geophys J Int 196, 1–14. https://doi.org/10.1093/GJI/GGT372

Ellis, M.A., Densmore, A.L., Anderson, R.S., 1999. Development of mountainous topography in the Basin Ranges, USA. Basin Research 11, 21–41. https://doi.org/10.1046/J.1365-2117.1999.00087.X/CITE/REFWORKS

Fang, X., Dupont-Nivet, G., Wang, C., Song, C., Meng, Q., Zhang, W., Nie, J., Zhang, T., Mao, Z., Chen, Y., 2020. Revised chronology of central Tibet uplift (Lunpola Basin). Sci Adv 6. https://doi.org/10.1126/SCIADV.ABA7298/SUPPL_FILE/ABA7298_SM.PDF

Flesch, L.M., Haines, A.J., Holt, W.E., 2001. Dynamics of the India-Eurasia collision zone. J Geophys Res Solid Earth 106, 16435–16460. https://doi.org/10.1029/2001JB000208

Gaina, C., Müller, R.D., Brown, B., Ishihara, T., Ivanov, S., 2007. Breakup and early seafloor spreading between India and Antarctica. Geophys J Int 170, 151–169. https://doi.org/10.1111/J.1365-246X.2007.03450.X/2/170-1-151-FIG011.JPEG

Gaina, C., Van Hinsbergen, D.J.J., Spakman, W., 2015. Tectonic interactions between India and Arabia since the Jurassic reconstructed from marine geophysics, ophiolite geology, and seismic tomography. Tectonics 34, 875–906. https://doi.org/10.1002/2014TC003780

Gangrade, B.K., Arora, S.K., 2000. Seismicity of the Indian peninsular shield from regional earthquake data. Pure Appl Geophys 157, 1683–1705. https://doi.org/10.1007/PL00001056/METRICS

Gerya, T., 2014. Precambrian geodynamics: Concepts and models. Gondwana Research 25, 442–463. https://doi.org/10.1016/J.GR.2012.11.008

Gerya, T. V., Perchuk, L.L., Burg, J.P., 2008. Transient hot channels: Perpetrating and regurgitating ultrahigh-pressure, high-temperature crust–mantle associations in collision belts. Lithos 103, 236–256. https://doi.org/10.1016/J.LITHOS.2007.09.017

Ghosh, D., Sen, J., Mandal, N., 2024. Periodicity in the Deccan Volcanism Modulated by Plume Perturbations at the Mid-Mantle Transition Zone. J Geophys Res Solid Earth 129, e2024JB029020. https://doi.org/10.1029/2024JB029020

Ghosh, P., Sengupta, D.P., 2020. Geodynamics of Gondwanaland. Springer Geology 213–232. https://doi.org/10.1007/978-3-030-15989-4_7

Gibbons, A.D., Barckhausen, U., Van Den Bogaard, P., Hoernle, K., Werner, R., Whittaker, J.M., Müller, R.D., 2012. Constraining the Jurassic extent of Greater India: Tectonic evolution of the West Australian margin. Geochemistry, Geophysics, Geosystems 13. https://doi.org/10.1029/2011GC003919

Gibbons, A.D., Zahirovic, S., Müller, R.D., Whittaker, J.M., Yatheesh, V., 2015. A tectonic model reconciling evidence for the collisions between India, Eurasia and intra-oceanic arcs of the central-eastern Tethys. Gondwana Research 28, 451–492. https://doi.org/10.1016/j.gr.2015.01.001

Gokarn, S.G., Rao, C.K., Selvaraj, C., Gupta, G., 2013. Crustal evolution and tectonics of the Archean Bundelkhand craton, Central India. Journal of the Geological Society of India 82, 455–460. https://doi.org/10.1007/S12594-013-0176-6/METRICS

Goswami, S., Bhagat, S., Pande, D., Choudhury, D.K., Saravanan, B., Sinha, D.K., 2023. Implication of deformation fabrics of schist-migmatite-gneiss and granite in understanding regional tectonics: Eastern Dharwar Craton (EDC), India. Proceedings of the Indian National Science Academy 89, 613–643. https://doi.org/10.1007/S43538-023-00173-X/METRICS

Gunnell, Y., Fleitout, L., 1998. Shoulder uplift of the Western Ghats passive margin, India: a denudational model. Earth Surf Process Landf 23, 391–404.

Gunnell, Y., Gallagher, K., Carter, A., Widdowson, M., Hurford, A.J., 2003. Denudation history of the continental margin of western peninsular India since the early Mesozoic – reconciling apatite fission-track data with geomorphology. Earth Planet Sci Lett 215, 187–201. https://doi.org/10.1016/S0012-821X(03)00380-7

Gupta, S., Kanna, N., Kumar, S., Sivaram, K., 2018. Crustal Thickness and Composition Variation along the Western Ghats of India through Teleseismic Receiver Function Analysis. Journal of the Geological Society of India 92, 523–528. https://doi.org/10.1007/S12594-018-1061-0/METRICS

Hager, B.H., 1991. Mantle Viscosity: A Comparison of Models from Postglacial Rebound and from the Geoid, Plate Driving Forces, and Advected Heat Flux, in: Glacial Isostasy, Sea-Level and Mantle Rheology. Springer Netherlands, Dordrecht, pp. 493–513. https://doi.org/10.1007/978-94-011-3374-6_23

Hahn, G., Kodl, G., de Wall, H., Schulz, B., Bestmann, M., Chauhan, N.K., 2020. Deformation in the Aravalli Supergroup, Aravalli-Delhi Mobile Belt, NW India and Tectonic Significance 23–55. https://doi.org/10.1007/978-3-030-40593-9_2

Heintz, M., Kumar, V.P., Gaur, V.K., Priestley, K., Rai, S.S., Prakasam, K.S., 2009. Anisotropy of the Indian continental lithospheric mantle. Geophys J Int 179, 1341–1360. https://doi.org/10.1111/J.1365-246X.2009.04395.X/3/179-3-1341-FIG012.JPEG

Hirth, G., Kohlstedt, D., 2003. Rheology of the upper mantle and the mantle wedge: a view from the experimentalists. Geophysical monograph-american geophysical union 138, 83–106.

Hofmann, A., Jodder, J., Xie, H., Bolhar, R., Whitehouse, M., Elburg, M., 2022. The Archaean geological history of the Singhbhum Craton, India – a proposal for a consistent framework of craton evolution. Earth Sci Rev 228, 103994. https://doi.org/10.1016/J.EARSCIREV.2022.103994

Hoggard, M.J., White, N., Al-Attar, D., 2016. Global dynamic topography observations reveal limited influence of large-scale mantle flow. Nature Geoscience 2016 9:6 9, 456–463. https://doi.org/10.1038/ngeo2709

Houseman, G., England, P., 1993. Crustal thickening versus lateral expulsion in the Indian-Asian continental collision. J Geophys Res Solid Earth 98, 12233–12249. https://doi.org/10.1029/93JB00443

Illa, B., Reshma, K.S., Kumar, P., Srinagesh, D., Haldar, C., Kumar, S., Mandal, P., 2021. Pn tomography and anisotropic study of the Indian shield and the adjacent regions. Tectonophysics 813, 228932. https://doi.org/10.1016/J.TECTO.2021.228932

Illarionov, V.K., Boyko, A.N., 2018. Geodynamic Aspects of the Evolution of the Northwestern Indian Ocean. Izvestiya - Atmospheric and Ocean Physics 54, 768–776. https://doi.org/10.1134/S0001433818070034/FIGURES/3

Jacob, J., Dyment, J., Ghosal, D., Dewangan, P., 2021. Strike-slip seismicity at the Andaman-Sumatra Subduction Zone: Role of the fracture zones and age of the subducting lithosphere. Tectonophysics 811, 228862. https://doi.org/10.1016/J.TECTO.2021.228862

Jagoutz, O., Bouilhol, P., Schaltegger, U.R.S., Müntener, O., 2019. The isotopic evolution of the Kohistan Ladakh arc from subduction initiation to continent arc collision. Geol Soc Spec Publ 483, 165–182. https://doi.org/10.1144/SP483.7

Jaiswal, K., Sinha, R., 2007. Probabilistic Seismic-Hazard Estimation for Peninsular India. Bulletin of the Seismological Society of America 97, 318–330. https://doi.org/10.1785/0120050127

Jayananda, M., Dey, S., Aadhiseshan, K.R., 2020. Evolving Early Earth: Insights from Peninsular India. Springer Geology 5–103. https://doi.org/10.1007/978-3-030-15989-4_2

Jayananda, M., Guitreau, M., Aadhiseshan, K.R., Miyazaki, T., Chung, S.L., 2023. Origin of the oldest (3600–3200 Ma) cratonic core in the Western Dharwar Craton, Southern India: Implications for evolving tectonics of the Archean Earth. Earth Sci Rev 236, 104278. https://doi.org/10.1016/J.EARSCIREV.2022.104278

Johnson, B.D., Powell, C.M.A., Veevers, J.J., 1980. Early spreading history of the Indian Ocean between India and Australia. Earth Planet Sci Lett 47, 131–143. https://doi.org/10.1016/0012-821X(80)90112-0

Kailasam, L.N., 1975. Epeirogenic studies in India with reference to recent vertical movements. Tectonophysics 29, 505–521. https://doi.org/10.1016/0040-1951(75)90178-X

Kale, V.S., 2002. Fluvial geomorphology of Indian rivers: an overview. Progress in Physical Geography: Earth and Environment 26, 400–433. https://doi.org/10.1191/0309133302PP343RA

Kale, V.S., Dole, G., Upasani, D., Pillai, S.P., 2017. Deccan plateau uplift: Insights from parts of western uplands, Maharashtra, India. Geol Soc Spec Publ 445, 11–46. https://doi.org/10.1144/SP445.2/ASSET/AC944E2D-CDFF-4081-9DE7-9281E74175EF/ASSETS/GRAPHIC/SP445-1505F14.JPEG

Karato, S., Wu, P., 1993. Rheology of the Upper Mantle: A Synthesis. Science (1979) 260, 771–778. https://doi.org/10.1126/SCIENCE.260.5109.771

Katz, M.B., 2000. Sri Lanka - India Intraplate Tectonics - Precambrian to Present. Gondwana Research 3, 3–5. https://doi.org/10.1016/S1342-937X(05)70052-6

Kaur, P., Chaudhri, N., Saha, L., Nasipuri, P., 2024. Crustal evolution of the Aravalli and Bundelkhand Archean nuclei, North Indian Block: recent advances and perspectives. Proceedings of the Indian National Science Academy 90, 196–208. https://doi.org/10.1007/S43538-024-00278-X/METRICS

Kent, D. V., Muttoni, G., 2008. Equatorial convergence of India and early Cenozoic climate trends. Proc Natl Acad Sci U S A 105, 16065–16070. https://doi.org/10.1073/PNAS.0805382105/ASSET/C392017F-5074-45AD-A735-13E0D4AC2513/ASSETS/GRAPHIC/ZPQ9990849560003.JPEG

Khan, S.D., Walker, D.J., Hall, S.A., Burke, K.C., Shah, M.T., Stockli, L., 2009. Did the Kohistan-Ladakh island arc collide first with India? GSA Bulletin 121, 366–384. https://doi.org/10.1130/B26348.1

Kirby, E., Whipple, K.X., 2012. Expression of active tectonics in erosional landscapes. J Struct Geol 44, 54–75. https://doi.org/10.1016/J.JSG.2012.07.009

Kiusalaas, J., 2015. Numerical Methods in Engineering with MATLAB®. Numerical Methods in Engineering with MATLAB®. https://doi.org/10.1017/CBO9781316341599

Krapež, B., Srinivasa Sarma, D., Ram Mohan, M., McNaughton, N.J., Rasmussen, B., Wilde, S.A., 2020. Tectonostratigraphy of the Late Archean Dharwar Supergroup, Dharwar Craton, India: Defining a tectonic history from spatially linked but temporally distinct intracontinental and arc-related basins. Earth Sci Rev 201. https://doi.org/10.1016/J.EARSCIREV.2019.102966

Krishna, K.S., Abraham, H., Sager, W.W., Pringle, M.S., Frey, F., Gopala Rao, D., Levchenko, O. V., 2012. Tectonics of the Ninetyeast Ridge derived from spreading records in adjacent oceanic basins and age constraints of the ridge. J Geophys Res Solid Earth 117. https://doi.org/10.1029/2011JB008805

Krishna, K.S., Michael, L., Bhattacharyya, R., Majumdar, T.J., 2009. Geoid and gravity anomaly data of conjugate regions of Bay of Bengal and Enderby Basin: New constraints on breakup and early spreading history between India and Antarctica. J Geophys Res Solid Earth 114. https://doi.org/10.1029/2008JB005808

Kumar, M.R., Saikia, D., Singh, A., Srinagesh, D., Baidya, P.R., Dattatrayam, R.S., 2013. Low shear velocities in the sub-lithospheric mantle beneath the Indian shield? J Geophys Res Solid Earth 118, 1142–1155. https://doi.org/10.1002/JGRB.50114

Kumar, V.P., Prakasam, K.S., Rai, S.S., Gupta, S., 2015. Upper-mantle anisotropy beneath the south Indian Shield: Influenced by ancient and recent Earth processes. Lithosphere 7, 108–116. https://doi.org/10.1130/L405.1

Larson, K.M., Bürgmann, R., Bilham, R., Freymueller, J.T., 1999. Kinematics of the India-Eurasia collision zone from GPS measurements. J Geophys Res Solid Earth 104, 1077–1093. https://doi.org/10.1029/1998JB900043

Levchenko, O. V., Sushchevskaya, N.M., Marinova, Y.G., 2021. The Nature and Evolution of the Ninetyeast Ridge: A Key Tectonic and Magmatic Feature of the East Indian Ocean. Geotectonics 55, 194–218. https://doi.org/10.1134/S0016852121020060/FIGURES/9

Mahoney, J.J., Duncan, R.A., Khan, W., Gnos, E., McCormick, G.R., 2002. Cretaceous volcanic rocks of the South Tethyan suture zone, Pakistan: implications for the Réunion hotspot and Deccan Traps. Earth Planet Sci Lett 203, 295–310. https://doi.org/10.1016/S0012-821X(02)00840-3

Mahoney, J.J., Macdougall, J.D., Lugmair, G.W., Gopalan, K., 1983. Kerguelen hotspot source for Rajmahal Traps and Ninetyeast Ridge? Nature 1983 303:5916 303, 385–389. https://doi.org/10.1038/303385a0

Maiti, G., Roy, A., Sen, J., Mandal, N., 2021. Impact of Decelerating India-Asia Convergence on the Crustal Flow Kinematics in Tibet: An Insight From Scaled Laboratory Modeling. Geochemistry, Geophysics, Geosystems 22, e2021GC009967. https://doi.org/10.1029/2021GC009967

Mandal, N., Bose, S., Baruah, A., Sarkar, S., 2015. First-order topography of the Himalayan Mountain belt: A deep-crustal flow analysis. Geol Soc Spec Publ 412, 5–23. https://doi.org/10.1144/SP412.9/ASSET/AE19F504-089A-45E4-9C17-2024891F2E48/ASSETS/GRAPHIC/SP412-1190F11.JPEG

Mandal, P., 2011. Upper mantle seismic anisotropy in the intra-continental Kachchh rift zone, Gujarat, India. Tectonophysics 509, 81–92. https://doi.org/10.1016/J.TECTO.2011.05.013

Mandal, S.K., Burg, J.P., Haghipour, N., 2017. Geomorphic fluvial markers reveal transient landscape evolution in tectonically quiescent southern Peninsular India. Geological Journal 52, 681–702. https://doi.org/10.1002/GJ.2833

Mandal, S.K., Fellin, M.G., Burg, J.P., Maden, C., 2015. Phanerozoic surface history of southern Peninsular India from apatite (U-Th-Sm)/He data. Geochemistry, Geophysics, Geosystems 16, 3626–3648. https://doi.org/10.1002/2015GC005977

Mandal, S.K., Lupker, M., Burg, J.P., Valla, P.G., Haghipour, N., Christl, M., 2015. Spatial variability of 10Be-derived erosion rates across the southern Peninsular Indian escarpment: A key to landscape evolution across passive margins. Earth Planet Sci Lett 425, 154–167. https://doi.org/10.1016/J.EPSL.2015.05.050

Mansour, J., Giordani, J., Moresi, L., Beucher, R., Kaluza, O., Velic, M., Farrington, R., Quenette, S., Beall, A., 2020. Underworld2: Python Geodynamics Modelling for Desktop, HPC and Cloud. J Open Source Softw 5, 1797. https://doi.org/10.21105/JOSS.01797

Martin, C.R., Jagoutz, O., Upadhyay, R., Royden, L.H., Eddy, M.P., Bailey, E., Nichols, C.I.O., Weiss, B.P., 2020. Paleocene latitude of the Kohistan-Ladakh arc indicates multistage India-Eurasia collision. Proc Natl Acad Sci U S A 117, 29487–29494. https://doi.org/10.1073/PNAS.2009039117/SUPPL_FILE/PNAS.2009039117.SD01.XLSX

Maurya, S., Montagner, J.P., Kumar, M.R., Stutzmann, E., Kiselev, S., Burgos, G., Rao, N.P., Srinagesh, D., 2016. Imaging the lithospheric structure beneath the Indian continent. J Geophys Res Solid Earth 121, 7450–7468. https://doi.org/10.1002/2016JB012948

McCaffrey, R., 2009. The tectonic framework of the sumatran subduction zone. Annu Rev Earth Planet Sci 37, 345–366. https://doi.org/10.1146/ANNUREV.EARTH.031208.100212/CITE/REFWORKS

McKenzie, D., 1978. Some remarks on the development of sedimentary basins. Earth Planet Sci Lett 40, 25–32. https://doi.org/10.1016/0012-821X(78)90071-7

McKenzie, D., Sclater, J.G., 1971. The Evolution of the Indian Ocean since the Late Cretaceous. Geophys J Int 24, 437–528. https://doi.org/10.1111/J.1365-246X.1971.TB02190.X

Meert, J.G., Pandit, M.K., 2015. The archaean and proterozoic history of Peninsular India: Tectonic framework for precambrian sedimentary basins in India. Geological Society Memoir 43, 29–54. https://doi.org/10.1144/M43.3/ASSET/B95394B5-5AB9-4E56-8259-13D038FF2A4E/ASSETS/IMAGES/LARGE/M43_CH03F13.JPG

Melluso, L., Mahoney, J.J., Dallai, L., 2006. Mantle sources and crustal input as recorded in high-Mg Deccan Traps basalts of Gujarat (India). Lithos 89, 259–274. https://doi.org/10.1016/J.LITHOS.2005.12.007

Miall, A.D., Catuneanu, O., Eriksson, P.G., Mazumder, R., 2015. A brief synthesis of Indian Precambrian basins: Classification and genesis of basin-fills. Geological Society Memoir 43, 339–347. https://doi.org/10.1144/M43.23

Minár, J., Evans, I.S., Jenčo, M., 2020. A comprehensive system of definitions of land surface (topographic) curvatures, with implications for their application in geoscience modelling and prediction. Earth Sci Rev 211, 103414. https://doi.org/10.1016/J.EARSCIREV.2020.103414

Ming-Yuan, L., 2009. The Realization of Curve Fitting with Matlab. Journal of Inner Mongolia University for the Nationalities.

Mishra, A., Chaubey, A.K., Kumar, S., Kumar, P.V., Kumar, P., Dubey, K.M., 2020. Does the Laxmi Ridge continue towards the Laccadive Ridge? New insights from an integrated geophysical study. J Asian Earth Sci 201, 104491. https://doi.org/10.1016/J.JSEAES.2020.104491

Mishra, A., Chaubey, A.K., Sreejith, K.M., Kumar, S., 2018. Crustal underplating and effective elastic plate thickness of the Laxmi Ridge, northern Arabian Sea. Tectonophysics 744, 82–92. https://doi.org/10.1016/J.TECTO.2018.06.013

Mishra, D.C., Chandra Sekhar, D. V., Venkata Raju, D.C., Vijaya Kumar, V., 1999. Crustal structure based on gravity–magnetic modelling constrained from seismic studies under Lambert Rift, Antarctica and Godavari and Mahanadi rifts, India and their interrelationship. Earth Planet Sci Lett 172, 287–300. https://doi.org/10.1016/S0012-821X(99)00212-5

Mishra, D.C., Gupta, S.B., Venkatarayudu, M., 1989. Godavari rift and its extension towards the east coast of India. Earth Planet Sci Lett 94, 344–352. https://doi.org/10.1016/0012-821X(89)90151-9

Mitchell, C., Widdowson, M., 1991. A geological map of the southern Deccan Traps, India and its structural implications. J Geol Soc London 148, 495–505. https://doi.org/10.1144/GSJGS.148.3.0495

Mittal, T., Richards, M.A., 2021. The Magmatic Architecture of Continental Flood Basalts: 2. A New Conceptual Model. J Geophys Res Solid Earth 126, e2021JB021807. https://doi.org/10.1029/2021JB021807

Mittal, T., Richards, M.A., Fendley, I.M., 2021. The Magmatic Architecture of Continental Flood Basalts I: Observations From the Deccan Traps. J Geophys Res Solid Earth 126. https://doi.org/10.1029/2021JB021808

Mohan, M.R., Asokan, A.D., Wilde, S.A., 2020. Crustal growth of the eastern dharwar craton: A neoarchean collisional orogeny? Geol Soc Spec Publ 489, 51–77. https://doi.org/10.1144/SP489-2019-108

Mohan, M.R., Piercey, S.J., Kamber, B.S., Sarma, D.S., 2013. Subduction related tectonic evolution of the Neoarchean eastern Dharwar Craton, southern India: New geochemical and isotopic constraints. Precambrian Res 227, 204–226. https://doi.org/10.1016/J.PRECAMRES.2012.06.012

Mohanty, D.D., Biswal, S., Yoshizawa, K., 2024. Decoupled deformation between crust and mantle beneath Indo-Burmese Wedge: A new seismotectonic model. Earth Planet Sci Lett 648, 119089. https://doi.org/10.1016/J.EPSL.2024.119089

Mohanty, P.K., Pradhan, Y., Nayak, S.R., Panda, U.S., Mohapatra, G.N., 2008. Sediment Dispersion in the Bay of Bengal. Monitoring and Modelling Lakes and Coastal Environments 50–78. https://doi.org/10.1007/978-1-4020-6646-7_5

Mohanty, S.P., 2023. Proterozoic basins of the Bundelkhand Craton, India: Correlations and significance in understanding the tectonic evolution. Geosystems and Geoenvironment 2, 100155. https://doi.org/10.1016/J.GEOGEO.2022.100155

Mohanty, S.P., 2021. The Bastar Craton of Central India: Tectonostratigraphic evolution and implications in global correlations. Earth Sci Rev 221, 103770. https://doi.org/10.1016/J.EARSCIREV.2021.103770

Mondal, M.E.A., Hussain, M.F., Ahmad, T., 2006. Continental growth of Bastar craton, central Indian shield during precambrian via multiphase subduction and lithospheric extension/rifting: evidence from geochemistry of gneisses, granitoids and mafic dykes.

Morgan, J.P., Smith, W.H.F., 1992. Flattening of the sea-floor depth-age curve as a response to asthenospheric flow. Nature 359, 524–527. https://doi.org/10.1038/359524a0

Mukherjee, A., Fryar, A.E., Thomas, W.A., 2009. Geologic, geomorphic and hydrologic framework and evolution of the Bengal basin, India and Bangladesh. J Asian Earth Sci 34, 227–244. https://doi.org/10.1016/J.JSEAES.2008.05.011

Mukhopadhyay, G., Mukhopadhyay, S.K., Roychowdhury, M., Parui, P.K., 2010. Stratigraphic correlation between different Gondwana Basins of India. Journal of the Geological Society of India 76, 251–266. https://doi.org/10.1007/S12594-010-0097-6/METRICS

Müller, R.D., Yatheesh, V., Shuhail, M., 2015. The tectonic stress field evolution of India since the Oligocene. Gondwana Research 28, 612–624. https://doi.org/10.1016/J.GR.2014.05.008

Neuharth, D., Brune, S., Glerum, A., Morley, C.K., Yuan, X., Braun, J., 2022a. Flexural strike-slip basins. Geology 50, 361–365. https://doi.org/10.1130/G49351.1

Neuharth, D., Brune, S., Wrona, T., Glerum, A., Braun, J., Yuan, X., 2022b. Evolution of Rift Systems and Their Fault Networks in Response to Surface Processes. Tectonics 41, e2021TC007166. https://doi.org/10.1029/2021TC007166

Nobre Silva, I.G., Weis, D., Scoates, J.S., Barling, J., 2013. The Ninetyeast Ridge and its Relation to the Kerguelen, Amsterdam and St. Paul Hotspots in the Indian Ocean. Journal of Petrology 54, 1177–1210. https://doi.org/10.1093/PETROLOGY/EGT009

Norton, I.O., Sclater, J.G., 1979. A model for the evolution of the Indian Ocean and the breakup of Gondwanaland. J Geophys Res Solid Earth 84, 6803–6830. https://doi.org/10.1029/JB084IB12P06803

O'Neill, C., Müller, D., Steinberger, B., 2003. Geodynamic implications of moving Indian Ocean hotspots. Earth Planet Sci Lett 215, 151–168. https://doi.org/10.1016/S0012-821X(03)00368-6

Panda, D., Kundu, B., Gahalaut, V.K., Rangin, C., 2020. India-Sunda Plate Motion, Crustal Deformation, and Seismic Hazard in the Indo-Burmese Arc. Tectonics 39, e2019TC006034. https://doi.org/10.1029/2019TC006034

Pandey, O.P., Agrawal, P.K., Negi, J.G., 1996. Evidence of low density sub-crustal underplating beneath western continental region of India and adjacent Arabian Sea: Geodynamical considerations. J Geodyn 21, 365–377. https://doi.org/10.1016/0264-3707(95)00036-4

Pandey, O.P., Agrawal, P.K., Negi, J.G., 1995. Lithospheric structure beneath Laxmi Ridge and late Cretaceous geodynamic events. Geo-Marine Letters 15, 85–91. https://doi.org/10.1007/BF01275411/METRICS

Patriat, P., Achache, J., 1984. India–Eurasia collision chronology has implications for crustal shortening and driving mechanism of plates. Nature 1984 311:5987 311, 615–621. https://doi.org/10.1038/311615a0

Peirce, J.W., 1978. The northward motion of India since the Late Cretaceous. Geophys J Int 52, 277–311. https://doi.org/10.1111/J.1365-246X.1978.TB04234.X

Peltzer, G., Tapponnier, P., 1988. Formation and evolution of strike-slip faults, rifts, and basins during the India-Asia Collision: An experimental approach. J Geophys Res Solid Earth 93, 15085–15117. https://doi.org/10.1029/JB093IB12P15085

Plavsa, D., Collins, A.S., Foden, J.D., Clark, C., 2015. The evolution of a Gondwanan collisional orogen: A structural and geochronological appraisal from the Southern Granulite Terrane, South India. Tectonics 34, 820–857. https://doi.org/10.1002/2014TC003706

Pons, M., Sobolev, S. V., Liu, S., Neuharth, D., 2022. Hindered Trench Migration Due To Slab Steepening Controls the Formation of the Central Andes. J Geophys Res Solid Earth 127, e2022JB025229. https://doi.org/10.1029/2022JB025229

Powell, C.M.A., Roots, S.R., Veevers, J.J., 1988. Pre-breakup continental extension in East Gondwanaland and the early opening of the eastern Indian Ocean. Tectonophysics 155, 261–283. https://doi.org/10.1016/0040-1951(88)90269-7

Prabhakar, B.C., Jayananda, M., Shareef, M., Kano, T., 2009. Petrology and geochemistry of late archaean granitoids in the northern part of Eastern Dharwar Craton, Southern India: Implications for transitional geodynamic setting. Journal of the Geological Society of India 74, 299–317. https://doi.org/10.1007/S12594-009-0137-2

Radha Krishna, M., Verma, R.K., Purushotham, A.K., 2002. Lithospheric structure below the eastern Arabian Sea and adjoining West Coast of India based on integrated analysis of gravity and seismic data. Mar Geophys Res (Dordr) 23, 25–42. https://doi.org/10.1023/A:1021288003781/METRICS

Radhakrishna, B.P., 1993. Neogene uplift and geomorphic rejuvenation of the Indian Peninsula. Curr Sci Vol. 64, No. 11/12, 787–793. https://doi.org/https://www.jstor.org/stable/24096189

Raju, D.S.N., 2008. Stratigraphy of India. ONGC Bull., Spec. Issue (43), 1.

Ramana, M. V., Nair, R.R., Sarma, K.V.L.N.S., Ramprasad, T., Krishna, K.S., Subrahmanyam, V., D'Cruz, M., Subrahmanyam, C., Paul, J., Subrahmanyam, A.S., Chandra Sekhar, D. V., 1994. Mesozoic anomalies in the Bay of Bengal. Earth Planet Sci Lett 121, 469–475. https://doi.org/10.1016/0012-821X(94)90084-1

Ranjan, S., Upadhyay, D., Abhinay, K., Srikantappa, C., 2020. Paleoarchean and Neoarchean Tonalite–Trondhjemite–Granodiorite (TTG) and granite magmatism in the Western Dharwar Craton, southern India: Implications for Archean continental growth and geodynamics. Precambrian Res 340. https://doi.org/10.1016/J.PRECAMRES.2020.105630

Rao, B.R., Rao, P.S., 1984. Historical seismicity of Peninsular India. Bulletin of the Seismological Society of America 74, 2519–2533. https://doi.org/10.1785/BSSA0740062519

Rao, D.G., Krishna, K.S., Sar, D., 1997. Crustal evolution and sedimentation history of the Bay of Bengal since the Cretaceous. J Geophys Res Solid Earth 102, 17747–17768. https://doi.org/10.1029/96JB01339

Rao, G.S., Radhakrishna, M., Sreejith, K.M., Krishna, K.S., Bull, J.M., 2016. Lithosphere structure and upper mantle characteristics below the Bay of Bengal. Geophys J Int 206, 675–695. https://doi.org/10.1093/GJI/GGW162

Ratheesh-Kumar, R.T., Dharmapriya, P.L., Windley, B.F., Xiao, W.J., Jeevan, U., 2020. The Tectonic “Umbilical Cord” Linking India and Sri Lanka and the Tale of their Failed Rift. J Geophys Res Solid Earth 125, e2019JB018225. https://doi.org/10.1029/2019JB018225

Raval, U., Veeraswamy, K., 2003. India-Madagascar Separation: Breakup Along a Pre-existing Mobile Belt and Chipping of the Craton. Gondwana Research 6, 467–485. https://doi.org/10.1016/S1342-937X(05)70999-0

Rehman, H.U., Seno, T., Yamamoto, H., Khan, T., 2011. Timing of collision of the Kohistan–Ladakh Arc with India and Asia: Debate. Island Arc 20, 308–328. https://doi.org/10.1111/J.1440-1738.2011.00774.X

Richards, F.D., Hoggard, M.J., White, N.J., 2016. Cenozoic epeirogeny of the Indian peninsula. Geochemistry, Geophysics, Geosystems 17, 4920–4954. https://doi.org/10.1002/2016GC006545

Roger Buck, W., 1986. Small-scale convection induced by passive rifting: the cause for uplift of rift shoulders. Earth Planet Sci Lett 77, 362–372. https://doi.org/10.1016/0012-821X(86)90146-9

Rogers, K.G., Goodbred, S.L., 2014. The Sundarbans and Bengal Delta: The World’s Largest Tidal Mangrove and Delta System. World Geomorphological Landscapes 181–187. https://doi.org/10.1007/978-94-017-8029-2_18

Roy, A., Mandal, N., Van Hunen, J., 2024. Dynamic evolution of competing same-dip double subduction: New perspectives of the Neo-Tethyan plate tectonics. Earth Planet Sci Lett 647, 119032. https://doi.org/10.1016/J.EPSL.2024.119032

Roy, A.B., Chatterjee, A., 2015. Tectonic framework and evolutionary history of the Bengal Basin in the Indian subcontinent. Curr Sci 9, 271–279. https://doi.org/https://www.jstor.org/stable/24905853

Roy, S.K., Kumar, M.R., Kanaujia, J., Gupta, S., Singh, B., Mandal, P., Srinagesh, D., 2024. Insights into the mechanisms forging seismic anisotropy in the upper mantle beneath India. Tectonophysics 888, 230454. https://doi.org/10.1016/J.TECTO.2024.230454

Roy, S.K., Srinagesh, D., Saikia, D., Singh, A., Kumar, M.R., 2012. Seismic anisotropy beneath the Eastern Dharwar craton. Lithosphere 4, 259–268. https://doi.org/10.1130/L198.1

Royden, L.H., Burchfiel, B.C., Van Der Hilst, R.D., 2008. The geological evolution of the Tibetan plateau. Science (1979) 321, 1054–1058. https://doi.org/10.1126/SCIENCE.1155371/ASSET/85943FBF-8019-422F-8691-6BDF90923918/ASSETS/GRAPHIC/321_1054_F6.JPEG

Ruetenik, G.A., Moucha, R., Hoke, G.D., 2016. Landscape response to changes in dynamic topography. Terra Nova 28, 289–296. https://doi.org/10.1111/TER.12220

Russo, R.M., Silver, P.G., 1994. Trench-Parallel Flow Beneath the Nazca Plate from Seismic Anisotropy. Science (1979) 263, 1105–1111. https://doi.org/10.1126/SCIENCE.263.5150.1105

Saha, D., Mazumder, R., 2012. An overview of the Palaeoproterozoic geology of Peninsular India, and key stratigraphic and tectonic issues. Geol Soc Spec Publ 365, 5–29. https://doi.org/10.1144/SP365.2

Saha, D., Patranabis-Deb, S., 2014. Proterozoic evolution of Eastern Dharwar and Bastar cratons, India – An overview of the intracratonic basins, craton margins and mobile belts. J Asian Earth Sci 91, 230–251. https://doi.org/10.1016/J.JSEAES.2013.09.020

Saha, G.K., Prakasam, K.S., Rai, S.S., 2020. Diversity in the peninsular Indian lithosphere revealed from ambient noise and earthquake tomography. Physics of the Earth and Planetary Interiors 306, 106523. https://doi.org/10.1016/J.PEPI.2020.106523

Saha, G.K., Rai, S.S., Prakasam, K.S., Gaur, V.K., 2021. Distinct lithospheres in the Bay of Bengal inferred from ambient noise and earthquake tomography. Tectonophysics 809, 228855. https://doi.org/10.1016/J.TECTO.2021.228855

Sandiford, D., Moresi, L., 2019. Improving subduction interface implementation in dynamic numerical models. Solid Earth 10, 969–985. https://doi.org/10.5194/SE-10-969-2019

Sandiford, D., Moresi, L., Sandiford, M., Yang, T., 2019. Geometric controls on flat slab seismicity. Earth Planet Sci Lett 527, 115787. https://doi.org/10.1016/J.EPSL.2019.115787

Sangode, S.J., Dongre, A., Bhagat, A., Meshram, D., 2022. Palaeomagnetic inclination anomaly in the Deccan traps and its geodynamic implications over the Indian plate. Journal of Earth System Science 131, 1–12. https://doi.org/10.1007/S12040-022-01917-X/TABLES/5

Satyabala, S.P., 2003. Oblique plate convergence in the Indo-Burma (Myanmar) subduction region. Pure Appl Geophys 160, 1611–1650. https://doi.org/10.1007/S00024-003-2378-0/METRICS

Sen, G., 2001. Generation of Deccan trap magmas. Proceedings of the Indian Academy of Sciences, Earth and Planetary Sciences 110, 409–431. https://doi.org/10.1007/BF02702904/METRICS

Sharma, K.K., 1987. Crustal growth and two-stage India-Eurasia collision in Ladakh. Tectonophysics 134, 17–28. https://doi.org/10.1016/0040-1951(87)90246-0

Singh, A.P., 1999. The deep crustal accretion beneath the Laxmi Ridge in the northeastern Arabian Sea: the plume model again. J Geodyn 27, 609–622. https://doi.org/10.1016/S0264-3707(98)00019-2

Singh, A.P., Mishra, D.C., 2002. Tectonosedimentary evolution of Cuddapah basin and Eastern Ghats mobile belt (India) as Proterozoic collision: gravity, seismic and geodynamic constraints. J Geodyn 33, 249–267. https://doi.org/10.1016/S0264-3707(01)00066-7

Singh, S.C., Moeremans, R., McArdle, J., Johansen, K., 2013. Seismic images of the sliver strike-slip fault and back thrust in the Andaman-Nicobar region. J Geophys Res Solid Earth 118, 5208–5224. https://doi.org/10.1002/JGRB.50378

Singh, V.K., Slabunov, A.I., Nesterova, N.S., Singh, M.M., Bhatt, S.C., 2021. Tectonostratigraphic Terranes of the Bundelkhand Craton (Indian Shield) 155–164. https://doi.org/10.1007/978-981-16-4122-0_10

Singh, V.K., Verma, S.K., Singh, P.K., Slabunov, A.I., Mishra, S., Chaudhary, N., 2020. Archean crustal evolution of the bundelkhand craton: Evidence from granitoid magmatism. Geol Soc Spec Publ 489, 235–259. https://doi.org/10.1144/SP489-2018-72

Sloan, R.A., Elliott, J.R., Searle, M.P., Morley, C.K., 2017. Active tectonics of Myanmar and the Andaman Sea. Geological Society Memoir 48, 19–52. https://doi.org/10.1144/M48.2

Sribin, C., Padma Rao, B., Rohilla, S., Jha, K., 2024. Crustal structure beneath the Western Dharwar Craton segment of Western Ghats: Insights from ambient noise correlation technique. J Asian Earth Sci 272, 106240. https://doi.org/10.1016/J.JSEAES.2024.106240

Steckler, M.S., Mondal, D.R., Akhter, S.H., Seeber, L., Feng, L., Gale, J., Hill, E.M., Howe, M., 2016. Locked and loading megathrust linked to active subduction beneath the Indo-Burman Ranges. Nature Geoscience 2016 9:8 9, 615–618. https://doi.org/10.1038/ngeo2760

Stolar, D., Roe, G., Willett, S., 2007. Controls on the patterns of topography and erosion rate in a critical orogen. J Geophys Res Earth Surf 112. https://doi.org/10.1029/2006JF000713

Subrahmanyam, C., Chand, S., 2006. Evolution of the passive continental margins of India—a geophysical appraisal. Gondwana Research 10, 167–178. https://doi.org/10.1016/J.GR.2005.11.024

Subrahmanyam, C., Gireesh, R., Chand, S., Raju, K.A.K., Rao, D.G., 2008. Geophysical characteristics of the Ninetyeast Ridge–Andaman island arc/trench convergent zone. Earth Planet Sci Lett 266, 29–45. https://doi.org/10.1016/J.EPSL.2007.10.016

Sun, H., 2005. Curve Fitting in Least-Square Method and Its Realization with Matlab. Ordnance Industry Automation.

Sun, J., Xiao, W., Windley, B.F., Ji, W., Fu, B., Wang, J., Jin, C., 2016. Provenance change of sediment input in the northeastern foreland of Pamir related to collision of the Indian Plate with the Kohistan-Ladakh arc at around 47 Ma. Tectonics 35, 315–338. https://doi.org/10.1002/2015TC003974

Sushchevskaya, N.M., Levchenko, O. V., Dubinin, E.P., Belyatsky, B. V., 2016. Ninetyeast ridge: Magmatism and geodynamics. Geochemistry International 54, 237–256. https://doi.org/10.1134/S001670291603006X/METRICS

Talukdar, D., Pandey, A., Chalapathi Rao, N. V., Kumar, A., Pandit, D., Belyatsky, B., Lehmann, B., 2018. Petrology and geochemistry of the Mesoproterozoic Vattikod lamproites, Eastern Dharwar Craton, southern India: evidence for multiple enrichment of sub-continental lithospheric mantle and links with amalgamation and break-up of the Columbia supercontinent. Contributions to Mineralogy and Petrology 173, 1–27. https://doi.org/10.1007/S00410-018-1493-Y/FIGURES/12

Talwani, M., Desa, M.A., Ismaiel, M., Sree Krishna, K., 2016. The Tectonic origin of the Bay of Bengal and Bangladesh. J Geophys Res Solid Earth 121, 4836–4851. https://doi.org/10.1002/2015JB012734

Talwani, M., Reif, C., 1998. Laxmi Ridge - A continental sliver in the Arabian Sea. Marine Geophysical Research 20, 259–271. https://doi.org/10.1023/A:1004674909280/METRICS

Thorne, R.L., Roberts, S., Herrington, R., 2012. Climate change and the formation of nickel laterite deposits. Geology 40, 331–334. https://doi.org/10.1130/G32549.1

Tiwari, P.K., Surve, G., Mohan, G., 2006. Crustal constraints on the uplift mechanism of the Western Ghats of India. Geophys J Int 167, 1309–1316. https://doi.org/10.1111/J.1365-246X.2006.03093.X/3/167-3-1309-FIG008.JPEG

Tiwari, V.M., Grevemeyer, I., Singh, B., Phipps Morgan, J., 2007. Variation of effective elastic thickness and melt production along the Deccan–Reunion hotspot track. Earth Planet Sci Lett 264, 9–21. https://doi.org/10.1016/J.EPSL.2007.08.023

Tomson, J.K., Dev, J.A., 2024. Tracing the crustal evolution of the Precambrian Southern Granulite terrane in East Gondwana: New insights from zircon U-Pb/Hf geochronology. GSA Bulletin 136, 2075–2096. https://doi.org/10.1130/B36777.1

Tucker, G.E., 2015. Landscape evolution. Crustal and Lithosphere Dynamics: Treatise on Geophysics, edited by: Watts, AB, Elsevier 593–630.

Tucker, G.E., Hancock, G.R., 2010. Modelling landscape evolution. Earth Surf Process Landf 35, 28–50. https://doi.org/10.1002/ESP.1952

Valdiya, K.S., 2001. Tectonic resurgence of the Mysore plateau and surrounding regions in cratonic Southern India. Curr Sci Vol.81, No.8, 1068–1089. https://doi.org/https://www.jstor.org/stable/24106531

Van Hinsbergen, D.J.J., Steinberger, B., Doubrovine, P. V., Gassmöller, R., 2011. Acceleration and deceleration of India-Asia convergence since the Cretaceous: Roles of mantle plumes and continental collision. J Geophys Res Solid Earth 116. https://doi.org/10.1029/2010JB008051

Veeraswamy, K., Raval, U., 2005. Remobilization of the palaeoconvergent corridors hidden under the Deccan trap cover and some major stable continental region earthquakes. Curr Sci 89, 522–530.

Vita-Finzi, C., 2004. Buckle-controlled seismogenic faulting in peninsular India. Quat Sci Rev 23, 2405–2412. https://doi.org/10.1016/J.QUASCIREV.2004.01.008

Wang, M.X., Santosh, M., Jayananda, M., Yang, C.X., Thomas, T.T., Kim, S.W., 2023. Trondhjemites from the Western Dharwar Craton, Southern India: Implications for Mesoarchean crustal growth. Lithos 462–463, 107410. https://doi.org/10.1016/J.LITHOS.2023.107410

Watts, A.B., Cox, K.G., 1989a. The Deccan Traps: an interpretation in terms of progressive lithospheric flexure in response to a migrating load. Earth Planet Sci Lett 93, 85–97. https://doi.org/10.1016/0012-821X(89)90186-6

Watts, A.B., Cox, K.G., 1989b. The Deccan Traps: an interpretation in terms of progressive lithospheric flexure in response to a migrating load. Earth Planet Sci Lett 93, 85–97. https://doi.org/10.1016/0012-821X(89)90186-6

Weissel, J.K., Hayes, D.E., Herron, E.M., 1977. Plate tectonics synthesis: The displacements between Australia, New Zealand, and Antarctica since the Late Cretaceous. Mar Geol 25, 231–277. https://doi.org/10.1016/0025-3227(77)90054-8

Weissel, J.K., Karner, G.D., 1989. Flexural uplift of rift flanks due to mechanical unloading of the lithosphere during extension. J Geophys Res Solid Earth 94, 13919–13950. https://doi.org/10.1029/JB094IB10P13919

Whipple, K.X., 2009. The influence of climate on the tectonic evolution of mountain belts. Nature Geoscience 2009 2:2 2, 97–104. https://doi.org/10.1038/ngeo413

Whipple, K.X., Meade, B.J., 2004. Controls on the strength of coupling among climate, erosion, and deformation in two-sided, frictional orogenic wedges at steady state. J Geophys Res Earth Surf 109. https://doi.org/10.1029/2003JF000019

White, R., McKenzie, D., 1989. Magmatism at rift zones: The generation of volcanic continental margins and flood basalts. J Geophys Res Solid Earth 94, 7685–7729. https://doi.org/10.1029/JB094IB06P07685

Whiting, B.M., Karner, G.D., Driscoll, N.W., 1994. Flexural and stratigraphic development of the west Indian continental margin. J Geophys Res Solid Earth 99, 13791–13811. https://doi.org/10.1029/94JB00502

Widdowson, M., 1997. Tertiary palaeosurfaces of the SW Deccan, Western India: Implications for passive margin uplift. Geol Soc Spec Publ 120, 221–248. https://doi.org/10.1144/GSL.SP.1997.120.01.15

Widdowson, M., Cox, K.G., 1996. Uplift and erosional history of the Deccan Traps, India: Evidence from laterites and drainage patterns of the Western Ghats and Konkan Coast. Earth Planet Sci Lett 137, 57–69. https://doi.org/10.1016/0012-821X(95)00211-T

Widdowson, M., Mitchell, C., 1999. Large-scale stratigraphical, structural and geomorphological constraints for earthquakes in the Southern Deccan Traps, India: The case for denudationally-driven seismicity. Mem. Geol. Soc. India 43(1), 425–452.

Yamato, P., Husson, L., Becker, T.W., Pedoja, K., 2013. Passive margins getting squeezed in the mantle convection vice. Tectonics 32, 1559–1570. https://doi.org/10.1002/2013TC003375

Zahirovic, S., Mller, R.D., Seton, M., Flament, N., Gurnis, M., Whittaker, J., 2012. Insights on the kinematics of the India-Eurasia collision from global geodynamic models. Geochemistry, Geophysics, Geosystems 13. https://doi.org/10.1029/2011GC003883

Zheng, G., Wang, H., Wright, T.J., Lou, Y., Zhang, R., Zhang, W., Shi, C., Huang, J., Wei, N., 2017. Crustal Deformation in the India-Eurasia Collision Zone From 25 Years of GPS Measurements. J Geophys Res Solid Earth 122, 9290–9312. https://doi.org/10.1002/2017JB014465

Chapter 6 | Plume-lithosphere interaction: Implications for Deccan volcanism

6.1. Previous studies: a synopsis

Continental rifts often exhibit spatiotemporal correlations with large igneous provinces (LIPs), such as the Deccan Trap in peninsular India, which generally cover vast areas of the continental surface, exceeding 1 million km² (Bryan and Ferrari, 2013; Ernst, 2014). Although the precise geodynamic relationship between flood basalt eruptions in LIPs and continental rifting remains uncertain, it is now well-established that these two large-scale processes, rifting and plume-driven LIP volcanism, interact in complex ways, leaving intertwined signatures in the geological record. Seismic tomographic studies (French and Romanowicz, 2015) often reveal a close spatial association between mantle plumes and continental rift events during specific periods in their geological evolution. This connection is supported by geophysical and geochemical anomalies observed along rift zones, such as positive Bouguer anomalies, increased seismic wave velocities, and elevated Moho depths (Funck et al., 2007; Kendall et al., 2006). Several authors argue that mantle plumes play a significant role in modulating rifting events, either by facilitating the migration of rift centers or causing their complete cessation, depending on the relative positions of the plume and the rift (Mittelstaedt et al., 2011; Whittaker et al., 2015). Understanding the mechanisms of plume–rift interaction has thus become a challenging and critical area of research since the early 1980s (Morgan, 1978), particularly to explain the widespread volcanism observed in continental regions (Koppers et al., 2021; Richards et al., 1989; White and McKenzie, 1995). In parallel, studies of mid-ocean ridge systems representing divergent oceanic plate boundaries have identified several key factors that govern plume–ridge interactions. These include seafloor spreading rates, plume buoyancy flux, and the spatial distance between the plume and the ridge (Ito et al., 2003; Kinchid et al., 1995; Mittelstaedt et al., 2011; Pang et al., 2023; Ribe, 1996; Ribe and Christensen, 1994; Sleep, 1997). Additionally, the trench-ward viscous drag of plates and rift-ward pressure-induced forces have been recognized as influential parameters (François et al., 2018)

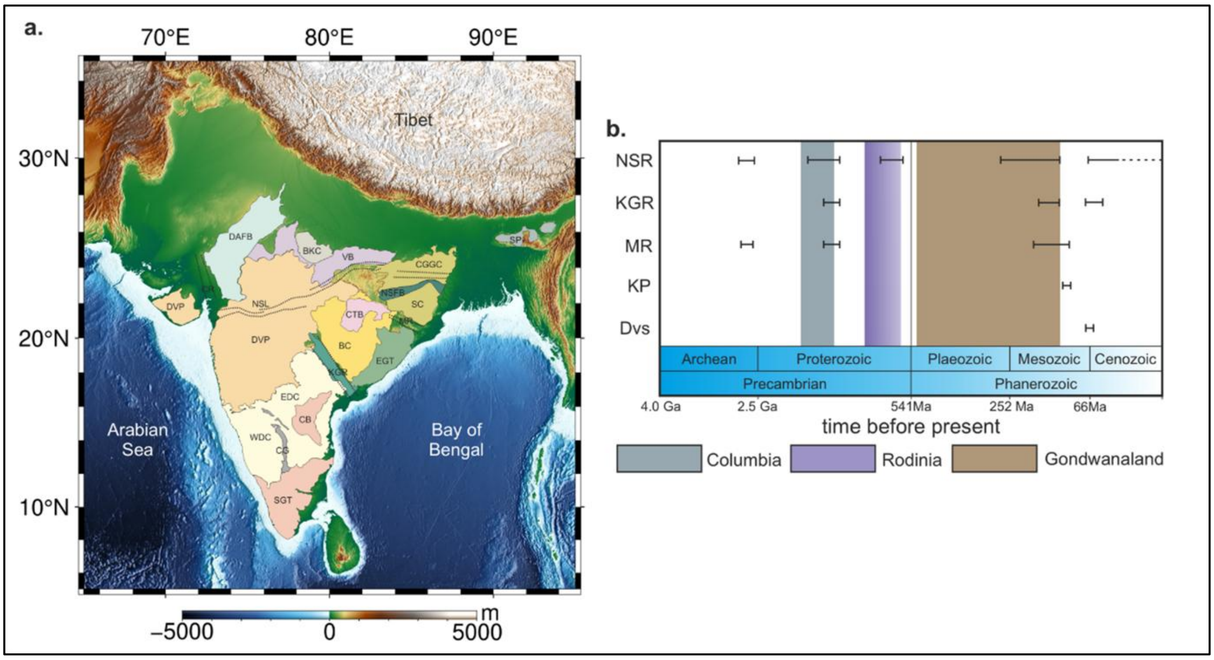

Figure 6.1 *(a) Geological setting of the Indian subcontinent showing major geological provinces, which constitute the Indian Peninsular craton and the continental-scale rift structures. DVP: Deccan volcanic province, DAFB: Delhi-Aravalli fold belt, BKC: Bundelkhand craton, VB: Vindyan basin, NSL: Narmada-Son lineament, CR: Cambay rift, CGGC: Chotanagpur Gneissic complex, NSFB: North Singhbhum fold belt, SC: Singbhum craton MR: Mahanadi Rift, CTB Chattisgarh Basin, BC: Bastar craton, KGR: Krishna Godavari Rift, EDC: Eastern Dharwar craton, WDC: Western Dharwar Craton, CG: Closepet Granite, CB: Cuddapah basin, SGT: Southern Granulite terrain. (b) A diagrammatic presentation of the activities of the NSL, KGR, MR, Kergueran, and Réunion plume throughout geological history.*

Laboratory experiments and numerical simulations have provided significant insights into the thermo-mechanical effects of plume–lithosphere interactions during rift evolution (Ribe and Christensen, 1994). Lithospheric heating caused by mantle upwelling and associated magma emplacement leads to mechanical weakening, which can greatly facilitate the rifting process (François et al., 2018). In turn, rifting enhances the extraction of melts generated by decompression melting in the asthenosphere. Divergent mantle flows beneath rift zones create regions of low dynamic pressure, which draw plume material toward the rift axis (Ribe and Christensen, 1994; Sleep, 1997). However, this ascent becomes more complex due to additional forces exerted by tectonic plate movements, which can pull plume material away from the axial zones of rift systems (Ribe and Christensen, 1999, 1994). These competing forces, gravitational and tectonic, play critical roles in modulating plume–rift interactions, yet their relative contributions remain poorly quantified. The plume-induced rifting model has successfully explained key features of many active and ancient rift systems, such as the volcanic patterns and basin formation observed in the East African Rift System (Issachar et al., 2024). Nevertheless, several aspects of plume-associated lithospheric phenomena remain unresolved. For instance, the mechanisms governing the distribution of hotspots, particularly ridge-ward spreading versus plate-drag spreading, are not yet fully understood. Addressing these gaps is essential for a more comprehensive understanding of the dynamic interplay between mantle plumes, lithospheric deformation, and tectonic processes.

Previous studies, as discussed earlier, have primarily focused on the mechanical and thermo-mechanical effects of mantle plumes on the overlying lithosphere, particularly in the context of interpreting continental rift tectonics (Burov & Gerya, 2014; Burov & Guillou-Frottier, 2005; Gibson et al., 1999; Kendall et al., 2005; Larsen & Saunders, 1998; Sleep, 1997). However, many continents host rift systems that predate specific plume events. Geological evidence indicates that these pre-existing rifts can significantly influence the ascent dynamics of mantle plumes, resulting in a strong spatiotemporal correlation between plume-associated magmatism and rift zones (Issachar et al., 2024). The mechanisms by which a pre-existing rift redirects a plume upon its encounter with the lithosphere, however, remain relatively underexplored. Recent model simulations by Pang et al. (2023) demonstrate that divergent mid-ocean ridges can strongly interact with off-axis plumes, redirecting plume material flow either toward or away from the ridge axis. This redirection depends on the interplay between plate drag and the gravitational force driving plume flow along the base of the sloping lithosphere. Their findings suggest that strong buoyant mantle plumes tend to flow toward the ridge axis under slow spreading conditions and small plume- ridge distances. Conversely, under fast spreading conditions and in the presence of smaller or intermediate plumes with larger plume–ridge distances, the flow is directed away from the ridge. While these results provide valuable insights into oceanic settings, further investigation is needed to understand the dynamics in continental environments. Specifically, the role of pre-existing rifts in modulating plume stagnation and remobilization beneath the lithosphere of mechanically strong continental plates remains an open question. Advancing this understanding is essential for elucidating the interactions between mantle plumes and continental lithosphere in tectonic and magmatic processes.

To investigate this issue in a continental geodynamic context, this study focus on the geological settings of the closely associated Deccan Volcanic Province (DVP) and major rift systems in peninsular India (Figure 6.1a). This rifted region experienced a remarkable volcanic event that produced extensive flood basalts exceeding 1.5 km in thickness and covering over 500,000 km². The DVP is genetically linked to the Reunion hotspot, which the northward-drifting Indian plate encountered around 66 Ma (Sprain et al., 2018). Geological evidence suggests that pre-existing rifts in the Indian continent significantly influenced plume-driven magmatic emplacement. One such rift is the Cambay Rift (CBR), which divides the Deccan Traps into two distinct units: north-west and south-west (Rao et al., 2015). The Cambay Rift, filled with Tertiary sediments, is interpreted as a failed rift formed by extensional tectonics. Other major rift systems in the Indian peninsula include the Godavari Graben (GG) and the Mahanadi Rift (MHR). Although these are passive features, they have left distinct surface imprints. Studies indicate that the GG has redirected magma pathways (Keller et al., 2008), cting as a potential zone for accumulating plume material. Another prominent tectonic feature is the Narmada-Son Lineament (NSL), an approximately east-west structure originating in the Archean era. The NSL divides various tectonic zones in northern and southern India (Kumar et al., 2015). All these paleo-rifts have existed since the Precambrian era within the Indian craton (Figure 6.1b) and are believed to have acted as zones of weakness during major geological events (Meert et al., 2010; Patranabis-Deb et al., 2020). Despite their potential importance, the influence of these pre-existing weak zones on the DVP—India's most remarkable volcanic event—remains largely unexplored. Understanding their role could provide valuable insights into the interaction between mantle plumes and lithospheric structures in shaping this geologic phenomenon, which sets the principal motivation of our present study.

This work integrates a thermo-mechanical geodynamic model to explore the influence of the Réunion plume on the reactivation of pre-existing rift zones within the Indian craton. Additionally, the model examines the feedback effects of this rift reactivation on the plume's repositioning during its interaction with the overlying lithosphere. This study reveals how the major rift systems in the Indian peninsula regulated the distribution of plume materials beneath the continental lithosphere during the Deccan volcanic event in the Cretaceous period. The study also highlights the striking differences between the eastern and western rift systems and their respective interactions with plumes. The chapter is organized as follows: the first section presents a comprehensive historical overview of two major Phanerozoic events—continental rifting and plume-driven Deccan volcanism—highlighting their spatial and temporal correlations. The second section outlines the modeling approach employed to study the mode of plume–rift interactions in a continental setting. Subsequently, the model results are presented, illustrating how rifting influences the repositioning of plumes during their interaction with the lithosphere as functions of various physical parameters, including plume size, ridge spreading rate, plume–rift distance, and lithospheric strength.

6.2. Continental rifts and Deccan volcanism

6.2.1. Rift tectonic history

The Indian rift system primarily comprises four major rifts: the Narmada-Tapti rift in central India, the Mahanadi and Godavari rifts in the Indian Peninsula, and the Cambay rift along the western margin (Figure 6.1a). The rift-controlled Narmada-Son valley region is thought to have originated during the Archean era and has been reactivated multiple times throughout subsequent geological events (Figure 6.1b) (Choubey, 1971; Kumar et al., 2015; Naveen et al., 2023). The Narmada-Tapti (NT) rift broadly follows E-W to ENE-WSW trending lineaments, marking a significant tectonic boundary between the southern Peninsular region and the northern foreland. These Precambrian lineaments, often referred to as lithospheric weak zones or paleo-rifts, appear to have played a critical role in the NT rift formation, with mafic intrusions aligning along these structural features. Similarly, the western continental margin exhibits numerous N-S to NNW-SSE oriented lineaments that facilitated rifting and the subsequent breakup of the Indian craton. Geochronological studies indicate that the Narmada-Son Lineament (NSL) formed during the Neoarchean to Neoproterozoic eras, experiencing multiple tectonic events between 2.2 and 0.9 Ga (Figure 6.1b). Some researchers suggest that the Mahakoshal group of rocks, located between the Son-Narmada Northern Fault (SNNF) and the Son-Narmada Southern Fault (SNSF), represents a back-arc rift environment associated with Paleo-Proterozoic subduction (~1.8 Ga) (Bhowmik et al., 2012; Chattopadhyay et al., 2020). This active subduction culminated during the Meso-Proterozoic (~1.5 Ga), resulting in a continent–continent collision.

The Mahanadi and Godavari rifts are considered extensions of the Central Indian Tectonic Zone (CITZ) to the eastern margin of India, thought to have originated during the breakup of the supercontinent Columbia between 1.7 and 1.5 Ga (Figure 6.1b). Plate reconstructions suggest that the Gondwanaland comprised several major cratons that amalgamated through continental collision tectonics by the end of the Proterozoic, maintaining this assembly until the Jurassic or Early Cretaceous periods. During the Cambrian period, East Gondwana comprised India, Madagascar, Western and Northern Australia, and East Antarctica, while West Gondwana comprised Africa and South America. These two parts developed a suture zone along a Neo-Proterozoic mobile belt (Ghosh, 2015; Unrug, 1996). In the Carboniferous period (330–320 Ma), the Gondwanaland collided with North America, Europe, and Siberia to form the supercontinent Pangea. Pangea remained intact until the Jurassic period, when it began to fragment due to successive rifting events. The breakup commenced with the separation of North America from Africa–South America, marked by the opening of the Central Atlantic Ocean around 195 Ma. This event is associated with extensive volcanism that created the vast (>1 million km^2) Central Atlantic Magmatic Province (CAMP) at approximately 201 Ma (Mchone, 2000), which is generally linked with the Triassic–Jurassic mass extinction event (Blackburn et al., 2013; Marzoli et al., 1999). Geological records indicate that these tectonic activities reactivated the eastern margin rifts, including the Mahanadi and Godavari rifts and the eastern part of the CITZ.

The Narmada-Tapti rift was reactivated later, during the Jurassic period (~175 Ma) (Figure 6.1b), when the western half of Gondwana (Africa and South America) began to separate from the eastern half (India, Madagascar, Australia, and Antarctica). Around 140 Ma, Africa and South America split, forming the South Atlantic Ocean. On the other hand, the separation of India and Madagascar from Antarctica and Australia formed the central Indian Ocean. This process is associated with the eruption of the Rajmahal Traps (115–118 Ma) in eastern India at (Baksi, 1995) and the Bunbury Traps (132 Ma) in Western Australia (Torsvik and Cocks, 2013). India finally broke away from Madagascar during the Late Cretaceous, accompanied by the eruption of the Deccan flood basalts. This massive volcanism occurred between 67 and 65 Ma (Chenet et al., 2007, spreadingest to east along preexisting structural weaknesses in the CITZ (Bhattacharji et al., 1996). This event also led to the formation of the Cambay rift (Rao et al., 2015). The extensive Deccan volcanism occurred in three distinct phases, resulting in the formation of a primary magmatic chamber at the crust-mantle boundary as an underplated layer (Ju et al., 2013) and a secondary magma chamber at shallow crustal levels (Bhattacharji et al., 1996) in the Narmada-Tapti region. The central portion of the CITZ and surrounding Mesozoic sediments are predominantly buried beneath Deccan flood basalts, which obscure the subsurface structure and pre-volcanic tectonics of the Narmada-Tapti zone. The primary landform of this rift valley is the Cretaceous peneplain, which was rifted and subsequently buried by extensive lava flows.

6.2.2. Geodynamics of the Deccan volcanism

The Deccan Volcanic Province (DVP) is stratigraphically divided into three principal subgroups based on volcanological and geochemical characteristics: the Kalsubai, Lonavala, and Wai subgroups. The Cretaceous–Paleogene boundary (KPB), dated to 66.043 ± 0.043 Ma (Sprain et al., 2018), falls within the Khandala, Bushe, or Poladpur Formations, approximately 165 ± 68 ka after the emplacement of the Kalsubai subgroup. Recent geochronological studies of the Deccan Traps (DTs), utilizing $^{40}Ar/^{39}Ar$ dating of plagioclase from basalt flows and U-Pb dating of zircon from ash-bearing intervals (Keller et al., 2012; Richards et al., 2015; Schoene et al., 2019, 2015), have constrained the sequence of eruption events. These investigations converge to the point that the main eruptive phases began shortly before the C30n-C29r geomagnetic reversal and ended after the C29r-C29n reversal. The formations above the KPB, belonging to the Wai subgroup, are distinct in their geochemistry and volcanological features, such as voluminous eruptions and greater susceptibility to weathering. Using $^{40}Ar/^{39}Ar$ geochronology, earlier studies identified four to five distinct eruption events at approximately 62.5, 63.7, 65.6, 66.6, 67.8, and 69.7 Ma (Chenet et al., 2007), suggesting time intervals of ~1–1.9 Ma between successive events. Similarly, Parsio et al. (2016) recognized five eruption peaks at 64.1, 65.2, 66.2, 67.5, and 69.6 Ma, with intervals ranging from ~1.1–2.1 Ma. More recent investigations utilizing high-precision U-Pb geochronology (Schoene et al., 2019)), have identified three to four discrete pulses during the main eruption phase near the KPB, each lasting less than 100 ka. These pulses include- First Pulse: Eruption of the lowermost seven formations (~66.3 - 66.15 Ma); Second Pulse: Emplacement of the Poladpur Formation (~66.1 - 66.0 Ma); Third Pulse: Formation of the Ambenali Formation (~65.9 - 65.8 Ma); Fourth and Final Pulse: Eruption of the uppermost Mahabaleshwar Formation (~65.6 - 65.5 Ma).

Recent studies have correlated the Deccan volcanic event with Réunion hotspot activities, explaining the underlying geodynamic processes in connection with the African Large Low Shear Velocity Province (LLSVP) (Ghosh et al., 2024). Glišović and Forte (2017) integrated data from the Deccan Continental Flood Basalts (CFB), the Réunion Ocean Island Basalts (OIB), and other similar hotspot tracks from a geophysical perspective and proposed a mantle plume hypothesis as the origin of the Deccan Large Igneous Province (LIP). The coeval relationship between Deccan volcanism and the plume-induced rapid acceleration of the Indian plate during the Cenozoic to late Cenozoic also supports this hypothesis. Interestingly, as with other hotspots, such as Iceland and Tristan da Cunha, the Réunion hotspot is located at the edge of the African LLSVP, suggesting that the LLSVP may have acted as a primary feeder for the plume, at least during the Cenozoic (Petersen et al., 2016; Zhao, 2015). Recent isotopic (Sr-Nd-Os) studies of primary magmas from Réunion provide geochemical evidence for a temporally stable mantle plume, with its primary reservoir linked to the African LLSVP. Furthermore, recent geodynamic models indicate that plume activity occurred episodically, controlled by its interactions with the 660-km transition zone (Ghosh et al., 2024).

The pre-existing continental rifts significantly influenced the pathways of plume materials and the massive eruption of Deccan basalts across the Indian craton. Some studies have shown that the eruption began along east-west trending pre-existing weak zones within the Central Indian Tectonic Zone (CITZ) (Bhattacharji et al., 1996). During the first phase of the eruption, the Réunion hotspot was positioned at the lithospheric base beneath the Nasik–Pune region. In the second phase, this position shifted to a new location beneath the west coast (Chenet et al., 2007; Ju et al., 2013). Additionally, Deccan Trap (DT) rocks have been reported from the Rajahmundry region, south of the Godavari Rift, suggesting that the plume activity reactivated the rift and facilitated magma eruptions through faults in the reactivated zone (Singh et al., 2012). Crustal velocity structures indicate significant magmatic underplating, extending from the western flank to the middle and eastern segments of the Narmada–Son Lineament (NSL) (Kaila et al., 1987; Singh, 1998). Geophysical observations show that the average crustal thickness near the NSL is approximately 40 km, deepening to ~55 km within the lineament zone. High Vp/Vs ratios (1.84) in the thicker crustal regions suggest an accumulation of mafic to ultramafic materials in the lower crust (Kumar et al., 2015; Rai et al., 2005). Similarly, in the Mahanadi Rift region, active seismic refraction studies have identified a ~10 km thick high-P-wave velocity (7.5 km/s) and high-density (3.05 g/cm^3) layer at the base of a 35–37 km thick crust (Behera et al., 2004). Researchers propose that these observations can be explained by Moho upwarping or crustal thinning in the rift zone, accompanied by the emplacement of thick, high-velocity materials. It has been hypothesized that the basaltic underplating in these regions may have originated from Kerguelen hotspot activity, which is also believed to be responsible for the ~130 Ma Rajmahal Traps in eastern India (Curray and Munasinghe, 1991; Krishna et al., 2012; Olierook et al., 2019). The complex nature of the Moho beneath the NSL and other basins, such as the Mahanadi and Godavari basins, is thus often attributed to magmatic underplating associated with rift environments. This magmatic underplating within the crust likely reflects lithospheric stretching and reactivation of the rift system.

6.3. Thermo-mechanical modelling

6.3.1. Approach

The models are constructed using 2D Cartesian geometry, encompassing a horizontal distance of 1000 km and a vertical extent of 440 km. The vertical domain is divided into seven horizontal compositional layers. The uppermost layer, which represents sticky air, has a thickness of 30 km. Beneath this, the crustal layer is divided into two sub-layers: the upper crust, 25 km thick, and the lower crust, 15 km thick. Below the crust, the mantle lithosphere has a thickness ranging from 40 to 80 km. The remaining portion of the model domain represents the upper mantle. To simulate plumes in the thermomechanical model, a semicircular material domain with a radius varying from 20 to 100 km is placed at the base of the model (Figure 6.2). A rectangular seed ialso introduced at the crust-mantle boundary to simulate pre-existing lithospheric heterogeneity. The model parameters and their corresponding values are detailed in Table A.2.

In order to solve the problem in ASPECT (on any other FEM based code), the domain has to be discretized. Our domain is discretized into quadrilateral finite elements. Basis functions are then defined for the independent variables such as velocity, pressure, temperature and compositional fields. Here we employ second-order polynomials for velocity, and first-order polynomials for pressure (Q_2Q_1 elements), and also second order polynomials for temperature and composition. We have always used square grid to solve our problem where all the cells have the same height and width. The model domain is subdivided in such a way that it has a finite element grid with uniform 2 km spacing. Adaptive mesh refinement (AMR) is turned off in all the models in order to avoid numerical errors.

The upper surface is considered as free surface in order to observe the change in elevation with time. For this we require zero stress on this surface. Since there will be flow across the surface we also need to have a dynamically deformable mesh. To handle the motion of the mesh with a free surface ASPECT incorporates the arbitrary Lagrangian-Eulerian (ALE) implementation.

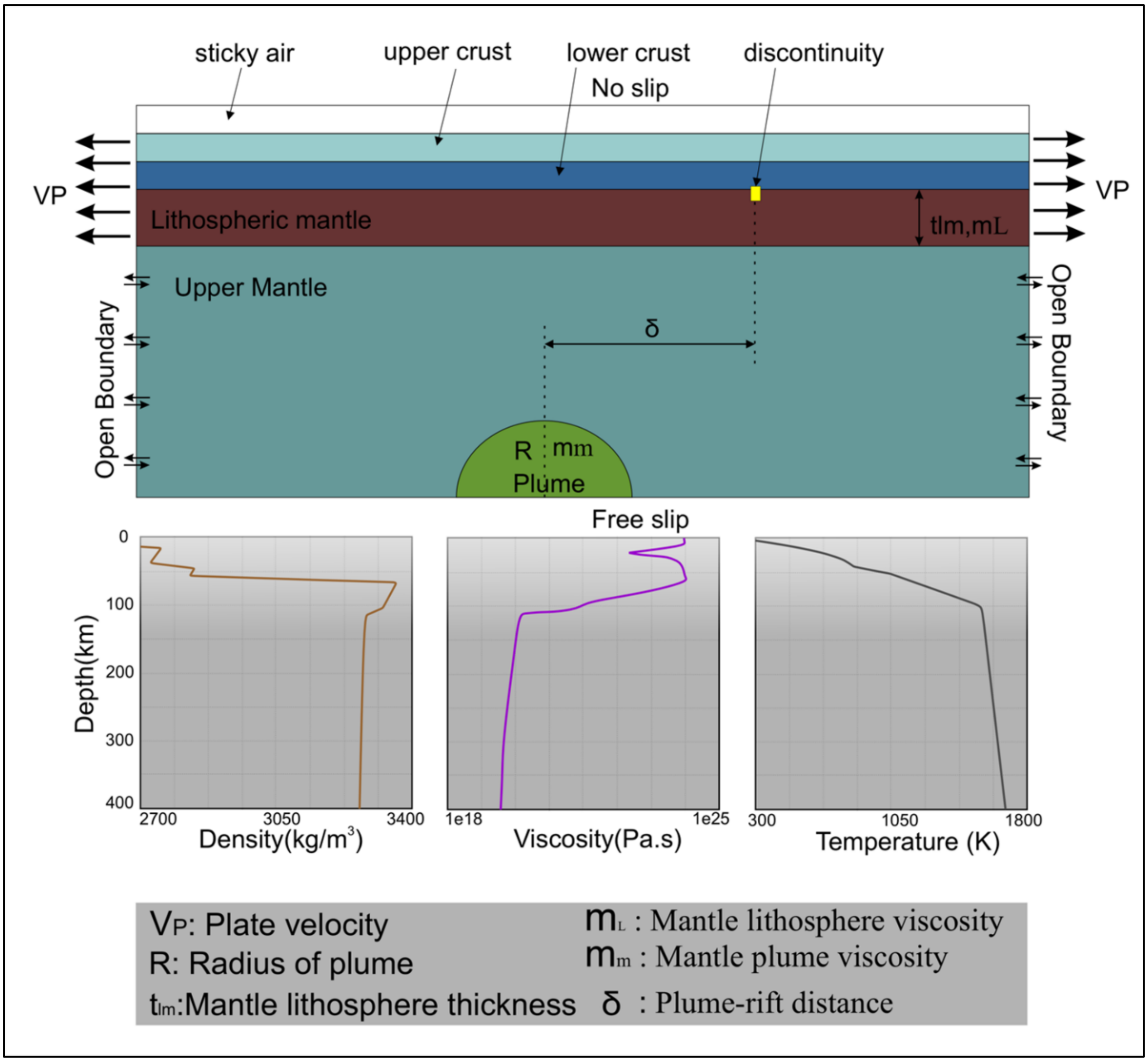

Figure 6.2 *Model setup and boundary conditions used for finite element modelling of the plume-rift interaction.*

To investigate plume-rift interactions observed in various intra-plate tectonic settings, we consider four key variables in this modeling approach: (1) plume-rift distance, (2) plume radius, (3) plate velocity, and (4) lithospheric strength. It is noteworthy that plume-rift interactions have played a significant role in the tectonic evolution of the Indian subcontinent, as several mantle plumes have interacted with the Indian craton during its northward drift in geological history. These include the Kerguelen plume (~120–117 Ma), the Marion plume (~90 Ma), and the Réunion plume (~66 Ma). Geological evidence indicates that various pre-existing rift systems, such as the Narmada Rift along the western craton and the Mahanadi-Godavari Rift along the eastern craton, reactivated during the plume events (Figure 6.1b). To examine their interactions under varying plate kinematics, we selected plate velocities ranging from 0.5 cm/year to 5 cm/year, representing the effects of slow and rapid drift velocities of the Indian craton on plume-lithosphere interactions. Additionally, the plume-rift distance was varied between 0 and 300 km. The radius of the initial plume domain at the model base was adjusted between 50 and 200 km to simulate plumes of varying sizes. Based on available literature data (Naliboff et al., 2020), the viscosity of the mantle lithosphere was set in the range of 5×10^{21} to 5×10^{22} Pa ·s to represent the subcratonic lithosphere of the Indian region accurately.

6.3.2. Reference model simulations

We conducted a series of simulation experiments to investigate how mantle plumes interact with continental lithosphere containing a pre-existing rift. The simulations reveal that plume evolution can follow one of three distinct pathways: 1) Asymmetric plume flow toward the rift, triggered by reactivation of the rift; 2) Plume stagnation, resulting from the cessation of rift activity; and 3) Plume drift, induced by the formation of a new rift. The dominance of any specific pathway is determined by the model variables (described in the previous section). Figure 6.3a illustrates a model simulation demonstrating the dominant rift-ward repositioning of a plume during its stagnation at the lithospheric base. In the initial stage, the buoyant plume head develops into a mushroom shape while exerting dynamic stresses on the mantle lithosphere, leading to significant surface uplift. The plume head also spreads horizontally, but this spreading is strongly asymmetric. The asymmetry arises from the pull of materials toward a low-pressure zone formed beneath the rift center. This dynamic pull also causes the plume axis to tilt toward the rift at an angle of approximately 10–15°. Subsequently, part of the plume material preferentially ascends along the reactivated rift zone, ponding beneath the rift axis (Figure 6.3a). Continued material ponding and the associated decompression melting locally increase dynamic pressure, leading to stress localization that weakens the crustal portion of the lithosphere. This weakening further facilitates the reactivation of the rift system during the emplacement of underplated materials (Figure 6.1a), resulting in high-amplitude (~ 20 km) upwraping of the Moho and development of negative surface topography (~ 1km) above the location of upwrapping (Figure 6.3b). On the opposite flank of the plume head, the material is pulled in much smaller volumes (<25%) and fails to penetrate the crustal lithosphere. Instead, this material stagnates at the lithospheric base. After 6-7 Ma of the initial event, the plume generates a second pulse, which follows a similar evolutionary path and drifts toward the rift axis. However, this second pulse has a much weaker effect on rift reactivation due to its smaller volume, lower dynamic pressure, and reduced decompression melting. The asymmetrical spreading of the plume generates a much larger buoyancy flux (calculated as the density anomaly multiplied by horizontal velocity; Figure 6.3c) on the rift-ward side compared to the opposite side. The velocity profiles show that rift-ward flows of plume material are significantly faster than those on the opposite side of the plume axis (Figure 6.3d). These profiles further suggest that the rift-ward flows exhibit Poiseuille flow characteristics, with maximum horizontal velocities occurring in the middle of the asthenospheric channel. The modeled velocity field patterns align with seismic anisotropy observations from the Réunion plume (Barruol et al., 2019). Notably, the plume head spreads significantly faster than the overriding plate (Figure 6.3d).

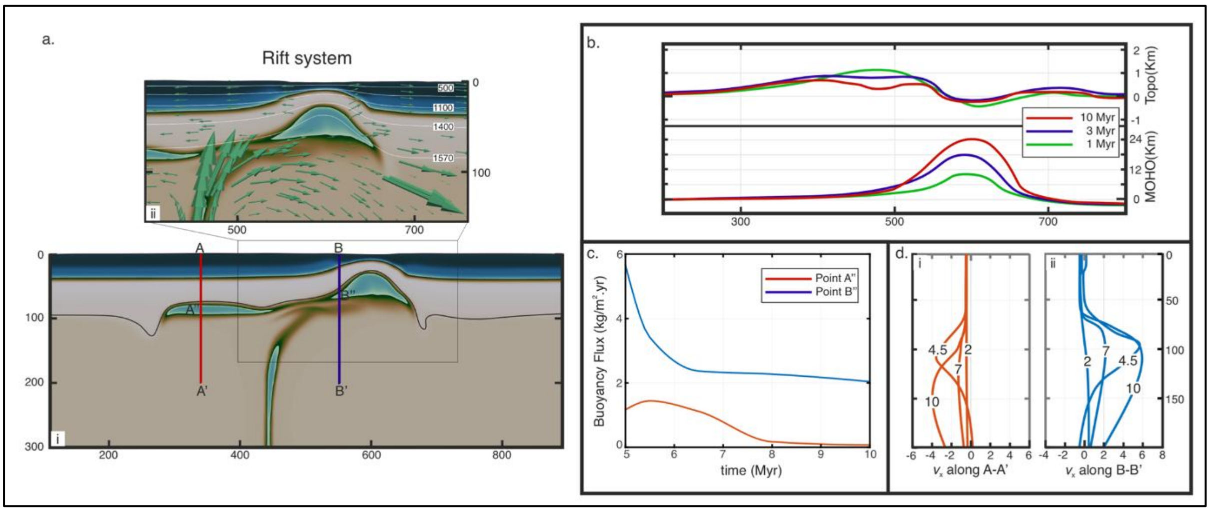

Figure 6.3 (*a. i) Numerical model simulation of ascending plume influenced by a pre-existing rift in the lithosphere for a small plume-rift distance (150 Km). Note that the rift induces an asymmetric spreading of the plume head and accumulation of plume materials beneath the rift axis (a detailed description is provided in the text). Green arrows in the magnified panel show the velocity field in the mantle. Calculated plots of (b) deflection of Moho and the surface topography varying with horizontal distance at different time instances (indicated in the colours in the insets) (c) Variation of the Buoyancy flux at two locations (AA' and BB') on either side of the plume axis shown in the inset in panel a. d) Depth wise profiles of horizontal velocity component (*V_x*) at AA' and BB'.*

Another reference simulation is presented in Figure 6.4 to show the evolutionary path of a plume as it tends to stagnate at the lithospheric base. The initial stages of evolution are similar to those described earlier. However, the plume begins to deform the overlying lithosphere after stagnation, resulting in the highest surface uplift directly above the plume head (Figure 6.4a-b). This contrasts with the previous model (Figure 6.3a-b), where the highest surface elevations occurred symmetrically on either side of the reactivated rift axis. Additionally, the plume head spreads symmetrically around its axis in an upright position with nearly equal buoyancy flux (Figure 6.4c) and lateral spreading velocities (~4 cm/yr) (Figure 6.4d), suggesting a significantly weak mechanical influence of the adjacent rift. This mode of interaction concentrates stresses primarily on the oceanic plate directly above the plume axis, exerting a slight mechanical weakening effect on the pre-existing rift zone. Overall, this model

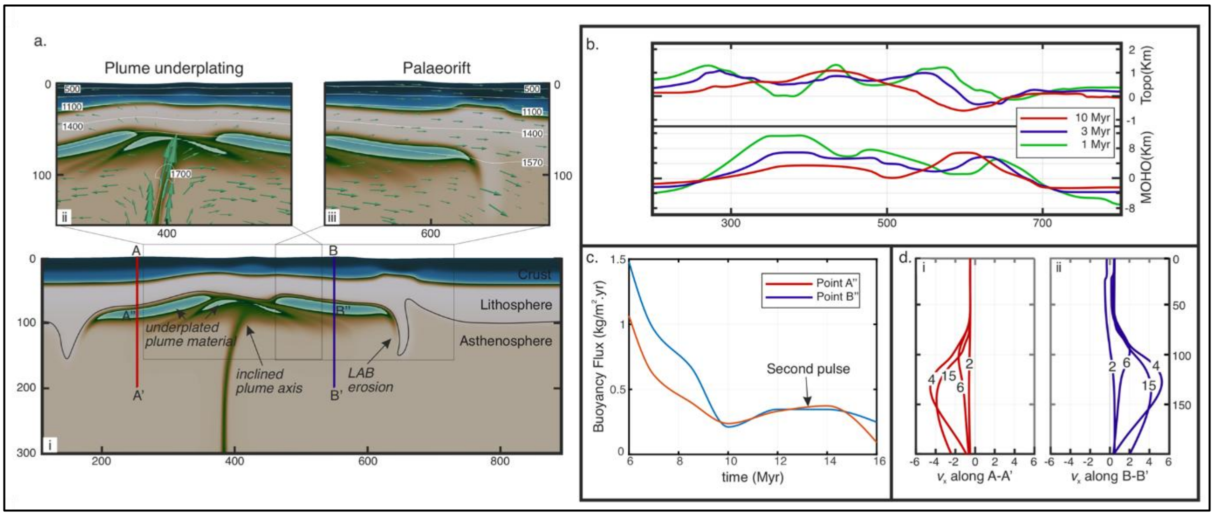

Figure 6.4 (*a. i) Numerical model simulation with intermediate plume-rift distance (200 km). It is to be noted that plumes undergo relatively weak interaction of the rift (on the right side) and eventually give rise to a more symmetrical plume underplating structure beneath the lithosphere with strong LAB erosions on either flank of the plume-head. Plume shows rift ward deflection implying some influence of palaeorift. Detail underplating patterns (a. ii) and downward lithospheric drag (a. iii) are sown in the enlarged views of the overlying panels. (b) The fluctuation of Moho and surface topography in the horizontal direction in different time transects are shown. c) variation of buoyancy fluxes in two locations of the plume-head on either side of the plume axis show at different time. d) Depth-wise profiles of horizontal velocity component (Vx) at AA' (d.i) and BB' (d.ii).*

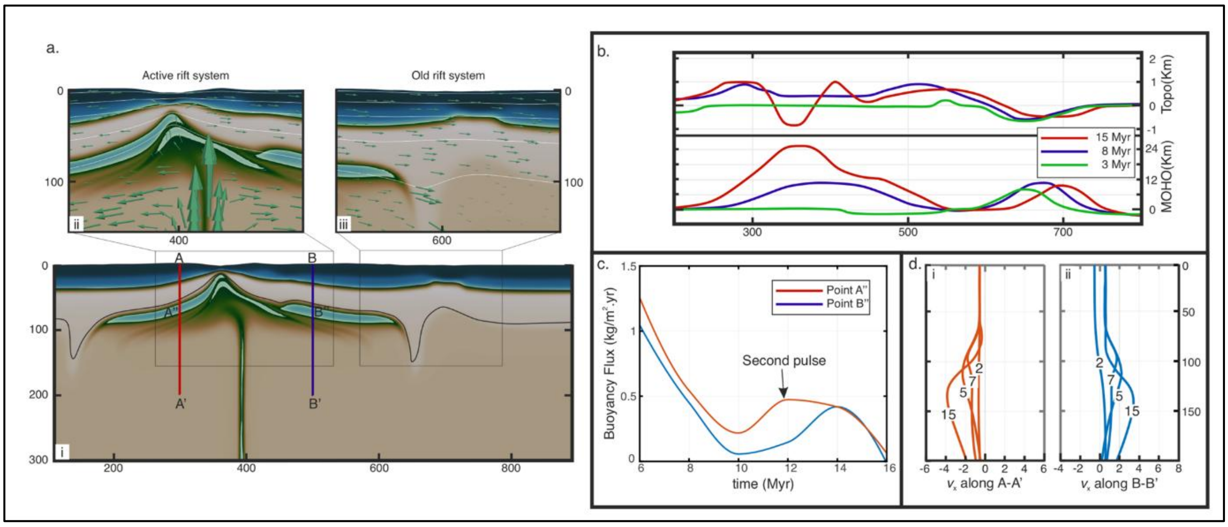

Figure 6.5 (*a. i) Numerical model simulation of plume evolution with large plume-rift distance (250 km). The Moho unwrapping is maximum, and it tilts opposite to the rift axis. It is to be noted that the plume materials accumulate beneath the newly formed rift (a. ii) due to higher rift induced divergent velocity, whereas the pre-existing rift failed to reactivate (a. iii). (b) The changes in Moho and surface topography along the horizontal direction are presented at different time intervals. (c)The variation in buoyancy fluxes at two distinct locations of the plume head (A'' and B''), on either side of the plume axis are shown over time.(d) Depth profiles of the horizontal velocity component (Vx) are provided at locations AA' (d.i) and BB' (d.ii).*

predicts the generation of small melt volumes from the initial plume pulse, with subsequent pulses producing even smaller volumes.

A third reference model is presented in Figure 6.5 to illustrate the evolutionary path of a plume in the absence of strong influence by the pre-existing rift. Following the plume's impingement into the mantle lithosphere, the model develops maximum MOHO upwrapping above the plume head (Figure 6.5b), which tilts opposite to the rift axis (Figure 6.5a). This tilting is attributed to stronger frictional shear from plate motion directed away from the rift. The plume materials of the primary pulse flow horizontally away from the rift and weaken the crustal lithosphere, resulting in the formation of a new rift in the impinged region (Figure 6.5a). The initiation of the new rift induces significant divergent velocities (~4cm/yr) in the crust (Figure 6.5d), creating a sink for plume material to underplate beneath the newly formed rift. In contrast, the pre-existing rift fails to strongly reactivate under the transformed crustal velocity conditions (Figure 6.5b), allowing the left flank of the plume to evolve with higher buoyancy fluxes and achieve maximum velocities (Figure 6.5c). This model highlights the role of plate motion in reversing the flow direction in the lithosphere, as reflected in the velocity profiles (Figure 6.5d). At 3 Ma, the horizontal component of plate velocity entirely dictates the magnitude of horizontal flows (2-3 cm/yr) in the plume material at the lithospheric base. This finding contrasts sharply with observations from the first reference simulation (Figure 6.3a), where plume materials flowed counter to the plate motion due to pressure drag from the reactivated pre-existing rift. Over time, however, the plume spreading velocity surpasses the plate velocity, dominating the system's dynamics (Figure 6.4d). This plume-dominated dynamic eventually forms a new rift at the point of flow divergence, which ceases the pre-existing rift activity.

6.3.3. Rift-plume interactions: parametric analyses

6.3.3.1 Plume axis - rift separation (δ)

We varied the horizontal distance (δ) between the lithospheric pre-existing weak zone (rift) and the plume axis in the model runs, keeping all other model parameters constant. For a large plume-rift distance (δ = 250 Km), the plume ascends through upper mantle to vertically encounter the lithospheric base at 0.8 Ma, producing nearly symmetrical flow divergence above the plume head (Figure 6.6a). During this interaction, the ascending plume induces upward flexural deformations in the lithosphere, developing high strain-rates in the crustal layer right above the plume axis. The pre-existing rift zone, however, remains under a low strain-rate condition, showing little or no reactivation (as indicated by a decreasing strain rate in Figure 6.6b). The first plume pulse progressively attains an active phase (1 Ma – 4 Ma) of stagnation in which the plume head migrates dominantly in the horizontal direction, dragging basal lithospheric materials to subduct symmetrically at either flank of the plume. At 1.29 Myr, the plume generates a second pulse, which similarly interacts with the lithosphere, leading to significant thinning of the mantle lithosphere. This pulse also produces a high- strain zone, aligned slightly off-axis with respect to the plume structure in the direction of rifting plate motion. From the model velocity field, it appears that the reactivation of the rift forces the plume head to impinge asymmetrically further into the lithosphere. Overall, they are characterised by low buoyancy flux ratio and low-velocity ratio beneath the original rift (Figure 6.6c-d).

Model with δ = 200 Km shows a similar evolutionary trend of the plume head prior to its encounter with the lithospheric base at 0.9 Myr. After impinging to the lithosphere, plume materials flow laterally in both directions towards and away from the rift axis. The plume impingement gives rise to a high-strain zone in the lithosphere directly above the plume axis, as observed in the δ = 200 Km model (Figure 6.6b). However, strong lateral flows cause this high-strain zone to disappear within a short period of time (1.2 Myr). The divergence motion in the plume drags the overlying lithospheric materials to flow in the horizontal directions above the stagnated plume material. Consequently, the plume dynamics becomes too weak to impinge into the lithosphere further. Further decrease in δ (= 150 Km) drastically changes the pattern of plume-lithosphere interaction. Unlike the previous model, this model develops strongly asymmetric high-strain zones in the lithosphere when the plume tends to interact with the overlying lithosphere (Figure 6.6b). The high-strain zones are characteristically aligned toward the rifting axis. The rift reactivation eventually pulls the impinging plume materials to accumulate beneath the rift axis and induces strong upwrapping of the Moho. However, the plume materials stagnated at the lithospheric base flow horizontally at higher rates to develop stronger drags to the lithosphere on the flank opposite to rift axis, resulting in asymmetric delamination of lithospheric mantle. Overall, they are characterised by a very high buoyancy flux ratio and high-velocity ratio beneath the original rift (Figure 6.6c-d).

6.3.3.2 Divergent velocity in rifting (V_p)

We ran a set of simulations by varying the pull velocity (Vp) at the edges of the model lithospheric plate, keeping the plume-rift distance δ was held constant at 200 Km). For V_p = 0.5cm/year, the plume head ascends at a 2 cm/year rate to encounter the lithospheric base at

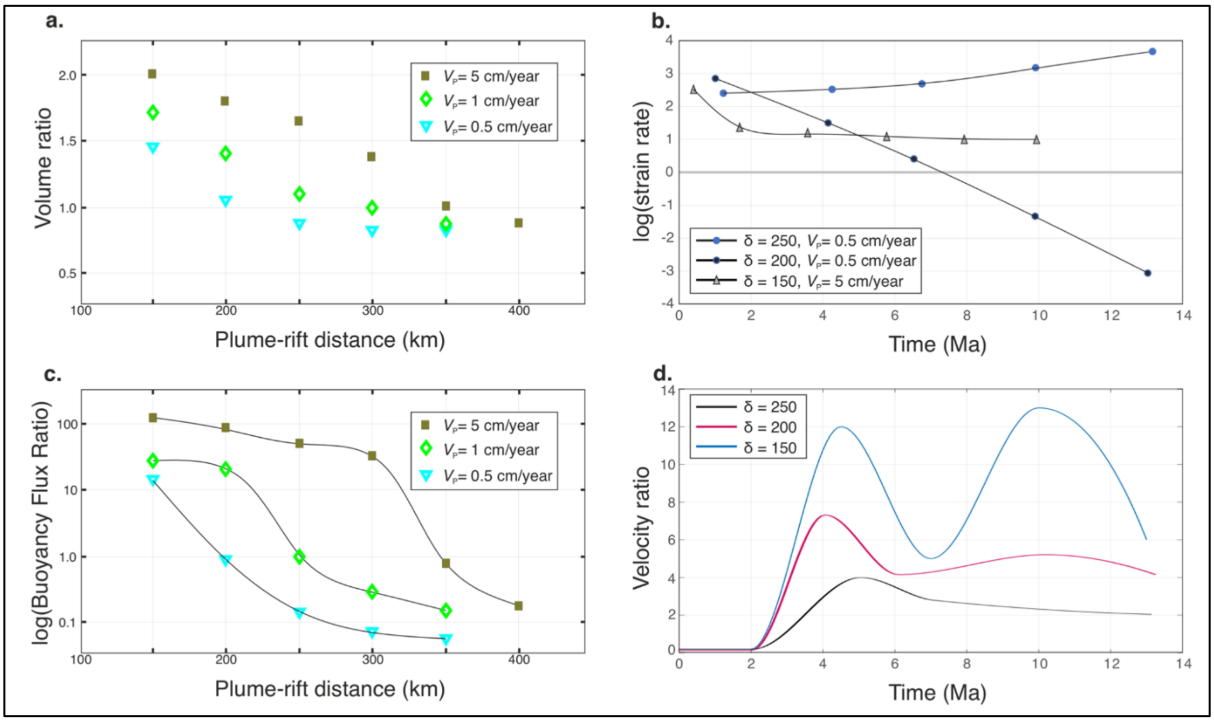

Figure 6.6 *Calculated plots from numerical models for different parametric values. (**a**) Variation of volume ratio of plume material between right- and left-branch of plume-head as a function of plume-rift distance in different plate velocity. (b) Calculated plots of strain rate with respect to time (in Ma) as a function of plume-rift distance and plate velocity. (c) Changes of plume-head buoyancy for different plume-rift distances at varying plate velocity. (d) Plots of horizontal velocity ratio at LAB depth and the surface of the plate.*

0.9 Myr. Its impingement into the lithosphere forces the plume materials to flow laterally towards and away from the rift axis. This divergent flow pattern drags the overlying lithospheric mantle, eventually delaminating and subducting at either plume flank. Increasing V_p accelerates the ascent rate (4 cm/year) of the plume, allowing the plume to interact with the lithosphere at a relatively shorter time (~ 0.8 Myr). The plume materials begin to spread divergently in horizontal directions upon impingement, as in the previous model. The second plume pulse produced after 3 Myr significantly weakens the lithosphere, leading to off-axial emplacement of a part of the plume materials in the direction of plate motion. Large V_p values (~5 cm/year) causes the plume head to become strongly asymmetrical before it interacts with the lithosphere (Figure 6.6d). This symmetric to asymmetric transition of the plume head occurs due to a more substantial drag of rift-ward mantle flows driven by the reactivation of the rift as well as the high buoyancy flux beneath the rift (Figure 6.6c). The rift-controlled kinematics forces the plume head toward the rift. After impinging into the base, the plume materials continue to flow toward the rift, ultimately channelizing through the rift axis in the lithosphere and give rise to large upwrapping of the Moho.

6.3.4. Interacting versus non-interacting rift-plume systems

Using a synthesis of the model results, we recognize three distinct plume-rift mechanisms: 1) Mechanism I- plume-induced reactivation of pre-existing rift and its feedback effect on rift-ward plume flow, 2) Mechanism II- plume stagnation at lithospheric base, accompanied by cessation of the pre-existing rift, and 3) Mechanism III- plume-induced neo-rifting in lithosphere, and its influence in plume remobilization. Each of these three mechanisms becomes operational under specific conditions of the following factors: horizontal separation between the plume axis and the pre-existing rift (δ), viscosity (η_L) of the overlying mantle lithosphere, continental plate velocity (V_P), and initial plume size (R) (Figure 6.7). Small δ, or high V_p or large R gives rise to the plume tectonic setting to evolve in Mechanism I, favouring the pre-existing rift to reactivate and pull most of the plume material to accumulate beneath its axial zone. This mechanism activates the pre-existing rift in determining the location of plume-driven volcanism away from the plume axis, as applicable for Deccan volcanisms. Our model suggests that the main eruption site of this volcanic event in the Indian craton was located away from the Reunion plume axis due to intense plume-rift interaction in Mechanism I. Increasing δ or V_p, or decreasing plume size lowers the plume-rift interaction, resulting in a transition from Mechanism I to III. Mechanism III allows a large volume fraction of the plume materials to flow in the direction opposite to the pre-existing rift. This condition fails to reactivate the rift but gives rise to new rifts in the overlying lithosphere, depending on η. The transitional mechanism (Mechanism II) stagnates plume materials at the lithospheric base, and the rift-ward flows become progressively weak, leading to the cessation of the pre-existing rift activities.

Mechanisms I (interacting plume-rift setting) and II (non-interacting plume-rift setting) yield contrasting melt generation patterns. An interacting system evolves through higher degrees of decompression melting, with the resulting melt potentially reaching the surface depending on the availability of fracture systems during the reactivation of the pre-existing rift. On the other hand, non-interacting systems can produce substantial amounts of melts when the overlying lithosphere is weak, allowing the plume materials to ascend to shallower depths (Figures 6.3a and 6.5a). Moreover, the present study reveals that these two mechanisms give rise to distinctive surface topography with significant differences in the Moho profiles (Figures 6.3b and 6.5b). Plume underplating and melt generation result in the unwrapping of Moho and the formation of a topographic high directly above the plume head in non-interacting conditions. However, plume-rift interaction adds complexities to the topographic response. The topography progressively subsides in rift reactivation, attaining more negative elevations over time, while the Moho depth decreases. As the plume encounters the lithosphere, the plume head starts to spread laterally and reactivate the rift system, which further reduces the surface topography and Moho depth, but in an asymmetric fashion in the case of an interacting plume-rift system. The old rift remains dormant for non-interacting systems, and a topographic low and Moho unwrapping occurs in the new rift location.

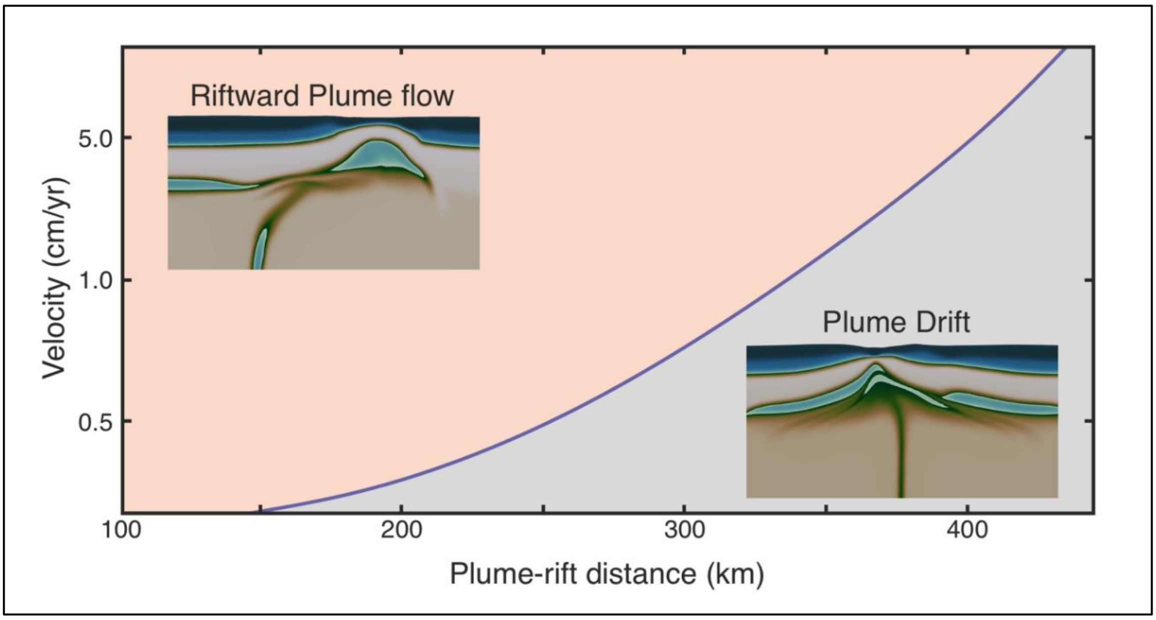

Figure 6.7 *Fields of interacting vs. non-interacting plume-paleo rift in space define by plume-rift distance (x-axis) and plate velocity (y-axis). Increasing plate velocity or decreasing plume-rift distance facilitates the development of an interacting plume-rift system, which gives rise to rift-ward plume flows.*

6.4. Appendix A

A.1. Governing equations

The code used for our numerical simulations is ASPECT, a massively parallel finite element code primarily designed for modelling thermal convection in the mantle. It consists of a small core that solves the basic fluid dynamics equations, and for other tasks, it relies on external libraries and plug-ins (Bangerth et al., 2022a, 2022b; Heister et al., 2017; Kronbichler et al., 2012). The code is based on the DEAL.II software library (Alzetta et al., 2018) and assumes that, at a regional length scale and geological time scale, earth materials may be treated as highly viscous fluid with infinite Prandtl number, and hence Stokes equations can be solved neglecting inertial forces. This leads to the following expression of the momentum equation:

$$-\nabla.\left(2\mu_{eff}\dot{\epsilon}(u)\right)+\nabla P=\rho g \qquad (6.1)$$

where μ_{eff} is the effective viscosity, $\dot{\epsilon}$ is the strain rate tensor, $u$is the velocity vector, ρ is the density, and $g$is the gravity vector. Materials the assumed incompressible leading to zero divergences of the velocity vector u:

$$\nabla.u=0 \qquad (6.2)$$

The effect of the temperature field should also be taken into account using the conservation of energy equation:

$$\rho C_P\left(\frac{\partial T}{\partial t}+u.\nabla T\right)-\nabla.\left(k+\upsilon_h(T)\right)\nabla T=H_r \qquad (6.3)$$

where C_P is the heat capacity, *T* is temperature, *k* is thermal conductivity, and H_r is the internal radiogenic heat production. υ_h is the artificial diffusivity that prevents the oscillations due to advection of the temperature field calculated following entropy viscosity method.To account for the advection of material properties, ASPECT relies on compositional fields that are advected with the flow (Gassmöller et al., 2018). Hence, the system of equations is closed by solving for a conservation equation for each compositional field as:

$$\frac{\partial c_i}{\partial t}+u.\nabla c_i-\nabla.\left(\upsilon_h(c_i)\right)\nabla c_i=0 \qquad (6.4)$$

where c_i is the *i*th compositional field. Artificial viscosity is again introduced to stabilize advection.

A.2. Constitutive nonlinear rheology

In ASPECT, material properties are implemented within the *Material model* module, which adapts a visco-plastic rheology. The model is incompressible and depends primarily on diffusion-dislocation and Drucker-Prager criterion, which can be combined into more complex rheologies.

At higher temperatures, materials experience nonlinear viscous deformation via power-law dislocation creep or grain boundary (or bulk) diffusion creep. These two rheologies can be expressed by strain rate and temperature-dependent viscosity as:

$$\mu_{eff}^{vis}=\frac{1}{2}A^{\frac{-1}{n}}d^{\frac{m}{n}}\dot{\epsilon}_{ii}^{\frac{(1-n)}{n}}\,exp\left(\frac{E+PV}{nRT}\right) \qquad (6.5)$$

where A is the prefactor, n is the stress exponent, $\dot{\epsilon}_{ii} = \sqrt{\frac{1}{2}\dot{\epsilon}'_{ij}\dot{\epsilon}'_{ij}}$ is the effective deviatoric strain rate, which is the square root of second invariant of deviatoric strain rate tensor, d is the grain size, m is the grain size exponent, E is the activation energy, V is the activation volume and R is the gas constant. In case of diffusion creep (μ_{eff}^{df}), n =1 and m>0, while for dislocation creep (μ_{eff}^{dl}) n>1 and m=0. At relatively low temperature the material behaviour is modelled using plastic rheology.

Table A.1 *Parameters for calculating material model*

	Upper crust	Lower crust	Lithospheric mantle	Upper mantle	Plume	Seed	Sticky air
Density *(kg m-3)*	2750	2900	3325	3300	3275	3325	1
Grain size *(m)*	1e-3						
Thermal expansivities	2e-5						
Heat capacities	750						
Prefactors for dl *(MPa^{-n} s^{-1})*	1.1e-28	1.0e-21	2.41e-16	5.5e-16	5.5e-16	1.1e-28	1e-19
Stress exponents for dl	4.0	3.0	3.5	3	3	4.0	1
Activation energies for dl *(J mol^{-1})*	223.e3	356.e3	540.e3	540.e3	540.e3	223.e3	0
Activation volumes for dl *(J Pa^{-1})*	0	0	0	14e-6	14e-6	0	0
Prefactors for df *(MPa^{-n} s^{-1})*	1.1e-11	1e-11	2.41e-11	5.41e-11	5.41e-11	1.1e-11	1.92e-11
Grain size exponents for df	0	0	2.5	2.5	2.5	0	0
Activation energies for df *(J mol^{-1})*	223.e3	356.e3	540.e3	540.e3	540.e3	223.e3	335e3
Activation volumes for df *(J Pa^{-1})*	0	0	0	14e-6	14e-6	0	4e-6

The effective viscosity is locally adapted so that the stress generated during deformation does not exceed the yield stress (viscosity rescaling method). The effective plastic viscosity is given by

$$\mu_{eff}^{pl} = \frac{\sigma_y}{2\dot{\epsilon}_{ii}} \tag{6.5}$$

where $\sigma_y$is the yield stress. Here, plasticity limits viscous stress via Drucker-Prager yield criterion given by:

$$\sigma_y = Ccos(\varphi) + Psin(\varphi) \tag{6.6}$$

where *C* is the cohesion and $\varphi$is the friction angle. This 2D form of the equation is equivalent to Mohr Coulomb yield surface and for $\varphi = 0$, the yield stress is fixed and equal to cohesion (Von Mises yield criterion).

In nature, under the same deviatoric stress, both viscous creeps act simultaneously. Hence, we consider composite viscous rheology by harmonically averaging μ_{eff}^{dl} and μ_{eff}^{df}

$$\mu_{eff}^{cp} = \frac{\mu_{eff}^{df}\mu_{eff}^{dl}}{\mu_{eff}^{df} + \mu_{eff}^{dl}} \tag{6.7}$$

Moreover, we assume that the viscous creep and plastic yielding are independent processes that can occur simultaneously, and the mechanism resulting in the lowest effective viscoplastic stress is favored:

$$\mu_{eff}^{vp} = min\left(\mu_{eff}^{pl}, \mu_{eff}^{cp}\right) \tag{6.8}$$

Strain weakening is included in the system by calculating the finite strain invariant through compositional fields within the material model and linearly reducing the cohesion and internal friction angle as a function of the finite strain magnitude. While calculating finite strain invariant (e_{ii}), a single composition field tracks the value of finite strain invariant via

$$e_{ii}^{t} = e_{ii}^{(t-1)} + \dot{e}_{ii}dt \tag{6.9}$$

where *t* and *t-1* are current and prior time steps, $\dot{e}_{ii}$ is the second invariant of the strain rate tensor, and *dt* is the time step size. When the accumulated strain is less than a given value, *C* and $\varphi$are constant. For accumulated strain values greater than this threshold, *C* and φ decrease linearly until the system reaches a certain maximum of accumulated strain is reached, after which they are kept constant again (Table A.1).

A.3. Model parameters and boundary conditions

The initial temperature profile is adiabatic with a potential temperature of 1600 K. This adiabatic profile is superimposed with a conductive temperature profile for the continental lithosphere. If the layer has thickness *dz*, then the temperature at, and heat flow through, the bottom of the layer (T_B, q_B) can be expressed in terms of the temperature and heat flow at the top of the layer (T_r, q_r) and properties (A,k) of the layer,

$$T_B = T_T + \frac{q_T}{k}\Delta z - \frac{A\Delta z^2}{2k} \tag{6.10}$$

$$q_B = q_T - A\Delta z \tag{6.11}$$

Equations (6.11) and (6.12) are applied to successive layers, resetting T_T and q_T at the top of each new layer with the values T_B and q_B solved for the bottom of the previous layer. A temperature perturbation of 200 K is added to the plume material at of the bottom boundary of the model.

The density is primarily dependent on the composition, but in a compressible medium, it also depends on pressure and temperature, whereas in an incompressible medium, it depends only on temperature. The density depends on pressure and temperature via the following two equations:

$$\rho_{incomp} = \rho_{ref}\left(1 - \alpha\left(T - T_{ref}\right)\right) \tag{6.12}$$

$$\rho_{comp} = \rho_{ref}\left(\beta\left(P - P_{surface}\right)\right)\left(1.0 - \alpha\left(T - T_{ref}\right)\right) \tag{6.13}$$

Since our visco-plastic model is incompressible in nature, the density variation will follow equation (6.13).

A viscosity profile is also needed to model plume and lithosphere interaction properly. The viscosity is calculated in ASPECT using flow laws given in section A.2. They depend on pressure, temperature, and strain rate. Our profile has a high viscosity upper crust followed by a relatively low viscosity lower crust, which follows a lithospheric mantle whose viscosity gradually decreases from high (equivalent to upper crust) to moderate due to an increase in temperature. This is followed by the upper mantle, which has even lower viscosity.

Table *A*.2 Model parameters used in numerical simulations

Parameters	**Values**
Model length(L)	1000km
Model height(H)	410km
Thickness- upper crust(t_{uc})	25km
lower crust(t_{lc})	15km
lithospheric mantle(t_{lm})	40-80km
Plume diameter	20-100km
Plate velocity	0.25-5cm/year
Plume-rift distance	0-300km
Surface Temperature (Ts1)	293 K
Temperature at upper crustal base (Ts2)	681 K
Temperature at lower crustal base (Ts3)	823 K
Temperature at the base of the lithosphere (Ts4)	1573 K
Model base temperature (Tb)	1700 K
Initial plume temperature (Tp)	1700-1900 K
Heat production at upper crust (A)	1.5e-6 W/m^3
Thermal conductivity- upper crust (k1)	2.5 W/m.K
lower crust (k2)	2.5 W/m.K
lithospheric mantle (k3)	3.5 W/m.K
Layer surface heat flow- upper crust (qs1)	0.065357 W/m^2
lower crust (qs2)	0.035357 W/m^2
lithospheric mantle (qs3)	0.035357 W/m^2

The boundary composition and temperature are the same as the initial composition and temperature. The bottom boundary is *free slip* and *isothermal,* with a maximum temperature of 1700 K. The top boundary is a *free surface* (or *free slip*) and *isothermal* with a minimum temperature of 293 K (or 273 K) (Table A.2). The side boundaries are *insulating* in nature. A prescribed diverging velocity profile of 0.25 cm/year to 5 cm/year is given in the lithosphere, which is well within the limit of slow-spreading ridge (Table 6.2). The vertical velocity on the side boundaries of the lithosphere is zero. This mass outflux through the lithosphere is counter balanced by mass influx in the mantle to conserve total mass.

6.5. Appendix B

B.1. Parametric Analysis

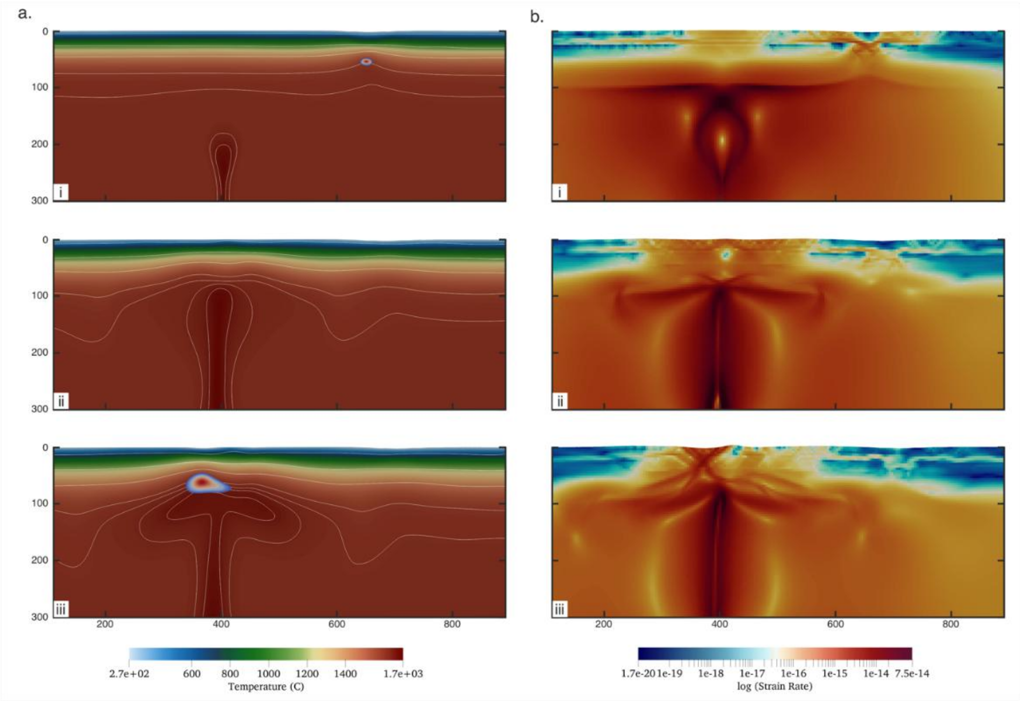

Figure B1 *Evolution of plume in the model with* δ *= 250 km and* V_P *= 0.5cm/year showing (a) temperature and (b) strain rate variations.*

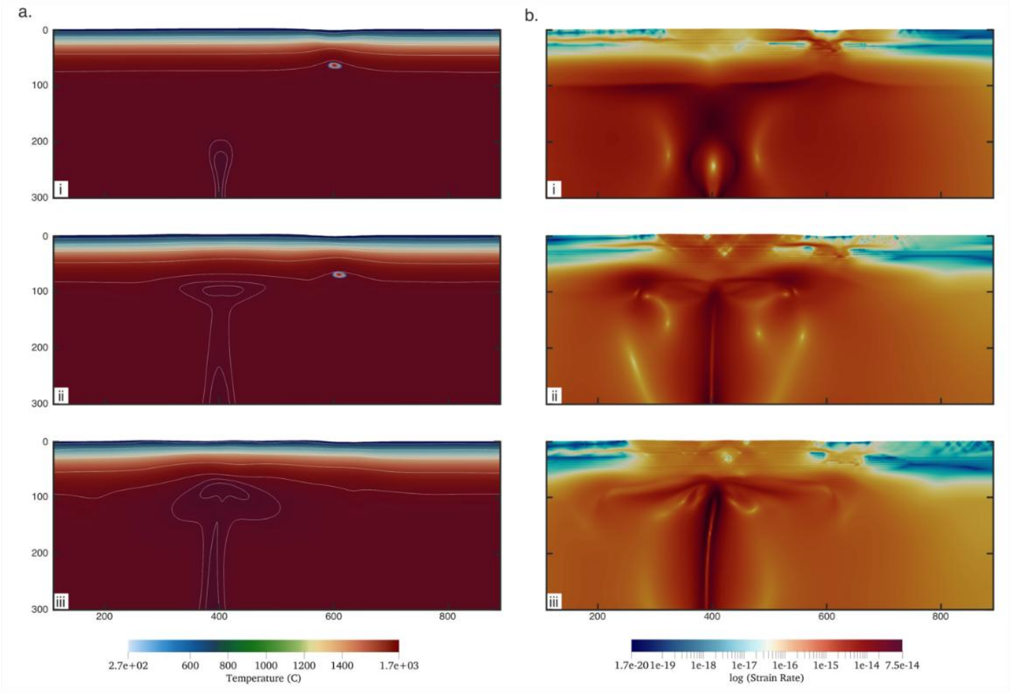

Figure B2 *Evolution of plume in the model with* δ *= 200 km and* V_P *= 0.5cm/year showing temporal change in (a) temperature and (b) strain rate.*

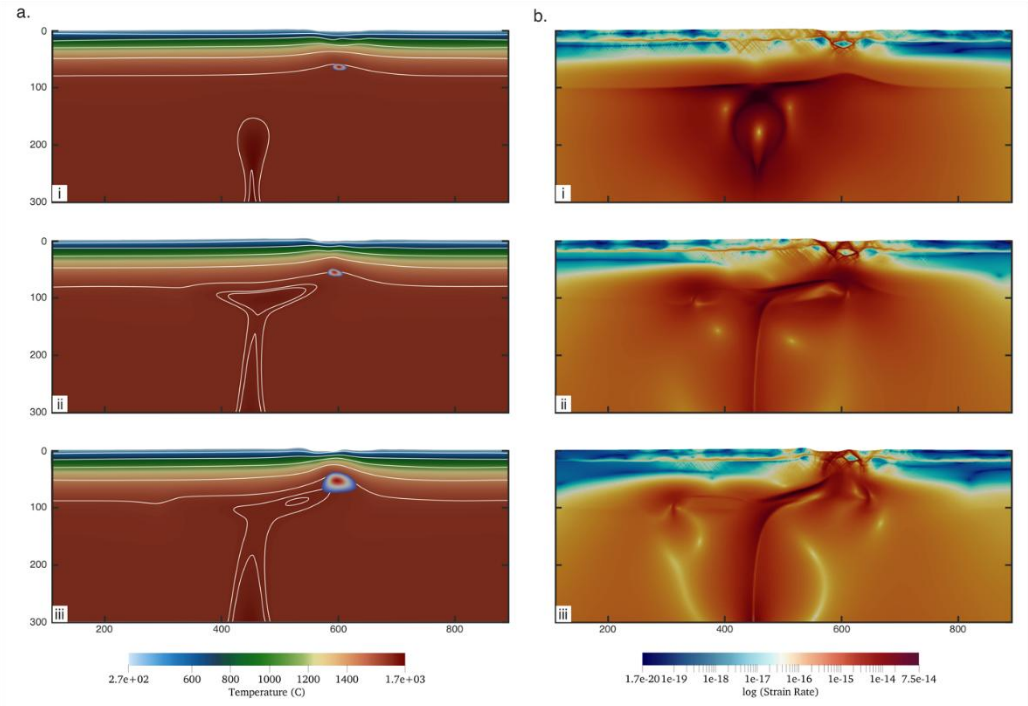

Figure B3 *Evolution of plume in the model with* δ *= 150 km and* V_P *= 0.5cm/year showing (a) temperature and (b) strain rate variations with time.*

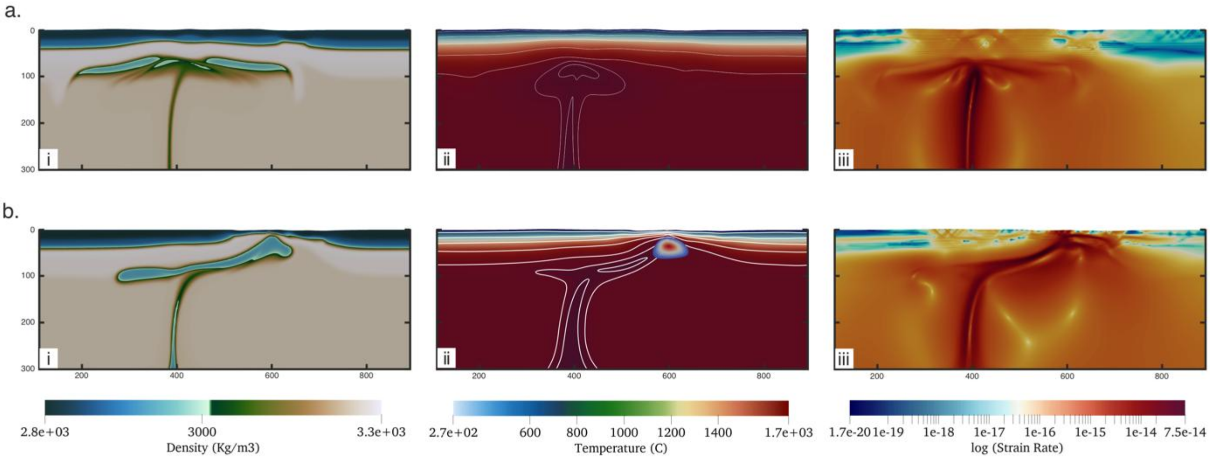

Figure B4 *Comparison of the model with (a)* δ *= 200 km and* V_P *= 0.5cm/year and (b)* δ *= 200 km and* V_P *= 5 cm/year showing (i) density, (ii) temperature, and (iii) strain rate variations.*

6.6. References

Alzetta, G., Arndt, D., Bangerth, W., Boddu, V., Brands, B., Davydov, D., Gassmöller, R., Heister, T., Heltai, L., Kormann, K., Kronbichler, M., Maier, M., Pelteret, J.P., Turcksin, B., Wells, D., 2018. The deal.II library, Version 9.0. Journal of Numerical Mathematics 26, 173–183. https://doi.org/10.1515/jnma-2018-0054

Baksi, A.K., 1995. Petrogenesis and timing of volcanism in the Rajmahal flood basalt province, northeastern India. Chem Geol 121, 73–90.

Bangerth, W., Dannberg, J., Fraters, M., Gassmoeller, R., Glerum, A., Heister, T., Myhill, R., Naliboff, J., 2022a. ASPECT v2.4.0. https://doi.org/10.5281/zenodo.6903424

Bangerth, W., Dannberg, J., Fraters, M., Gassmoeller, R., Glerum, A., Heister, T., Myhill, R., Naliboff, J., 2022b. Advanced Solver for Problems in Earth's ConvecTion, User Manual. https://doi.org/10.6084/m9.figshare.4865333

Basantaray, A.K., Mandal, A., 2022. Interpretation of gravity–magnetic anomalies to delineate subsurface configuration beneath east geothermal province along the Mahanadi rift basin: a case study of non-volcanic hot springs. Geothermal Energy 10. https://doi.org/10.1186/s40517-022-00216-4

Behera, L., Sain, K., Reddy, P.R., 2004. Evidence of underplating from seismic gravity studies in the Mahanadi delta eastern India and its tectonic significance. J Geophys Res Solid Earth 109, 1–25. https://doi.org/10.1029/2003JB002764

Bhattacharji, S., Chatterjee, N., Wampler, J.M., Nayak, P.N., Deshmukh4, S.S., 1996. Indian Intraplate and Continental Margin Rifting, Lithospheric Extension, and Mantle Upwelling in Deccan Flood Basalt Volcanism near the K/T Boundary: Evidence from Mafic Dike Swarms1. J Geol 104, 379–398.

Bhowmik, S.K., Wilde, S.A., Bhandari, A., Pal, T., Pant, N.C., 2012. Growth of the Greater Indian Landmass and its assembly in Rodinia: Geochronological evidence from the Central Indian Tectonic Zone. Gondwana Research 22, 54–72. https://doi.org/10.1016/j.gr.2011.09.008

Blackburn, T.J., Olsen, P.E., Bowring, S.A., Mclean, N.M., Kent, D. V, Puffer, J., Mchone, G., Rasbury, E.T., Et-Touhami, M., 2013. Zircon U-Pb Geochronology Links the End-Triassic Extinction with the Central Atlantic Magmatic Province. Science (1979) 340, 941–945.

Bryan, S.E., Ferrari, L., 2013. Large igneous provinces and silicic large igneous provinces: Progress in our understanding over the last 25 years. Bulletin of the Geological Society of America. https://doi.org/10.1130/B30820.1

Burov, E., Gerya, T., 2014. Asymmetric three-dimensional topography over mantle plumes. Nature 513, 85–89. https://doi.org/10.1038/nature13703

Burov, E., Guillou-Frottier, L., 2005. The plume head-continental lithosphere interaction using a tectonically realistic formulation for the lithosphere. Geophys J Int 161, 469–490. https://doi.org/10.1111/j.1365-246X.2005.02588.x

Chattopadhyay, A., Bhowmik, S.K., Roy, A., 2020. Tectonothermal evolution of the Central Indian Tectonic Zone and its implications for Proterozoic supercontinent assembly: The current status. Episodes 43, 132–144. https://doi.org/10.18814/epiiugs/2020/020008

Chaudhuri, A.K., Deb, G.K., 2003. Proterozoic Rifting in the Pranhita-Godavari Valley: Implication on India-Antarctica Linkage. Gondwana Research 7, 301–312.

Chenet, A.L., Quidelleur, X., Fluteau, F., Courtillot, V., Bajpai, S., 2007. 40K-40Ar dating of the Main Deccan large igneous province: Further evidence of KTB age and short duration. Earth Planet Sci Lett 263, 1–15. https://doi.org/10.1016/j.epsl.2007.07.011

Choubey, V.D., 1971. Narmada-Son Lineament, India. Nature 232, 38–40.

Curray, J.R., Munasinghe, T., 1991. Origin of the Rajmahal Traps and the 85°E Ridge: Preliminary reconstructions of the trace of the Crozet hotspot. Geology 19, 1237–1240.

Ernst, R.E., 2014. Large Igneous Provinces. Cambridge University Press.

François, T., Koptev, A., Cloetingh, S., Burov, E., Gerya, T., 2018. Plume-lithosphere interactions in rifted margin tectonic settings: Inferences from thermo-mechanical modelling. Tectonophysics 746, 138–154. https://doi.org/10.1016/j.tecto.2017.11.027

French, S.W., Romanowicz, B., 2015. Broad plumes rooted at the base of the Earth's mantle beneath major hotspots. Nature 525, 95–99. https://doi.org/10.1038/nature14876

Funck, T., Jackson, H.R., Louden, K.E., Klingelhöfer, F., 2007. Seismic study of the transform-rifted margin in Davis Strait between Baffin Island (Canada) and Greenland: What happens when a plume meets a transform. J Geophys Res Solid Earth 112. https://doi.org/10.1029/2006JB004308

Gassmöller, R., Lokavarapu, H., Heien, E., Puckett, E.G., Bangerth, W., 2018. Flexible and Scalable Particle-in-Cell Methods With Adaptive Mesh Refinement for Geodynamic Computations. Geochemistry, Geophysics, Geosystems 19, 3596–3604. https://doi.org/10.1029/2018GC007508

Ghosh, D., Sen, J., Mandal, N., 2024. Periodicity in the Deccan Volcanism Modulated by Plume Perturbations at the Mid-Mantle Transition Zone. J Geophys Res Solid Earth 129. https://doi.org/10.1029/2024JB029020

Ghosh, G.K., 2015. Interpretation of Gravity Anomaly and Crustal Thickness Mapping of Narmada-Son Lineament in Central India. Journal of Geological Society of India 86, 263–274.

Gibson, S.A., Thompson, R.N., Leonardos, O.H., Dickin, A.P., Mitchell, J.G., 1999. The limited extent of plume-lithosphere interactions during continental flood-basalt genesis:

geochemical evidence from Cretaceous magmatism in southern Brazil. Contributions to Mineralogy and Petrology 137, 147–169.

Glišović, P., Forte, A.M., 2017. On the deep-mantle origin of the Deccan Traps. Science (1979) 355, 613–616. https://doi.org/10.1126/science.aah4390

Heister, T., Dannberg, J., Gassmöller, R., Bangerth, W., 2017. High accuracy mantle convection simulation through modern numerical methods - II: Realistic models and problems. Geophys J Int 210, 833–851. https://doi.org/10.1093/gji/ggx195

Issachar, R., Haas, P., Augustin, N., Ebbing, J., 2024. Rift and plume: a discussion on active and passive rifting mechanisms in the Afro-Arabian rift based on synthesis of geophysical data. Solid Earth 15, 807–826. https://doi.org/10.5194/se-15-807-2024

Ito, G., Lin, J., Graham, D., 2003. Observational and theoretical studies of the dynamics of mantle plume-mid-ocean ridge interaction. Reviews of Geophysics 41. https://doi.org/10.1029/2002RG000117

Jain, S.C., Nair, K.K.K., Yedekar, D.B., 1995. Geology of the Son-Narmada-Tapti lineament zone in Central India.

Ju, W., Hou, G., Hari, K.R., 2013. Mechanics of mafic dyke swarms in the Deccan Large Igneous Province: Palaeostress field modelling. J Geodyn 66, 79–91. https://doi.org/10.1016/j.jog.2013.02.002

Kaila, K., Murty, P., Mall, D., Dixit, M., Sarkar, D., 1987. Deep seismic soundings along Hirapur-Mandla profile, central India. Geophysical Journal of the Royal Astronomical Society 89, 399–404.

Kaila, K.L., Murty, P.R.K., Rao, V.K., Venkateswarlu, N., 1990. Deep seismic sounding in the Godavari Graben and Godavari (coastal) Basin, India. Tectonophysics 173, 307–317.

Keller, G., Adatte, T., Bhowmick, P.K., Upadhyay, H., Dave, A., Reddy, A.N., Jaiprakash, B.C., 2012. Nature and timing of extinctions in Cretaceous-Tertiary planktic foraminifera preserved in Deccan intertrappean sediments of the Krishna-Godavari Basin, India. Earth Planet Sci Lett 341–344, 211–221. https://doi.org/10.1016/j.epsl.2012.06.021

Keller, G., Adatte, T., Gardin, S., Bartolini, A., Bajpai, S., 2008. Main Deccan volcanism phase ends near the K-T boundary: Evidence from the Krishna-Godavari Basin, SE India. Earth Planet Sci Lett 268, 293–311. https://doi.org/10.1016/j.epsl.2008.01.015

Kendall, J.-M., Pilidou, S., Keir, D., Bastow, I.D., Stuart, G.W., Ayele, A., 2006. Mantle upwellings, melt migration and the rifting of Africa: insights from seismic anisotropy. Geological Society, London, Special Publications 259, 55–72.

Kendall, J.M., Stuart, G.W., Ebinger, C.J., Bastow, I.D., Keir, D., 2005. Magma-assisted rifting in Ethiopia. Nature 433, 146–148. https://doi.org/10.1038/nature03161

Kinchid, C., Ito, G., Gable, C., 1995. Laboratory investigation of the interaction of off-axis mantle plumes and spreading centres. Nature 376, 758–761.

Koppers, A.A.P., Becker, T.W., Jackson, M.G., Konrad, K., Müller, R.D., Romanowicz, B., Steinberger, B., Whittaker, J.M., 2021. Mantle plumes and their role in Earth processes. Nat Rev Earth Environ. https://doi.org/10.1038/s43017-021-00168-6

Krishna, K.S., Abraham, H., Sager, W.W., Pringle, M.S., Frey, F., Gopala Rao, D., Levchenko, O. V., 2012. Tectonics of the Ninetyeast Ridge derived from spreading records in adjacent oceanic basins and age constraints of the ridge. J Geophys Res Solid Earth 117. https://doi.org/10.1029/2011JB008805

Kronbichler, M., Heister, T., Bangerth, W., 2012. High accuracy mantle convection simulation through modern numerical methods. Geophys J Int 191, 12–29. https://doi.org/10.1111/j.1365-246X.2012.05609.x

Kumar, M.R., Singh, A., Kumar, N., Sarkar, D., 2015. Passive seismological imaging of the Narmada paleo-rift, central India. Precambrian Res 270, 155–164. https://doi.org/10.1016/j.precamres.2015.09.013

Larsen, H., Saunders, A., 1998. Tectonism and volcanism at the southeast Greenland rifted margin: a record of plume impact and later continental rupture. Proceedings of the Ocean Drilling Program, Scientific Results 152.

Marzoli, A.M., Renne, P.R., Piccirillo, E.M., Ernesto, M., Bellieni, G., Min, A.D., 1999. Extensive 200-Million-Year-Old Continental Flood Basalts of the Central Atlantic Magmatic Province. Science (1979) 284, 616–618.

Mchone, J.G., 2000. Non-plume magmatism and rifting during the opening of the central Atlantic Ocean, Tectonophysics.

Meert, J.G., Pandit, M.K., Pradhan, V.R., Banks, J., Sirianni, R., Stroud, M., Newstead, B., Gifford, J., 2010. Precambrian crustal evolution of Peninsular India: A 3.0 billion year odyssey. J Asian Earth Sci 39, 483–515. https://doi.org/10.1016/j.jseaes.2010.04.026

Mishra, D.C., 1977. Possible extensions of the Narmada-Son lineament towards Murray Ridge (Arabian Sea) and the eastern syntaxial bend of the Himalayas. Earth Planet Sci Lett 36, 301–308.

Mittelstaedt, E., Ito, G., Van Hunen, J., 2011. Repeat ridge jumps associated with plume-ridge interaction, melt transport, and ridge migration. J Geophys Res Solid Earth 116. https://doi.org/10.1029/2010JB007504

Morgan, W.J., 1978. Rodriguez, Darwin, Amsterdam, ..., A second type of Hotspot Island. J Geophys Res Solid Earth 83, 5355–5360. https://doi.org/10.1029/jb083ib11p05355

Naliboff, J.B., Glerum, A., Brune, S., Péron-Pinvidic, G., Wrona, T., 2020. Development of 3-D Rift Heterogeneity Through Fault Network Evolution. Geophys Res Lett 47. https://doi.org/10.1029/2019GL086611

Naveen, P.U., Sathapathy, S.K., Giri, Y., Singh, A.P., Radhakrishna, M., Rao, C.V., 2023. Crustal structure across the Central part of Narmada-Son Lineament, India based on the interpretation of aeromagnetic and gravity data: Geological implications. J Asian Earth Sci 255. https://doi.org/10.1016/j.jseaes.2023.105765

Olierook, H.K.H., Jiang, Q., Jourdan, F., Chiaradia, M., 2019. Greater Kerguelen large igneous province reveals no role for Kerguelen mantle plume in the continental breakup of eastern Gondwana. Earth Planet Sci Lett 511, 244–255. https://doi.org/10.1016/j.epsl.2019.01.037

Pang, F., Liao, J., Ballmer, M.D., Li, L., 2023. Plume-ridge interactions: Ridgeward versus plate-drag plume flow. Solid Earth 14, 353–368. https://doi.org/10.5194/se-14-353-2023

Patranabis-Deb, S., Saha, D., Santosh, M., 2020. Tracking India within precambrian supercontinent cycles, in: Springer Geology. Springer, pp. 105–143. https://doi.org/10.1007/978-3-030-15989-4_3

Petersen, S. V., Dutton, A., Lohmann, K.C., 2016. End-Cretaceous extinction in Antarctica linked to both Deccan volcanism and meteorite impact via climate change. Nat Commun 7, 1–9. https://doi.org/10.1038/ncomms12079

Prasad, K.N.D., Singh, A.P., Tiwari, V.M., 2018. 3D upper crustal density structure of the Deccan Syneclise, Central India. Geophys Prospect 66, 1625–1640. https://doi.org/10.1111/1365-2478.12675

Qureshy, M.N., 1982. Geophysical and Landsat lineament mapping — An approach illustrated from west-central and south India. Photogrammetria 37, 161–184.

Rai, S.S., Kumar, T.V., Jagadeesh, S., 2005. Seismic evidence for significant crustal thickening beneath Jabalpur earthquake, 21 May 1997, source region in Narmada-Son lineament, central India. Geophys Res Lett 32, 1–5. https://doi.org/10.1029/2005GL023580

Rao, K.M., Kumar, M.R., Rastogi, B.K., 2015. Crust beneath the northwestern Deccan Volcanic Province, India: Evidence for uplift and magmatic underplating. J Geophys Res Solid Earth 120, 3385–3405. https://doi.org/10.1002/2014JB011819

Ribe, N.M., 1996. The dynamics of plume-ridge interaction 2. Off-ridge plumes. J Geophys Res Solid Earth 101, 16195–16204. https://doi.org/10.1029/96jb01187

Ribe, N.M., Christensen, U.R., 1999. The dynamical origin of Hawaiian volcanism, Earth and Planetary Science Letters.

Ribe, N.M., Christensen, U.R., 1994. Three-dimensional modeling of plume-lithosphere interaction. J Geophys Res 99, 669–682. https://doi.org/10.1029/93JB02386

Richards, M.A., Alvarez, W., Self, S., Karlstrom, L., Renne, P.R., Manga, M., Sprain, C.J., Smit, J., Vanderkluysen, L., Gibson, S.A., 2015. Triggering of the largest Deccan eruptions by the Chicxulub impact. Bulletin of the Geological Society of America 127, 1507–1520. https://doi.org/10.1130/B31167.1

Richards, M.A., Duncan, R.A., Courtillot, V.E., 1989. Flood Basalts and Hotspot Tracks: Plume Heads and Tails. Science (1979) 246, 103–107.

Schoene, B., Eddy, M.P., Samperton, K.M., Keller, C.B., Keller, G., Adatte, T., Khadri, S.F.R., 2019. U-Pb constraints on pulsed eruption of the Deccan Traps across the end-Cretaceous mass extinction. Science (1979) 363, 862–866. https://doi.org/10.1126/science.aau2422

Schoene, B., Samperton, K.M., Eddy, M.P., Keller, G., Adatte, T., Bowring, S.A., Khadri, S.F.R., Gertsch, B., 2015. U-Pb geochronology of the Deccan Traps and relation to the end-Cretaceous mass extinction. Science (1979) 347, 182–184. https://doi.org/10.1126/science.aaa0118

Singh, A., Kumar, M.R., Kumar, N., Saikia, D., Solomon Raju, P., Srinagesh, D., Rao, N.P., Sarkar, D., 2012. Seismic signatures of an altered crust and a normal transition zone structure beneath the Godavari rift. Precambrian Res 220–221, 1–8. https://doi.org/10.1016/j.precamres.2012.07.006

Singh, A., Singh, C., Kennett, B.L.N., 2015. A review of crust and upper mantle structure beneath the Indian subcontinent. Tectonophysics. https://doi.org/10.1016/j.tecto.2015.01.007

Singh, A.P., 1998. 3-D Structure and geodynamic evolution of accreted igneous layer in the Narmada-Tapti region (India). J Geodyn 25, 129–141.

Sleep, N.H., 1997. Lateral flow and ponding of starting plume material. J Geophys Res Solid Earth 102, 10001–10012. https://doi.org/10.1029/97jb00551

Sprain, C.J., Renne, P.R., Clemens, W.A., Wilson, G.P., 2018. Calibration of chron C29r: New high-precision geochronologic and paleomagnetic constraints from the Hell Creek region, Montana. Bulletin of the Geological Society of America 130, 1615–1644. https://doi.org/10.1130/B31890.1

Torsvik, T.H., Cocks, L.R.M., 2013. Gondwana from top to base in space and time. Gondwana Research. https://doi.org/10.1016/j.gr.2013.06.012

Unrug, R., 1996. The assembly of Gondwanaland. Episodes 19, 11–20.

White, R.S., McKenzie, D., 1995. Mantle plumes and flood basalts. J Geophys Res 100. https://doi.org/10.1029/95jb01585

Whittaker, J.M., Afonso, J.C., Masterton, S., Müller, R.D., Wessel, P., Williams, S.E., Seton, M., 2015. Long-term interaction between mid-ocean ridges and mantle plumes. Nat Geosci 8, 479–483. https://doi.org/10.1038/NGEO2437

Zhao, D., 2015. The 2011 Tohoku earthquake (Mw 9.0) sequence and subduction dynamics in Western Pacific and East Asia. J Asian Earth Sci 98, 26–49. https://doi.org/10.1016/j.jseaes.2014.10.022

Chapter 7 | Discussions and Conclusions

The research undertaken in this thesis has advanced our understanding of the dynamic coupling between mantle processes, tectonic forces, and surface expressions, showcasing their critical role in shaping the Earth's lithosphere and topography. Combining robust theoretical frameworks and cutting-edge numerical simulations, this study addresses a number of fundamental geodynamic questions, offering their model interpretations, backed by detailed geological and geophysical observations. The interplay between dynamic and tectonic processes has been explored across a spectrum of geological settings, which lead to new insights into the driving mechanisms of varied mid-ocean ridge morphologies, stress regimes in the lithosphere, the eastward tilting of Peninsular India, and plume-rift interactions during major magmatic events. The thesis emphasizes the role of mantle flow, melt dynamics, and lithospheric deformation in controlling the observed diversity of Earth's surface features, as outlined below.

The mid-ocean ridge (MOR) systems investigated in this thesis evolve through mutual influences of magmatic and tectonic processes to form axial highs and lows, where the mush dynamics, sub-crustal viscosity variations, and magmatic supply are found to be crucial factors in modulating the ridge topography. Similarly, the studies presented in Chapter 6 constitute a new theoretical framework of the eastward tilt of Peninsular India, which is attributed to combined effects of lithospheric flexure, mantle-driven uplift, and isostatic adjustments. The findings offer a refined perspective on the evolution of stable cratonic regions. The analysis of plume-rift interactions within the Deccan volcanic province sheds light on how pre-existing rift structures might modulate the ascent behaviour of the Reunion plume, influencing its magma migration, emplacement patterns, and the spatial distribution of volcanic activities.

The principal findings of this research are comprehensively presented and discussed in the following sections. These discussions synthesize the observed topographic and geodynamic features in the context of underlying mantle and tectonic processes, bridging numerical model results with geological realities. The insights gained not only enhance our understanding of the Earth’s surface topography and its evolution, but also provide a framework for interpreting similar geodynamic phenomena in other regions of the world. This integrated approach underscores the interconnection of mantle processes and lithospheric dynamics in shaping the Earth's surface, highlighting the need for multidisciplinary perspectives to resolve outstanding geodynamic challenges.

7.1. MOR Axial Topography: complex issues

7.1.1. Effects of sub-crustal melt accumulation

Using a three-dimensional graphical plot (Figure 3.9), the study presented in Chapter 3 has shown the effective viscosity (μ_{eff}) of MC as a function of the suspension viscosity (μ_M) and the volume fraction of crystal-bearing melts (φ) in the system. An increment of μ_M by an order of 7 (2 to 9), accompanied by an increase of φ from ~40% to 50%, i.e., pure melt fraction anywhere between 8% and 30%, would eventually increase μ_{eff} from 10^{12} to 10^{14} Pa s (Figure 7.1a). This inverse relation of μ_{eff} with φ resolves the apparently contradictory observations, axial highs in the magma-rich EPR ridges (key et al., 2013), and flat ridge topography in the magma-poor MAR. The same explanation applies to the topographic transition, high to flat in SEIR at $103^0$35'E, where both sides are somehow rifted (Carbotte et al., 2016). It is noteworthy that the inverse μ_{eff} - φ relation occurs below a threshold slope of the μ_M versus φ curve, as demonstrated in Figure 7.1b. The threshold regression line shows that increasing φ initially reduces μ_{eff}, followed by a compensatory rise, ultimately attaining the same μ_{eff} value. Under a threshold condition, across-axis asymmetric sub-ridge melt distributions beneath MORs can thus hardly break their axial topographic symmetry (Evans et al., 1999). Figure 7.1c shows different possible paths of μ_{eff} variations with μ_M and φ. μ_M and φ (blue dotted line) can locally fluctuate in ridge settings due to some variations in the strain rate. This fluctuation results in an unsteady state of μ_{eff}, ultimately leading to a local instability in the axial topography. In specific cases, μ_{eff} can remain steady over a broad range of non-linear μ_M - φ regression, as shown in Figure 7.1d. Such a sub-crustal condition is possibly required for the long-timescale relative stability of axial morphologies, as reported from many MORs (Rowley et al., 2016).

The viscosity model also yields μ_M - φ relations that support contrasting observations from fast and slow spreading ridges, axial high topography in fast ridges with high melt percentages, whereas axial flat or valley topography in slow ridges with low melt contents. We now provide simple numerical estimates to discuss the MC viscosity as a function of crystal-bearing melt viscosity (μ_M) and molar volume percentage (φ) of melt suspension using the mixture rheology curve in Figure 7.1. For a given value of μ_M, e.g., 10^5 Pa s, the MC viscosity can be as low as 10^{12} Pa s if $\varphi = 50\%$. Considering the crystal-free, pure melt viscosity in the

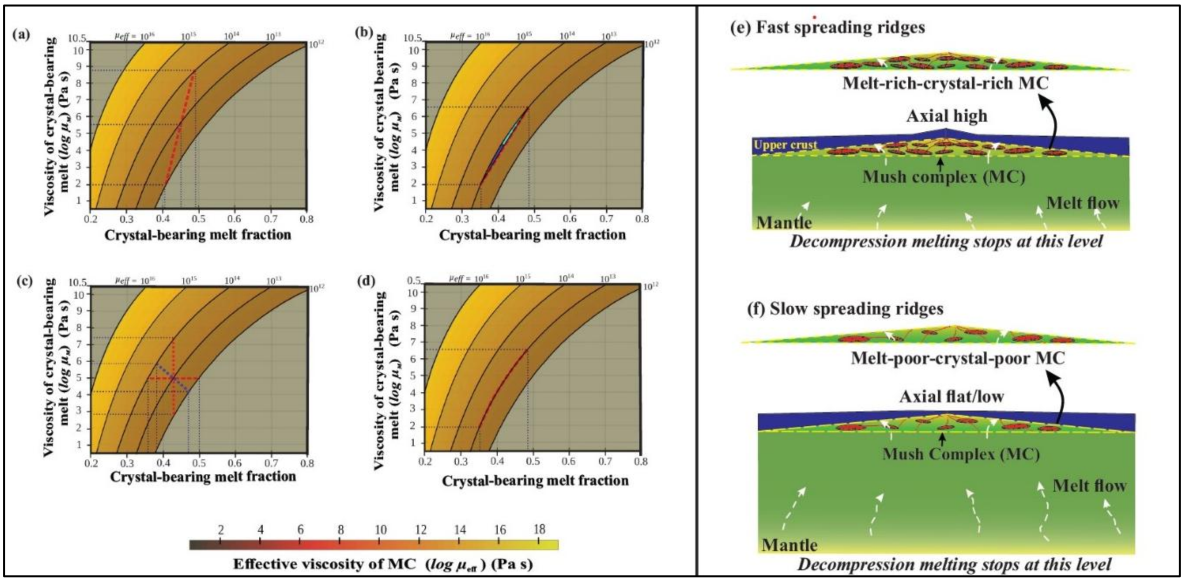

Figure 7.1 *Projection of the 3D plots for MC viscosity (presented in Figure 3.9) on a 2D frame defined by volume percentage (φ) and viscosity (μ_M) of crystal-bearing melt (i.e., melt-suspension). (a) A specific regression where a large increase in μ_M (an order of 10^7 Pa s) with a moderate rise (~10%) in φ enhances the effective viscosity (μ_{eff}) of MC by up to two orders. (b) A linear regression of μ_M with φ involving a limited change in μ_{eff}, where a zone of a small decrease is followed by a zone of little increase (shaded with different colours), ultimately leading to the same μ_{eff} under a specific combination of the μ_M and φ variation. It is to be noted that the red dotted line defines a critical slope line; a regression below this line would result in a lowering of μ_{eff}, whereas above it would increase μ_{eff}. (c) A regression (blue dotted line) of a smaller change in μ_M (~ 10^1 Pa s) as well as a lower change (~5%) in φ showing modification of μ_{eff} by up to 1 order of magnitude. Note that a similar order of change in μ_{eff} is possible when one of the two parameters: φ or μ_M varies, keeping the other constant, as indicated by red dotted lines. (d) A steady-state condition of μ_{eff} in complex with varying φ and μ_M along a particular regression (dashed red line). (e) and (f) Cartoon diagrams of the sub-crustal phenomena at typical fast- and slow-spreading ridges, showing the possibility of higher and lower effective viscosities in a melt-rich-crystal-rich and a melt-poor-crystal-poor condition, respectively.*

order of 10^2 Pa s, the suspension (i.e., crystal-bearing melts) must contain solid crystals by 60-70% to attain its viscosity in the order of 10^5 Pa s (discussed in the earlier section). It means the pure melt percentage in the complex must be in the range of 15 to 20%. The graphs (Figure 7.1) show an inverse relation of the mush viscosity with melt suspension content; μ_{eff} becomes 10^{14} Pa s as φ decreases to 36%, which corresponds to a pure melt fraction of 11-15%. This melt fraction estimate would be further low if the polydispersity and polymodality factors were considered in the calculation. Similarly, an increase in μ_M(e.g., 10^5 to 10^7 Pa s) can yield the MC viscosity (μ_{eff}) in the order of 10^{14} Pa s for φ = 40% (Figure 7.1). On the other hand, both μ_M and φ in the mush can increase to yield the same mush viscosity, i.e., 10^{14} Pa s for φ = 57%, and μ_M = 10^{10} Pa s (Figure 7.1). Such a high melt suspension viscosity is possible when the crystal content is extremely large, say 80%, i.e., low pure melt fraction, 11-12% in the mush complex, at very shallow level. The two schematics in Figures 7.1e and 7.1f show sub-crustal melt bodies and magma conduits (MC region) with contrasting suspension characteristics at the two types of ridges. The mush complexes in faster ridges generally have melts with larger phenocrysts and groundmasses in larger volume fractions than those in slow-spreading ridges. Consequently, a higher effective viscosity of MC due to higher crystal content, polydispersity, and polymodality (Figures 7.1a and 7.1e), produce axial high topography in fast ridges. On the other hand, the opposite suspension characteristics sets in a low viscosity condition (Figures 7.1a and 7.1f) beneath slow ridges, which gives rise to axial valley or flat topography. Melt contents in the MC can, however, fluctuate due to a number of factors, such as sub-crustal solidifications and numerous volcanic events in the process of new crust formation. A concerted operation of the following three processes: 1) mid-oceanic ridge eruptions, 2) sub-crustal solidifications (Mandal et al., 2018), and 3) continuous convective upwelling of partial melts (Sarkar et al., 2014) can modulate the μ_M - φ regression to maintain a steady-state μ_{eff} condition (Figure 7.1d) required for the stable axial topography.

The dynamics of sub-ridge mush complex primarily depends on lava and magma scale characteristics. The theoretical treatment considers their length, time, volume and strain rate scales based on the available data of successive volcanic eruptions in the literature (details provided in Chapter 3). The strain rate range, 10^{-3} s^{-1} - 10^{-12} s^{-1} is appropriately represented at the interface points in the fluid simulations, taking into account the variations in magma flow volumes and conduit size. As an example, for a given time and conduit size an increase in magma volume by an order of 2 will enhance the strain rate, which may exceed a threshold value resulting in shear thinning and lowering of the suspension viscosity by an order of 1 to 2.5. In summary, this approach allows us to cover the whole range of viscous stress in mid-oceanic ridges in describing the dynamic phenomena such as diking and eruptions.

7.1.2. Axial topographic growth: Mechanisms and their validation

Several MOR models have attempted to integrate sub-ridge thermomechanical processes in the mantle-lithosphere, giving a spectrum of competing mechanisms, such as magmatic upwelling versus hydrothermal cooling (Chen et al., 2022), tectonic extension versus diking (Buck et el., 2005), fault-driven collapse versus isostatic compensation (Escartin et al., 2008; Lin and Parmentier, 1990), overpressure building versus release of magma chambers (Gudmundsson 2012; Reverso et al., 2014), and fluid convection versus matrix compaction (Katz 2010). The MOR model conceptualized in this thesis invokes a sub-ridge mechanism of porous convection with synkinematic melting-solidification processes to describe the FSI mechanics. The convection-driven upwelling occurs at a depth of cessation of the adiabatic decompression melting. this study use this threshold depth to introduce random temperature points (range 800^0C to 1400^0C) on a narrow region beneath the MOR axis (*cf.* Chapter 3; Figure 3.13). This random thermal perturbation (RTP) initiates the convection in the porous upper mantle, where the porous convective flow accompanies melting and solidifications in the sub-ridge shallow upper mantle and sub-crustal regions mediated an enthalpy transfer process. The flows are always geometrically asymmetric due to concerted effects of the RTP, porous convection (Katz 2010) and the intermixing of multiple convection cells and melting-solidification processes.

The convective flows induced in the MC develop normal stresses at its interface with the overlying crust, as modelled through a fluid structure interaction (FSI). The effective viscosity of MC and its kinematic condition determines the magnitude of normal stresses transmitted to the overlying solid crust. The kinematic conditions of the MC are nominally transmitted to the overlying crust together with the dynamic conditions as an implementation of the Robin transmission condition in the FSI mechanism (Badia et al., 2008). In the FSI formulation the shear stresses are generally excluded, considering that the differential velocity across the interface is small. However, for lower MC viscosities this factor can be significant due to existence of strong relative motion. The stress transmission eventually results in deformations in the elastic crust to produce an axial topography. The effective viscosity of MC plays a critical role in controlling the magnitude of transmitted stresses that ultimately determine the vertical reliefs in the overlying elastic crust. Decreasing MC viscosities consequently results in a transition of high to flat axial topography. However, density takes the lead role to maintain flat topography at lower MC viscosities ($\leq 10^{12}$ Pa s) (Figure 3.19).

Consider some generic parameters of the natural MOR systems to test the validity of the FSI mechanism proposed in this study. The flow data of MC support the dynamic magma budget of mid oceanic ridge calculated and validated with natural ridge processes in previous studies (Mandal et al., 2018). The melt budget suggests eruptible melts amount to 8 -10 % of the total upwelling melt beneath MORs, that means, 3.7×10^6 m^3 / yr in a 500 km long ridge. Secondly, the model presented here treats MC as a fluid region consisting of liquid mixtures of crystal bearing melts and host rocks. Its viscosity analysis yields a value in the range 10^{12} to 10^{14} Pa s, which is comparable to that of lower-crustal magma bodies in MORs. For example, Chenevez et al., (1998) estimated the viscosity of gabbroic mushes within the axial magma chamber as 10^{15} Pa s from Oman ophiolites. On the other hand, experiments have shown viscosity in the order of 10^{11} Pa s for lower crusts containing melts by 20-25% (Picard et al., 2013). Similarly, Fontaine et al., (2017) estimated an effective viscosity of 10^{13} Pa s for sub-crustal regions in the melt-rich fast spreading ridges showing axial highs, as produced in our model (Figure 3.17a). The spectrum of melt percentages at MC, as predicted from the present rheological calculations (30-80%, see Figure 3.9 a-d), is supported by earlier estimates (see Figure 3.7). The strain rates in the MC (10^{-3} s^{-1} to 10^{-11} s^{-1} with a median value of 10^{-5} s^{-1}) also agree well with those recorded in natural MOR systems. The FSI model shows that the timescale of mid oceanic ridge processes to stabilize (Figure 3.15) is 6 Myr, which is comparable to those reported in the literature (Gerya 2013).

7.1.3. Axial topography: a model versus nature comparison

In the quantitative analysis of axial topography, the median relief of natural ridge systems has been considered to estimate the vertical anomaly with respect to the average seafloor depth (2600 m, Searle and Escartin 2013). I chose an across-axis section of the EPR at 17°N (Lin and Parmentier, 1998) to compare its long wave axial-high topography with those obtained from our model. The 17°N section displays a first-order characteristic topography consisting of a sharp axial high (maximum elevation: H ~ 400 m, axial width: W ~ 40 km), flanked by a symmetric pair of flat regions (width ~ 60 km), and narrow, weak depression zones away from the high. The axial topography shows a good match with that produced in the model simulation ($\mu_{eff} = 10^{14}$ Pa s, $H \sim 500$ m and $W \sim 30$ km) (Figure 7.2a). The model finding is also validated along-axis model topographic patterns with the available natural data. Figure 7.3a shows a comparative analysis of the Juan de Fuca (JdF) ridge-segment (44°30'N to 49° N) topography and the $\mu_{eff} = 10^{14}$ Pa s model axis relief (at 7 Myr model run-time). The JdF ridge includes a seamount, and six major segments form reliefs with their median close to the model value (220 m). The model and the natural ridge systems show remarkable similarity in terms of the relief density distribution and scatter (Figure 7.3a). Geologically, the JdF ridge (JdFR) with moderate spreading rates (60 mm/yr) receives lateral magma supply from the neighbouring Cobb hotspot and axial seamounts. Enhanced fractional crystallization with efficient cooling (Chadwick et al., 2005) away from the hotspot regions thus produces a viscous magma-enriched sub-crustal melt-rich system, which in turn facilitates the growth of axial high topography, as predicted from high-viscosity FSI model (Figure 7.3a). Additional notable features of JdFR are: 1) the axial seamount does not significantly differ from the adjoining parts of the axial ridge segment in terms of the crystal content of their magmas (Chadwick et al., 2005), and 2) the excess melt volume is compensated by forming a thick crust. However,

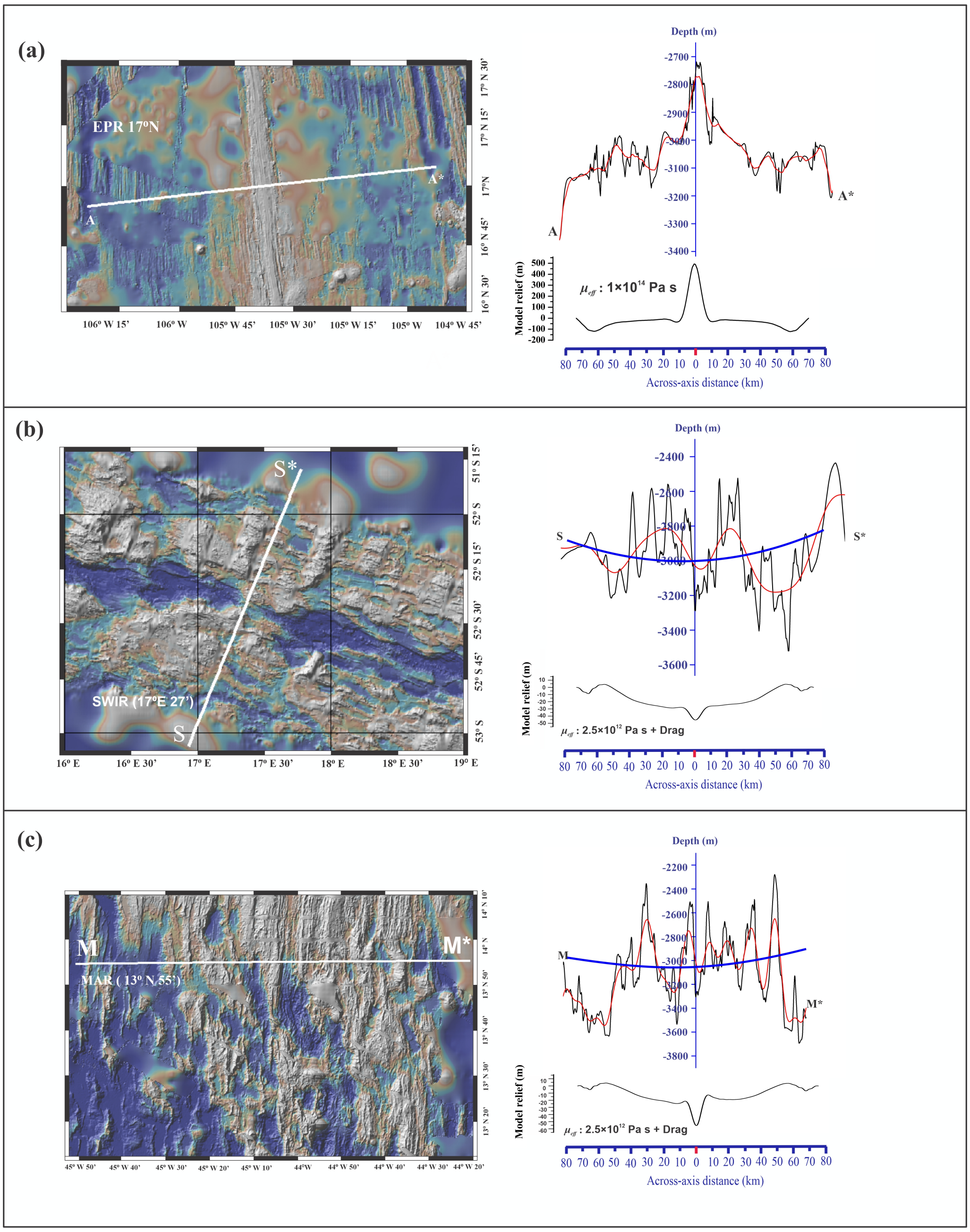

Figure 7.2 *Comparison of the cross-axis topographic profiles between nature and model: (a) a high viscosity ($\mu_{eff} = 10^{14}$ Pa s) model versus EPR 17°N. (b) a low-viscosity ($\mu_{eff} = 2.5\times10^{12}$ Pa s) model with drag force and SWIR 17°27'E. (c) a low-viscosity ($\mu_{eff} = 2.5\times10^{12}$ Pa s) with drag force and MAR 13°55'N. Red lines show polynomial fits (higher order) to the original natural data (in black). Blue lines indicate a second-degree polynomial fit for the SWIR and MAR. The EPR section displays a good match with the model topography [maximum ridge elevation (H): 400 m (model) and 500 m (nature), axial width (W): 40 km (model) and 30 km (nature), similar 'neck's in both sides]. The SWIR section also show a similarity with the model in their first-order axial topography, barring quantitative differences [H: - 40 m (model) and - 400 m (nature), W: 20 km (model) and 40 km (nature)]. The MAR section matches fairly with the first-order model topography, but with difference in their magnitude [H: - 60 m (model) and - 600 m (nature), W : 15 km (model) and 10 km (nature)]. MOR data source: GeoMapApp (**http://www.geomapapp.org/**)/CC BY.*

there is a possibility of narrow, focused upward magma flux to the axial seamount's base, resulting in enhancement of the normal flux in JdFR by three times (West et al., 2003), as reflected from higher upwelling velocity/strain rates in this region. The ridge seamount thus represents a local feature to enhance the vertical strain rates over the common viscous behaviour of the underlying mush and give rise to topographic characteristics observed in the corresponding model, where the positive relief is larger than the maxima by 60%, and ten times the median value (Figure 7.3a).

Across-axis model topographic profiles are compared with two sets of nearly flat topography from ultraslow SWIR and slow-spreading MAR extrapolated directly from the GeoMap database. These two ridges exhibit predominantly rifted valley topography. I thus chose two narrow segments, where rifting is not a dominant ridge process, as indicated by thick crust, but they show weak axial valleys or flat axial topography. A topographic profile from the low-viscosity (μ_{eff} = 2.5x10^{12} Pa s) MC model compares well with the first-order valley geometry (17°27' E, Grindlay et al., 1998) in the SWIR, when the off-axis depressions due to extensional faulting are excluded (Figure 7.2b). In the case of MAR, another profile of the same model run grossly reproduces the ridge profile (13°55' N, Mallows and Searle, 2012), which consists of a narrow, shallow valley at the ridge flanked by flat off-axis stretches (Figure 7.2c). However, there are large differences in the magnitudes of axial depression topography between the natural settings and the corresponding models (e.g., ~30 m in model vs. ~100 m in SWIR, ~50 m in model vs. ~150 m in MAR, $13^0$55' N) but they show a first-order similarity in their axial zone topography, e.g., across-axis width (~ 80 km) of the gentle axial depressions. However, the higher-order off-axis topographic elements in model and nature do not perfectly match with one another (Figure 7.2c). These higher-order mismatches perhaps result from strong effects of tectonic (tensile) stresses, as compared to relatively weak rheological effects of the underlying mush complex.

The model results are again validated with a number of natural along-axis topographic profiles from SEIR (87°30' E to 93°30' E). These profiles show a marked similarity in their relief patterns (Figure 7.3b) with those in the model run for moderate effective MC viscosity (μ_{eff} = 3x10^{13} Pa s at 7 Myr run time). At the western portion the SEIR has a significant influence of melt plumes (Baker et al., 2014), and developed a first-order transform discontinuity and a prominent overlapping spreading centre. Overall, the ridge, deepening towards the east (Sempere et al., 1997), displays along-axis roughness of its relief fairly in agreement with our model. The western part of SEIR, extending up to 90°E receives mantle-derived melts from the Kerguelen-Heard hotspot, as suggested by the $^{87}Sr/^{86}Sr$ ratio enrichment. Alternatively, there is a possibility for greater availability of partial melts due to a greater mean depth of melting, which is correlated with the He isotope ratio peak at 88^0E (see Mahoney et al., 2002 and references therein). Both the cases can give rise to a condition of high magma percentage and low magma viscosity in the portion of SEIR of our present concern, which might retain μ_{eff} at moderate values (~ 3 x 10^{13} Pa s), as derived from the viscosity calculations (Figure 7.1b).

A positive correlation of the along-axis model topography with the southern part of the EPR and the northern segment of the PAR (42°S – 46°30' S) support the present model interpretations (Figure 7.3b). The latter is thought to be stable for more than 50 Myr (Rowley et al., 2016). Its median relief matches well with that of a high μ_{eff} (= 7x10^{13} Pa s) model. On the other hand, the EPR ridge segment shows a lower relief variance than the model (Figure 7.3c). The overall topographic parity allows us to predict the viscosity of melt-rich sub-crustal region in the order of 10^{13} Pa s for this particular ridge segment. Applying the two-phase viscosity model, this study suggests that although this region is rich in melt content, it gains relatively high viscosity due to a large volume fraction of solid crystals in the melt suspensions. The relatively lower along-axis variance in the EPR ridge topography, as compared to that in the corresponding model, results from a number of possible factors, such as longitudinal stability of the ridge position, continuous deep-seated upwelling, and overwhelming viscous magmatic control (Rowley et al., 2016). A rate balance between the melt supply and crystallization can account for a steady-state effective viscosity of the underlying melt-bearing regions to sustain such stable ridge-axis topography (Figure 7.1d).

This discussion leads us to suggest the following. The magma-rich EPR has retained a high-viscosity condition of the melt-bearing sub-crustal regions to produce narrow axial high, as produced in our simulation with μ_{eff} = 5x10^{13} - 10^{14} Pa s. Hotspot fed and rapidly cooling melts in the JDFR has a sub-ridge MC with the highest viscosity (μ_{eff} = 10^{14} Pa s), and their produced an axial high elevation comparable to that in the model. On the other hand, the western SEIR is rich in moderately viscous melt suspensions but becomes melt-poor, resulting in deep rifted axial valley topography in the eastward direction (Sempere et al. 1997; Baker et al., 2014). The analysis suggests a moderate sub-crustal viscosity (μ_{eff}) has formed axial high topography in western SEIR, which agrees well with the simulation result for μ_{eff} = 1-5x10^{13} Pa s. Our FSI model for μ_{eff} ~ 10^{12} Pa s points to an appreciable mismatch on the along-axis model topography with those observed in the magma poor MAR and SWIR (both slow-

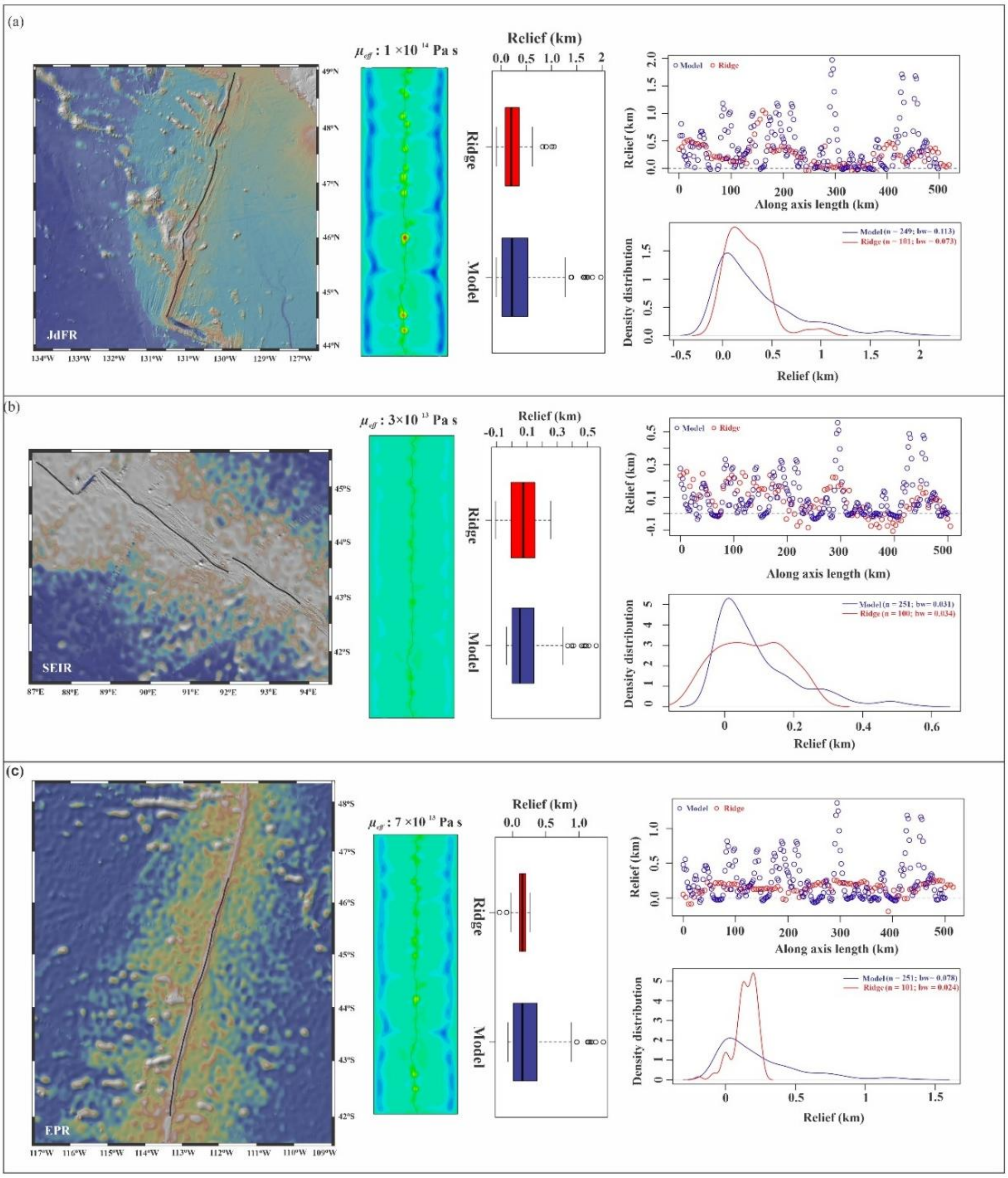

Figure 7.3 *Comparison between natural and model along axix topography: (a) A high viscosity (μ_{eff} =10^{14} Pa s) model and JdFR (44°30' N to 49°N). (b) A moderate viscosity (μ_{eff} =3×10^{13} Pa s) model and eastern SEIR (87°30' E to 93°30' E). (c) A moderately high viscosity (μ_{eff} =7×10^{13} Pa s) and EPR (42°S to 46°30'S).The box plots, scatter plots, and density distributions are also shown, along with the natural ridge bathymetry and the evolved model ridge axis elevations. For JdFR, the along-axis profiles show matching topography with the model [median relief : 0.2043 km (natural) and 0.22 km (model); density peak : 0.12 km (natural) and 0.05 km (model)]; SEIR and EPR profiles are also in good agreement with the model topography: for SEIR, median relief : 0.076 km (natural) and 0.054 km (model); density peak : 0.05 km (natural) and 0.02 km (model); and for EPR, median relief : 0.15 km (natural) and 0.15 km (model); density peak : 0.22 km (natural) and 0.04 km (model). Natural data source: GeoMapApp (**http://www.geomapapp.org/)**/CC BY.*

spreading), albeit showing a reasonable match with the across-axis first-order curvatures in their non-rifted segments. The analysis suggests that the MAR and SWIR topography are not entirely controlled by the rheological setting of their sub-crustal and lower crustal mush complexes. This mismatch indicates the possibility of tensile stress regimes to govern the axis topography where the flow-driven stresses at the base in case of slow-spreading ridges become relatively weak due to low-viscosity condition in the underlying mantle (e.g., Lin and Parmentier, 1989). This model also shows a weak match of the along-axis model topography with the Reykjanes ridge topography where the relief is significantly higher than the model relief even in high-viscosity ($\mu_{eff} \sim 10^{14}$ Pa s) simulations (Figure 7.4). It is noteworthy that the

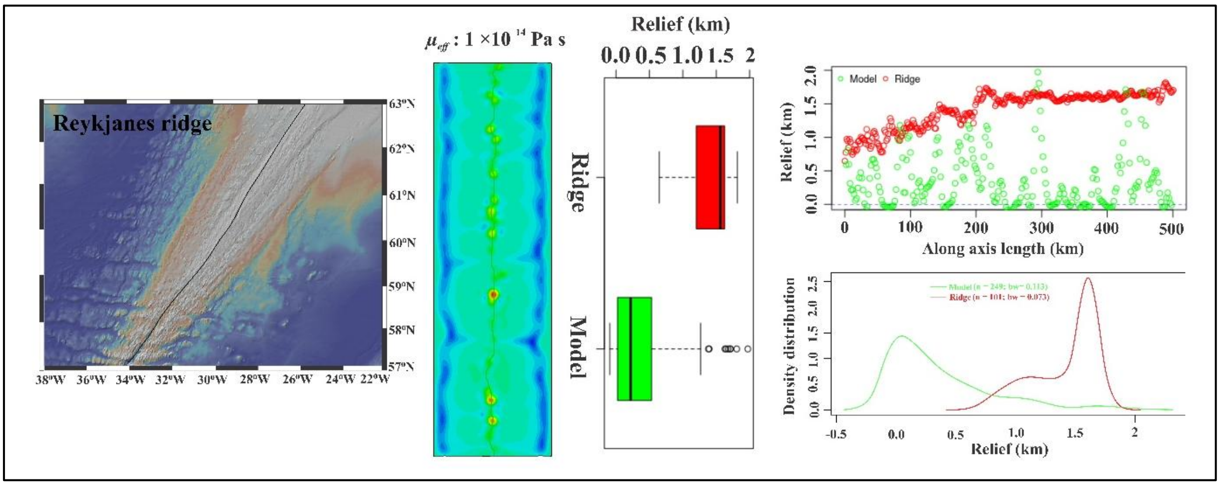

Figure 7.4 *Comparison between natural and model along-axis topography of Reykjanes Ridge (44°30'N to 49°N). A high viscosity model ($\mu_{eff} = 10^{14}$ Pa s) is shown in same panel producing axial high topography. The box plots, scatter plots, and density distributions are also shown, along with the natural ridge bathymetry and the evolved model ridge axis elevations. Natural data source: GeoMapApp (**http://www.geomapapp.org/**)/CC BY*

600 km long slow (2 cm/year full spreading rate) Reykjanes ridge (57.9^0 N to 62.1^0 N) is thought to have evolved under the influence of Iceland mantle plume, as evident from its large oblique spreading characteristics (28^0 from the spreading normal) and its V shaped plan view Searle et al., 1998, White et al., 1995). This might be the reason for the topographic mismatch. Axial relief in the present model correlates positively with crystal contents, polymodality and polydispersity in the MC that enhances the melt suspension viscosity, and in turn, the effective viscosity of the MC. Faster spreading ridges show crystallization at shallower depths (Wanless and Shaw 2012) and they also undergo greater mixing of their crystal phases (olivine, plagioclase and clinopyroxene) of different sizes and shapes at subcrustal / lower crustal MC

(Lissenberg et al., 2019). The predominance of crystal suspensions sets in a high-viscosity rheological condition that explains the axial highs at faster spreading segments. In contrast, crystallization at slow spreading ridges typically occurs at greater depths (Herzberg 2004), allowing the melts to transport through melt channels, but loosing heavier (olivine) larger crystal in their pathways due to slow ascent velocities (Lange et al., 2013). In effect, slow spreading ridges are likely to produce MCs with low crystal contents and lower polymodality and polydispersity that result in setting up a low-viscosity setting and weak normal stress transfer in the topographic process.

7.1.4. Concluding points

The main outcomes of this study are as follows:

- One-way Fluid-Structure coupling between a sub-crustal melt accumulation zone and the overlying solid elastic crust, has been implemented with the framework of a computational fluid dynamics modelling of convective heat and mass transfer. The model results demonstrate that the effective viscosity of the melt-rich zones can play a critical role in modulating the axial high versus flat topography.
- The mush complex (MC) dynamics involving crystallization in its melt suspensions at the lithospheric base largely governs the ridge axis topography.
- A complete description of the MOR mechanical setting demands viscosity analysis on two scales- one at magma body/conduit scale, which is tackled by utilizing suspension theory, and mush scale, which is dealt with a modified Arrhenius equation.
- The effective viscosity of MC varying in the range 10^{12} Pa s to 10^{14} Pa s produces a full spectrum of the non-rifted axial high to flat (1.27 km to - 0.06 km) topography. Typical axial highs form in the viscosity range of 10^{13} Pa s - 10^{14} Pa s, whereas axial lows in the viscosity range of 10^{12} Pa s- $5x10^{12}$ Pa s.
- The onset of relative vertical displacements in central axial regions occurs at the time of upwelling melt-bearing mushy materials to interact with the overlying crust. The process forms a stable topography on a time scale of ~ 6 to 7 Myr, characterized by central axial highs and off-axis depressions on their flanks.
- This viscosity based new model explains the following characteristics of natural MORs: a) axial high topography in melt-rich ridge systems (e.g., EPR) and first-order axial valley in melt-poor ridges (e.g., SWIR and MAR), b) transformation of ridge topography due to drastic changes in subcrustal magma constituency (e.g., SEIR), c) axial seamount as a location of high upwelling rates (e.g., JdFR) and d) stability of axial topography in large

temporal and spatial settings (e.g., Southern EPR) as an outcome of the competing factors, such as viscosity and volume percentage of crystal-bearing melt suspensions that maintain the effective viscosity of mush complex almost at a constant level.

- The FSI modelling constrains the viscosities of sub-crustal mushy regions in the following MOR systems: 10^{14} Pa s for JdFR, $5x10^{13}$ - 10^{14} Pa s for EPR, 1 - $5x10^{13}$ Pa s for western SEIR.

7.2. 3D Stress Fields at MORs

7.2.1. The model estimates: an overview

The stresses at MORs were earlier analysed as a function of various factors, such as magmatic diking, plate spreading, and thermal effects (Choi et al., 2008). Luttrell and Sandwell (2012) showed the topographic reliefs of MOR segments as another factor to control a long and a short wavelength stress field. Their study suggests biaxial stress conditions in the MOR settings, where the ridge perpendicular tensile stresses attain magnitudes in the range 10 to 100 MPa, but with significantly low ridge-parallel tensile stresses (a maximum of 20 MPa). Using a 2D boundary element model of the regional dyke systems in Iceland, Gudmundsson, (2003) estimated the dyke-tip tensile stress in the order of 10^2 MPa under compressive stresses of multiple elastic crustal layers.(Kühn and Dahm, 2004), on the other hand, calculated the deviatoric stresses in a MOR from a simple boundary element model. Their stress estimates vary on a wide spectrum, 0.05 MPa to 5.3 GPa. Similarly, the visco-plastic 3D MOR model of Gerya (2013) yields deviatoric stresses in the range ~ 1 MPa to 1 GPa.

The model estimates presented in Chapter 4 also show that the axial averages of directional stresses at MORs can be large, where their maxima can go up to 1 – 2 GPa (Figures 4.4 and 4.5). This finding implies that a strong-stress field in the MOR systems can originate entirely from the sub-ridge mush dynamics. In the axial zones the axis-perpendicular and -parallel stress medians lie within ~270 MPa and ~250 MPa, respectively, whereas in the off-axis regions the stress medians are relatively low (maximum ~80 MPa and ~50 MPa). This FSI model describes the full range of MOR stress fields in the perspective of sub-ridge mush dynamics, a factor not considered in earlier models. In addition, this model explains synchronous development of the across-ridge shear stresses with the axial stresses.

7.2.2 Formation of ridge segments and segment boundaries

Based on their along-axis length, offset length and durability, the MOR segmentation can be categorized into the following four types. a) *Transform fault segments* (Segment Length

(SL): 300-500 km; Offset Length (OL) : >30 km; Duration (Du) : >10 Myr) b) *Second order segments* (SL : 20-100 km at SSR and 50-250 km at FSR; OL : 2-30 km; Du : 1-10 My) c) *Third order segments* (SL : 10-50 km, OL : 0.5-2 km; Du : 0.01-1 Myr) d) *Fourth order segments* (SL : ~10 km; OL : <1 km; Du : ~0.001 Myr) (Macdonald et al., 1988). The FSI-based stress model allows to map these segment boundaries observed in natural MORs as ridge-perpendicular zones of compressive stress concentration (Figures 7.5a.i-a.ii). Narrow high-compressive stripes define the primary magmatic segments, covering an across-axis length of ~ 60 km. The segments occur in different orders, with their along-axis wavelengths ranging from 30 km to 150 km (Figures 7.5a.i), which agree with the second-order segmentation of ridge morphology. The FSI model also produces short, narrow high-compressive stress zones transverse to the axis, giving rise to higher-order segmentation structures. These smaller segments can be compared with the third-order MOR segments. The secondary transverse segment boundaries, however, die out away from the ridge axis, leaving a few large segments as the MOR matures with time (7 Myr) (Figure 7.5a.i).

Consider now a set of natural MORs to compare their segmentation structures with our model observations. The southern part (66° – 56°S) of the intermediate to fast spreading (~ 54-56 mm/yr) Pacific-Antarctic ridge (PAR) (Ondréas et al., 2001) consists of three segments (SL = 70-80 km) and two rift – rift overlapping spreading centres (OSC) (Figure 7.5b.i). Its middle part has varied topography, forming valleys, flat and highs, and spreading rates increasing from 56 mm/yr to 66 mm/yr northward over an axial distance of 650 km. The Heirtzler transform fault (TF) divides this part into two zones, southern zone consisting of five segments (SL = 30-150 km), and northern zone consisting of relatively small, but four prominent segments. The fast-spreading (68-74 mm/yr) northern part of the PAR, on the other hand, has an axial high of 1100 km length, segmented by three major transform faults (SL = 50-80 km, OL = 40-60 km) (Figure 7.5b.i). The ridge also contains a number of primary magmatic segments. The transform and non-transform segment boundaries are manifested as gravity low lines (Ondréas et al., 2001) (Figure 7.5b.i). The present model produces along-axis compression/tension zones, forming large and small stress segments with their along-axis dimensions of 10-30 km and 40-150 km, respectively in close association. The similarity of non-transform segmentation patterns between the model and nature suggest that complex sub-ridge mushy flows is a responsible factor for the segmentation process in a mid-ocean ridge system. For further

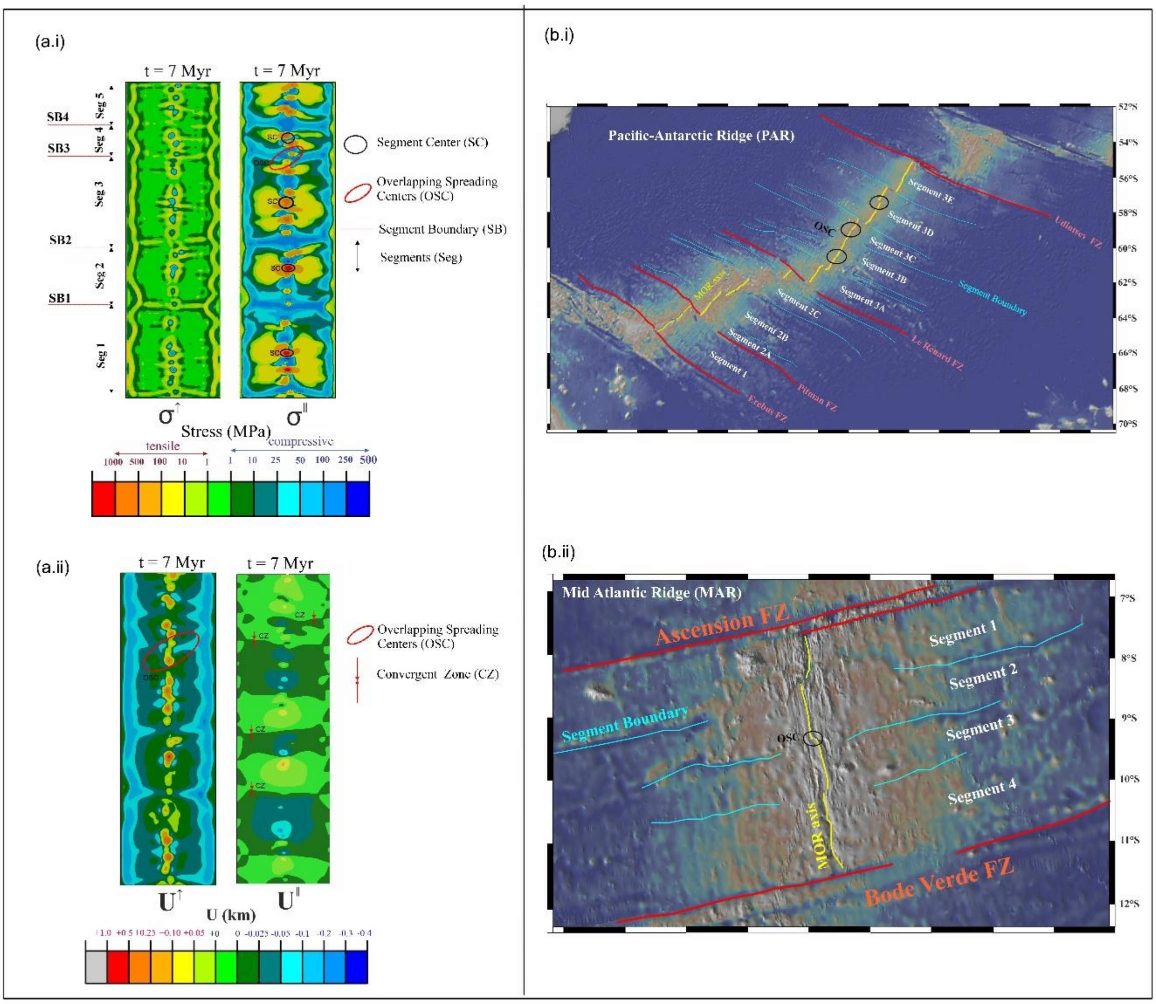

Figure 7.5 *Contours of vertical stress ($\sigma^{\uparrow}$) and ridge-parallel stress ($\sigma^{//}$) at 7 Myr (a.i), and contour plots of the vertical ($U^{\uparrow}$) and ridge-parallel displacements ($U^{//}$) (a.ii), showing different mid oceanic ridge segmentation features, including segment centers, overlapping spreading centers, and segment boundaries. (b.i) Segments of the Pacific Atlantic Ridge and (b.ii) the Mid Atlantic Ridge, displaying morphological features similar to those inferred from the FSI model.*

validation of the model calculated stress fields, I compare them with the segmentation patterns of MAR (7ºS – 12ºS) (Figure 7.5b.ii), which, in overall, represent a typical slow-spreading (~32 mm/yr) ridge (DeMets et al., 1994). This portion of MAR has four segments (length: 70 km to 100 km); the two central segments show rifted axial highs, flanked by typical valleys in the north and south segments (Bruguier et al., 2003). The segment boundaries are marked by little offsets, where the discontinuity between two central segments is arguably marked by an OSC (Bruguier et al. 2003). This model study suggests that convergent boundaries (CZ in Figure 7.5a.ii) that define primary magmatic segment (PMS) boundaries, as discussed above develop in the zone where two neighbouring magmatic spreading cells meet each other to form the first-order segmentation by compressive stripes on a wavelength of 40-150 km (Figure 7.5a.i). The finding also accounts for the smaller segments as a manifestation of small-scale convection cells beneath the ridge axis. Both PAR and MAR have many inactive or fossil ridges in association with new ridges (Bruguier et al., 2003; Ondréas et al., 2001). Such inactive states of the ridges result from paucity of partial melt supply to the shallow level. MOR segment boundaries are marked by narrow vertical tensile stress ($\sigma^{\uparrow,t}$) zones, which originated from the meeting lines of upwelling in the adjoining cells. These plate boundaries are topographically low zones, appearing as fracture zones in the natural ridges (Figure 7.5b.i). The topographic parity between the model and nature thus validates sub-ridge mush dynamics as a controlling factor of the segmentation process in MORs, like PAR.

Orthogonal offsetting is also a common segmentation mechanism in PAR and MAR on multiple wavelengths: ~50 km, ~70 km and ~100 km. Our FSI model suggests that the shear stress field can act as a destabilizing factor during the MOR evolution, leading to segmented structures by lateral offsetting. It is hypothesized that OSCs form at the meeting zone of two adjoining topographic reliefs with a lateral offset, which are found in the evolved model ridge (7 Myr) (Figure 7.5a.i-a.ii), marked by two topographic highs with a lateral offset of ~ 10 km (Figure 7.5a.i). The morphology resembles those observed in northern PAR (Figure 7.5b.i) and MAR (Figure 7.5b.ii). The ridge-parallel stress patterns in the model show a very narrow transverse compressive zone, sandwiched between two tensile zones over the adjacent axial highs at OSC (Figure 7.5a.i).

7.2.3. Tectonics of ridge-parallel hills

Despite a wide variation in the genetic MOR models, they converge at least to a point that the axial topographic morphologies originate from extensional crustal tectonics. However, crustal extension due to normal faulting can account for not more than 20% of the axial spreading in slow spreading ridges, which is further lower in case of fast spreading ridges (Bicknell et al., 1987; Macdonald, 1977; Solomon et al., 1988). One of the prevailing thoughts invokes the possible role of thermal stresses, attributed to differential cooling of the upper part of the oceanic crust to account for such shortcoming. A major problem adheres to this proposition as the calculated thermal stresses are too low to cause yielding in the elastic-plastic crust in forming ridge-parallel normal faults (Turcotte, 1974). Off-axis ridge-parallel highs and reliefs often occur in association with fast as well as slow spreading ridges on a stretch of hundreds of kilometres (Goff, 1991), characterized by smooth surface topography, which rules out the possibility of normal faulting as a primary process of their formation. Some studies have proposed this type of second-order topography as a manifestation of the whole-crust

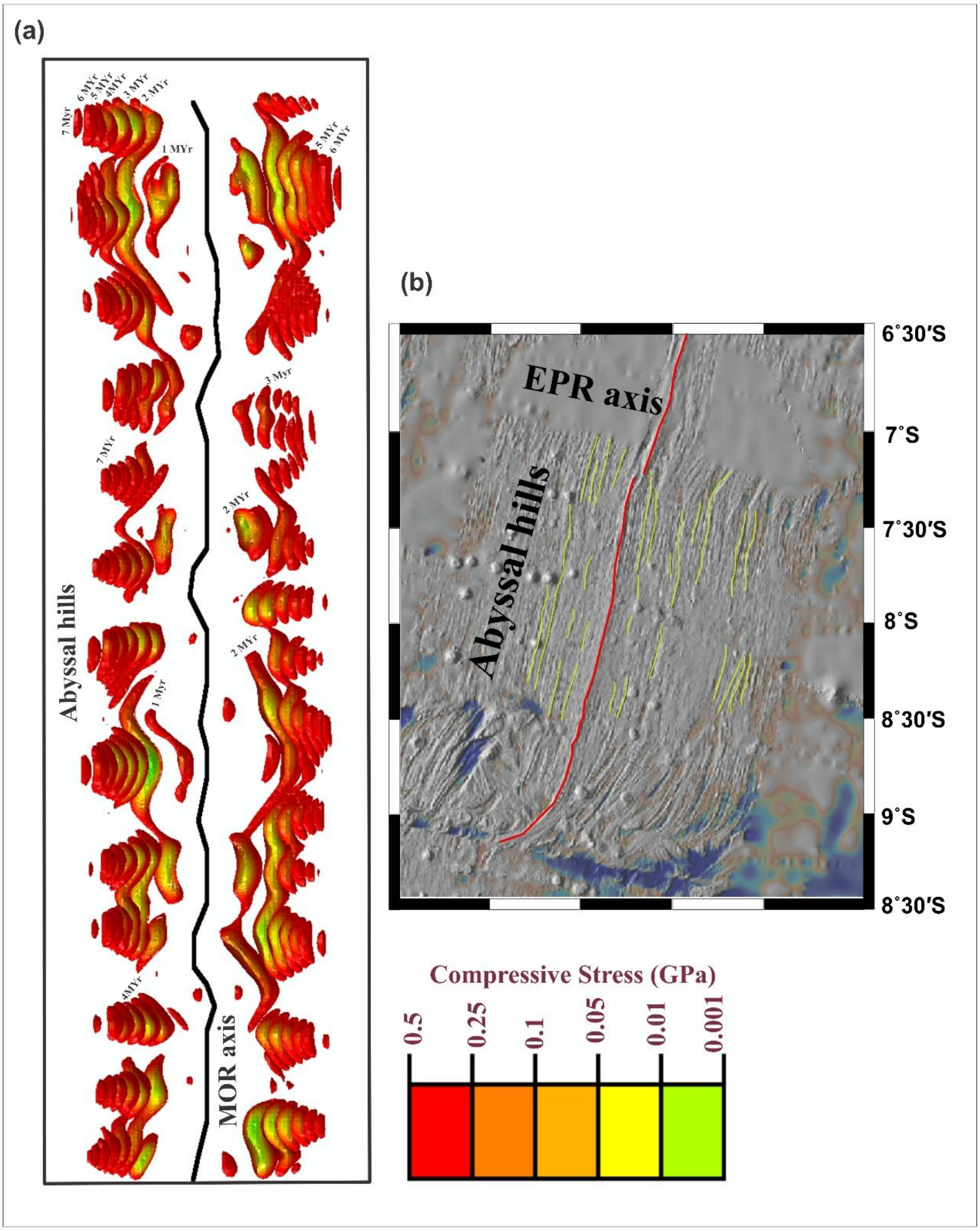

Figure 7.6 (*a) Across-axis compressive stress (*$\sigma^{\perp,c}$*) fields of a MOR obtained from the FSI model simulations. It is noteworthy that the model produces compression stress regimes in the form of ridge parallel stripes, which closely resemble ridge-parallel abyssal hill ranges. (b) An EPR segment with systematically arranged ridge-parallel abyssal hills.*

deformations (Buck et al., 2005). The model results suggest that across-axis compressional tectonics (Figure 7.6) can play a dominant role in shaping the seafloor away from the ridge. Both compressive and tensile stress regimes are simultaneously active in the upper crust, as they originate from the tractions offered by the same 3D viscous flows of sub-ridge mushy materials. The compressive regimes become strong in magnitude, almost twice that of the tensile stresses at off-axis locations (Figure 7.6), to form positive topographic elevations on the seafloor by contractional crustal deformations. To explore their dynamics, I use the ridge-normal compressive stress maps (Figure 7.6a) derived from the model runs at an interval of 1 Myr. This time interval is chosen based on the time scale of magmatic pulses in the seafloor topographic evolution (Crowley et al., 2015).

A threshold ridge-perpendicular compressive stress (1 MPa) is set in mapping the stress zones to show the hill patterns at an instant during the spreading of a ridge axis. The hills localize discretely as lenticular bodies with their long dimensions (10 to 80 km) parallel to the ridge axis. Most of them are narrow in width (1 to 10 km) (Figure 7.6a). They drift away from the axis in course of the spreading process, leaving the space for hill growth in the next time step. The process eventually gives rise to a row of ridge parallel hills formed sequentially away from the axis (Figure 7.6a). Individual hills in successive steps grow in length, forming a first-order ridge-parallel morphology in wavy fashion with wavelengths to vary between 25 and 200 km. In overall, the morphology has a maximum horizontal width (10 km), tapering to a width of 1 km on a ridge-parallel distance of 20 to 70 km. The locational variation of off-axis compressive stress regimes also indicates different characteristics of faults at central and distal parts of the segments as well as along-axis gradient in the stress field (Behn et al., 2002).

The off-axis compressional topography grows synchronously with the rugged axial topography by normal faulting in the tensile regime, as observed in the present model. To support this finding, I choose the EPR (6°-9° S) (Figure 7.6b), a fast-spreading ridge as an example. The bathymetric map of the seafloor around the ridge clearly reveals l ridge-parallel hills on either side of the axial zone over a stretch of 50 km. The stress map shows that the compression fronts consist of a row of isolated maximum compressive stress zones at different time intervals (1-7 Myr), which would act as potential locations of topographic peaks aligned with the ridge-parallel off-axis highs. Smooth topographic hills, reported from the MAR occur as isolated ridge-parallel hills with a strike length of 15 to 30 km and an elevation between 500 to 2000 meters. Several petrological studies have shown exhumation of lower crusts onto the ocean floor at MORs as an alternative mechanism of ophiolite emplacements (Dilek and Furnes, 2011), commonly observed in subduction zones and other convergent plate boundaries. The present model supports that such thrusting is possible to occur at a distance of 20 km from a ridge axis, where the crust can develop enough compressive stresses required for its shear failure and thrusting.

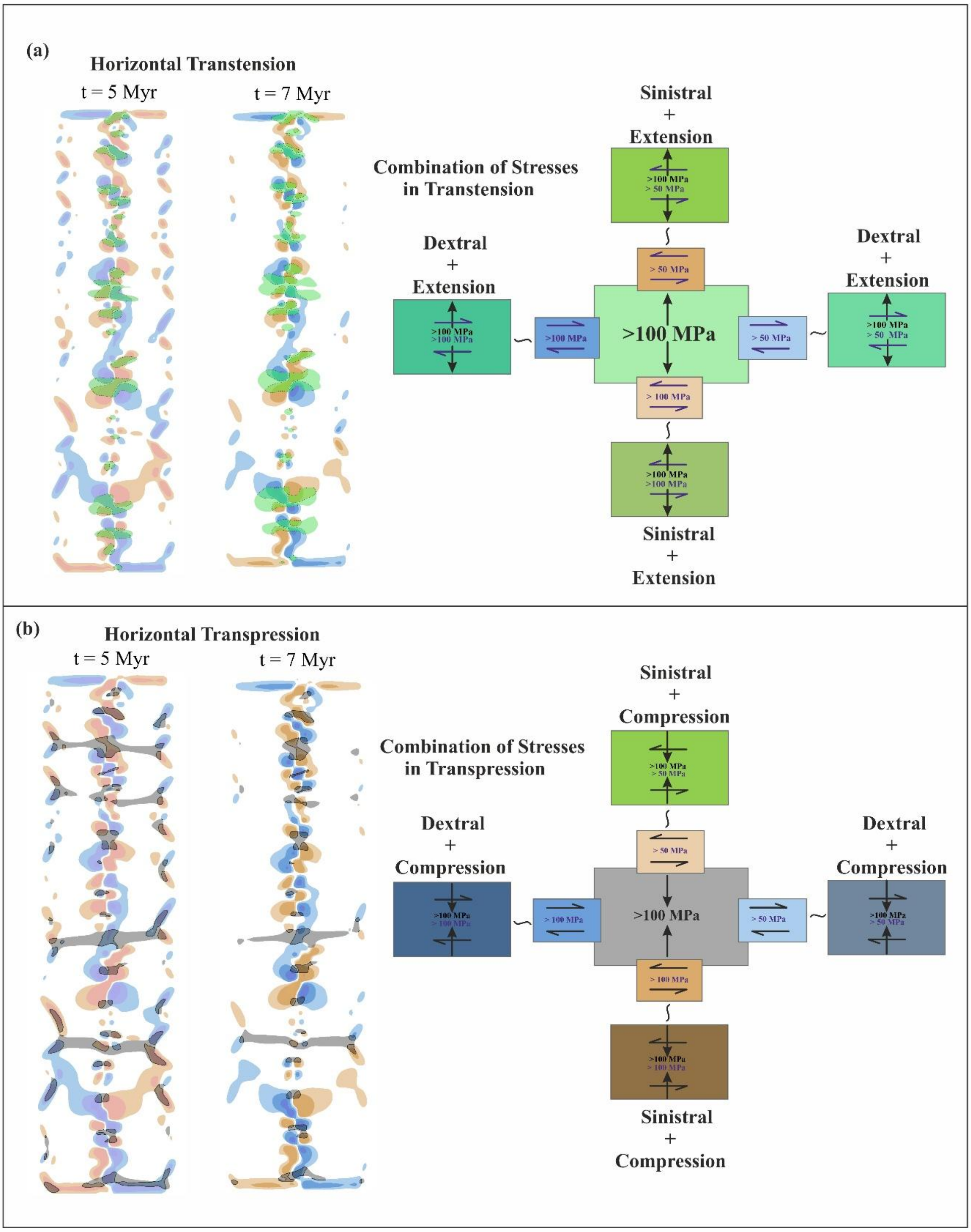

Figure 7.7 (*a) Vertical and Horizontal transtensional stress fields. Areas enclosed by black outlines denote the transtensional zone. A cartoon diagram is also provided to show sinistral and dextral shears along with the axis-parallel tension. (b) Similar contour presentation for axis-parallel compression.*

7.2.4. Horizontal transpression and transtensional regimes

Transform and non-transform offsets are common types of structural discontinuities in MOR systems, which are generally linked to their shear stress fields in the crustal upper layer (Behn et al., 2002; Neves et al., 2004; Persaud et al., 2017; Pollard and Aydin, 1984). Some studies accounted for thermal stresses to explain the origin of orthogonal transform offsets (Choi et al., 2008). Mechanical shear stresses are also held responsible for offset generation, considering that shear strength is low in the spreading direction (Freund and Merzer, 1976; Oldenburg, 1975). Two parallel ridges can link-up with each other by a ridge transverse strike-slip fault along the direction of low across-axis shear strength of the oceanic crust (Maia et al., 2016). All these models/hypotheses, however, do not explain orthogonal segmentation of single straight ridges, as observed in many MORS, e.g., Mid Atlantic ridge (Carbotte et al., 1991). Our present study finds no consistent relation between the shear stress and across-axis segment boundaries. Furthermore, superimposition of the horizontal shear stress fields on those of along-axis tensile and compressive stresses does not yield any orthogonal segmentation pattern (Figure 7.7a-b).

I compare an MAR stress map (Figure 7.8a) with the along-axis compression and cumulative shear derived von-Misses stress obtained from our FSI model. Across-axis failure zones in the MAR (Figure 7.8b) form segmented structures which broadly agree with the von-Mises stress localization pattern in the model. Also, two along-axis compressive zones are observed in the MAR (red arrows in Figure 7.8b; close to at 31° 15′ discordant zone; and close to 38°; Fox et al., 1991). It is to be noted that these stress maps should be treated as qualitative, where the exact location can show departures by 20 to 40 km (Luttrell and Sandwell, 2012). One of the two along-axis compression zones defines the 31° 15′ discontinuity, which was recorded as a segment boundary during the MAR survey in the 31 ° to 34° 30′ S sector (Carbotte et al., 1991; Grindlay et al., 1991; Kuo and Forsyth, 1988). This segment boundary shows only ~8 km offset (Figure 7.8b), oblique to both the ridge and transform trends (Fox et al. 1991). This boundary and other non-transform segment boundaries (for example, 32 ° 30′ S and 33 ° 30′ S) are of magmatic origin, and their small offsets (8 km to 30 km) are attributed to isolated magmatic segments (Carbotte et al., 1991). It is also noteworthy that both the secondary segment boundaries at 31°15′ and close to 38° are associated with some shear stresses, apart from the fact that the large offset fracture zones are dominated by shear, as evident from the stress maps (Figure 7.8b). The hypothesis of magmatic segmentation, validated by gravity analysis (Kuo and Forsyth, 1988), multibeam data (Grindlay et al., 1991), magnetic analysis (Carbotte et al., 1991), and earthquake focal mechanism solutions (Luttrell and Sandwell, 2012) agree with the across-axis structures obtained from our mush dynamic models.

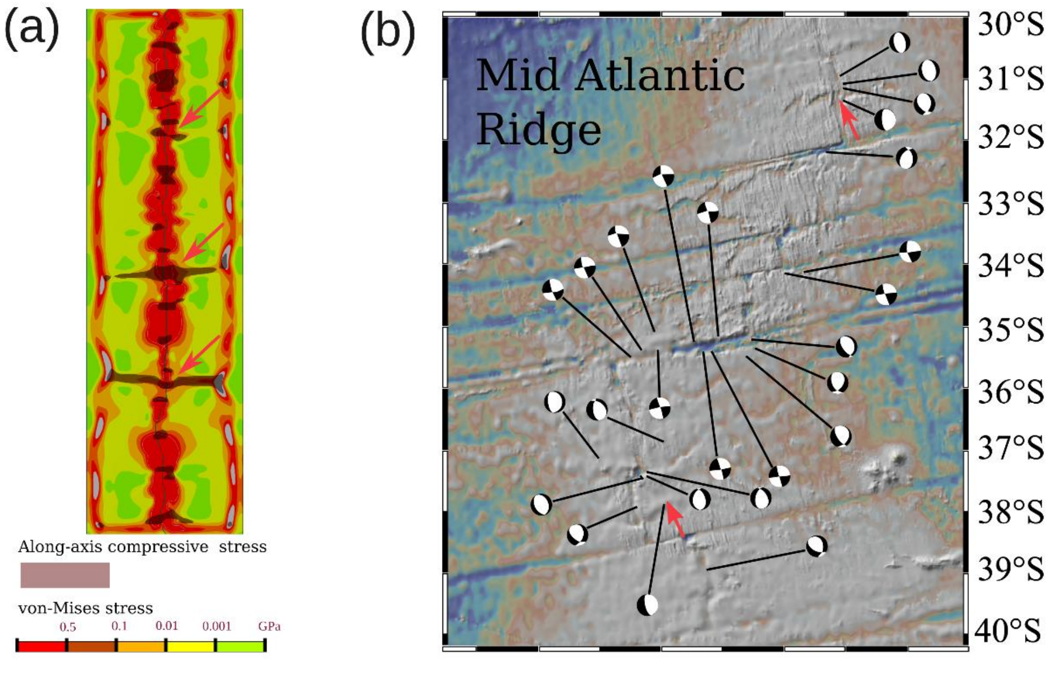

Figure 7.8 (*a) Calculated plots of the von-Misses stresses (*σ^{vm}*) and along-axis compressive stresses (*$\sigma^{\|,c}$*). The von-misses stresses localize preferentially in an array of ridge normal bands, resulting in MOR segmentation (red arrow). (b) A portion of the MOR showing two ridge segments (red arrow).*

Using earthquake data several earlier studies have recognized along-axis tensile as well as compressional stresses at transform segment boundaries (Parnell-Turner et al., 2017; Rundquist and Sobolev, 2002). Some investigations suggested the ridge topography as a potential factor for tensile stress generation along the ridge trend to create a trans-tensional tectonic setting in transform fault zones (Lonsdale, 1994). Transpression at MOR is typically conceived along transform faults, where a shear is thought to result from the opposing motion of two ridge segments, linked by a transform fault (Maia et al., 2016). This plate model implies that the shear and the compression originate from a single kinematics determined by two ridges approaching each other due to the spreading. This transpression model is applicable to a system with decreasing ridge offset, but not a setting with increasing offset. Most of the earlier studies interpreted transtensional and transpressional zones in terms of tectonic movements. The present model provides a new explanation, claiming that sub-ridge mush activities can also produce transtensional kinematics in MORs.

7.2.5. Concluding points

The principal finding of this work are as follows:

- Multi-ordered convection of sub-ridge mushy materials, produced by decompression melting under random thermal perturbations is the key physical process to determine the dynamics of mid-ocean ridges.
- The mechanical coupling of mushy convection with the elastic crust, treated as fluid-structure interaction, develops a spatially complex stress field in a mid-ocean ridge, forming characteristic segmented stress localization patterns. This interaction dynamics can produce simultaneously along- and across-axis horizontal compression/tension as well as across-axis shear stress. Their median magnitudes can range 17 MPa to 100 MPa at steady states (after 7 Myr), implying that the magmatic process can largely contribute to the ridge dynamics, in addition to plate spreading. Along-axis compression and across-axis shear stress in MORs can originate from the interaction of underlying mush convection with the overlying elastic crust.
- MORs evolve dominantly under strong ridge normal tension in their axial zones, coupled with off-axis ridge-normal compression belts, which can be equated with off-axis ridge-parallel hills commonly observed in natural settings.
- Along-axis compressive stresses localize in a row of narrow stripes across the ridge axis, resulting in segmentation of the stress field on a wavelength of 40-150 km. The second-order morphological segmentation of MORs reported in literature conforms to this stress segmentation characteristics, suggesting their origin linked to the sub-ridge upwelling processes.
- The estimated median axial stress magnitudes at MOR are in the scale of a few hundreds of MPa (< 250 MPa), and off-axis stresses are less than the axial stresses (< 100 MPa). The top crustal layer develops stresses lower than the corresponding deeper crustal layer. Off-axis compression stresses attain their peak values with a phase lag of a million years or more after the peak attainment of tensile stresses.

7.3. River system and Topography of Peninsular India

7.3.1. Dynamics of the River System

The model simulations in chapter 5 suggest that the persistently eastward flows of the Indian peninsular rivers over vast distances (hundreds of kilometres) are primarily driven by the continental scale (first-order) topographic gradient, which originates from a complex geodynamic influence of the sub-lithospheric mantle flows, as discussed in section 3.2.2. The resulting escarpment relief acts as a barrier, preventing the rivers from eroding the terrain along shorter, westward pathways toward the Arabian Sea. The resilience of the WG escarpment against the erosion at high rates (mean erosion rate: 48.6 ± 20.9 mMa^{-1}, Mandal et al., 2015; Mandal et al., 2015) underscores a dynamic interplay between tectonics and fluvial processes to sustain its positive physiographic relief on long time scales. The ongoing tectonic uplift (Figure 5.12) of the escarpment counters erosion-driven denudation, maintaining the eastward topographic slope and guiding the river systems toward the Bay of Bengal. This eastward polarization of the drainage pattern has led to a geomorphic asymmetry in the IP landform over geological time (Figure 5.1).

The major rivers originating from the Deccan Plateau, such as the Godavari, Krishna, and Cauvery, have transported vast quantities of sediment, depositing them into the Bay of Bengal over an extended geological timeframe, suggesting that the river system has been consistently transporting continental sediments to the Bay of Bengal for a significant period (Rao et al., 1997). This continuous sediment supply implies a remarkably stable and persistent eastward drainage pattern, which is a direct consequence of long-term tectonic activity across the Indian Plate (IP). Moreover, the sedimentary records preserved in the Bay of Bengal offer a valuable archive of the region’s tectonic and climatic history. The ongoing deposition of sediments reflects a dynamic landscape where the stability of the eastward-sloping topography has been maintained over millions of years. These long-term sedimentation patterns point to sustained tectonic activity in the Indian craton, which has played a crucial role in preserving the eastward-flowing drainage system. The numerical model results (Figures 5.9-5.11) further support the idea that the long-term eastward topographic gradient has been a key feature of the landscape’s evolution in peninsular India.

7.3.2. Asymmetric PI topography and tectonic models

The Indian craton occurs between two oceanic lithospheres of contrasting ages: the relatively young Indian Ocean lithosphere to the west and the older Bay of Bengal lithosphere to the east. The Indian lithosphere, which is a part of the larger Indo-Australian Plate has been engaged in complex interactions with the surrounding plates. Historically, the Indian plate has undergone a large northward drift, primarily driven by mantle convection and plate tectonic forces, following its breakup from the ancient supercontinent Gondwana. This drift ultimately led to the collision with the Eurasian plate, giving rise to the Himalayan orogeny. However, this northward movement alone cannot explain the persistent eastward tilt of the peninsular topography. The sharply elevated, linear, north-south trending topographic high, most notably represented by the Western Ghats escarpment, suggests focused tectonic activity along the western margin. This is further evidenced by observable seismic activity in the region (Catherine et al., 2007; Jha et al., 2023; Sribin et al., 2024). These observations point to the necessity for alternative tectonic models that can better account for the current movements and topographic features of the Indian plate.

A plume model has been proposed to explain the development of peninsular topography, suggesting that mantle plumes are responsible for the uplift and volcanic activity observed in the region (Cox, 1989, 1980; Watts and Cox, 1989; Widdowson and Cox, 1996). However, this model fails to fully explain the linear topography, which several workers have shown to be a product of neotectonic movements (Mandal et al., 2017; Mandal et al., 2015; Mandal et al., 2015). In addition, plume-driven topography is typically axisymmetric, which contrasts sharply with the N-S trending linear elevations of the Western Ghats with east-directed topographic slopes, the magnitudes of which increases from north to south, as shown in Figure 5.5. Furthermore, paleo-topographic studies indicate that the plume event that occurred around 65 Ma ago cannot sustain the extremely steep topographic slopes observed in the Western Ghats over such a long geological timescale. The persistence of these slopes suggests that the Western Ghats must have undergone slow, continuous uplift in more recent geological times (Richards et al., 2016). The ongoing uplift history is not in agreement with the rapid, short-lived topographic changes typically associated with mantle plume events. In summary, the plume model does not seem to adequately account for the long-term topographic stability and eastward tilting observed in the Indian peninsula. A geodynamic model used to examine the asymmetric IP topography must be in compliance with the contrasting subsidence rates between the Bay of Bengal (model subsidence rate = 1.67 cm/year) and the Arabian Sea (Figure 7.9a) and the ongoing tectonic uplift of the Western Ghats. This study reveals a connection between this differential subsidence with the uplift tectonics of the WG in controlling the asymmetric IP topography, and maintaining spatially persistent eastward slopes.

7.3.3. The Western Ghat Escarpment: A Geodynamic Response

The Western Ghats (WG) escarpment exhibits a step-like form, characterized by a dramatic elevation drop from approximately 2,000 m to 500 m towards the west. Several hypotheses have been proposed to explain the origin of this escarpment, though each has its own limitations. One hypothesis suggests that the escarpment formed as a rift shoulder during the break-up of Gondwana, following the separation of the Indian plate from Madagascar and

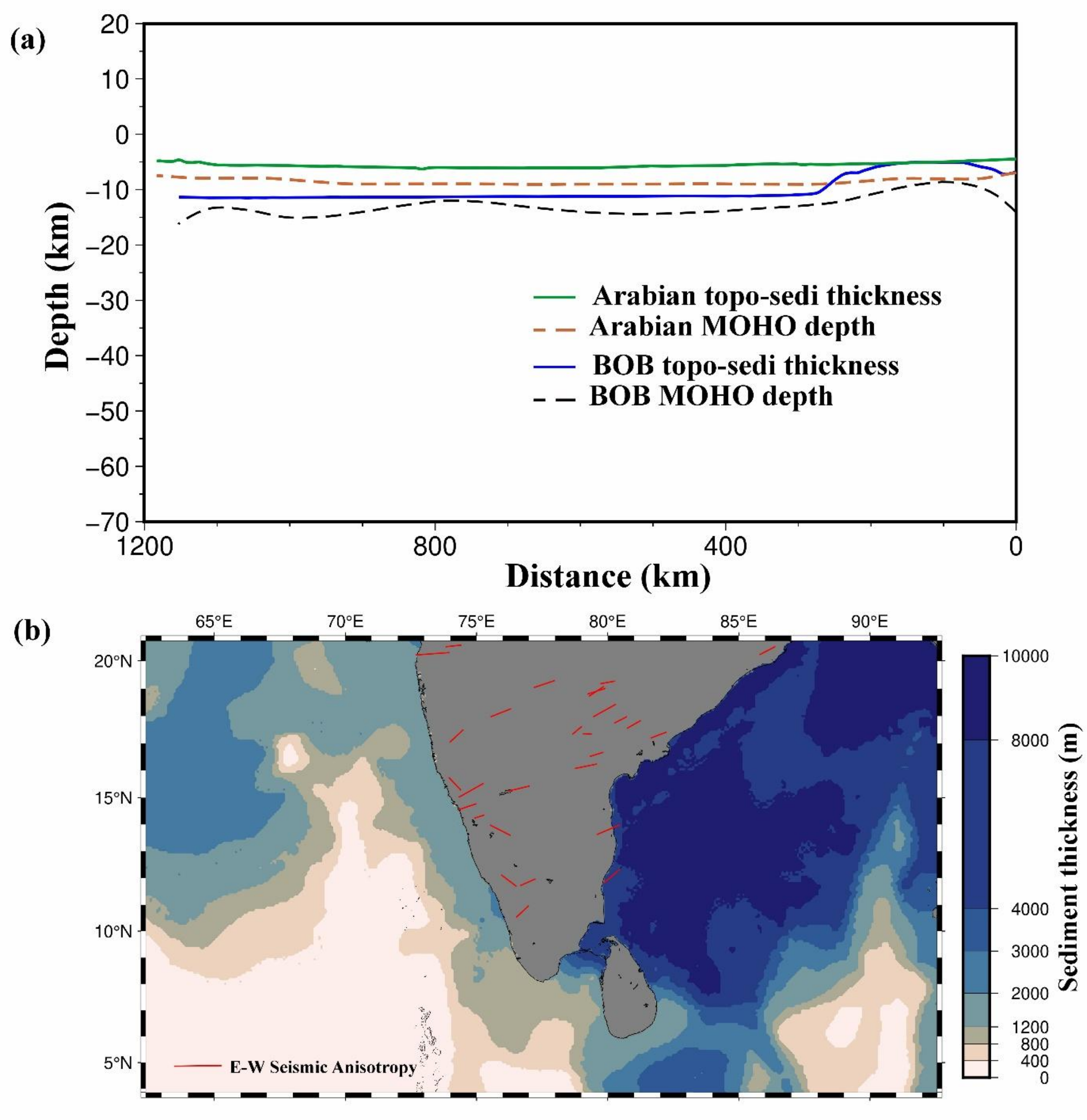

Figure 7.9 *(a) Graphical plots of the depths of top sediment surfaces and the crustal base (MOHO) in the Arabian Sea and the Bay of Bengal. The plots indicate a greater subsidence rate and sediment accumulation in the Bay of Bengal, correlating with deeper Moho depths, as compared to that in the Arabian Sea. (b) Sediment thickness map (in meters) across the Indian Ocean region, showing significantly thicker sediment columns in the Bay of Bengal (up to ~10,000 m), compared to that in the Arabian Sea (generally < 4000 m). Red arrows indicate east-west seismic anisotropy in the sublithospheric mantle, reflecting variations in mantle flow.*

Africa (Chatterjee et al., 2013). However, this model does not fully account for the continuous uplift observed in more recent geological times (Radhakrishna, 1993; Richards et al., 2016). Another hypothesis proposes that the escarpment resulted from flexural uplift due to the loading and unloading of sediments along the western margin. While this explanation can account for some aspects of the topography, it fails to explain the linearity of the escarpment and the specific north-south topographic variation observed in the Western Ghats. A third hypothesis attributes the formation of the escarpment to mantle plume activity, suggesting that thermal buoyancy could have uplifted the region. However, plume-driven topography is typically axisymmetric, whereas the Western Ghats form a long, linear feature, which does not align with this model as discussed in the preceding section.

The shortcomings discussed above highlight the need for a more comprehensive model that offers a self-consistent interpretation of the Western Ghats (WG) dynamics, based on observed geological and geophysical signatures. These include neotectonic movements (Mandal et al., 2017), the maintenance of anomalously steep topography despite surface erosion (Mandal et al., 2015), seismic activity (Jha et al., 2023), and E-W seismic anisotropy in the sublithospheric mantle (Jaiswal and Sinha, 2007). Collectively, these geological signals suggest that the origin of the Western Ghats is linked to deep-lithospheric processes. Our geodynamic modelling demonstrates that the Indian plate's tectonic setting, with contrasting lithospheric ages of the Bay of Bengal (BOB) and the Arabian Sea, generates E- and W-directed mantle flows, respectively. These flows converge into a focused upwelling zone at the western margin of the Indian craton, leading to the uplift of the Western Ghats and the formation of a topographic high. The presence of E-W seismic anisotropy (Becker et al., 2012), (Figure 7.9b) observed in the region, provides strong evidence supporting westward sublithospheric mantle flows in our model. Furthermore, this geodynamic framework explains the ongoing uplift of the Western Ghats, which is necessary to sustain the steep slopes of the WG Escarpment over geological timescales. In conclusion, the dynamic topography of the Western Ghats is primarily a result of lithosphere-mantle kinematic interactions, driven by westward sublithospheric mantle flows beneath the Bay of Bengal region (Figure 7.10).

The Bay of Bengal, with its denser lithosphere, has experienced significantly higher subsidence compared to its counterpart, the Arabian Sea, to the west (Figure 7.9a) This differential subsidence has led to focused uplift along the western margin of the Indian Peninsula (IP), as demonstrated in the model simulations presented in Chapter 5. Our geodynamic model suggests that the uplift rate in the Western Ghats has been primarily influenced by the higher subsidence rates in the Bay of Bengal, a correlation supported by observed subsidence rates in the Bay and the uplift rates in the Western Ghats. The numerical simulations are consistent with these observed rates, providing robust validation for our model results. The differential subsidence in the oceanic basins on either side of the IP (Figure 7.9a), combined with deep-mantle flow dynamics, is the primary cause of the topographic asymmetry, which is reflected in the consistent eastward surface slopes and drainage patterns. This model not only explains the present-day topography of the Western Ghats, but also offers a framework for understanding the long-term evolution of the IP's topography on a continental scale (Figure 7.10).

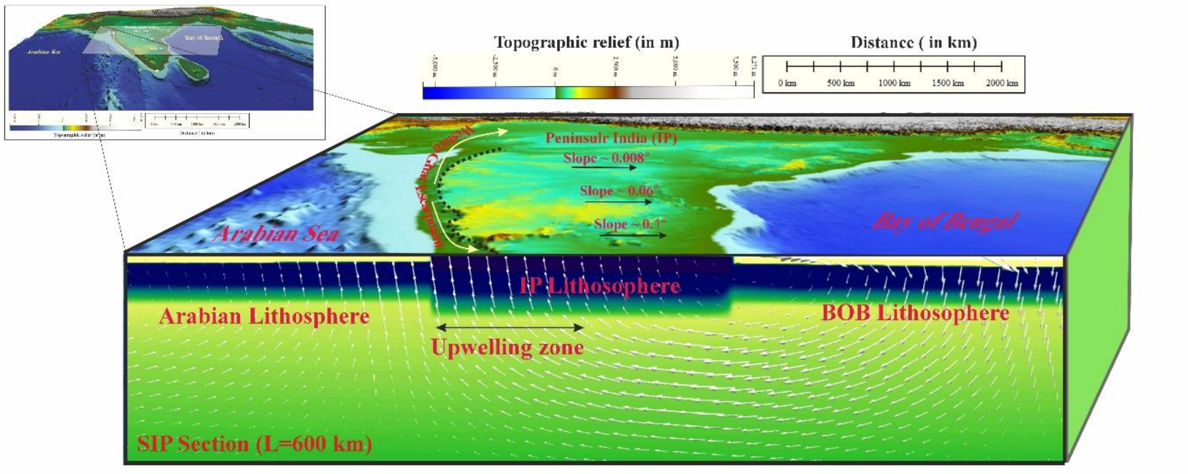

Figure 7.10 *A 3D perspective of the asymmetric topography in Indian peninsula in relation to the model-generated sublithospheric mantle flows. The Western Ghats Escarpments lies above the upwelling zone in the mantle, implying the control of westward sub-lithospheric flows triggered by subsidence in the BOB lithosphere. The cross-section spans the SIP section (L= 600 km) along the Peninsular India.*

7.3.4. The Eastward Topographic Slopes: Model Estimates

The model results suggest that the southward increase in topographic slope is a consequence of the westward migration of the mantle upwelling zone. This migration becomes an effective factor in rotating the continental lithosphere of narrower width and developing steeper surface slopes in the south. The present model estimates qualitatively agree with the observed north-to-south variation in topographic slopes discussed above. Despite the overall attainment of the model in capturing the qualitative trends in topographic slopes, the estimated values, however, tend to overestimate the actual slope magnitudes as measured from the Digital Elevation Model (DEM). Such discrepancies are common in geodynamic modelling, where simplifications and assumptions that are often necessary to address the complexities of natural systems can result in some discrepancies. In the case of the Western Ghats and the Indian Peninsular Plateau (IP), this overestimation is likely due to the exclusion of synkinematic surface erosion in the current model. It is well established that surface slopes evolve through the combined effects of tectonic uplift and concurrent erosion processes. Studies have shown quantitatively that erosion can significantly modify topographic slopes (e.g., DiBiase and

Whipple, 2011). In regions like the Western Ghats, where intense rainfall, tropical climates, and high erosion rates are prevalent, the topographic slopes are significantly reduced by surface erosion, as weathering and fluvial processes dominate the landscape evolution (Mandal et al., 2015). The major rivers originating from the Western Ghats—such as the Godavari, Krishna, and Cauvery—transport vast quantities of sediment eastward, ultimately depositing them in the Bay of Bengal. These sediment accumulations provide clear evidence of the strong erosional forces shaping the topographic slopes of the region. Since the present model primarily focuses on tectonic uplift and mantle dynamics while excluding the influence of erosion, it tends to somewhat overestimate the magnitudes of the eastward slopes in the IP. Although the model overestimates the topographic slopes, it offers valuable insights into the underlying tectonic and mantle dynamics that have shaped the Indian Peninsular Plateau.

7.3.5. Concluding points

The main outcome of this work are as follows:

- This study provides a novel geodynamic perspective on the first-order asymmetric topography of the Indian Peninsular Plateau, revealing its connection to the broader plate tectonic configuration. A key finding is that a significant lithospheric density difference between the Bay of Bengal and the Arabian Sea, due to their contrasting ages, plays a crucial role in generating gravitational dynamics that tilt the plateau to the east.
- This dynamic condition induces both westward and eastward sub-lithospheric mantle flows beneath the Bay of Bengal and the Arabian Sea. The westward mantle flow predominates in capturing nearly the entire sub-lithospheric region of the Indian continent before encountering the eastward flows, which leads to upwelling along the western margin of the Peninsular India (IP). This focused upwelling causes tilting in the plateau, resulting in a first-order topographic slope to the east. The magnitude of this eastward slope increases progressively from the northern to the southern part of the Peninsular India. Model simulations indicate that this southward increase of the topographic slope is the result of the westward migration of the upwelling zone.
- Along the western margin of the plateau, the Peninsular India features a prominent physiographic feature: the Western Ghats, a north-south trending escarpment that stretches for approximately 1300 kilometers and exhibits a significant relative relief of ~ 800 meters. This study suggests that the Western Ghats escarpment is a direct

manifestation of large-scale geodynamic processes. The differential subsidence in the Bay of Bengal generates westward mantle flows, which focus into upwelling along the western edge of Peninsular India. This upwelling results in positive topographic relief, preferentially along the western flank of the Peninsular Craton, leading to the formation of the Western Ghats escarpment.

- Finally, the geodynamic model presented here integrates the development of the tilted Peninsular Plateau with subsidence in the Bay of Bengal and focused uplift along the Western Ghats.

7.4. Plume-rift interaction: implications for the Deccan Volcanism

7.4.1. Deccan volcanic materials in rifted basins: model interpretations

The model results presented in Chapter 6 in the context of how the pre-existing rifts in the Indian peninsula might have affected the Reunion plume in its encounter with the Indian continental lithosphere. Considering the plume – continental lithosphere interactions obtained from the model simulations, we suggest that a part of the plume (<10 % of the total plume head volume) contributed to material supply for the magma generation during the Deccan volcanic event (Figure 6.3a). Our model results indicate that the rift reactivation can split the plume head, and drag a part of it to the rift zone when the rift-plume distance is significantly close (< 200 km). The rift-plume distance calculated from their paleo-pole positions corresponding to the timing of Deccan volcanism supports our proposition that the occurrence of continental rifts significantly influenced the plume stagnation and its repositioning at the lithospheric base. The northward drifting Indian landmass progressively increased its distance from the Reunion plume, ceasing the rift-plume interaction. From the model results, we suggest attaining this non-interaction state after the main phase when the rift –plume distance became > 400 km (Figure 6.5).

We chose a mantle plume of equivalent size (~150 km) in our model to simulate the Indian tectonic setting controlled by the Reunion plume activity beneath the Indian craton. The model introduces a pre-existing rift at a distance similar to that between the Reunion plume and CITZ around ~75-66 Ma. Our model results suggest that during Deccan volcanism the plume was close enough to reactivate the Narmada-Tapti rift, resulting in drifting of a part of the plume towards the rift, which eventually produced a substantial amount of partial melts required for underplating and subsequent magmatism along the rift zone (Figure 6.3a). The topographic highs and lows observed in our model closely match with the topographic undulations in the Indian craton attributed to the Reunion activity (Figure 6.3b), as reported by several authors (Ghosh, 2015; Kumar et al., 2015; Prasad et al., 2018). Additionally, the model findings indicate that Moho upwarping beneath the plume offshoots (Figure 6.3b) corresponds well with the elevated Moho depth observed in regions of positive Bouguer gravity anomalies (Kumar et al., 2015; Singh, 1998).

7.4.2. The Narmada-Son rift and the Reunion plume: their interactions

The Narmada-Son lineament (NSL) shows a total strike length of nearly 1200 km, extending in the E–W direction from 72.5◦E to 82.5◦E. The lineament forms a prominent linear tectonic feature in the western part of the Indian subcontinent (Figure 7.11a). Some studies consider the NSL as a suture zone between two contrasting geological terrains: the Bundelkhand proto-continent to the north and the Dharwar proto-continent to the south of it (Choubey, 1971). In a broader perspective, the NSL occurs in the Central Indian Tectonic Zone, which is recognized as a collision zone to account for the amalgamation of Singhbhum, Bastar, and Dharwar cratons in the south and the Bundelkhand craton in the north during the late Archean time (Jain et al., 1995). A group of authors claim that the NSL is a continental rift zone which has experienced reactivation multiple times since the Proterozoic (e.g., Choubey, 1971). From the available geophysical data, Mishra (1977) identifies the NSL as a typical rift structure, extending up to the Murray ridge in the Arabian Sea (Figure 7.11a).

A direction of earlier studies suggests that the stratigraphic signatures of NSL is akin to a horst-type tectonic setting, bordered by the Son-Narmada and the Tapti faults to its north and south, respectively (Qureshy, 1982). The regional gravity anomaly pattern locates the Tapti-Narmada-Son zone as a broad region of gravity high, in which the NSL occurs as a narrow zone of low gravity (Qureshy, 1982). There are two major seismically active faults: the Narmada south fault (NSF) and the Narmada north fault (NNF) (Figure 7.11a), bounding the NSL. The origin of NSF and NNF is traced back to the middle to late Archaean tectonic events (Choubey, 1971; Jain et al., 1995). The region between these two fault systems is covered with alluvial deposits and late Archean greenstone belts. To the north of NSL lies Precambrian terrains: the Vindhyan basin (750–1721 Ma) and the Bundelkhand craton (2.5 Ga), whereas much younger units, the Deccan volcanics (~65 Ma old) on the south (Singh 2015).

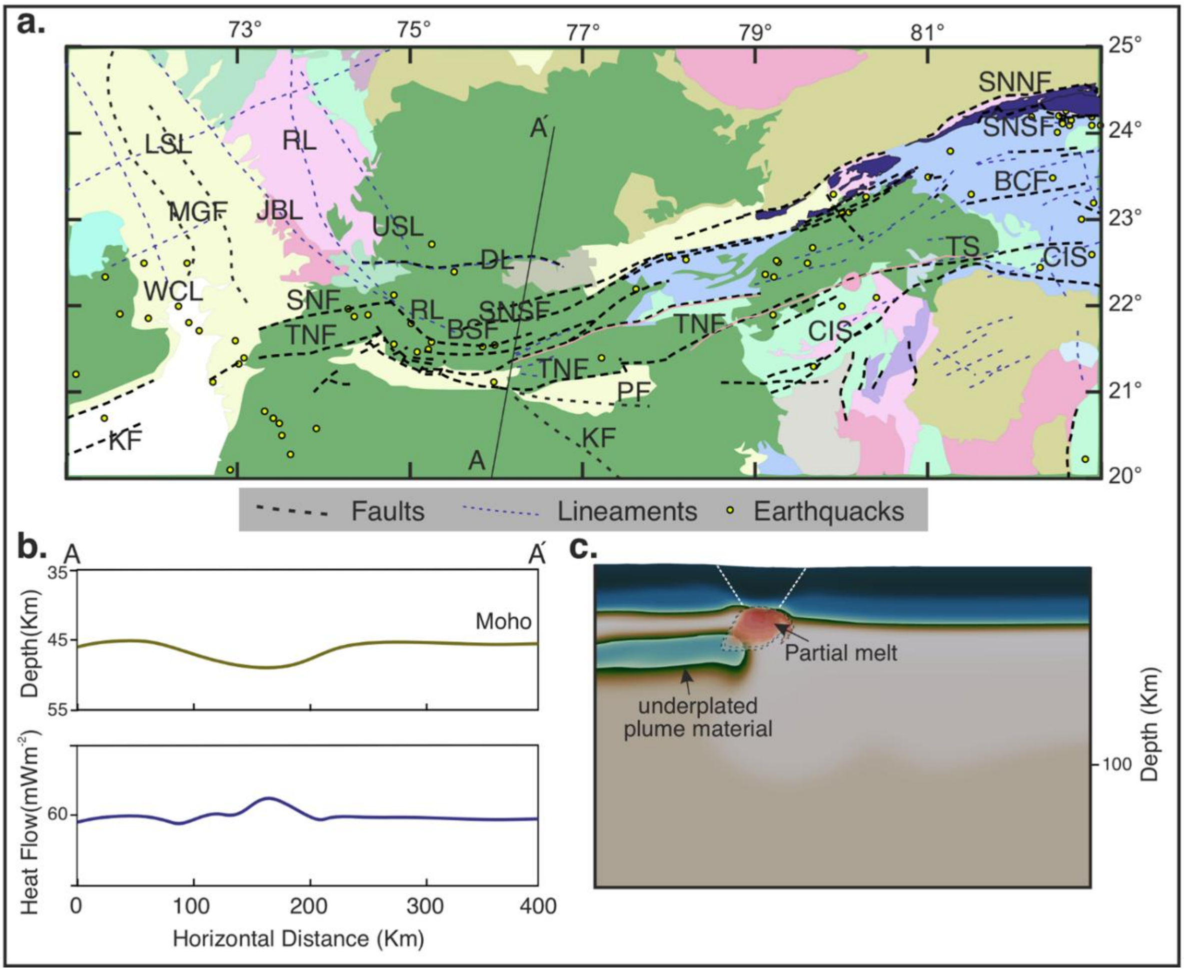

Figure 7.11 *(a) A geological map showing the detailed pattern of major lineaments in the Narmada son rift system. (b) Horizontal variations of Moho depth and heat flows along the section AA' in panel b. Note that Moho down wrapping and high heat flow regime localization are marked at the same location above the rift. (c)Model simulation showing the localization of the partial melting beneath the pre-existing rift. Abbreviations used are SNNF: Son-Narmada North Fault, SNSF: Son-Narmada South Fault, TS: Tan Shear, CIS: Central Indian Shear. SNF: Son–Narmada Fault; TNF: Tapti North Fault; BSF; Barwani Sukta Fault; PF: Purna Fault; KF: Kaddam Fault.*

The high Bouguer gravity anomalies in the NSL are attributed to high-density materials in the lower crust, which were emplaced by large-scale asthenospheric upwelling (Singh, 1998). Interestingly, Rai et al., (2005) report a 52 km Moho down warp across the lineament, whereas an average Moho depth of 40 km elsewhere in the Indian craton. Additionally, the crust beneath the NSL yields V_p/V_s ratios (1.84) significantly higher than those (1.73) in the surrounding regions. These geophysical observations support the possibility of a high-density mafic mass at depth compensating the crustal root, as reflected in a small topographic variation (200 m) across the lineament. To explain the cause of the seismically active current state, the authors suggest that the presence of such an anomalous mass in the deep crust perhaps developed gravity-induced stresses in the lower crust, resulting in crustal failure along the pre-existing Narmada-Son fault to generate earthquakes.

Our model results show that plume materials can flow laterally toward a rift if the lithosphere is sufficiently strong (viscosity > 10^{22} Pa s), or the plate drifts at fast rates (> 4cm/year) (Figure 6.7). It is to be noted that both the conditions are valid for the Indian plate tectonic setting. This rift-driven flow eventually led to the accumulation of plume materials in the asthenosphere beneath the rift zone. They underwent partial melting and underplating beneath the NSL (Figure 7.11b), as inferred from positive Bouger anomaly within this region. The model findings also indicate that the northward rapid movement of the Indian plate forced the plume head to tilt in the upper mantle by a significant amount, which further facilitated the rift-ward migration of the plume materials. Model calculations indicate that the lateral drift velocity of the plume reached ~ 10 cm/year, implying that the plume materials took approximately 8-10 Myr to reach the basement of NSL and Cambay basin.

7.4.3. Godavari and Mahanadi rifts: influence of the Reunion plume

Godavari rift consists of three major faults (WNW-ESE trending Kadam fault (KF); the Kinnerasani Godavari fault (KGF); the Godavari valley fault (GVF) that adjoin the rift, suggest recent tectonic activities evidenced by moderate levels of seismicity (Figure 7.12a) (Chaudhuri and Deb, 2003). Geophysical studies show a prominent increase in crustal thickness in the rift (Figure 7.12b), marked by a sudden increase in seismic wave velocity and a weak Moho (Kaila et al., 1990; Singh et al., 2012) with respect to that in the Eastern Dharwar craton. The geophysical anomalies are associated with a high heat-flow rate in the rift region (Figure 7.12c) (Singh et al., 2015). However, the craton displays the mantle transition zone at 410 and 660 km transition zone beneath the rift (Singh et al., 2012), as expected normally. These observations rule out the possibility of a deep-mantle upwelling zone beneath the Godavari rift, instead suggest the occurrence of a sill-like intrusion, which can justify the rheological contrast (high seismic wave velocity), Moho down wrapping and the lower availability of partial melts in this region. Our model results for a moderate plume-rift distance comply with these findings, suggesting that the plume materials spread out asymmetrically under the rift influence and underplate at the lithospheric base beneath the rift region (Figure 7.12c). The underplating eventually gives rise to high heat flow and an overall increase in crustal thickness, as found beneath the Godavari rift region. The underplated plume materials were depleted, resulting in lower degrees of partial melting beneath the rift, as revealed by the geological sequences in the Godavari rift region.

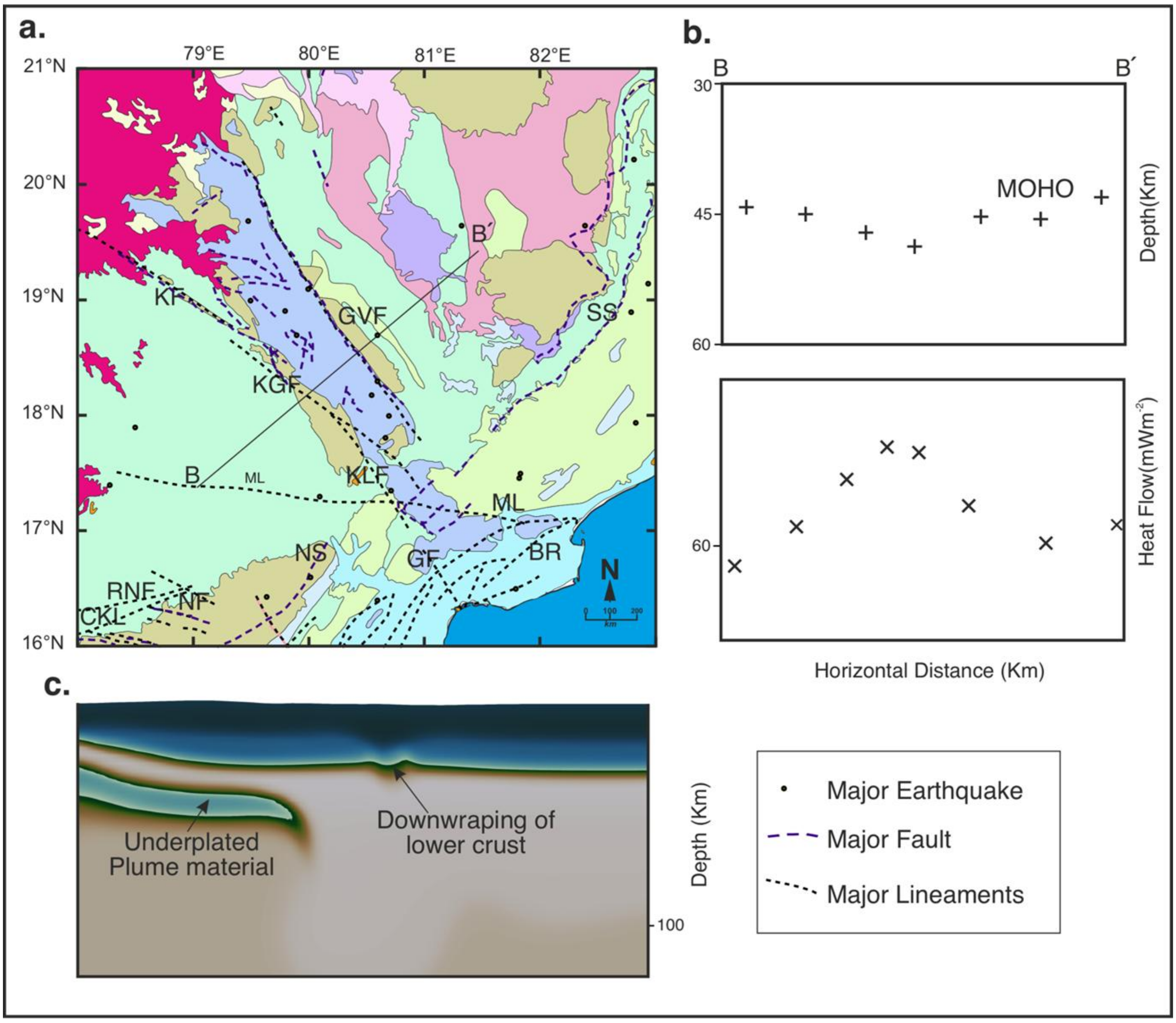

Figure 7.12 (*a) A map showing the geological settings in the Krishna-Godavari rift system. (b) The systematic Moho depth and corresponding heat flow along the section BB' (c) Model simulation showing underplating of the plume materials beneath the lithosphere, coupled with a selectively strong drag of the mantle lithosphere. It is to be noted that Moho down wrapping and high heat flow occur preferentially at the age of the underplated plume material. Abbreviations used are DVP: Deccan Volcanic Province; EDC: Eastern Dharwar Craton; GR: Godavari rift; EGMB: Eastren Ghat Mobile Belt; KF: Kaddam Fault; KGF: Kinnerasani-Godavari Fault; KLF: Kolleru-Lake Fault; GVF: Godavari Valley Fault.*

Unlike the NSL and Cambay basins, the Mahanadi rifts display signatures of underplating and subsequent volcanisms of early Cretaceous, which are, however, linked to the earlier Kerguelen plume event (Behera et al., 2004). However, the mode of their plume-rift interaction was similar to that described for the Reunion plume, leading to an offset of the Kerguelen plume from the Indian craton. As the Indian plate moved due north-west during this Kerguelen event, the plume materials of the Kerguelen hotspot were dragged towards the rifts to underplate at the base of the Mahanadi rift, leading to upwrapping of the Moho, as revealed from geophysical studies (Basantaray and Mandal, 2022; Behera et al., 2004). No such evidence of interaction was found since the late Cretaceous time, and the Mahanadi rift has remained dormant most of the Cenozoic. From our model, we decipher that the plume-rift distance between the Réunion plume and Mahanadi rift at 66 Ma was large compared to the NSL and Godavari rift. Thus, The Mahanadi rift had a weak interaction with the Reunion plume, resulting in no underplating of the plume materials, as observed in the present model and supported by geophysical evidence (Behera et al., 2004).

7.4.4. concluding points

The principal findings of this study are concluded below:

- Using 2D thermomechanical numerical models, this study provides new insights into the modes of plume–rift interaction in a continental tectonic setting, which explain the interplay between the Réunion plume event and the palaeo-rift system in the Indian craton.
- The model results suggest that the interaction depends primarily on the lateral distance between the plume and the rift and the lithospheric plate velocity. Small plume-rift distance or high plate velocity empowers the pre-existing rift in pulling a substantial amount of fertile plume materials to accumulate beneath the rift axis, which eventually undergoes partial melting, leading to reactivation of the rift system due to the higher buoyancy flux. For a large plume-rift distance or low plate velocity, on the other hand, the plume materials escape the rift-pull, and underplate beneath the lithospheric base with little or no melt production, leaving the rift system without any reactivation.
- These model findings allow us to suggest that the Narmada-Tapti rift, which was close to the Réunion hotspot during Cretaceous time forced a large amount of plume materials to drift towards the rift. The fertile plume materials then underwent melting, resulting in Moho upwraping due to their high buoyancy flux, and subsequent reactivation of the palaeorift.
- The Godavari basin, located further away from the plume epicentre during this time, had little influence from the Reunion plume, and thereby did not involve any significant melting as the plume materials were depleted. The Godavari rift setting led to underplating of the plume head at the lithospheric base, followed by Moho downwraping as the buoyancy flux was relatively low.

- These model interpretations are aligned with the geophysical observations that suggest the occurrence of partial melts beneath the Narmada-Tapti region, whereas significant underplating with noticeable crustal thickening beneath the Godavari rift.

7.5. References

Badia, S., Nobile, F., & Vergara, C. (2008). Fluid–structure partitioned procedures based on Robin transmission conditions. *Journal of Computational Physics*, *227*(14), 7027-7051. https://doi.org/10.1016/j.jcp.2008.04.006

Baker, E. T., Hémond, C., Briais, A., Maia, M., Scheirer, D. S., Walker, S. L., ... & Chen, Y. J. (2014). Correlated patterns in hydrothermal plume distribution and apparent magmatic budget along 2500 km of the Southeast Indian Ridge. *Geochemistry, Geophysics, Geosystems*, *15*(8), 3198-3211.https://doi.org/10.1002/2014GC005344

Basantaray, A.K., Mandal, A., 2022. Interpretation of gravity–magnetic anomalies to delineate subsurface configuration beneath east geothermal province along the Mahanadi rift basin: a case study of non-volcanic hot springs. Geothermal Energy 10. https://doi.org/10.1186/s40517-022-00216-4

Becker, T.W., Lebedev, S., Long, M.D., 2012. On the relationship between azimuthal anisotropy from shear wave splitting and surface wave tomography. J Geophys Res Solid Earth 117. https://doi.org/10.1029/2011JB008705

Behera, L., Sain, K., Reddy, P.R., 2004. Evidence of underplating from seismic gravity studies in the Mahanadi delta eastern India and its tectonic significance. J Geophys Res Solid Earth 109, 1–25. https://doi.org/10.1029/2003JB002764

Behn, M.D., Lin, J., Zuber, M.T., 2002. Mechanisms of normal fault development at mid-ocean ridges. J Geophys Res Solid Earth 107. https://doi.org/10.1029/2001jb000503

Bicknell, J.D., Sempere, J.C., Macdonald, K.C., Fox, P.J., 1987. Tectonics of a fast spreading center: A Deep-Tow and sea beam survey on the East Pacific rise at 19°30′ S. Mar Geophys Res (Dordr) 9. https://doi.org/10.1007/BF00338249

Bruguier, N.J., Minshull, T.A., Brozena, J.M., 2003. Morphology and tectonics of the Mid-Atlantic Ridge, 7°-12°S. J Geophys Res Solid Earth 108. https://doi.org/10.1029/2001jb001172

Buck, W. R., Lavier, L. L., & Poliakov, A. N. (2005). Modes of faulting at mid-ocean ridges. *Nature*, *434*(7034), 719-723.https://doi.org/10.1038/nature03358

Carbotte, S. M., Smith, D. K., Cannat, M., & Klein, E. M. (2016). Tectonic and magmatic segmentation of the Global Ocean Ridge System: a synthesis of observations. *Geological Society, London, Special Publications*, *420*(1), 249-295.https://doi.org/10.1144/SP420.5

Carbotte, S., Welch, S.M., MacDonald, K.C., 1991. Spreading rates, rift propagation, and fracture zone offset histories during the past 5 my on the Mid-Atlantic Ridge; 25°-27°30′ S and 31°-34°30′ S. Mar Geophys Res (Dordr) 13. https://doi.org/10.1007/BF02428195

Catherine, J.K., Gahalaut, K., Gahalaut, V.K., 2007. Role of flexure in earthquake triggering along the Western Ghat escarpment, India. J Asian Earth Sci 31, 104–111. https://doi.org/10.1016/J.JSEAES.2007.04.005

Chadwick, J., Perfit, M., Ridley, I., Jonasson, I., Kamenov, G., Chadwick, W., ... & Smith, M. (2005). Magmatic effects of the Cobb hot spot on the Juan de Fuca Ridge. *Journal of Geophysical Research: Solid Earth*, *110*(B3).https://doi.org/10.1029/2003JB002767.

Chatterjee, S., Goswami, A., Scotese, C.R., 2013. The longest voyage: Tectonic, magmatic, and paleoclimatic evolution of the Indian plate during its northward flight from Gondwana to Asia. Gondwana Research 23, 238–267. https://doi.org/10.1016/J.GR.2012.07.001

Chaudhuri, A.K., Deb, G.K., 2003. Proterozoic Rifting in the Pranhita-Godavari Valley: Implication on India-Antarctica Linkage. Gondwana Research 7, 301–312.

Chen, J., Olive, J. A., & Cannat, M. (2022). Thermal regime of slow and ultraslow spreading ridges controlled by melt supply and modes of emplacement. *Journal of Geophysical Research: Solid Earth*, *127*(4), https://doi.org/10.1029/2021JB023715.

Chenevez, J., P. Machetel, and A. Nicolas (1998), Numerical models of magma chambers in the Oman ophiolite, J. Geophys. Res., 103(B7), 15,443–15,455. *https://doi.org/10.1029/98JB00597*

Choi, E. seo, Lavier, L., Gurnis, M., 2008. Thermomechanics of mid-ocean ridge segmentation. Physics of the Earth and Planetary Interiors 171. https://doi.org/10.1016/j.pepi.2008.08.010

Choi, E. seo, Lavier, L., Gurnis, M., 2008. Thermomechanics of mid-ocean ridge segmentation. Physics of the Earth and Planetary Interiors 171. https://doi.org/10.1016/j.pepi.2008.08.010

Choubey, V.D., 1971. Narmada-Son Lineament, India. Nature 232, 38–40

Cox, K.G., 1980. A Model for Flood Basalt Vulcanism. Journal of Petrology 21, 629–650. https://doi.org/10.1093/PETROLOGY/21.4.629

Cox, K.G., 1989. The role of mantle plumes in the development of continental drainage patterns. Nature 342, 873–877. https://doi.org/10.1038/342873A0

DeMets, C., Gordon, R.G., Argus, D.F., Stein, S., 1994. Effect of recent revisions to the geomagnetic reversal time scale on estimates of current plate motions. Geophys Res Lett 21. https://doi.org/10.1029/94GL02118

DiBiase, R.A., Whipple, K.X., 2011. The influence of erosion thresholds and runoff variability on the relationships among topography, climate, and erosion rate. J Geophys Res Earth Surf 116. https://doi.org/10.1029/2011JF002095

Dilek, Y., Furnes, H., 2011. Ophiolite genesis and global tectonics: Geochemical and tectonic fingerprinting of ancient oceanic lithosphere. Bulletin of the Geological Society of America 123. https://doi.org/10.1130/B30446.1

Escartín, J., Smith, D. K., Cann, J., Schouten, H., Langmuir, C. H., & Escrig, S. (2008). Central role of detachment faults in accretion of slow-spreading oceanic lithosphere. *Nature*, *455*(7214), 790-794. https://doi.org/10.1038/nature07333

Evans, R. L., Tarits, P., Chave, A. D., White, A., Heinson, G., Filloux, J. H., ... & Unsworth, M. J. (1999). Asymmetric electrical structure in the mantle beneath the East Pacific Rise at 17S. *Science*, *286*(5440),752756.https://doi.org/10.1126/science.286.5440.752

Fontaine, F. J., Rabinowicz, M., & Cannat, M. (2017). Can high-temperature, high-heat flux hydrothermal vent fields be explained by thermal convection in the lower crust along fast-spreading M id-O cean R idges?. *Geochemistry, Geophysics, Geosystems*, *18*(5), 1907-1925. https://doi.org/10.1002/2016GC006737

Fox, P.J., Grindlay, N.R., MacDonald, K.C., 1991. The Mid-atlantic Ridge (31°S-34°30′S): Temporal and spatial variations of accretionary processes. Mar Geophys Res (Dordr) 13. https://doi.org/10.1007/BF02428193

Freund, R., Merzer, M., 1976. The formation of rift valleys and their zigzag fault patterns. Geol Mag 113. https://doi.org/10.1017/S0016756800041315

Gerya, T. V. (2013). Three-dimensional thermomechanical modeling of oceanic spreading initiation and evolution. *Physics of the Earth and Planetary Interiors*, *214*, 35-52. https://doi.org/10.1016/j.pepi.2012.10.007

Ghosh, G.K., 2015. Interpretation of Gravity Anomaly and Crustal Thickness Mapping of Narmada-Son Lineament in Central India. Journal of Geological Society of India 86, 263–274.

Goff, J.A., 1991. A global and regional stochastic analysis of near-ridge abyssal hill morphology. J Geophys Res 96. https://doi.org/10.1029/91jb02275

Grindlay, N. R., Madsen, J. A., Rommevaux-Jestin, C., & Sclater, J. (1998). A different pattern of ridge segmentation and mantle Bouguer gravity anomalies along the ultra-slow spreading Southwest Indian Ridge (15° 30′ E to 25° E). *Earth and Planetary Science Letters*, *161*(1-4), 243-253.https://doi.org/10.1016/S0012-821X(98)00154-X

Grindlay, N.R., Fox, P.J., MacDonald, K.C., 1991. Second-order ridge axis discontinuities in the south Atlantic: Morphology, structure, and evolution. Mar Geophys Res (Dordr) 13. https://doi.org/10.1007/BF02428194

Gudmundsson, A. (2012). Magma chambers: Formation, local stresses, excess pressures, and compartments. *Journal of Volcanology and Geothermal Research*, *237*, 19-41. https://doi.org/10.1016/j.jvolgeores.2012.05.015

Gudmundsson, A., 2003. Surface stresses associated with arrested dykes in rift zones. Bull Volcanol 65. https://doi.org/10.1007/s00445-003-0289-7

Jain, S.C., Nair, K.K.K., Yedekar, D.B., 1995. Geology of the Son-Narmada-Tapti lineament zone in Central India.

Jha, K., Padma Rao, B., Sribin, C., Silpa, S., 2023. Analysis of seismic noise of broadband seismological stations installed along the Western Ghats. J Seismol 27, 325–342. https://doi.org/10.1007/S10950-023-10138-8/FIGURES/11

Kaila, K.L., Murty, P.R.K., Rao, V.K., Venkateswarlu, N., 1990. Deep seismic sounding in the Godavari Graben and Godavari (coastal) Basin, India. Tectonophysics 173, 307–317.

Katz, R. F. (2010). Porosity-driven convection and asymmetry beneath mid-ocean ridges. *Geochemistry, Geophysics, Geosystems*, *11*(11). https://doi.org/10.1029/2010GC003282

Key, K., Constable, S., Liu, L., & Pommier, A. (2013). Electrical image of passive mantle upwelling beneath the northern East Pacific Rise. *Nature*, *495*(7442), 499-502. https://doi.org/10.1038/nature11932

Kühn, D., Dahm, T., 2004. Simulation of magma ascent by dykes in the mantle beneath mid-ocean ridges. J Geodyn 38. https://doi.org/10.1016/j.jog.2004.06.002

Kumar, M.R., Singh, A., Kumar, N., Sarkar, D., 2015. Passive seismological imaging of the Narmada paleo-rift, central India. Precambrian Res 270, 155–164. https://doi.org/10.1016/j.precamres.2015.09.013

Kuo, B.Y., Forsyth, D.W., 1988. Gravity anomalies of the ridge-transform system in the South Atlantic between 31 and 34.5° S: Upwelling centers and variations in crustal thickness. Mar Geophys Res (Dordr) 10. https://doi.org/10.1007/BF00310065

Lange, A. E., Nielsen, R. L., Tepley III, F. J., & Kent, A. J. (2013). The petrogenesis of plagioclase‐phyric basalts at mid‐ocean ridges. *Geochemistry, Geophysics, Geosystems*, *14*(8), 3282-3296. https://doi.org/10.1002/ggge.20207

Lin, J., & Parmentier, E. M. (1990). A finite amplitude necking model of rifting in brittle lithosphere. *Journal of Geophysical Research: Solid Earth*, *95*(B4), 4909-4923. https://doi.org/10.1029/JB095iB04p04909

Lissenberg, C. J., MacLeod, C. J., & Bennett, E. N. (2019). Consequences of a crystal mush-dominated magma plumbing system: a mid-ocean ridge perspective. *Philosophical Transactions of the Royal Society A*, *377*(2139), 20180014. https://doi.org/10.1098/rsta.2018.0014

Lonsdale, P., 1994. Geomorphology and structural segmentation of the crest of the southern (Pacific-Antarctic) East Pacific Rise. J Geophys Res 99. https://doi.org/10.1029/93JB02756

Luttrell, K., Sandwell, D., 2012. Constraints on 3-D stress in the crust from support of mid-ocean ridge topography. J Geophys Res Solid Earth 117. https://doi.org/10.1029/2011JB008765

Macdonald, K.C., 1977. Near-bottom magnetic anomalies, asymmetric spreading, oblique spreading, and tectonics of the Mid-Atlantic Ridge near lat 37°N. Bulletin of the Geological Society of America 88. https://doi.org/10.1130/0016-7606(1977)88<541:NMAASO>2.0.CO;2

Mahoney, J. J., Graham, D. W., Christie, D. M., Johnson, K. T. M., Hall, L. S., & Vonderhaar, D. L. (2002). Between a hotspot and a cold spot: isotopic variation in the Southeast Indian Ridge asthenosphere, 86 E–118 E. *Journal of Petrology*, *43*(7), 1155-1176. https://doi.org/10.1093/petrology/43.7.1155

Maia, M., Sichel, S., Briais, A., Brunelli, D., Ligi, M., Ferreira, N., Campos, T., Mougel, B., Brehme, I., Hémond, C., Motoki, A., Moura, D., Scalabrin, C., Pessanha, I., Alves, E., Ayres, A., Oliveira, P., 2016. Extreme mantle uplift and exhumation along a transpressive transform fault. Nat Geosci 9. https://doi.org/10.1038/ngeo2759

Mallows, C., & Searle, R. C. (2012). A geophysical study of oceanic core complexes and surrounding terrain, Mid-Atlantic Ridge 13° N–14° N. *Geochemistry, Geophysics, Geosystems*, *13*(6).https://doi.org/10.1029/2012GC004075

Mandal, N., Sarkar, S., Baruah, A., & Dutta, U. (2018). Production, pathways and budgets of melts in mid-ocean ridges: An enthalpy based thermo-mechanical model. *Physics of the Earth and Planetary Interiors*, *277*, 55-69.https://doi.org/10.1016/j.pepi.2018.01.008

Mandal, S.K., Burg, J.P., Haghipour, N., 2017. Geomorphic fluvial markers reveal transient landscape evolution in tectonically quiescent southern Peninsular India. Geological Journal 52, 681–702. https://doi.org/10.1002/GJ.2833

Mandal, S.K., Fellin, M.G., Burg, J.P., Maden, C., 2015. Phanerozoic surface history of southern Peninsular India from apatite (U-Th-Sm)/He data. Geochemistry, Geophysics, Geosystems 16, 3626–3648. https://doi.org/10.1002/2015GC005977

Mandal, S.K., Lupker, M., Burg, J.P., Valla, P.G., Haghipour, N., Christl, M., 2015. Spatial variability of 10Be-derived erosion rates across the southern Peninsular Indian escarpment: A key to landscape evolution across passive margins. Earth Planet Sci Lett 425, 154–167. https://doi.org/10.1016/J.EPSL.2015.05.050

Mishra, D.C., 1977. Possible extensions of the Narmada-Son lineament towards Murray Ridge (Arabian Sea) and the eastern syntaxial bend of the Himalayas. Earth Planet Sci Lett 36, 301–308

Neves, M.C., Bott, M.H.P., Searle, R.C., 2004. Patterns of stress at midocean ridges and their offsets due to seafloor subsidence. Tectonophysics 386. https://doi.org/10.1016/j.tecto.2004.06.010

Oldenburg, D.W., 1975. A Physical Model for the Creation of the Lithosphere. Geophysical Journal of the Royal Astronomical Society 43. https://doi.org/10.1111/j.1365-246X.1975.tb00642.x

Ondréas, H., Aslanian, D., Géli, L., Olivet, J.L., Briais, A., 2001. Variations in axial morphology, segmentation, and seafloor roughness along the Pacific-Antarctic Ridge between 56°S and 66°S. J Geophys Res Solid Earth 106. https://doi.org/10.1029/2000jb900394

Parnell-Turner, R., Sohn, R.A., Peirce, C., Reston, T.J., MacLeod, C.J., Searle, R.C., Simão, N.M., 2017. Oceanic detachment faults generate compression in extension. Geology 45. https://doi.org/10.1130/G39232.1

Persaud, P., Tan, E., Contreras, J., Lavier, L., 2017. A bottom-driven mechanism for distributed faulting in the Gulf of California rift. Tectonophysics 719–720. https://doi.org/10.1016/j.tecto.2016.11.024

Picard, D., L. Arbaret, M. Pichavant, R. Champallier, and P. Launeau (2013), The rheological transition in plagioclase-bearing magmas, J. Geophys. Res. Solid Earth, 118, 1363–1377, doi:*10.1002/jgrb.50091*.

Pollard, D.D., Aydin, A., 1984. PROPAGATION AND LINKAGE OF OCEANIC RIDGE SEGMENTS. J Geophys Res 89. https://doi.org/10.1029/JB089iB12p10017

Prasad, K.N.D., Singh, A.P., Tiwari, V.M., 2018. 3D upper crustal density structure of the Deccan Syneclise, Central India. Geophys Prospect 66, 1625–1640. https://doi.org/10.1111/1365-2478.12675

Qureshy, M.N., 1982. Geophysical and Landsat lineament mapping — An approach illustrated from west-central and south India. Photogrammetria 37, 161–184.

Radhakrishna, B.P., 1993. Neogene uplift and geomorphic rejuvenation of the Indian Peninsula. Curr Sci Vol. 64, No. 11/12, 787–793. https://doi.org/https://www.jstor.org/stable/24096189

Rai, S.S., Kumar, T.V., Jagadeesh, S., 2005. Seismic evidence for significant crustal thickening beneath Jabalpur earthquake, 21 May 1997, source region in Narmada-Son lineament, central India. Geophys Res Lett 32, 1–5. https://doi.org/10.1029/2005GL023580

Rao, D.G., Krishna, K.S., Sar, D., 1997. Crustal evolution and sedimentation history of the Bay of Bengal since the Cretaceous. J Geophys Res Solid Earth 102, 17747–17768. https://doi.org/10.1029/96JB01339

Reverso, T., Vandemeulebrouck, J., Jouanne, F., Pinel, V., Villemin, T., Sturkell, E., & Bascou, P. (2014). A two-magma chamber model as a source of deformation at Grímsvötn Volcano, Iceland. *Journal of Geophysical Research: Solid Earth*, *119*(6), 4666-4683. https://doi.org/10.1002/2013JB010569

Richards, F.D., Hoggard, M.J., White, N.J., 2016. Cenozoic epeirogeny of the Indian peninsula. Geochemistry, Geophysics, Geosystems 17, 4920–4954. https://doi.org/10.1002/2016GC006545

Rowley, D. B., Forte, A. M., Rowan, C. J., Glišović, P., Moucha, R., Grand, S. P., & Simmons, N. A. (2016). Kinematics and dynamics of the East Pacific Rise linked to a stable, deep-mantle upwelling. Science advances, 2(12), e1601107. https://doi.org/10.1126/sciadv.1601107

Rundquist, D. V., Sobolev, P.O., 2002. Seismicity of mid-oceanic ridges and its geodynamic implications: A review. Earth Sci Rev. https://doi.org/10.1016/S0012-8252(01)00086-1

Sarkar, S., Baruah, A., Dutta, U., & Mandal, N. (2014). Role of random thermal perturbations in the magmatic segmentation of mid-oceanic ridges: Insights from numerical simulations. Tectonophysics, 636, 83-99. https://doi.org/10.1016/j.tecto.2014.08.008

Searle, R. C., & Escartin, J. (2013). The rheology and morphology of oceanic lithosphere and mid-ocean ridges.

Searle, R. C., Keeton, J. A., Owens, R. B., White, R. S., Mecklenburgh, R., Parsons, B., & Lee, S. M. (1998). The Reykjanes Ridge: structure and tectonics of a hot-spot-influenced, slow-spreading ridge, from multibeam bathymetry, gravity and magnetic investigations. *Earth and Planetary Science Letters*, *160*(3-4), 463-478. https://doi.org/10.1016/S0012-821X(98)00104-6

Sempéré, J. C., & Cochran, J. R. (1997). The Southeast Indian Ridge between 88 E and 118 E: Variations in crustal accretion at constant spreading rate. Journal of Geophysical Research: Solid Earth, 102(B7), 15489-15505. https://doi.org/10.1029/97JB00511

Singh, A., Kumar, M.R., Kumar, N., Saikia, D., Solomon Raju, P., Srinagesh, D., Rao, N.P., Sarkar, D., 2012. Seismic signatures of an altered crust and a normal transition zone structure beneath the Godavari rift. Precambrian Res 220–221, 1–8. https://doi.org/10.1016/j.precamres.2012.07.006

Singh, A., Singh, C., Kennett, B.L.N., 2015. A review of crust and upper mantle structure beneath the Indian subcontinent. Tectonophysics. https://doi.org/10.1016/j.tecto.2015.01.007

Singh, A.P., 1998. 3-D Structure and geodynamic evolution of accreted igneous layer in the Narmada-Tapti region (India). J Geodyn 25, 129–141.

Solomon, S.C., Huang, P.Y., Meinke, L., 1988. The seismic moment budget of slowly spreading ridges. Nature 334. https://doi.org/10.1038/334058a0

Sribin, C., Padma Rao, B., Rohilla, S., Jha, K., 2024. Crustal structure beneath the Western Dharwar Craton segment of Western Ghats: Insights from ambient noise correlation technique. J Asian Earth Sci 272, 106240. https://doi.org/10.1016/J.JSEAES.2024.106240

Turcotte, D.L., 1974. Are transform faults thermal contraction cracks? J Geophys Res 79. https://doi.org/10.1029/jb079i017p02573

Wanless, V. D., & Shaw, A. M. (2012). Lower crustal crystallization and melt evolution at mid-ocean ridges. *Nature Geoscience*, *5*(9), 651-655. https://doi.org/10.1038/ngeo1552

Watts, A.B., Cox, K.G., 1989a. The Deccan Traps: an interpretation in terms of progressive lithospheric flexure in response to a migrating load. Earth Planet Sci Lett 93, 85–97. https://doi.org/10.1016/0012-821X(89)90186-6

West, M., Menke, W., & Tolstoy, M. (2003). Focused magma supply at the intersection of the Cobb hotspot and the Juan de Fuca ridge. Geophysical Research Letters, 30(14). https://doi.org/10.1029/2003GL017104

White, R. S., Bown, J. W., & Smallwood, J. R. (1995). The temperature of the Iceland plume and origin of outward-propagating V-shaped ridges. *Journal of the Geological Society*, *152*(6), 1039-1045. https://doi.org/10.1144/GSL.JGS.1995.152.01.26

Widdowson, M., Cox, K.G., 1996. Uplift and erosional history of the Deccan Traps, India: Evidence from laterites and drainage patterns of the Western Ghats and Konkan Coast. Earth Planet Sci Lett 137, 57–69. https://doi.org/10.1016/0012-821X(95)00211-T

Publications

- **Sen, J**., Sarkar, S., & Mandal, N. (2023). Control of mush complex viscosity on mid-ocean ridge topography: A fluid–structure model analysis. *Physics of Fluids*, *35*(6). https://doi.org/10.1063/5.0152667

- **Sen, J.**, Sarkar, S., & Mandal, N. (2023). Complexity in the 3D stress fields of mid-ocean ridge tectonics: a manifestation of sub-crustal mush dynamics. Under review in *Physics of Earth and Planetary Interiors* (Manuscript id: PEPI-D-23-00189**).** (doi: 10.31223/X5GD5S.)

- **Sen, J.**, Roy, A., & Mandal, N. (2024). Decoding the Eastward Tilt of the Indian Peninsular Plateau: Insights from Geodynamic Modelling. Under review in *Geochemistry, Geophysics and Geosystems* (Manuscript id: 2025GC012205). (doi: 10.31223/X56F0R)

- Ghosh, D., **Sen, J.**, & Mandal, N. (2025). Rift-Induced Repositioning of Mantle Plumes Beneath the Indian Lithosphere: Implications for Deccan Volcanism. In prep for *Earth and Planetary Science Letters.* (doi: *10.31223/X59Q73)*

- Ghosh, D., **Sen, J.**, & Mandal, N. (2024). Periodicity in the Deccan volcanism modulated by plume perturbations at the mid-mantle transition zone. *Journal of Geophysical Research: Solid Earth*, *129*(6), e2024JB029020. https://doi.org/10.1029/2024JB029020

- Dasgupta, R., **Sen, J.**, & Mandal, N. (2021). Bending curvatures of subducting plates: old versus young slabs. *Geophysical Journal International*, *225*(3), 1963-1981. https://doi.org/10.1093/gji/ggab070

- Maiti, G., Roy, A., **Sen, J.**, & Mandal, N. (2021). Impact of Decelerating India-Asia Convergence on the Crustal Flow Kinematics in Tibet: An Insight From Scaled Laboratory Modeling. *Geochemistry, Geophysics, Geosystems*, *22*(11), e2021GC009967. https://doi.org/10.1029/2021GC009967